
# Studying Greenland ice sheet processes with high-resolution digital elevation models

Laura Isobel Melling, MSci (Hons)

Lancaster Environment Centre

Lancaster University

This thesis is submitted for the degree of

Doctor of Philosophy

April 2025

"THAT'S MORTALS FOR YOU, Death continued. THEY'VE ONLY GOT A FEW YEARS IN THIS WORLD AND THEY SPEND THEM ALL IN MAKING THINGS COMPLICATED FOR THEMSELVES. FASCINATING."

— Terry Pratchett, Mort

# Declaration

I declare that the work presented within this thesis is both, to the best of my knowledge and understanding, original and my own work. The material presented herein has not been submitted, either in whole or in part, for the award of a higher degree at this, or any other, university. This thesis does not exceed the maximum permitted word limit of 80,000 for the main text. The approximate word count is 60,230.

*Laura Isobel Melling*

# Studying Greenland ice sheet processes with high-resolution digital elevation models

Laura Isobel Melling, MSci (Hons)
Lancaster Environment Centre, Lancaster University
This thesis is submitted for the degree of *Doctor of Philosophy*, April 2025

# Abstract

Ice sheets are vast expanses of ice. The Greenland ice sheet (GrIS) is the second largest ice sheet on Earth at 1.7 million km$^2$ and is currently losing mass at an accelerating rate, contributing ~14 mm to global sea level rise between 1992 and 2020. Understanding the processes driving this mass imbalance is essential for projecting ice sheet evolution. This thesis explores methods for studying key GrIS processes using digital elevation models (DEMs), focusing on supraglacial lake depth estimation, floating ice tongue identification, and grounding line delineation.

Chapter 4 assesses the use of DEMs for measuring supraglacial lake depth, comparing ArcticDEM and ICESat-2 LiDAR-derived bathymetry with estimates from the radiative transfer equation (RTE) applied to Sentinel-2 imagery. While elevation-based methods agree strongly ($r$ = 0.98), RTE-derived depths show large biases and uncertainties with the green band overestimating depths by ≤ 153% and the red band underestimating depths by ≤ 63%. This highlights limitations in current optical approaches, demonstrating the value of multi-sensor validation for improving volume estimates.

Chapter 5 introduces an approach for identifying floating ice tongues using DEM deviation analysis across fifteen northern Greenland glaciers. The method identifies floating ice signatures on five lobes, confirms the absence of signatures on eight, and suggests ambiguous signatures on two. This provides a proof-of-concept that DEMs can be used to dynamically locate floating ice signatures.

Chapter 6 combines ArcticDEM with a tidal model to detect timestamped grounding lines based on tidal flexure. This method yields > 200 new grounding line estimates across three major glaciers, identifying a previously undocumented 3.45 km² ice tongue on one of these glaciers as of 2018.

These studies provide new tools for monitoring ice sheet processes, and their findings will support future research into the impact of climate change on our ice sheets and their stability.

# Publications

I confirm that the work submitted is my own, except where work which has formed part of jointly authored publications has been included. The contributions of myself and the other authors to this work have been explicitly indicated below. I confirm that appropriate credit has been given within this thesis where reference has been made to the work of others.

The research described in Chapter 4 is published as L. Melling et al. (2024), “Evaluation of satellite methods for estimating supraglacial lake depth in southwest Greenland”, The Cryosphere, https://doi.org/10.5194/tc-18-543-2024. L. Melling led the study and was supervised by A. Leeson, M. McMillan, and J. Maddalena. J. Bowling provided code to analyse the digital elevation models, E. Glen provided the lake inventory data, and M. Winstrup, L. Sandberg Sørensen, and R. Lørup Arildsen processed the ICESat-2 ATL03 data. All co-authors contributed to manuscript editing. This publication is an extension of the research I undertook during my master’s degree and constitutes a significant addition to the original work. These additions are detailed in the chapter cover page directly preceding Chapter 4.

The research described in Chapter 5 is prepared as a manuscript to be submitted as, “An inventory of northern Greenland’s floating ice tongues using high-resolution digital elevation models”. L. Melling led the study and was supervised by M. McMillan, J. Maddalena, and A. Leeson. M. Möller provided data pertaining to Flade Isblink. LM, M. McMillan, JM, and M. Möller contributed to manuscript editing.

The research described in Chapter 6 is prepared as a manuscript to be submitted as, “A new grounding line detection method using high-resolution digital elevation models and a tide model”. L. Melling led the study and was supervised by M. McMillan, J. Maddalena, and A. Leeson. LM, MM, and JM contributed to manuscript editing.

# Acknowledgements

This research was funded by the 4DGreenland ESA grant received by Malcolm McMillan and Amber Leeson and hosted at Lancaster University. I would like to express my gratitude for this financial support and the opportunities it afforded me.

I would additionally like to thank my supervisors; Malcolm McMillan, Amber Leeson, and Jennifer Maddalena, for their patience, encouragement, and support over the last four years. Working with you has given me experiences and opportunities that I am unlikely to otherwise have had, and I am grateful that you have provided me with the opportunity to develop my research skills and ideas.

I am also grateful for the support of Jade Bowling, Emily Glen, Louise Sandberg-Sørensen, Mai Winstrup, Rasmus Lørup Arildsen, and Marco Möller who have not only supplied me with various datasets, but also provided advice, support, and valuable insights as co-authors on my papers. Also, thank you to Alex Bush and Steven Palmer for their time and effort in reading and examining this thesis.

To those members of the glaciology group at Lancaster University whom I have not yet named, and to all the researchers at the UK NERC Centre for Polar Observation and Modelling, as well as the whole 4DGreenland team – this thesis is a testament to the skills and knowledge that I gained from you all, thank you.

Most importantly, I would like to thank my friends and family for their unwavering support and love. Knowing that I have people on whom I can rely for anything and everything has helped me more than you could ever know.

And finally, Sam. When I felt like quitting, you were there to listen to me. When I cried, you were there to hug me. And all the way through, you made me feel loved. I love you, Bub. Thank you.

# Abbreviations and acronyms

| | |
|---|---|
| 79N | 79 North Glacier |
| AIS | Antarctic ice sheet |
| AMOC | Atlantic meridional overturning circulation |
| ASTER | Advanced Spaceborne Thermal Emission and Reflection Radiometer |
| ASTER GDEM | Advanced Spaceborne Thermal Emission and Reflection Radiometer Global Digital Elevation Model |
| ATLAS | Advanced Topographic Laser Altimeter System |
| AUV | autonomous underwater vehicle |
| AVHRR | Advanced Very High Resolution Radiometer |
| CCI | Climate Change Initiative |
| CGAN | Convolutional generative adversarial network |
| CNÉS | Centre National d'Études Spatiales |
| CNN | Convolutional neural network |
| DEM | digital elevation model |
| DInSAR | differential interferometric synthetic aperture radar |
| ECV | essential climate variable |
| ERS | European Remote-Sensing Satellite |
| FES2022 | Finite Element Solution Model (2022) |
| GCOS | Global Climate Observing System |
| GEEDiT | Google Earth Engine Digitisation Tool |
| GIS | geographic information system |
| GrIS | Greenland ice sheet |

| | |
|---|---|
| ICESat | Ice, Cloud and land Elevation Satellite |
| InSAR | interferometric synthetic aperture radar |
| IPCC | Intergovernmental Panel on Climate Change |
| LiDAR | light detection and ranging |
| MODIS | Moderate Resolution Imaging Spectroradiometer |
| MISI | marine ice sheet instability |
| NAC | north Atlantic current |
| NEGIS | Northeast Greenland Ice Stream |
| PCRA | pseudo crossover radar altimetry |
| PGC | Polar Geospatial Center |
| RCP | representative concentration pathway |
| REMA | Reference Elevation Model of Antarctica |
| RGT | reference ground track |
| RMSD | root mean square difference |
| RPC | rational polynomial coefficient |
| RTE | radiative transfer equation |
| RTLA | repeat-track laser altimetry |
| SAR | synthetic aperture radar |
| SAR DROT | synthetic aperture radar differential range offset tracking |
| SETSM | Surface Extraction from TIN-based Searchspace Minimization |
| SfM | structure-from-motion |
| SMB | surface mass balance |
| SP | sampling point |
| SRTM | Shuttle Radar Topography Mission |

| | |
|---|---|
| THC | thermohaline circulation |
| TIN | triangulated irregular network |
| TMOC | tidal motion offset correlation |
| UAV | unmanned aerial vehicle |
| UNFCCC | United Nations Framework Convention on Climate Change |
| WNCC | weighted normalised cross-correlation |

# Contents

# List of Figures

# List of Equations

# LIST OF TABLES

# Chapter 1

# 1 Introduction – Glaciological principles and ice sheet background

This chapter outlines the geographic and climatic significance of ice sheets, particularly the Greenland ice sheet (GrIS), and their critical role in global climate regulation and sea level rise. I discuss how the ice sheets influence heat and oceanic circulation, weather patterns, and the ice-albedo feedback, which accelerates ice melt. Here, I also remark on the potential consequences of ice sheet mass loss, including the impact on global sea levels, climate systems, and coastal populations. This chapter concludes with a discussion of the importance of monitoring ice sheet dynamics, including supraglacial lakes and grounding lines, which are essential for improving climate models and informing policy decisions on sea level rise and related risks.

## 1.1 Geographic and climatic significance

Our planet has two major ice sheets, the GrIS and the Antarctic ice sheet (AIS) (Figure 1.1). The AIS is the largest at 12.3 million $km^2$, followed by the GrIS at 1.7 million $km^2$ (Goelzer et al., 2017; Otosaka et al., 2023). The ice sheets are important for heat regulation, ocean currents, atmospheric currents, and localised weather patterns, and regulation of the global climate is a key factor for each of these systems. The ice sheets buffer the range of variation experienced by the climate both temporally and spatially (also known as climatic variance) (Harper et al., 2012). This thesis focuses on the GrIS.

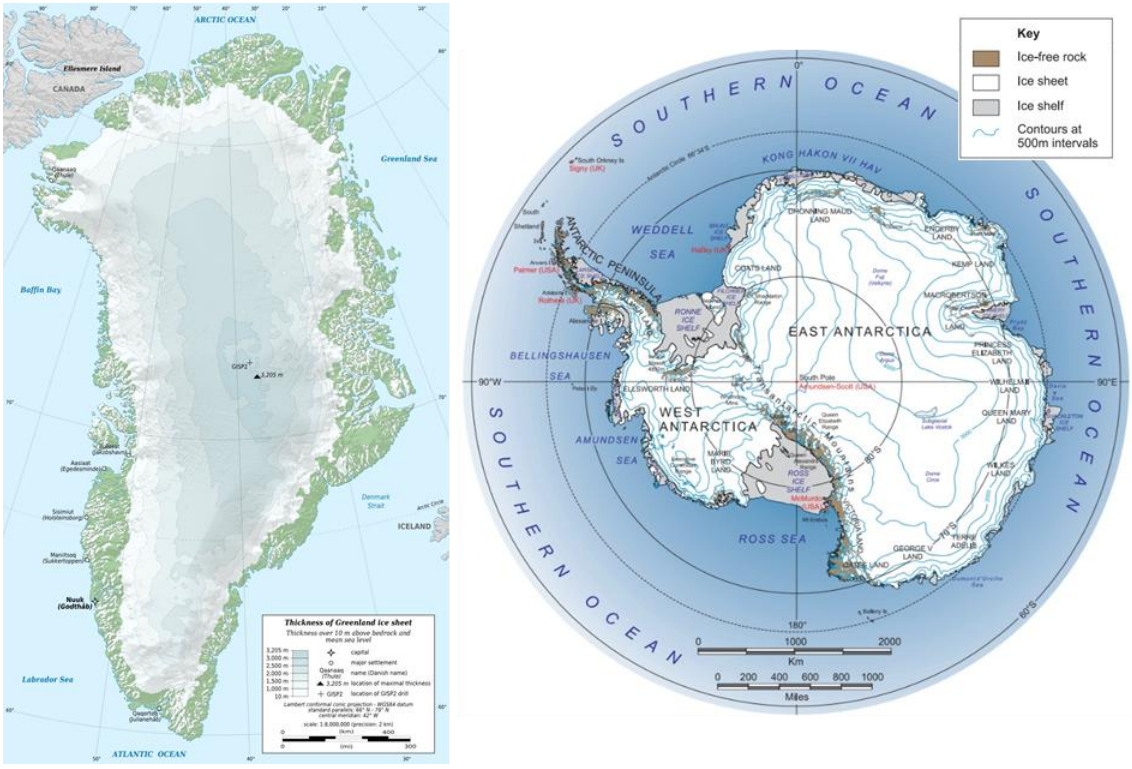


Figure 1.1: The GrIS with ice thickness (left) and the AIS (right) (image credits: (GrIS) Eric Gaba – Wikimedia Commons user: Sting, and (AIS) Landsat Image Mosaic of the Antarctica team https://lima.usgs.gov/documents/LIMA_overview_map.pdf).

Ice sheets also play direct and indirect roles in global sea level rise. Direct contributions include freshwater melt and calved icebergs entering the oceans from marine terminating glaciers. Ice sheets also contribute indirectly to sea level rise through the ice-albedo feedback. Albedo is a measure describing the ability of a surface to reflect incoming solar radiation, and it dictates the amount of radiation that the surface will absorb (Figure 1.2). The ice-albedo feedback is where the albedo of the ice sheet surface decreases, causing the ice sheet to absorb more solar radiation and accelerating ice melt rate. Darker surfaces have a lower albedo meaning that they absorb more energy, whereas lighter surfaces have higher albedo values, meaning they reflect more energy. Fresh snow has an albedo of 0.7-0.85 (Alexander et al., 2014) whereas bare ice has a much lower albedo of 0.31-0.57 (Wehrlé et al., 2021). Changes in temperature and in precipitation patterns caused by climate change will shift the relative proportions of ice and snow in favour of ice, and the ice sheet will be darker.

Representative concentration pathways (RCPs) represent different scenarios of greenhouse gas emissions and global temperature rises. Models suggest that unmitigated growth in greenhouse gas emissions with a global temperature rise of 4.3°C (RCP 8.5)

will likely result in significant environmental changes over the next millennium, including the complete loss of ice from the GrIS (Aschwanden et al., 2019). Aschwanden et al. (2019) found that the effect of glacial isostatic adjustment (where the Earth's crust moves vertically in response to ice loading) was negligible on the centennial time scale and was much less than the variance of their ensemble simulations after a millennium. Their ensemble predictions for RCP 8.5 estimated a global mean sea level rise of 7.27 m after 1000 years.

This complete loss of ice from the GrIS would mean that more of the Sun's radiation is absorbed by the Earth than at present, and our environments will become hotter, leading to more powerful storm systems, wetter winters, and dangerously high temperatures in summer (Ebi et al., 2021).

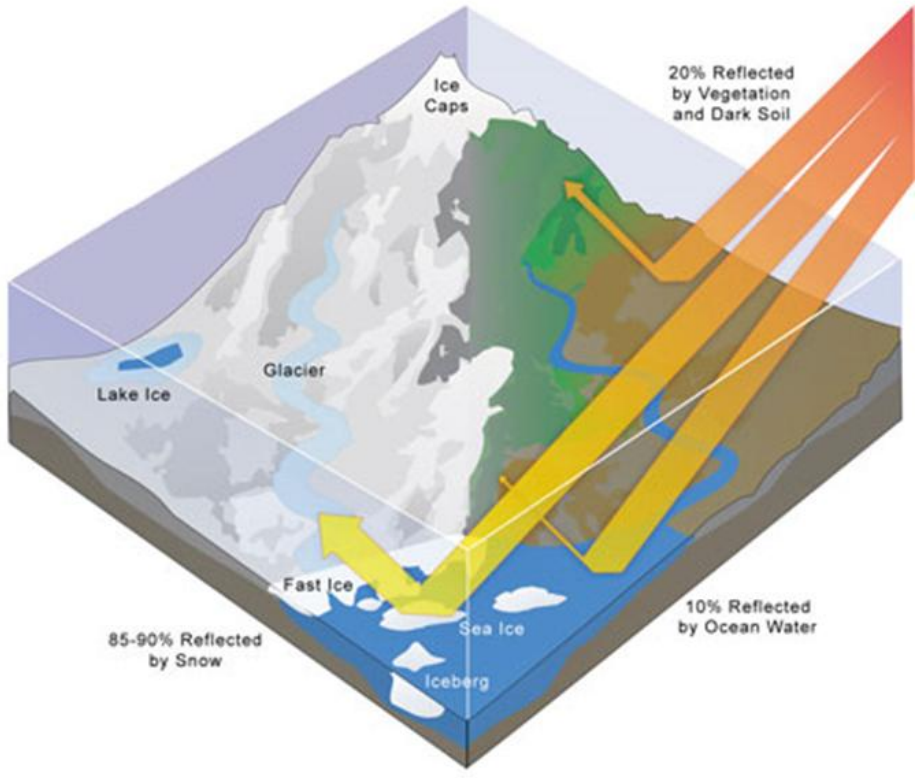


Figure 1.2: A schematic of albedo (adapted from Nelson (2021)).

Between 1992 and 2020, global mean sea levels rose by ~21 mm (Otosaka et al., 2023). Ice sheet mass loss is one component of the total global sea level rise budget, and others include thermal expansion, mountain glacier melt and post-glacial rebound (also known as glacial isostatic adjustment). Where the AIS has contributed ~7 mm to sea level rise between 1992 and 2020, the GrIS has contributed double at ~14 mm (Otosaka et al.,

2023). Complete melting of the GrIS represents a potential sea level rise of ~7 m (The IMBIE Team, 2020). By 2100, under RCP 8.5, estimates predict an additional 145–230 mm (179 mm mean) of global sea level rise from the ice sheets, with current measurements tracking this RCP most closely compared to other pathways (Horton et al., 2020; Slater et al., 2020) (Figure 1.3).

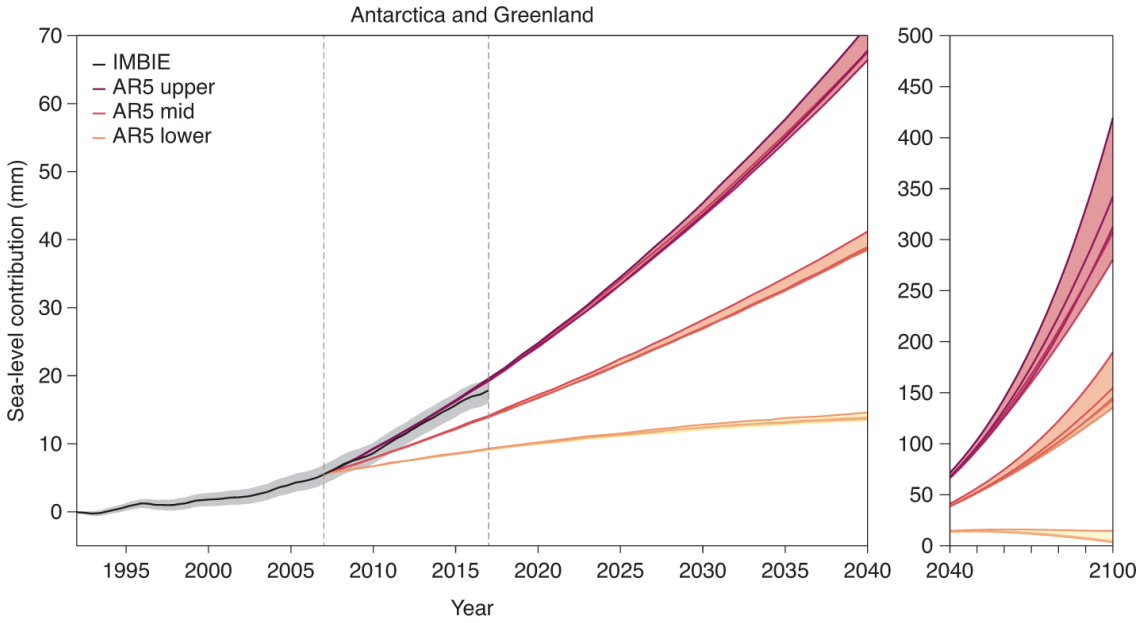


Figure 1.3: The AIS and GrIS contributions to global sea level (black) and IPCC fifth assessment report (AR5) projections for 1992–2040 (left) and 2040–2100 (right). AR5 pathways are indicated by darker lines in order of increasing emissions: RCP 2.6, RCP 4.5, RCP 6.0, SRES A1B and RCP 8.5. Shaded areas show the AR5 scenario spread and the estimated observation error. Dashed vertical lines bound the 2007-2017 period when the satellite observations and AR5 projections overlap (Slater et al., 2020).

This could have major geopolitical and humanitarian consequences in the coming decades (Figure 1.4), with an estimated 44-66 million people exposed annually to coastal flooding from ice sheet contributions to sea level rise under RCP 8.5 (Kulp and Strauss, 2019).

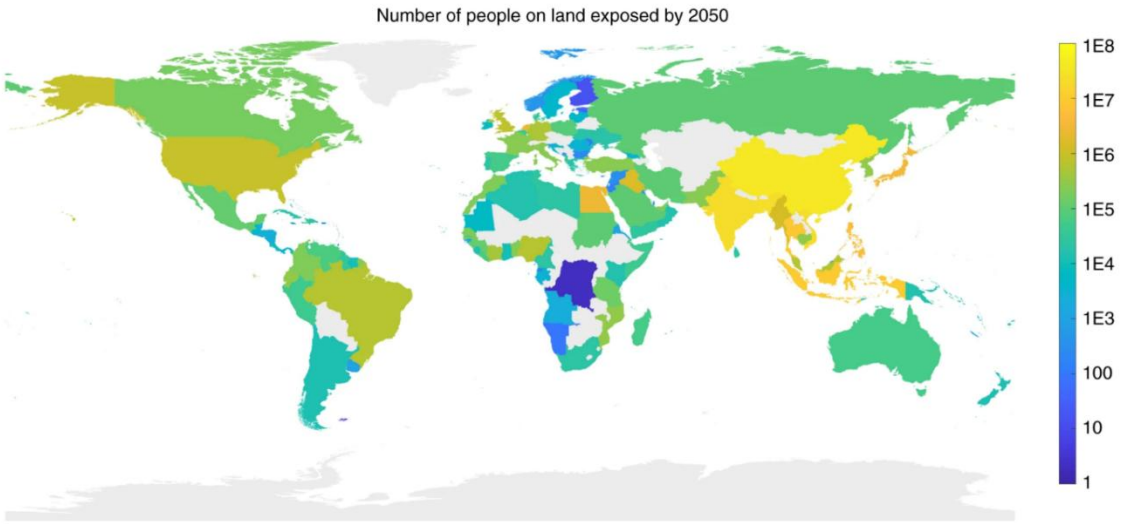


Figure 1.4: The number of people exposed to coastal flooding by 2050 assuming RCP 4.5 (Kulp and Strauss, 2019).

## 1.2 Ice sheet interactions with global climate systems

Ice sheet monitoring is important not only because of the roles of ice sheets as incoming radiation reflectors and contributors to global sea level rise but also as factors in thermal insulation and global heat exchange for atmospheric and oceanic modelling.

Ice sheets represent an intrinsic factor in thermal insulation and heat exchange. Monitoring ice calving and meltwater flux into the oceans is important because these processes can affect ocean circulation patterns as cold, fresh water enters global climate circulations (Dey et al., 2024). The Atlantic meridional overturning circulation (AMOC) is a key component of the thermohaline circulation (THC). It delivers warm, saline water to the upper layers of the north Atlantic and cold, less-saline water to the lower layers of the south Atlantic (Figure 1.5). This circulation plays a key role in the delivery of warm water to western Europe and relies on a delicate balance of cool and warm water input from the polar and tropical regions, respectively. If this balance were to shift towards an increased cool, freshwater input from the polar regions due to higher meltwater output and increased calving rates, the AMOC could weaken or completely shut down (van Westen et al., 2024). This is because freshwater has a lower density than saltwater and an increased freshwater input from the ice sheets would reduce the density of surface waters in the north Atlantic. This reduced density would prevent the surface water from sinking, preventing the circular thermal movement of water in the north Atlantic current (NAC). The decreased activity of the NAC would disrupt the environment of the British Isles

which are dependent on the NAC as a mediator of their local air and ocean temperatures (McCarthy et al., 2023).

With increased cool water flux into the AMOC from ice sheets, the ocean circulation may reach an irreversible tipping point by 2057 (Ditlevsen and Ditlevsen, 2023). Currently, the AMOC acts to tilt the surface the Atlantic Ocean, with the Gulf Stream pulling water away from the North American eastern seaboard through the exertion of a strong pressure gradient. This current effectively lowers the local sea level of the North American east coast compared to the average level of Atlantic Ocean. Even in a circumstance where the AMOC was only weakened, the rate of dynamic sea level rise across the North American east coast would increase as the influence of the Gulf Stream decreased (Little et al., 2019), and ecological productivity in the north Atlantic would be severely affected with the reduction of nutrients reaching the surface waters. Phyto- and zooplankton stocks within the north Atlantic would halve due to this reduction in nutrient cycling (Schmittner, 2005), greatly affecting the marine food web which relies on these primary producers and consumers as the base of nutrients for all marine life (Michaels and Silver, 1988).

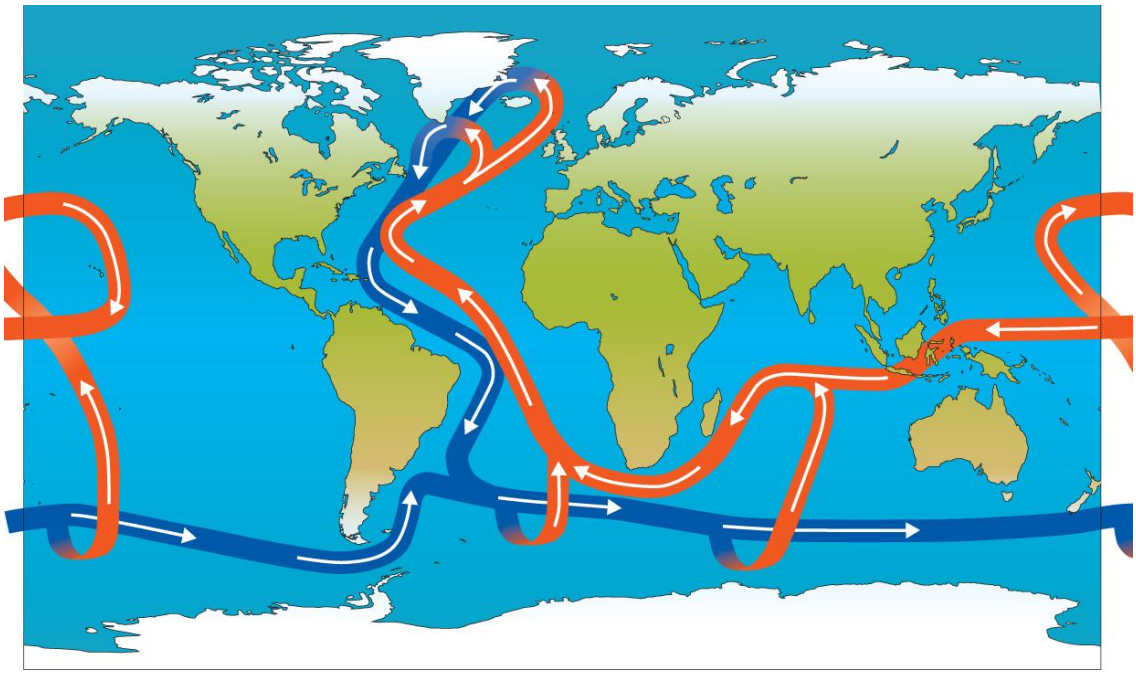

Figure 1.5: Global ocean circulations with cold deep waters in blue and warm surface waters in red (image credit: Met Office, https://www.metoffice.gov.uk/binaries/content/gallery/metofficegovuk/images/blog-images/2024/global-conveyor-diagram.jpg).

The THC is one of many global circulation systems and the potential weakening of the AMOC would threaten the THC and many of these other circulations (Figure 1.6). Amongst those affected would be atmospheric circulations which are responsible for Europe's climate and weather. If the delivery of warm water to the north Atlantic reduces, we would experience cooler temperatures in western Europe, leading to shifts in local atmospheric circulation (McCarthy et al., 2023). This would change precipitation patterns, causing both more intense droughts and heavier rainfall events (Kautz et al., 2022). Additionally, changes to the AMOC could instigate changes to the jet streams, further affecting climate and weather across the globe (Meccia et al., 2024).

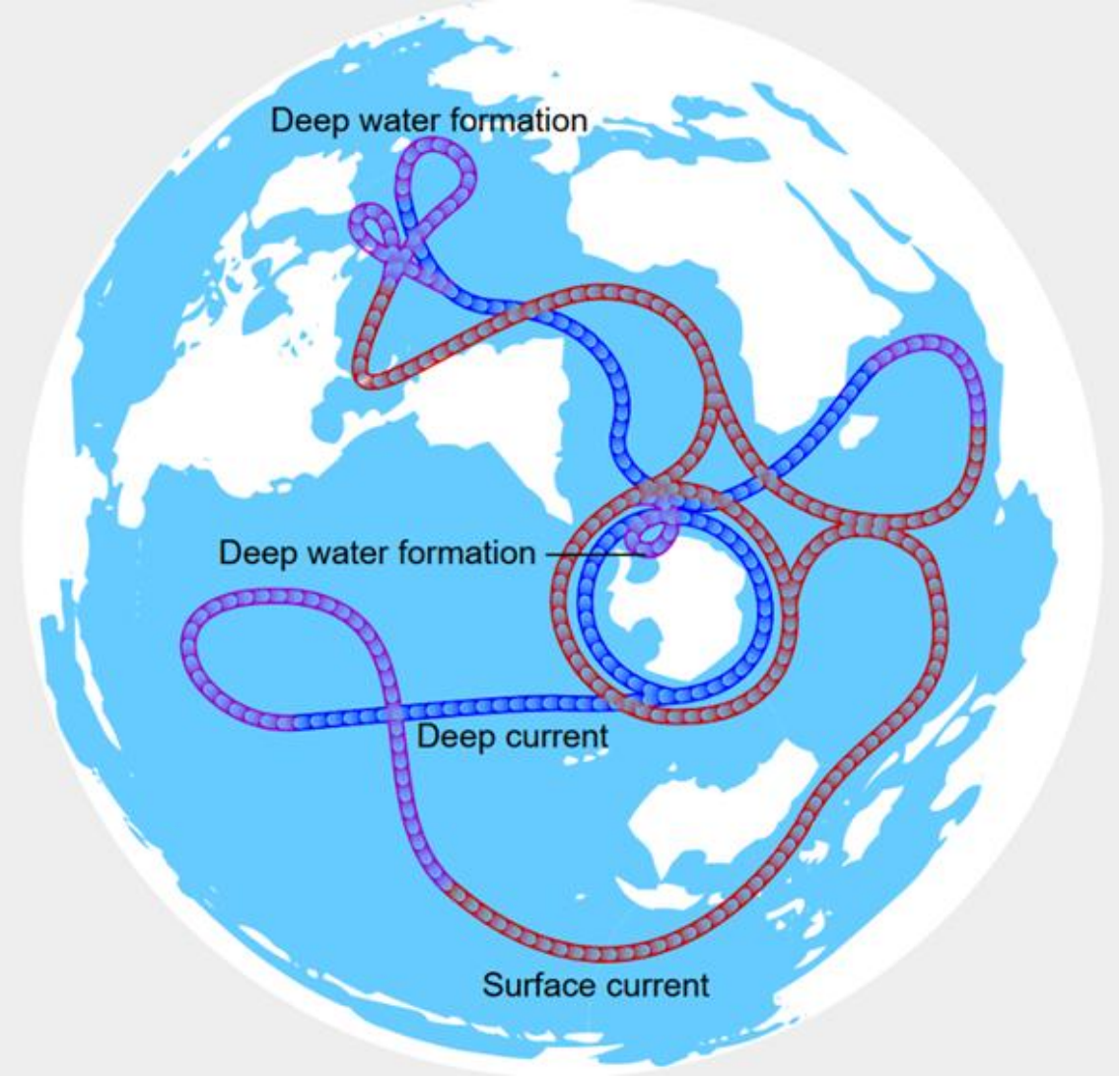


Figure 1.6: The AMOC in relation to the global THC (image credit: CMG Lee, Wikimedia Commons. Animation available at https://upload.wikimedia.org/wikipedia/commons/a/ab/Thermohaline_circulation.svg).

Climate models rely on accurate representations of the behaviour of our ice sheets (Smith et al., 2021). Data from ice sheet monitoring, including measurements of ice thickness, surface elevation changes, and ice dynamics, contribute directly to these models, and allow us to better predict future ice loss (e.g. Goelzer et al., 2017; Otosaka et al., 2023). Without accurate data, models may over- or underestimate future sea level rise and climate shifts such as the potential collapse of the AMOC. For instance, if the surface mass balance-elevation relationship (where ice at lower elevations melts at a faster rate) were ignored for the modelling of GrIS sea level rise contribution by 2100, we would underestimate the ice sheet's contributions to sea level rise by 4.4%. This increases to 9.6% by 2200 (Edwards et al., 2014).

Ice sheets interact with both the atmosphere and the ocean, and accurate data is necessary to couple our ice sheet models with atmospheric and oceanic models to simulate how changes in the ice sheet could affect other climate systems. Resultingly, accurate ice sheet monitoring is required not only to produce accurate ice sheet models, but to aid accurate prediction of all climate systems on our planet. By integrating ice sheet dynamics into other climate models, we can estimate how our climate could evolve under different scenarios of greenhouse gas emissions and global temperature increases (e.g. Dietz and Koninx, 2022; Dong et al., 2022). Understanding the volume of ice which may be lost from the GrIS or AIS in response to a given temperature rise helps model the future impacts on sea levels, coastal communities, and global ecosystems (e.g. Li et al., 2023b). Without accurate ice sheet data, our ability to predict and respond to climate change would be significantly hindered, with serious consequences for vulnerable populations, ecosystems, and infrastructure worldwide.

## 1.3 Mass balance and ice flow mechanics

### 1.3.1 Mass balance

Glaciers and ice sheets gain and lose mass through a balance of accumulation and ablation processes. Snow compacts over time to form the constituent layers of firn and ice observed on glaciers and ice sheets, representing the primary factor of mass gain. Mass loss occurs primarily through surface melting, iceberg calving and basal melting.

Surface mass balance (SMB) is the term used to describe the net gain (accumulation) or loss (ablation) from surface processes, with a focus on atmospheric interactions. Primarily, gain is via precipitation (snow, sleet, freezing rain, graupel, and hail), but also

includes, to a lesser degree, wind-blown snow, avalanching, and hoar frost. Loss is primarily through surface meltwater runoff from atmospheric melting and, to a lesser degree, wind-blown snow, avalanching, and sublimation. SMB tells us about the climate's direct surface impact and can be used to model surface processes. Total mass balance describes SMB plus dynamic ice loss via calving and ocean interactions which gives us a more complete understanding of the ice body's net balance and provides us with the data required to predict sea level rise.

The difference between the total mass gained and lost is known as the mass balance. Glaciers and ice sheets with positive mass balance are growing, whereas ones with negative mass balance are shrinking. Long-term negative mass balance of ice sheets contributes directly to global sea level rise. A glacier will exhibit areas where the mass balance is positive and areas where it is negative. The net result of these values tells us if the glacier is growing or shrinking.

We can estimate ice-sheet mass balance at large scales using three main remote sensing approaches; the geodetic method, the mass budget (input-output or IO) method, and the gravimetry method. The geodetic method measures surface elevation over time to calculate ice volume change and converts this to mass change by assuming average ice and firn densities. The mass budget method quantifies mass balance by comparing the mass gain from snowfall to the mass loss from surface melting, iceberg calving and basal melting. The gravimetry method uses changes in repeat satellite gravimetry observations and geophysical modelling to infer total mass change over time.

Together, these methods provide us with data about ice-sheet mass balance changes and are required to predict future sea level rise contributions from the ice sheets.

### 1.3.2 Ice flow mechanics

Due to gravitational forces, ice moves from the higher, colder interior of the GrIS to the lower, warmer margins where it is discharged into the oceans. The rate of this ice flow is affected by factors such as basal melt (affecting lubrication at the ice–bed interface), ice viscosity, and surface slope. Changes to the patterns or rate of ice flow can indicate larger changes in the climate such as increased air or ocean temperatures.

Ice sheets behave differently to glaciers in their ice flow mechanics. Where an ice sheet flows outwards in all directions from the centre under the force of gravity, glaciers generally flow in one direction. This flow profile is from high elevation to low elevation,

with the caveat that ice flow direction is dictated to a large extent by the bed topography, meaning that deviations can cause the ice flow to adopt an indirect path to the terminus. Ice flow in both ice sheets and glaciers is a function of surface slope, ice thickness, and basal lubrication. At the summit of an ice sheet, the surface slopes are the shallowest so ice flow is relatively slow at perhaps a few metres a year. At the coast, the ice flow speeds can reach up to several kilometres per year. For instance, Sermeq Kujalleq, a glacier on the GrIS, reached ice flow speeds of 17 km/yr in 2012 (Joughin et al., 2014). In some cases, fast ice motion can begin closer to the ice sheet interior and create a feature known as an ice stream. These are 'rivers' of fast-flowing ice bounded by slower-moving ice such as the Northeast Greenland Ice Stream (NEGIS) which terminates at Nioghalvfjerdsbræ (79N) and Zachariæ Isstrøm.

Glacial ice flow is not necessarily constant. Some glaciers are subject to cyclical ice flows known as surges and are referred to as 'surging' or 'surge-type'. These glaciers typically have a long period of quiescence (inactivity) where thinning and downwasting dominate the ablation zone and the glacier thickens in the accumulation zone. During this time the glacier moves slowly relative to its average speed. This is followed by short, often periodical, periods of high velocity (surges) relative to the glacier's average speeds where the front can advance dramatically and the ice reserves built in the upper reaches during the quiescent phase are depleted. Surges can be either Svalbard-type, where the flow acceleration is driven by a change from cold to temperate conditions at the ice–bed interface (Clarke, 1976), or Alaskan-type, where basal water pressure build up initiates surge propagation, and the release of water causes surge termination (Kamb, 1985).

## 1.4 Factors affecting mass loss

Ice sheet contribution to global sea level rise can be calculated from ice sheet mass loss. Ice sheet mass loss contributes to global sea level rise via two processes, ice discharge (the flow of ice from the inland ice to the ocean) and melt. The major forcing factors attributed to mass loss are atmospheric and oceanic where atmospheric factors include air temperature increases over the ice sheet and oceanic forcing factors include sea temperature rise.

### 1.4.1 Atmospheric factors

GrIS mass loss is increasing (Otosaka et al., 2023) (Figure 1.7). Although this mass loss is dominated by ice dynamics, surface melt is becoming increasingly responsible and is

predicted to increase more in the future (Scambos et al., 2021). This increase in surface melt is driven by increased air temperatures over the GrIS, and extreme melt years are becoming more common, with 2012 and 2019 experiencing summer net thinning of 1.78±0.24 m and 1.91±0.50 m in the ice sheet ablation zone, respectively (Slater et al., 2021).

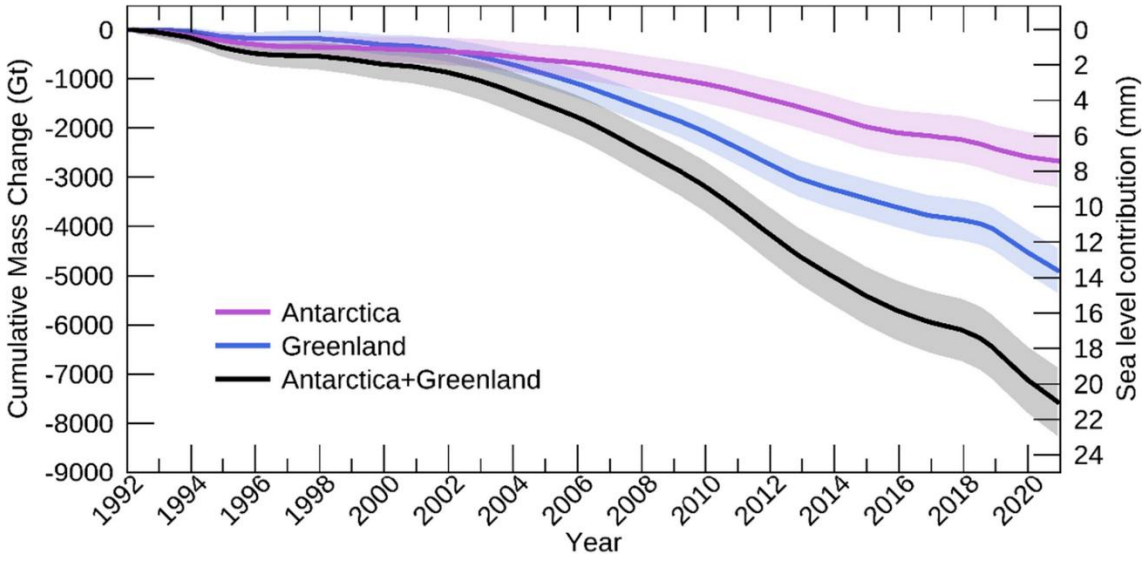


Figure 1.7: A time-series of the AIS and GrIS cumulative mass change derived from satellite gravimetry, satellite altimetry, and mass budget estimates (Otosaka et al., 2023).

Surface melt can leave the ice sheet as surface runoff, but in doing so it creates a complex hydrological system on the ice sheet surface, consisting of streams, ponds, and slush fields (Figure 1.8). When the water pools in surface depressions – whose locations are dictated by the bedrock topography (Echelmeyer et al., 1991; Krawczynski et al., 2009) – they are known as supraglacial lakes (where supra means ‘above’). These lakes function as surface water storage and reduce the amount of surface runoff. The supraglacial hydrology of the GrIS has become more active in the last few decades, with the increase in water volume largely attributed to atmospheric warming causing an increase in surface water (Slater et al., 2021). Additionally, the distribution of these lakes in migrating further inland with rising air temperatures (Glen et al., 2025).

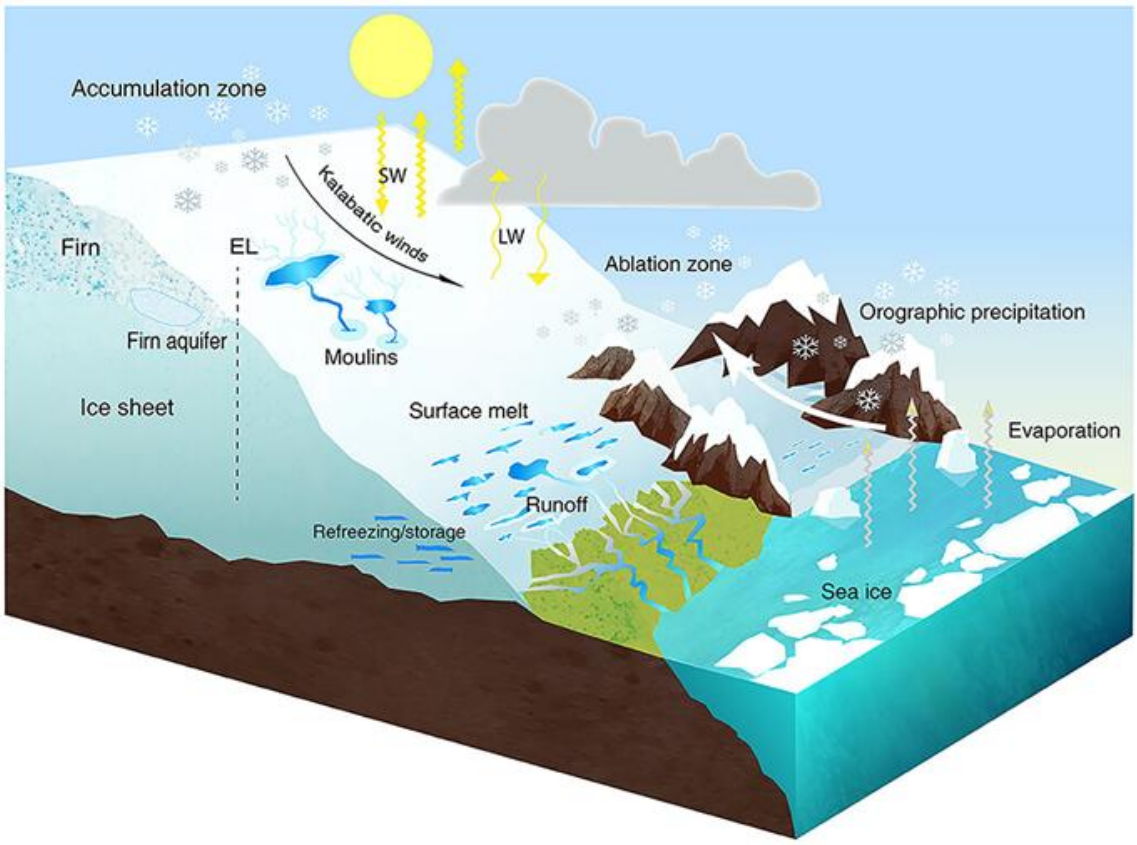


Figure 1.8: An illustration of the surface mass balance processes on the GrIS (Lenaerts et al., 2019).

Supraglacial lakes can persist for weeks to months and may drain through the ice sheet to the bed via moulins (vertical shafts in the ice), overtop and drain via the surface, or refreeze during the colder winter months (Selmes et al., 2013) (Figure 1.9). Their formation and drainage have significant impacts on ice sheet dynamics. When the lake volume reaches a critical mass, hydrofracture may occur. This process describes the mechanism by which the overbearing weight of water weakens the ice below the lake, opening cracks through which the water may drain. These lakes may drain in as little as 2 hours (Das et al., 2008). The crevasses conduct water into the englacial and subglacial environments through subsurface routing where the water may reach the ice–bedrock interface and be routed into subglacial lakes (Palmer et al., 2015), or lubricate the region and reduce frictional forces (Fitzpatrick et al., 2013; Christoffersen et al., 2018; Maier et al., 2023; Tedesco et al., 2013; Tuckett et al., 2019). However, some research suggests that the annual motion of certain glaciers is insensitive to high-input periods such as the summer melt event of 2012, with slower winter ice flow speeds than previous low melt

years (Tedstone et al., 2013). This suggests that ice-bedrock lubrication may be more important in some regions of the GrIS than others.


Figure 1.9: Images of a: (a) supraglacial channel on the ice surface, (b) supraglacial lake, and (c) moulin (image credits: (a) M. Tedesco, (b) J. Gulley, and (c) J. Gulley).

Additionally, the presence of supraglacial lakes reduces surface albedo, meaning they absorb more solar radiation and contribute to further ice melting. The deeper these lakes, the lower their surface albedo. Accurate depth detection allows for better modelling of this positive feedback loop, improving predictions of future melt rates. Improved knowledge of lake depth also improves our modelling of subsurface hydrology. This is essential for determining how the ice sheet-bedrock interface may respond to increased surface water input caused by increasing air temperatures.

### 1.4.2 Oceanic factors

Ice sheet monitoring enhances our understanding of the floating extensions of glaciers by providing crucial insights into their dynamics, including velocities, calving events, and the formation of surface fractures. The interaction between the floating extensions of glaciers and the ocean water is another key area of study which aids our understanding of ice dynamics. Ocean currents beneath ice tongues on the GrIS can increase basal melting of the floating extension (e.g. Ciracì et al., 2023; Wang et al., 2024). By monitoring these processes, we can predict how long these floating extensions may remain intact and estimate the volume of water that they could indirectly contribute to sea level rise through the removal of buttressing within the fjord (e.g. Etourneau et al., 2019).

The grounding line represents the transition between grounded ice (in contact with the bedrock at the ice base) and floating ice (Figure 1.10). This transition zone is a critical indicator of ice sheet stability as changes in grounding line position directly affect ice sheet mass loss, ice flow speed, and the subsurface area which interacts with the ocean waters. If the grounding line retreats inland, it means the ice sheet is losing stability, increasing the risk of accelerated ice loss. The marine ice sheet instability (MISI) theory states that once the grounding line retreats past a certain threshold on a retrograde bed,

ice loss becomes self-sustaining, leading to rapid collapse of the glacier (Schoof, 2007). Improved detection of grounding lines helps determine whether key regions of our ice sheets are approaching this tipping point. However, unstable grounding line positions can occur on prograde beds in the presence of buttressing, and stable positions can occur on retrograde beds (Haseloff and Sergienko, 2018; Sergienko and Wingham, 2022). Therefore, knowledge of the bed slope alone is not sufficient to predict the stability of ice sheet grounding lines.

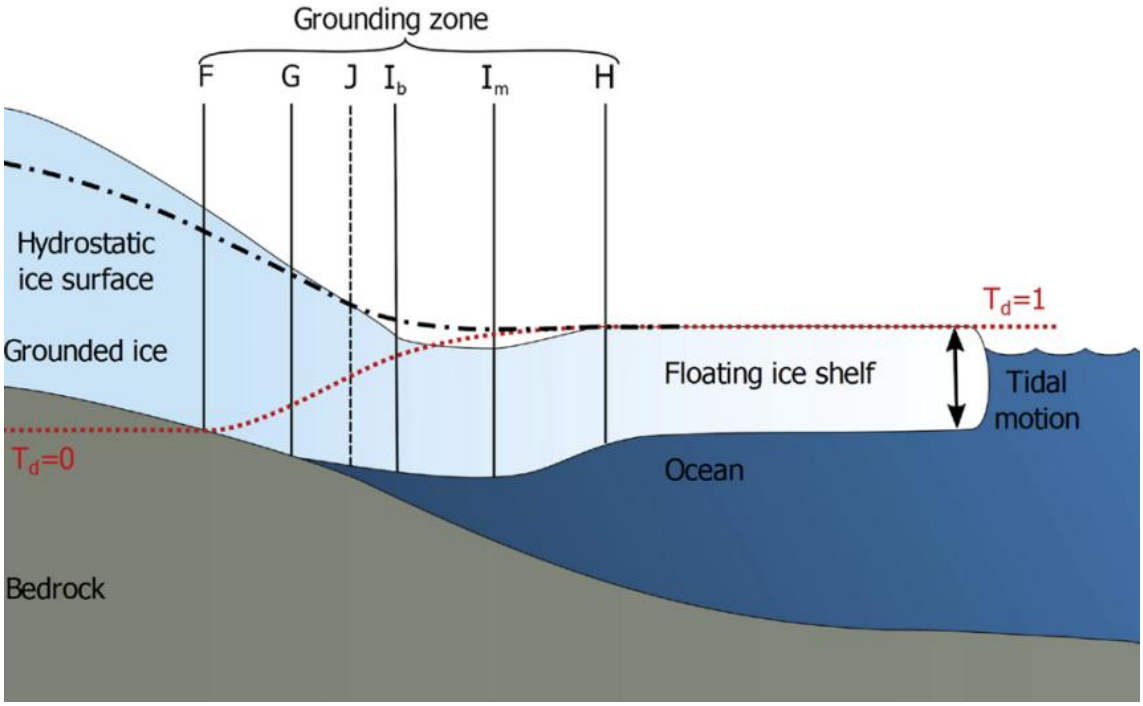


Figure 1.10: Schematic drawing of the grounding zone features of an idealised ice sheet. F: landward limit of tidal ice flexure (hinge line), G: true grounding line, J: Point of first hydrostatic equilibrium, $I_b$: break in slope, $I_m$: local elevation minimum, H: landward limit of stable hydrostatic equilibrium (freely floating ice), black dashed-and-dotted line: the hypothetic elevation of the ice in hydrostatic equilibrium, red dotted line: dimensionless amplitude of tidal flexure: $T_d = 0$ on grounded ice and $T_d = 1$ on freely floating ice (Friedl et al., 2020).

Ocean warming melts ice shelves from below, thinning the ice and causing grounding line retreat. Accurate detection techniques aid in quantifying the rate at which ocean-driven melting could destabilise ice sheets. Knowing the grounding line position allows for better estimates of basal melting beneath ice shelves, which is crucial for modelling the expected lifetime of the ice shelf or tongue under different ocean temperature conditions. Increases in ocean temperatures at the margins of the ice sheet cause basal melting on the floating extensions of glaciers (Wekerle et al., 2024). This results in the thinning, and

eventual collapse of these floating extensions, often in the form of calving events at the terminus. Calving events on floating extensions produce tabular icebergs as opposed to the stereotypical non-tabular icebergs which calve from the fronts of grounded glaciers. Calving events reduce the buttressing effect which these floating extensions exert on their upstream glaciers (Schoof et al., 2017). Additionally, increased ocean temperatures reduce the presence of sea ice which occupies the fjords of, primarily, northern Greenland during winter. Sea ice can reduce the inflow of warmer ocean waters into the fjords, thermally damming the shelf's basal region and helping maintain the cool fjord temperatures (Stranne et al., 2021). A reduction in this sea ice means that the fjords are becoming ice-free during the winter months, allowing for both the year-round calving of glacier ice, and increased basal melt from the margins of the GrIS.

## 1.5 Relevance to policy making

Monitoring the distribution and dynamics of supraglacial lakes and the migration of grounding lines allows us to improve our models by ensuring we correctly simulate complex ice sheet processes. By calibrating our models with Earth observation data, we can more confidently use these models to predict future change. This reduces the uncertainty of our estimates, and governments and disaster response agencies can use this data to assess potential risks to global sea level rise, providing early warning for vulnerable coastal regions. Additionally, economic activities such as fishing, shipping, and tourism near and on the GrIS rely on stable ice conditions, so robust evidence is required to inform policy concerning these activities. Governments and international organisations such as the Intergovernmental Panel on Climate Change (IPCC) and the United Nations Framework Convention on Climate Change (UNFCCC) rely on accurate ice sheet data related to ice loss and sea level rise to set emission reduction targets and funding priorities.

# 2 Introduction – Data and methods

## 2.1 Using digital elevation models to monitor Greenland

Here, I provide an overview of key advancements in glaciological research, focusing on the evolution and application of digital elevation models (DEMs) and their role in studying ice sheets. This section covers the historical development of DEMs, from early analogue methods to modern high-resolution satellite-based techniques. Next, I examine the historical context of methods for estimating supraglacial lake depths, identifying grounding lines, and enhancing the accuracy of ice sheet monitoring through new technologies such as light detection and ranging (LiDAR), machine learning, and drones. Additionally, this section explores the current (limited) use of DEMs in certain areas, particularly grounding line research, and highlights promising new methods to optimise their use in improving our understanding of ice dynamics and sea-level rise projections.

### 2.1.1 A brief introduction to DEMs

DEMs are three-dimensional representations of elevation data (Figure 2.1). Over the past decade, DEMs have become more widely available due to advancements in production techniques and increased availability, and some datasets are now completely freely accessible (e.g. Howat et al., 2022; Porter et al., 2022). In brief, the datasets with coverage of the GrIS are; ArcticDEM (Polar Geospatial Center) (Porter et al., 2022, 2023), the Advanced Spaceborne Thermal Emission and Reflection Radiometer Global DEM (ASTER GDEM) (NASA) (Abrams et al., 2020), the Greenland Ice Mapping Project DEM (NASA) (Howat et al., 2014), TanDEM-X (DLR – German Aerospace Center) (Zink et al., 2007) and BedMachine (Morlighem et al., 2022).

DEMs are either three-dimensional datasets which represent the terrain as a full three-dimensional surface or 2.5-dimensional datasets which represent the surface on a regular grid with one elevation value per grid cell. Three-dimensional DEMs have x, y and z coordinates and often present as irregularly spaced points or triangulated irregular networks (TINs). In these datasets it is possible to have multiple points in the same x,y coordinate but with a different z coordinate as the terrain may contain complex geometry such as a cave or overhang. 2.5-dimensional DEMs are two-dimensional surfaces with a height attribute, and these datasets cannot have multiple height values for the same x,y location. These DEMs are regularly gridded which means that they are more

computationally efficient to process than three-dimensional DEMs. Converting from three-dimensional DEMs to 2.5-dimensional DEMs requires spatial interpolation as these two formats have differences in grid size (the distance between the centre points of the adjacent cells in the grid) and resolution (the smallest terrain feature that can be meaningfully represented in the DEM). Interpolation can smooth or distort terrain, creating artefacts.

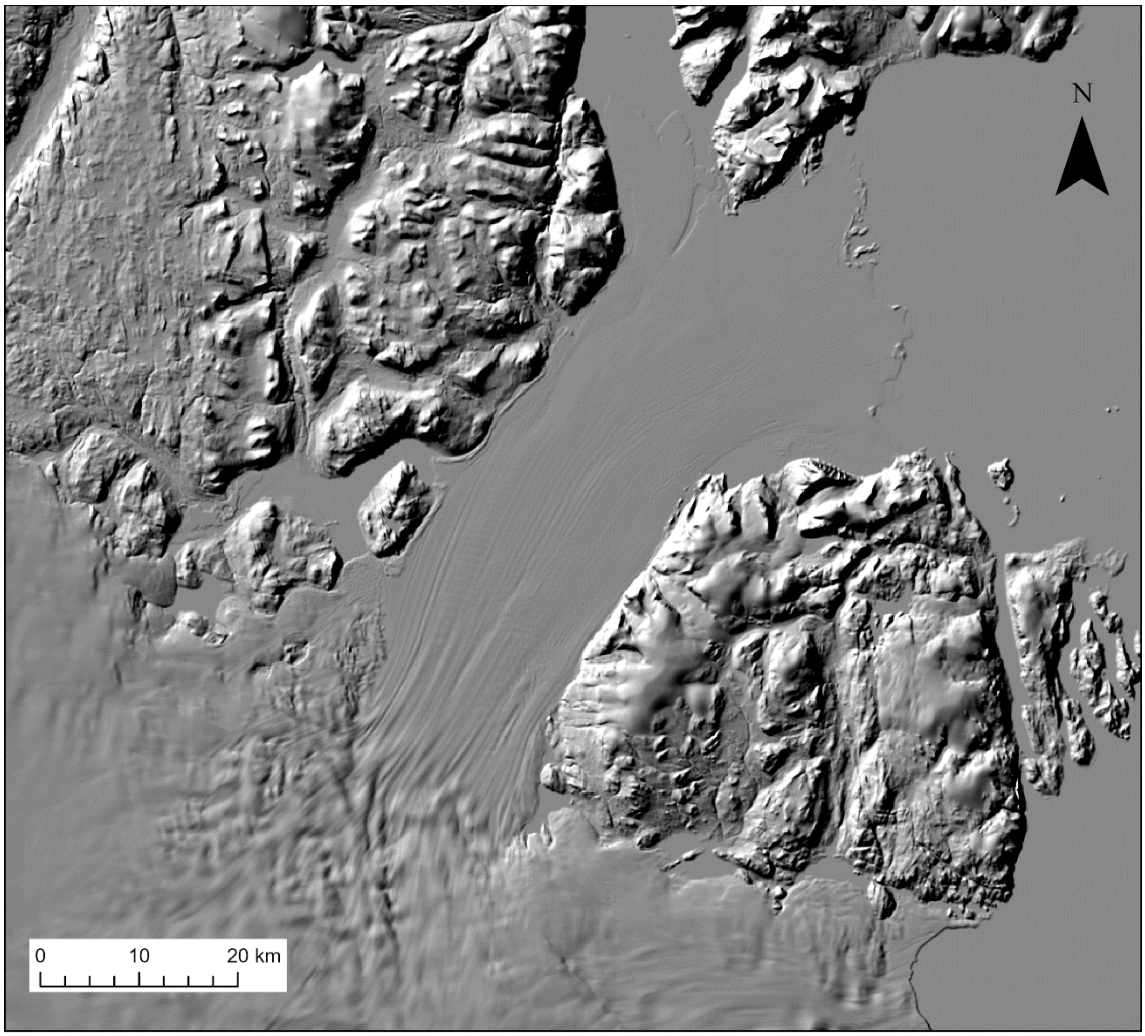


Figure 2.1: Hillshade of Nioghalvfjerdsbræ (79N Gletsjer) from the ArcticDEM mosaic product, accessed through OpenTopography (Porter et al., 2023). A hillshade is a cartographic technique where a lighting effect is added to a map based on the variations within the elevation dataset.

### 2.1.2 The history of DEMs

This section details the evolution of DEM use in glaciology, from early analogue methods to the advent of computer-generated DEMs in the 20th Century (Figure 2.2). Satellite remote sensing in the 1990s and 2000s, such as NASA's Shuttle Radar Topography

Mission (SRTM) and the Advanced Spaceborne Thermal Emission and Reflection Radiometer (ASTER), expanded the use of DEMs, with recent advancements like ArcticDEM and the Reference Elevation Model of Antarctica (REMA) offering high-resolution data for detailed glacier monitoring. Here, I also discuss the benefits of high-resolution DEMs.

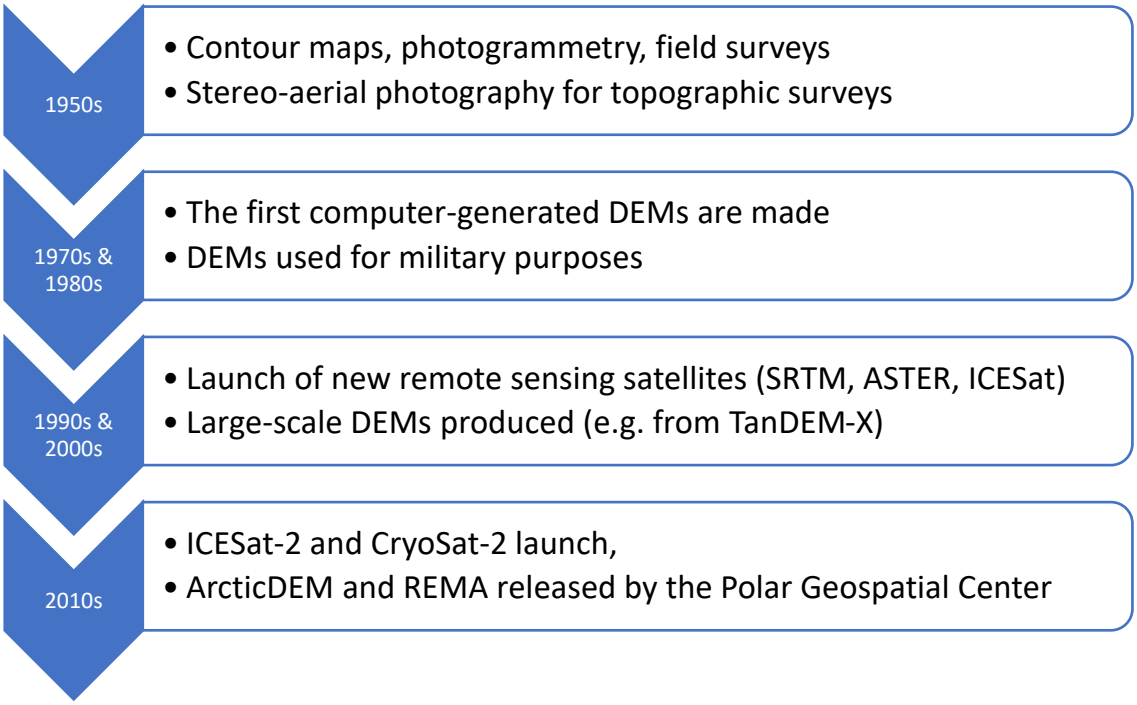


Figure 2.2: Timeline of the history of DEMs.

### 2.1.2.1 Evolution of DEM use in glaciology

The use of DEMs in glaciology, and indeed science in general, is relatively recent due to their nature as digital objects. Before DEMs existed, glaciologists relied on contour maps, photogrammetry, and field surveys to estimate glacier volume and elevation changes of our ice sheets (e.g. Fox and Cooper, 1998; Weidick, 1968). The emergence of digital computing in the mid-20th century allowed for the development of the very early DEMs.

From the 1950s onward, stereo aerial photographs were used to manually derive topographic data for glaciers (Roscoe, 1952). Although this process was largely analogue, this was one of the earliest forms of "digital" elevation modelling which paved the way for stereophotogrammetric techniques in later decades. In the 1970s–1980s, the first computer-generated DEMs were produced using digitised contour maps and stereophotogrammetry, adopting similar principles to cross-view stereograms. Some of

these earliest DEMs were created for military and cartographic purposes (Dawid and Pokonieczny, 2023).

In the 1990s, satellite remote sensing meant that DEMs could be made more easily, with data more readily available as new sensors provided more frequent and higher-resolution elevation data. NASA's SRTM launched in 2000 and provided near-global topographic coverage with a resolution of 90 m, with some regions benefitting from a higher resolution of 30 m (Farr et al., 2007). Although SRTM became one of the first widely available, high-resolution DEM datasets used for glacier research, it was limited to non-polar regions (~60°N to ~60°S) (Figure 2.3) (Farr et al., 2007). In 2009, data derived from the ASTER sensor on NASA's Terra satellite, which would become colloquially known as ASTER GDEM, provided near-global coverage at 30 m resolution (Abrams et al., 2010). Its stereo imaging capability allowed for the production of DEM time series, an essential element in the study of glacier elevation change over time.

The TanDEM-X mission produces a global, high-resolution DEM with 12 m spatial resolution (Zink et al., 2007). The first Ice, Cloud and land Elevation Satellite (ICESat; 2003–2010) provided high-precision laser altimetry data, which meant ice sheet elevation changes could be tracked with centimetre accuracy (Schutz et al., 2005). Its successor, ICESat-2 (2018–present), improved upon its predecessor's spatial resolution and sampling density (Markus et al., 2017). This allows for more accurate surface elevation retrieval and supports finer-scale DEM generation through spatial interpolation and cross-validation. In contrast, CryoSat-2 (2010–present) uses radar altimetry, which can penetrate the firn layer and sense through cloud cover but provides lower spatial resolution and less precision over steep terrain (Yang et al., 2022). Together, these missions complement DEM products by providing accurate elevation reference data and time series for surface change detection.

Figure 2.3: The spatial coverage of SRTM (Cowan and Cooper, 2005).

Recent advances in DEM technology have provided unprecedented detail to glaciological studies, helping us monitor climate change impacts. ArcticDEM (with coverage of the Arctic) and the REMA are the first continent-wide, high-resolution (2 m) DEMs (Figure 2.4) (Howat et al., 2022; Porter et al., 2022). Created using WorldView stereo imagery from Maxar Technologies, these datasets enable precise glacier volume change analysis, though minor elevation variations may occur due to DEM artefacts. The European Space Agency's CryoSat-2 satellite provides radar altimetry data to track ice sheet elevation changes (Laxon et al., 2013).

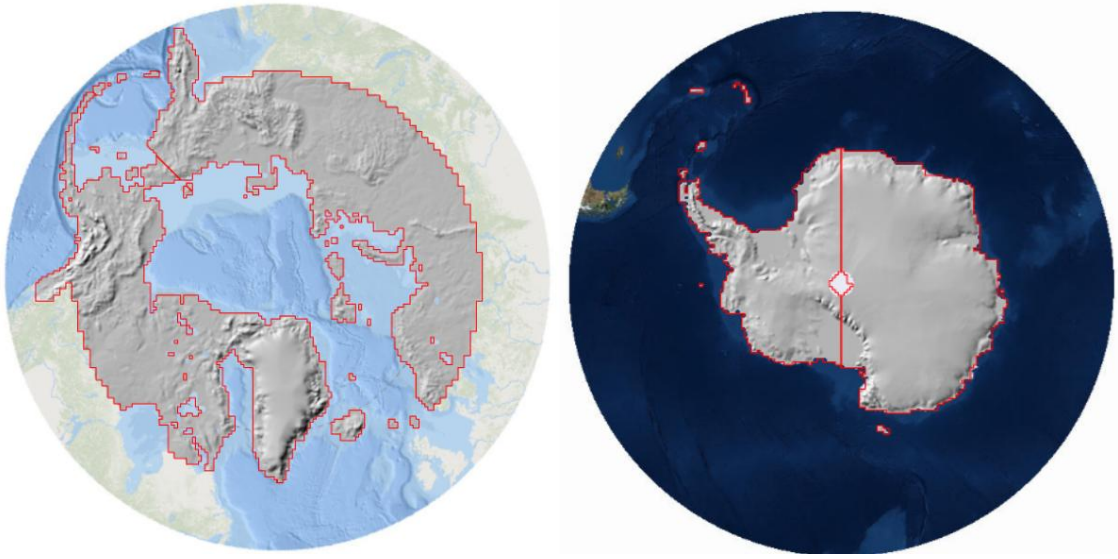

Figure 2.4: ArcticDEM (left) and REMA (right) spatial coverage (Howat et al., 2022; Porter et al., 2023).

#### 2.1.2.2 DEM production methods

Digital elevation models of Greenland are produced using a range of methods, and each has distinct advantages, limitations, and implications for subsequent analysis. Ground-based surveys and digitised contour maps provide locally accurate elevations, but data are often sparsely distributed which necessitates interpolation to form continuous surfaces (Li et al., 2017). Optical photogrammetry, from either aerial or satellite imagery, can generate high-resolution, spatially continuous DEMs (Porter et al., 2022). However, the performance relies directly on visible light and so is sensitive to cloud cover, snow, and ice reflectivity, which can introduce gaps and/or noise.

Radar-based techniques, including single- or repeat-pass interferometric synthetic aperture radar (InSAR), provide accurate elevation measurements and are largely independent of cloud cover due to their reliance on microwave signals. However, radar signals can penetrate into snow and firn layers, leading to artificial depressions in the output DEM (Bannwart et al., 2024). Satellite and airborne altimetry (laser or radar) offer precise point measurements over large areas, but their tracks can be spatially distant, requiring interpolation to create a continuous DEM. This interpolation can introduce artefacts, particularly in steep or complex terrain.

The production method also influences the relationship between grid size and effective resolution. While raster DEMs (2.5-dimensional) may have fine grid spacing, the actual ability to resolve terrain features is limited by the density of the source data and method-specific uncertainties. Therefore, understanding the strengths and weaknesses of each approach is essential for interpreting DEM artefacts, assessing data quality, and selecting the most appropriate datasets for glaciological studies.

#### 2.1.2.3 Advantages of high-resolution datasets for capturing ice sheet characteristics

High-resolution datasets have significantly improved our understanding of ice sheet processes and characteristics, enabling more precise measurements of surface changes, ice flow, and subglacial topography. The increasing availability of high-resolution datasets has transformed glaciology by providing detailed insights into how ice sheets respond to climate change and other external forces. Here I provide an overview of the advantages of high-resolution datasets in studying ice sheets.

High-resolution datasets provide improved accuracy and enhanced detection abilities in studies of ice sheet surface elevation changes. With these datasets, we can measure elevation changes over small spatial scales, revealing localised melt or accumulation that may remain undetected in coarser-resolution datasets, including improved detection of supraglacial hydrological systems and surface melt features. Additionally, high-resolution altimetry datasets, such as those from ICESat-2 (laser altimetry), provide precise elevation measurements allowing for the quantification of elevation changes. These changes, when combined with snow and firn densities, allow for the estimation of mass balance changes (e.g. Ravinder et al., 2024; Smith et al., 2023). Temporally, these datasets allow us to calculate volume changes over time, enabling a more refined understanding of potential regional thinning/thickening patterns. Typically, altimetry studies produce elevation changes in 5 km resolution grids which are then aggregated to produce volume estimates at the basin scale (e.g. Yang et al., 2022; Zhang et al., 2022). Higher spatial resolution of our data also helps to reduce interpolation errors, making volume change estimates, and thus volume-to-mass estimates, more reliable.

Ice sheets exhibit a range of small-scale flow features, such as ice streams, shear margins, and localised accelerations, which can be missed in coarse-resolution models and altimetry datasets. High-resolution DEMs allow us to resolve these fine-scale features. For example, high-resolution DEMs can be used to monitor crevasse evolution over time (Chudley et al., 2025). This enables us to monitor structural weaknesses that could signal the evolution of a crevasse (Figure 2.5). For field researchers and mountaineers, crevasses can be deadly, making the ability to map these small features even more important.

Figure 2.5: Crevasses on Qajuutaap Sermia in south Greenland (image credit: J. Box).

Subglacial DEMs, derived from radar surveys (e.g. BedMachine Antarctica and BedMachine Greenland (Morlighem et al., 2022; Morlighem, 2022)), are crucial for understanding how bedrock topography influences ice dynamics. High-resolution radar data allows us to study basal roughness (which controls sliding and deformation), and subglacial valleys and ridges (which impact ice stream routing and stability). The better resolution of subglacial DEMs means we can capture the structure of subglacial lakes and channels, which influence ice sheet movement through basal lubrication (Figure 2.6) (Livingstone et al., 2022). High-resolution data have helped identify previously unknown subglacial water networks, which can drain suddenly and impact ice velocity (Malczyk et al., 2020).

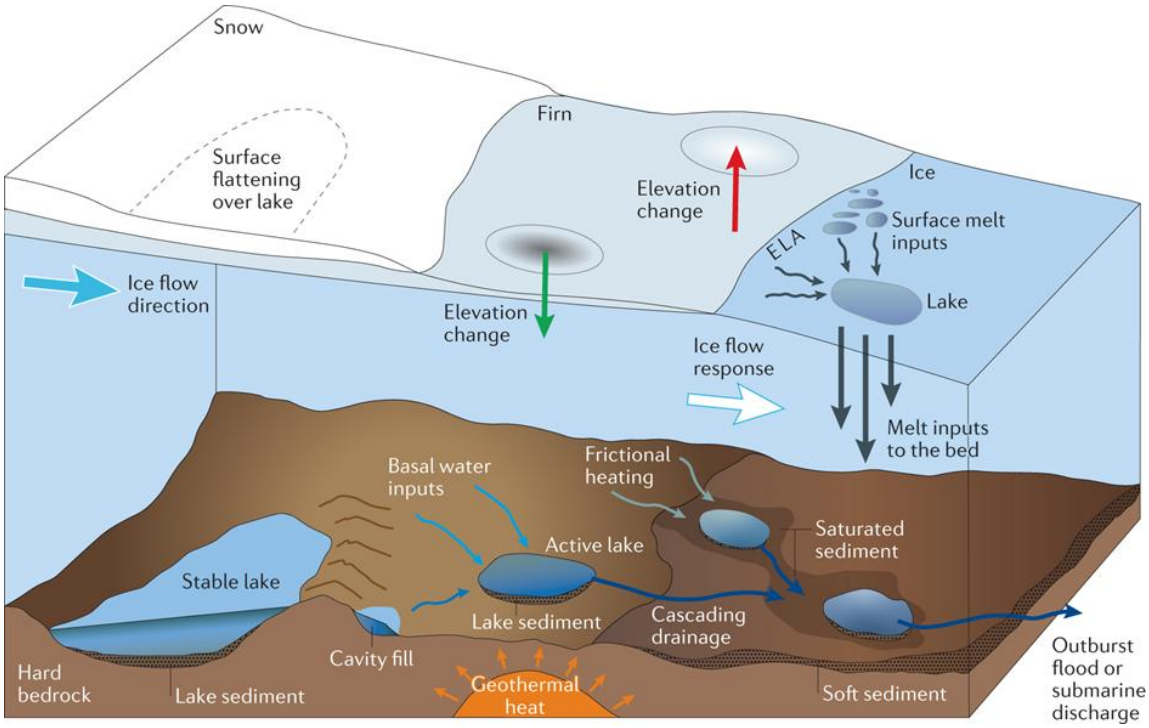


Figure 2.6: The subglacial hydrological system of ice sheets and glaciers (Livingstone et al., 2022).

Combining these high-resolution DEMs with surface density models (from radar and firn models) results in better estimates of ice mass changes (Smith et al., 2023). This allows us to have a better understanding of surface processes, with firn compaction and melting/refreezing processes affecting ice sheet elevation changes (Li and Zwally, 2011).

High-resolution DEMs have significantly advanced ice sheet research by facilitating detailed analyses of surface elevation changes, ice flow dynamics, and subglacial processes that were previously unresolved. They enable the monitoring of ice shelf thinning, rift propagation, and iceberg calving with a level of detail that was not possible with coarser DEMs (e.g. Dai et al., 2024; Shiggins et al., 2023). Recent studies using DEM time series have demonstrated the capability to forecast major ice shelf calving events (North and Barrows, 2024). In addition to their observational applications, DEMs are important inputs for ice sheet models, which require accurate elevation data to project future ice mass loss and contributions to sea level rise. However, coarse-resolution DEMs may fail to adequately resolve glacier geometries, introducing uncertainties in model projections (e.g. Rignot et al., 2003).

The ability to capture fine-scale elevation variations is essential for improving sea-level rise projections and for refining our understanding of ice sheet stability and response to

climate forcing. As remote sensing technology continues to develop, the increasing availability of high-resolution datasets will further enhance ice sheet monitoring and modelling efforts, leading to improved predictions of future change.

### 2.1.3 Lake depths and the radiative transfer equation

This section explores the evolution of methods for estimating supraglacial lake depths, from early observations by explorers to modern techniques (Figure 2.7). It covers the development of remote sensing methods, including the use of the radiative transfer equation (RTE), and highlights advancements in unmanned aerial vehicles (UAVs), LiDAR, and machine learning models. This section also discusses the strengths and limitations of these methods, with a focus on how technological progress has improved our ability to measure lake depths accurately.

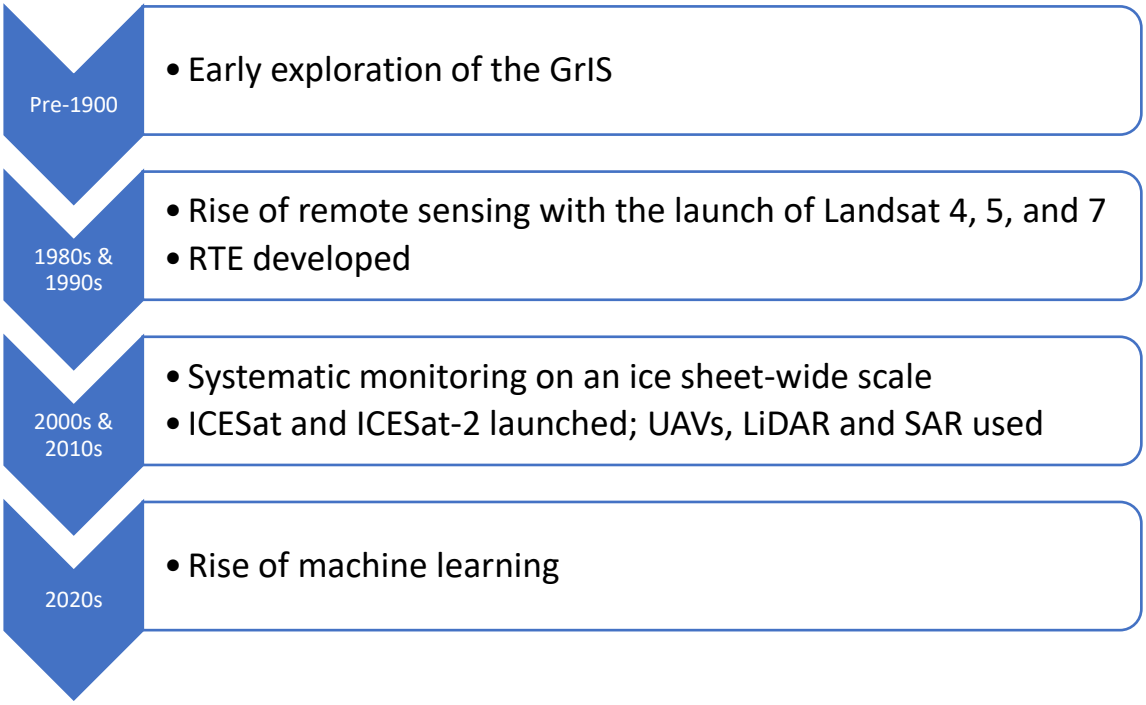


Figure 2.7: Timeline of the history of supraglacial lake depth measurements.

#### 2.1.3.1 Historical context for lake depth methods

Before 1900, early explorers and glaciologists, such as those on Arctic and Antarctic expeditions (Figure 2.8), observed surface meltwater ponds on glaciers and ice sheets (Peary, 1887; Tarr, 1897). During these expeditions, systematic depth measurements were not taken, but written records noted the presence of surface lakes. These first scientific observations of supraglacial lakes lacked the technology to measure accurate lake depths.

Due to the inaccessibility of supraglacial lakes, depth sounding, as practised on ships, was considered unfeasible.

Figure 2.8: Arctic explorers Robert Peary (left) and his assistant, Matthew Henson (right), after whom Henson Gletsjer in northern Greenland is named (image credits: Wikimedia Commons user: Skewing, Wikimedia Commons user: H. Cheng).

The 1980s and 1990s marked the rise of remote sensing and launch of the multispectral scanner and thematic mapper Landsat satellites (Landsat 4 and Landsat 5) and the enhanced thematic mapper (Landsat 7). Basic spectral reflectance techniques, such as the RTE, were developed to estimate water depth based on colour (Maritorena et al., 1994; Philpot, 1987, 1989). In the 1990s, the introduction of improved remote sensing tools, such as the Moderate Resolution Imaging Spectroradiometer (MODIS) (Justice et al., 1998) and the Advanced Very High Resolution Radiometer (AVHRR) (Cracknell, 1997), enabled better lake *detection* but field studies continued to have limited success in measuring supraglacial lake *depth*. Around this time, photogrammetry techniques began to be applied to estimate lake volume, but this was necessarily at a relatively small spatial and temporal scale (Benn and Evans, 1997).

Advances in satellite technology and imaging resolution in the early 2000s and 2010s meant that more sophisticated optical depth estimation models were developed using Landsat and ASTER satellite data (Sneed and Hamilton, 2007). The relationship between water colour and depth was studied, with the introduction of empirical relationships

between the two for application to remotely sensed optical data (Sneed and Hamilton, 2011).

Further technological advancements in the 2010s led to the adoption of UAVs for high-resolution photogrammetry and structure-from-motion (SfM) techniques (e.g. Bash et al., 2018; Benoit et al., 2019; Rossini et al., 2018). This meant that lake drainage basins could be mapped, making historical lake depth calculation possible through scene differencing. Improvements in LiDAR technology from aircraft and satellites provided improved surface elevation data, allowing for more precise lake volume and depth calculations (Jóhannesson et al., 2013). The launch of ICESat, a laser altimeter, helped map ice surface changes and indirectly provided lake depth information, though the sampling capabilities of this method are limited by the spacing of the satellite's reference ground tracks (RGTs) (Chen and Duan, 2022). During this period, synthetic aperture radar (SAR) was also used to track lakes and lake drainage events.

Since 2020, continued improvements to UAVs and drone-mounted LiDAR have also allowed more localised, high-precision studies (e.g. Ren et al., 2024; Yang et al., 2020; Zhao et al., 2025). These techniques are limited to small case studies due to operational costs and site accessibility. Most recently, since 2023, machine learning models have been developed to refine depth estimates from satellite data often using multi-sensor approaches (e.g. combining optical, radar, and LiDAR, e.g. Arndt and Fricker, 2024; Xiao et al., 2023; Zhou et al., 2025). However, LiDAR-based methods experience issues with bottom photon return and the 'multiple surface returns' phenomenon which causes difficulty determining the location of the bottom in shallow lakes. Use of these methods also limits the maximum depth of the lakes which can be studied. ICESat-2 depth detection is limited to lakes up to 7 m deep (Fair et al., 2020). Additionally, their use of ICESat-2 introduces issues with the spatial sampling due to the spacing of the acquisition beams.

#### 2.1.3.2 Summary of existing studies

Existing studies of supraglacial lake depth have developed various satellite-based methods, each with distinct advantages and limitations. Physics-based modelling methods such as the RTE as pioneered by Philpot (1987) have laid the foundation for many lake depth studies. These studies apply the RTE to optical satellite imagery, such as Sentinel-2, to estimate lake depth based on spectral properties of water (Moussavi et al., 2020;

Philpot, 1987). However, the accuracy of depth estimates is affected by variations in the calculation of spectral radiance loss, atmospheric conditions, and assumptions about water clarity, which can introduce errors (Sneed and Hamilton, 2007).

Other methods, such as laser altimetry, use photon refraction to directly measure lake depth (Fair et al., 2020). The launch of ICESat-2 in 2018 allowed for the study of lakes with an along track resolution of 0.7 m (Markus et al., 2017; Xiao et al., 2023; Zhou et al., 2025). Figure 2.9 shows the beam pattern spacing of ICESat-2 at the Equator, where the distance between the left and right beams in a pair is ~90 m, the distance between pairs is ~3.3 km, and the distance between repeats of the six-beam pattern (i.e. the distance between RGTs) is ~29 km. These beam patterns converge at high latitudes. At 80°N, the distance between the left and right beams of a pair is still ~90 m, but the distance between pairs is ~1.6 km, and the distance between RGTs is ~4.8 km (Neumann et al., 2019). Unfortunately, ICESat-2 only provides 1-D profiles along these discrete satellite tracks, making it difficult to capture lake variability across space. This means that many lakes may be impossible to sample as they are not crossed by a satellite track. Additionally, it has a 91 day repeat period (Markus et al., 2017) which inhibits the assessment of rapid hydrological changes in supraglacial lakes such as lake drainage events which can take place in as little as two hours (Das et al., 2008).

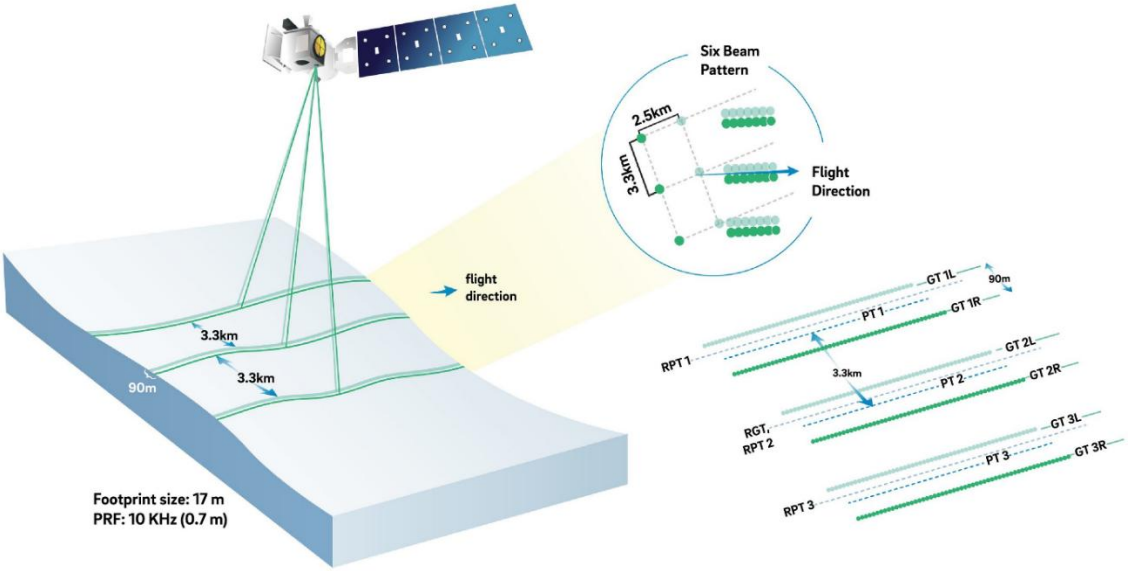


Figure 2.9: Diagram of the six-beam pattern from the Advanced Topographic Laser Altimeter System (ATLAS) instrument onboard ICESat-2, and how it measures ice thickness at the Equator (Smith et al., 2019).

DEMs provide high-resolution elevation data, allowing lake depth estimates to be derived from underlying ice topography (Yang et al., 2019). However, this data is often temporally sparse, with months between acquisitions, and is prone to gaps caused by cloud cover.

Some studies have derived empirical models from the regression of in situ data and correlated this with remote sensing data to estimate depth (e.g. Legleiter et al., 2014; Pope et al., 2016; Tedesco and Steiner, 2011). Although the depths attained by these methods have been shown to define a reasonable level of accuracy against local in situ data ($r^2$ = 0.615–0.93), empirical regression coefficients implicitly consider local optical and environmental effects and are therefore specific to the region where the in situ measurements were taken (Tedesco and Steiner, 2011). This means they are not generalisable and are unsuitable for large-scale application across the ice sheet.

#### 2.1.3.3 Lack of methods integrating DEMs with optical imagery and altimetry for validation

Given the spatial and temporal limitations of existing methodologies, combining multiple methods could improve confidence in lake depth estimates, particularly in areas where ground truth data is unavailable. Prior to the publication of Melling et al. (2024), as detailed in full in Chapter 4, and the subsequent publication of Lutz et al. (2024), no studies had yet integrated DEMs with optical imagery and satellite altimetry for validation of lake depths. As such, a systematic comparison of these datasets would allow for an increase in our confidence in lake depth detection methods.

### 2.1.4 Grounding line identification

In this section, I examine the history and advancements in methods for identifying grounding lines on ice sheets, starting with early theoretical concepts in the 19th Century and progressing through the evolution of remote sensing techniques (Figure 2.10). We begin with the foundational observations of early explorers, followed by the development of seismic surveys and radar sounding in the mid-20th Century. The introduction of satellite-based methods, such as radar altimetry and interferometric SAR (InSAR), in the 1990s and 2000s significantly improved the accuracy of grounding line detection. The section concludes with a discussion of recent advances in satellite missions, including ICESat-2 and CryoSat-2, and the growing understanding of grounding line dynamics, especially in relation to tidal fluctuations and ocean-driven melting.

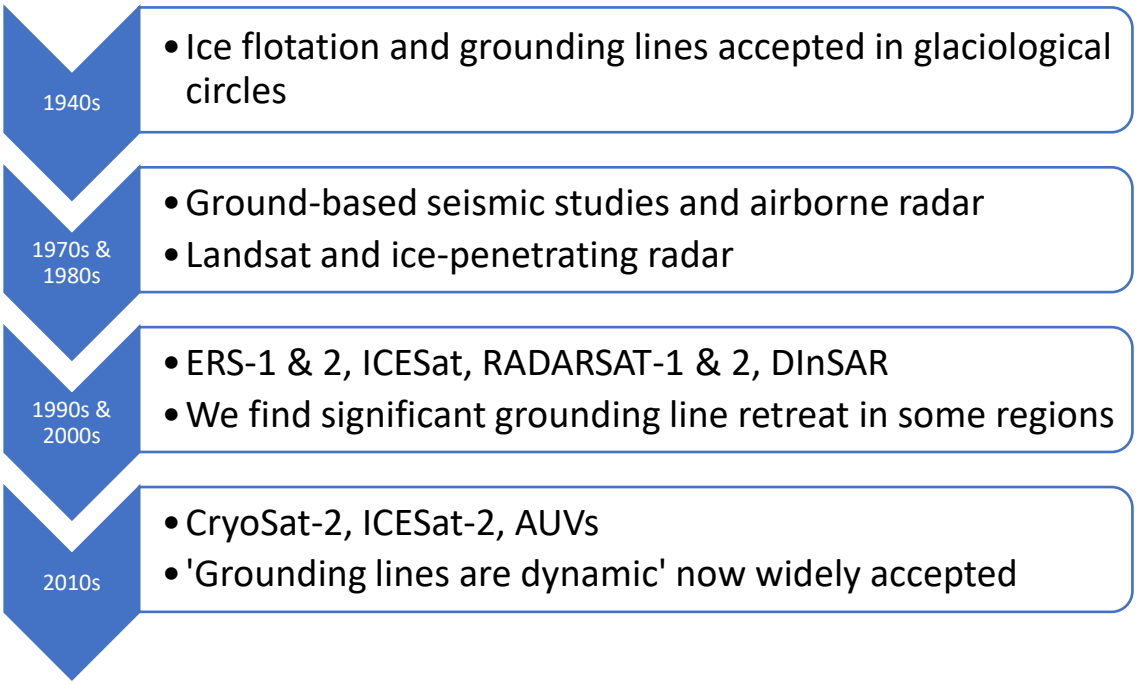


Figure 2.10: Timeline of the history of grounding line delineation.

#### 2.1.4.1 Historical context for grounding line delineation

Before the 1900s, early observations of ice sheets laid the basis for the theoretical understanding of grounding line existence with early explorers of the GrIS describing floating ice shelves (Peary, 1887). By the 1940s, the concept of ice flotation and grounding lines became well-accepted in glaciological circles (Sverdrup et al., 1942). However, early researchers had no means by which to precisely locate these grounding lines.

The 1970s ushered in a new age of remote sensing, with ground-based seismic surveys and airborne radar sounding used to measure ice thickness and infer where ice flotation begins (Pawlowicz, 1972). These techniques help to estimate basal conditions which are key factors in the calculation of grounding line location. However, these estimates were based on data of sparse spatial and temporal resolution.

Landsat 1 was launched in 1972 and provided the first large-scale maps of Antarctic ice shelves (Wulder et al., 2022). In the 1970s and 80s, ice-penetrating radar, a form of radio echo sounding, allowed for detection of the ice sheet base (Robin, 1975; Crabtree and Doake, 1982) and, in the 1990s, the concept of tidal flexure was fully accepted (Vaughan, 1995). This meant that grounding lines could be identified by measuring ice movement

in response to the ocean tides (e.g. Jacobel et al., 1994; Powell et al., 1996; Riedel et al., 1999).

The emergence of satellite remote sensing in the 1990s and 2000s, such as the European Remote-Sensing Satellite (ERS)-1 and -2 radar altimetry missions, provided better ice surface elevation data, improving the accuracy and precision of grounding line detection (Rignot et al., 2001). Additionally, differential InSAR (DInSAR) techniques were introduced, allowing precise measurement of ice shelf flexing and deformation and capitalising on the understanding that floating ice moves vertically in response to the tides (Park et al., 2013; Sykes et al., 2009). In the early 2000s, studies began to identify significant grounding line retreat in some regions, linking ice loss to ocean-driven melting (Schoof, 2007).

The introduction of new satellite missions in the 2000s allowed for even more precise estimates of grounding line location. Data from ICESat, a laser altimetry mission launched by NASA in 2003, refined grounding line locations based on ice surface elevation changes (Freer et al., 2023) and DInSAR data from RADARSAT-1 and RADARSAT-2 helped track grounding line migration in the Antarctic Ross and Filchner ice shelves (Gray et al., 2002). Studies also began to recognise the role of warm ocean currents in grounding line retreat, improving our understanding of ice shelf-ocean dynamics (Hill et al., 2024).

Improvements to satellite capabilities improved our ability to determine grounding line location. CryoSat-2 was launched in 2010 after the failed launch of CryoSat-1 in 2005, improving our radar altimetry measurements and providing higher-resolution ice elevation data (Laxon et al., 2013). CryoSat-2 boasts the ability to detect changes in ice thickness as small as 1.6 cm per year (sea ice) and 0.17 cm per year (land ice) and has a repeat cycle of 369 days (Francis et al., 2007). ICESat-2, the successor to the ICESat mission, was launched in 2018 and improved grounding line tracking using laser altimetry (Markus et al., 2017). Advanced DInSAR techniques using data from Sentinel-1 enabled higher temporal monitoring of grounding line changes (Friedl et al., 2020). Studies also used in situ oceanographic data from autonomous underwater vehicles (AUVs) such as Icefin (Figure 2.11) to confirm grounding line retreat beneath ice shelves (Schmidt et al., 2023). The understanding that grounding line position is dynamic rather than static, and

changes with tides is now widely accepted, with the area over which the grounding line fluctuates termed the grounding zone (Fricker et al., 2009; Brunt et al., 2010, 2011).

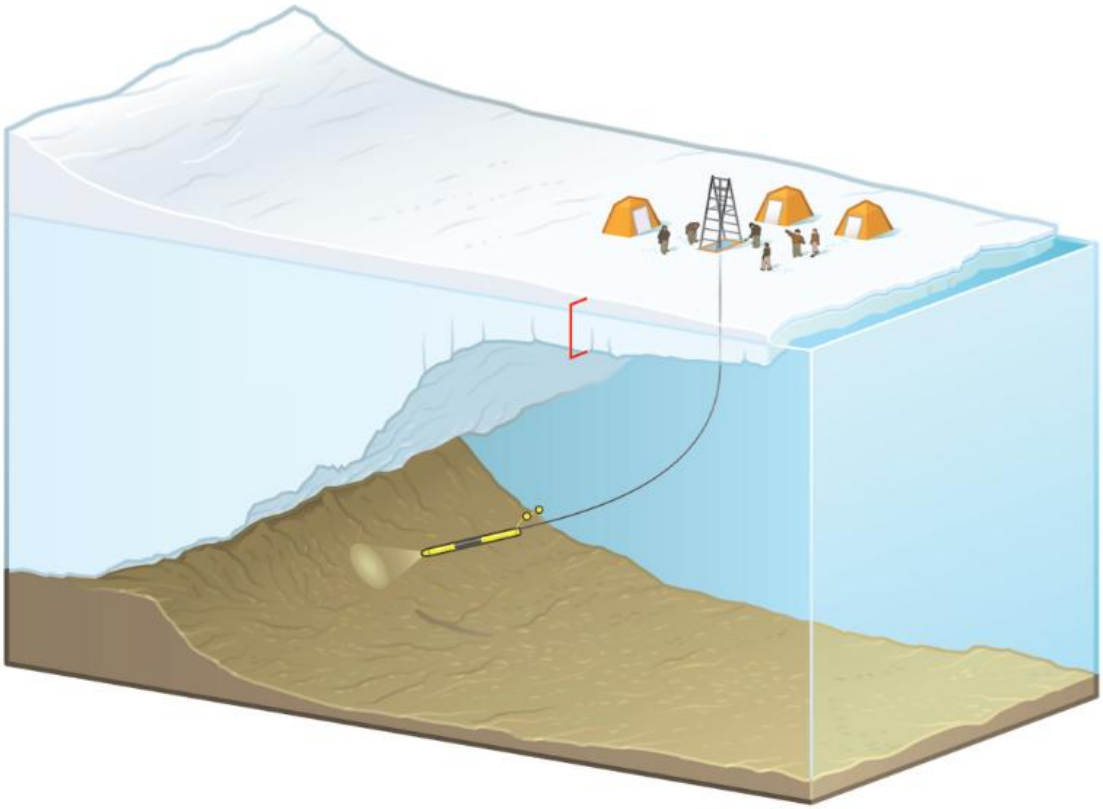

Figure 2.11: Infographic showing deployment of the Icefin submersible AUV (image credit: M. Rogalski).

### 2.1.4.2 Summary of existing studies

Grounding line detection studies have predominantly focused on Antarctica, primarily due to its extensive ice shelves and the critical role grounding lines play in ice sheet stability (Rignot et al., 2011; Mohajerani et al., 2021; Ross et al., 2024). In comparison, the GrIS features fewer extensive floating ice tongues, leading to comparatively less emphasis on grounding line studies (Wekerle et al., 2024; Zeising et al., 2024). However, Greenland's floating ice tongues, such as the Nioghalvfjerdsbræ (also known as 79 North or 79N) and Petermann Gletsjer are crucial in buttressing inland ice flow (Mayer et al., 2018; Millan et al., 2022a). The disintegration of these ice tongues could lead to accelerated glacier flow and increased ice loss (Nick et al., 2013; Millan et al., 2023; Hill et al., 2018b).

Studying Greenland's ice tongues is essential, as their stability directly influences ice sheet dynamics and sea level rise (Millan et al., 2023). Recent observations have

documented extensive thinning and high basal melt rates on the floating tongue of 79N, highlighting the need for focused research in this region (Mayer et al., 2018). By enhancing our understanding of Greenland's grounding lines and floating ice tongues, we can improve predictions of ice sheet behaviour and global sea level changes and develop a better understanding of ocean forcing.

Delineating grounding lines on the GrIS presents unique challenges due to the dynamic and heterogeneous nature of the marine-terminating glaciers. Traditional methods, such as optical imagery and radar sounding, can struggle to accurately identify grounding lines due to cloud cover and radar scattering (Uratsuka et al., 1996; Friedl et al., 2020). The presence of surface meltwater and crevassing can affect shading in optical imagery, and subglacial hydrology and varying ice thicknesses may affect the effectiveness of radar sounding techniques. Accurately delineating Greenland’s grounding lines is crucial for understanding the stability of the ice sheet, as errors can lead to ice loss miscalculation, underestimating the contribution of rapidly thinning floating tongues to sea level rise.

### 2.1.5 Potential use of DEM datasets for glaciological applications

Within this section I highlight key advancements in DEM technology. I then discuss the potential for the use of DEMs in certain glaciological applications, particularly grounding line delineation. Techniques such as stacking DEMs to detect tidal flexure zones and integrating DEM data with tidal models offer promising new methods for more accurate grounding line mapping, which could significantly improve sea-level rise predictions.

#### 2.1.5.1 Key advancements in DEM technology

Deep-learning techniques, such as the use of a type of convolutional neural network (CNN) known as convolutional generative adversarial networks (CGANs), have improved our void-filling abilities for DEMs in data-poor areas (Ruiz-Lendínez et al., 2023). This, in addition to higher spatial resolutions of the input data, helps improve our confidence in results and reduce interpolation inaccuracy by increasing the frequency of data points from which to interpolate. This means we are interpolating over relatively shorter distances between data points and thus can be more confident in our interpolation. Overall, the higher availability, spatial resolution, and temporal resolution of contemporary DEMs allow for more in-depth and accurate study of ice sheets than ever before, with platforms such as OpenTopography and Google Earth Engine providing the means by which we may research the planet’s icy terrains.

#### 2.1.5.2 Opportunities to expand DEM application in grounding line research and beyond

High-resolution DEMs can enhance our understanding of ice sheet dynamics, glacier mass balance, and geomorphological processes (e.g. Millan et al., 2023). For example, DEMs have been employed to assess glacier thinning by comparing surface elevations over time, providing insights into mass loss and contributing to sea level rise projections (von Albedyll et al., 2018).

DEMs are instrumental in modelling glacier-bed topography, which is essential for understanding subglacial water flow and predicting glacier movement (Morlighem et al., 2022). DEMs also aid in assessing surface elevation changes which contribute to mass balance studies and help in evaluating potential glacial hazards (Dai et al., 2024). For example, high-resolution DEMs have been used to monitor changes in glacier volume and to model potential flood paths from glacial lake outburst floods in the Himalayas (Figure 2.12) (Hazra and Krishna, 2022; Siddique et al., 2024).

Figure 2.12: The aftermath of a glacial lake outburst flood in Sikkim, India on 4th October 2023 (image credit: P. Rao).

Despite their extensive use in glaciology (e.g. Lara et al., 2025; Liston et al., 2025; Wang et al., 2024), great potential remains to exploit DEMs for new applications, particularly floating ice and grounding line delineation. An example of how DEMs may be used to define the extent of floating ice involves stacking DEMs to analyse surface elevation

changes. By examining deviations across these stacked models, we could identify zones of tidal flexure. These are the areas where ice shelves flex due to tidal forces (Friedl et al., 2020). This method could allow for relatively precise mapping of floating ice tongue extent by detecting the transition between grounded ice and floating ice, which is crucial for understanding ice sheet stability and predicting potential sea level rise from calved and melted ice.

A further technique for use on marine-terminating glaciers could integrate DEMs with tidal modelling, allowing for grounding line detection. By correlating DEM-derived surface elevations with tidal cycles, it may be possible to distinguish between high and low tide positions of the ice shelf. This approach would offer temporal snapshots of the grounding line as its location responds to tidal forces, thereby supplementing the current SAR-derived inventory of grounding lines which has historically suffered from spatial and temporal gaps (e.g. Millan et al., 2023).

These new approaches offer promising avenues for floating ice and grounding line mapping that may help augment our current inventories on the GrIS. Expanding the use of DEMs in these ways may significantly enhance our understanding of ice sheet dynamics and improve predictions related to sea level rise.

## 2.2 Theoretical, technical and methodological foundations

Accurately determining both supraglacial lake depth and grounding line position is essential for understanding ice sheet dynamics and their broader implications for climate change and sea level rise. This section explores the theoretical foundations, their technical applications, and their limitations. First, I focus on ArcticDEM and the production of this dataset using the SETSM algorithm. After this, I explore electromagnetic theory and how different wavelength bands within the spectrum interact with water, ice, and snow, which governs the way supraglacial lake depth can be empirically calculated. From here, I examine existing approaches for supraglacial lake depth estimation, categorising them into radiative transfer-based methods, radar-based techniques, SfM-, and DEM-based methods, and in situ field measurements. I then focus on grounding lines, outlining the physical principles governing their behaviour, the datasets that support their analysis, and the various techniques used for their identification. By critically reviewing these methods, I provide a framework for evaluating the potential of DEM-based approaches in both contexts, establishing the foundation for the novel methodologies explored in subsequent chapters.

### 2.2.1 ArcticDEM and the SETSM algorithm

The primary dataset used in this thesis is ArcticDEM, a 2.5D raster DEM generated using the Surface Extraction from TIN-based Search-space Minimization (SETSM) algorithm (Noh and Howat, 2017). SETSM is an automated, stereo-photogrammetric DEM generation method that extracts gridded surface elevation from single-pair, spaceborne, stereoscopic imagery, such as from WorldView-1 and -2 satellites.

First, the algorithm orthorectifies the input data, applies sensor models, and removes radiometric artifacts. The relative bias between the stereo images' rational polynomial coefficient (RPC) sensor models is then corrected, without the need for ground control points. This correction ensures that corresponding features align exactly along the projected rays of the sensor models. The raw imagery is downsampled with Gaussian smoothing and iteratively processed through successively higher-resolution images until the desired grid resolution is achieved. This pyramidal processing model helps preserve high-frequency features while smoothing out low-resolution ones.

Next, the algorithm identifies matching positions and calculates optimal elevation values using weighted normalised cross-correlation (WNCC). The matching process is

constrained by a defined minimum and maximum height range, which is determined by the sensor model and the uncertainty of the data. This uncertainty is dynamically adjusted with each iteration, based on the previous results. WNCC is applied iteratively at regular height intervals between the minimum and maximum heights. These intervals are defined by the pyramid resolution and the viewing geometry of the images.

If no seed DEM is provided, after the first pyramid level, matching is performed on both uncorrected and geometrically corrected images, using three orientation-invariant kernels of different sizes. In the absence of a seed DEM, the first matching iteration uses only uncorrected images. Matches are considered successful if the correlation value exceeds a threshold that scales with the pyramid level.

At each level of the pyramid, the algorithm constructs a triangulated irregular network (TIN) of derived heights, which is refined using the results from the previous iteration. The minimum and maximum heights for each matching position are updated by combining the earlier results with each point's properties and the updated object space surface. Once the desired output resolution is reached, the final DEM is created by interpolating grid points that lack matches from the final TIN, using inverse distance weighting to smooth the output.

The SETSM algorithm relies on a number of assumptions. Firstly, it assumes that the RPC sensor models are accurate. If these models are incorrect, then the algorithm will search for matching points in the wrong locations. This means that SETSM can only tolerate small, locally consistent errors which could be corrected as bias, rather than large and/or spatially variable RPC errors which would break the matching step. Additionally, the algorithm finds matching points based on elevation so if the scene has low contrast – such as in the case of fresh snow or smooth ice – it becomes difficult to find accurate matches, making DEM production in the interior of ice sheets less reliable. SETSM also assumes that the two images in the stereo-pair were acquired simultaneously or near-simultaneously. However, analysis of ArcticDEM imagery stereo-pair acquisition dates suggests that the algorithm is sometimes used to produce DEMs from non-concurrent stereo-pairs (Figure 2.13). If these images are acquired at different times, there may be evidence of real elevation change for which the algorithm cannot correct.

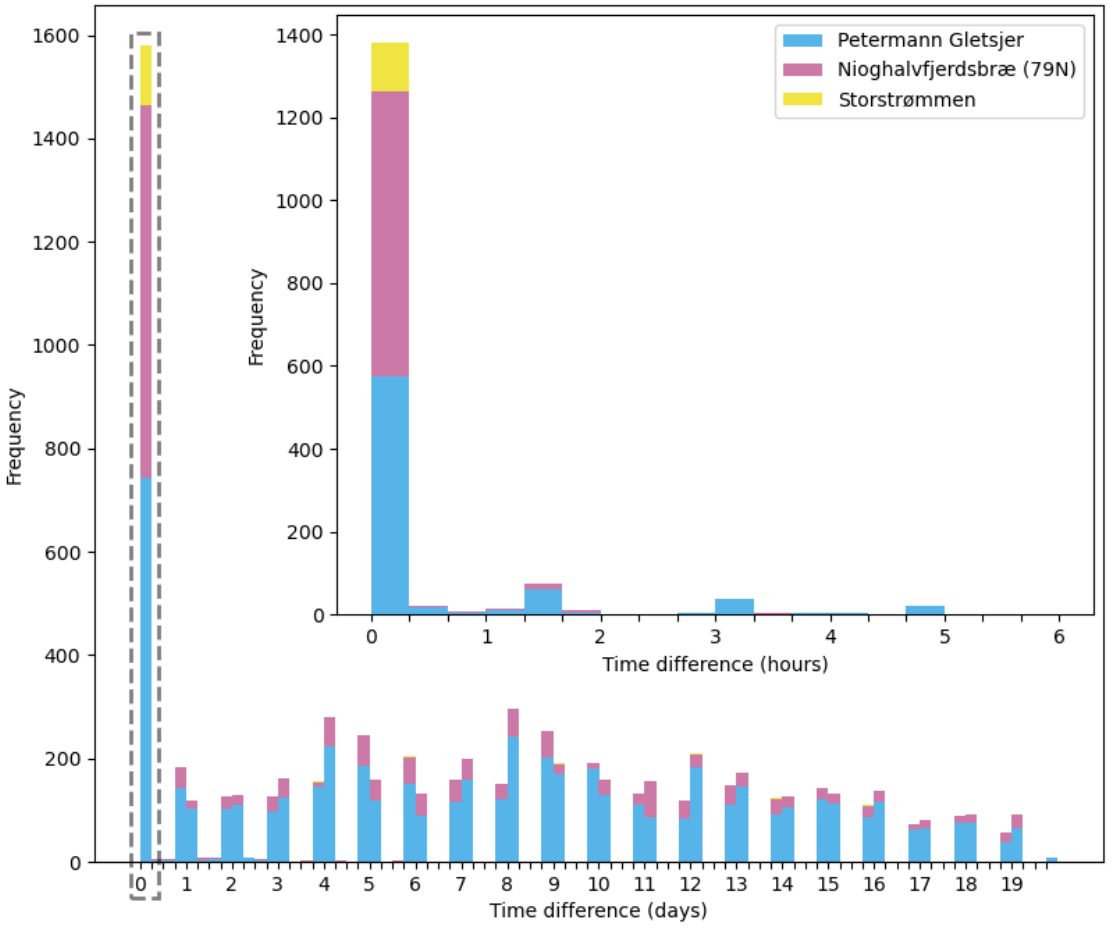


Figure 2.13: The acquisition date time differences of each ArcticDEM digital elevation model's stereo-pair used in the method presented in Chapter 6.

The SETSM algorithm has multiple sources of uncertainty. These include:

- image correlation errors in low contrast areas – low texture images cause unreliable correlation between stereo-pairs,
- residual RPC errors – small angular errors in satellite orientation could result in metres of vertical error creating offsets between adjacent DEM strips,
- missing areas from steep terrain – one image may see an area that its stereo-pair does not, meaning the algorithm cannot match the pixels and the area must be interpolated,
- acquisition time differences – non-simultaneous stereo-pair acquisitions have a higher uncertainty due to potential differences in real elevations.

These uncertainties indicate method limitations, of which the acquisition time difference appears to have the most impact within practical application of SETSM. The PGC use the

SETSM algorithm to produce ArcticDEM. However, the difference in acquisition dates between the stereo-pair images can be over two weeks (Figure 2.13), indicating that the uncertainties associated with these DEMs are likely higher than those with simultaneous or near-simultaneous acquisitions.

### 2.2.2 Supraglacial lake depth

In this section, I explore the current methods used to determine the depths of supraglacial lakes, highlighting both remotely sensed and field-based approaches. These methods draw upon various theoretical and technical foundations and can be categorised into optical and radiative transfer-based methods, radar-based techniques, structure-from-motion and DEM-based methods, as well as in situ field measurements. Each of these approaches has its own strengths and limitations, with some being more applicable at larger scales and others requiring direct measurements. This section examines the key methods used for lake depth estimation, discussing their underlying principles, applications, and associated challenges, particularly focusing on the radiative transfer equation and its assumptions, which form the basis of many remote sensing techniques. By reviewing these approaches, I establish the context for evaluating the radiative transfer equation's effectiveness and accuracy, especially in relation to other methods.

#### 2.2.2.1 Electromagnetic theory

The term 'electromagnetic spectrum' describes the full range of electromagnetic radiation, from radio waves to gamma waves (Figure 2.14). The electromagnetic spectrum is broadly subdivided into the following wavelength bands (in order of largest to smallest wavelength): radio wave, micro-wave, infrared, visible light, ultraviolet, x-rays, and gamma rays.

The way that electromagnetic radiation interacts with snow, ice, and water is wavelength-dependent. The wavelength controls how much energy is absorbed, scattered and transmitted by the surface material. Additionally, differences in the absorption, scattering and transmission properties of snow, ice, and water arise from structural and compositional differences. The air-ice mixture of snow causes strong scattering, pure ice produces less scattering but greater absorption of longer wavelengths, and water exhibits even stronger absorption due to molecular vibrations and scattering.

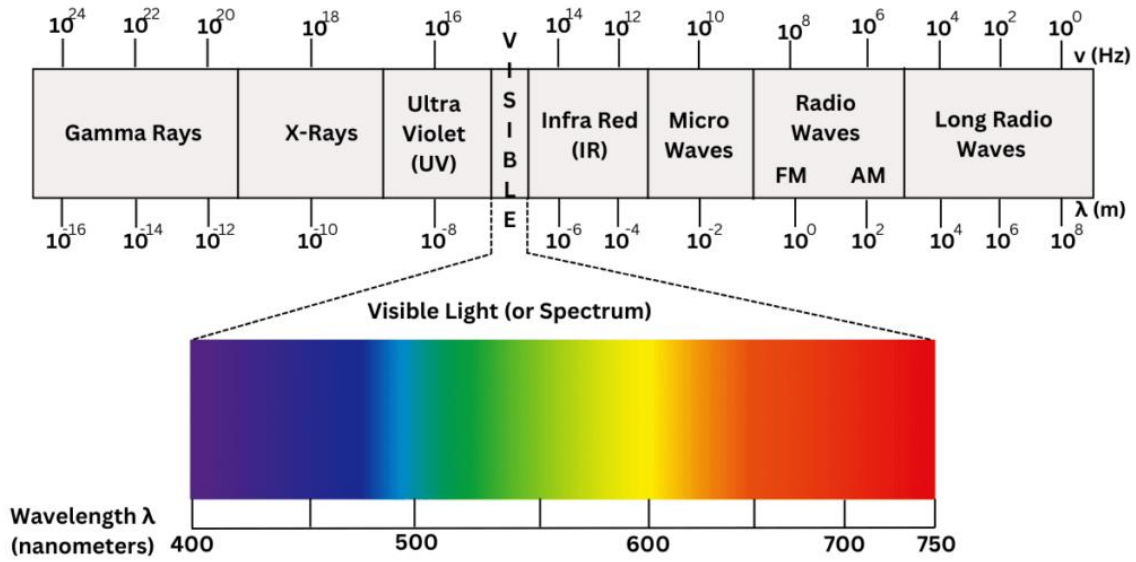


Figure 2.14: The full electromagnetic spectrum, with inset spectrum of visible light (image credit: scienly.com).

Atmospheric gases absorb radiation selectively, meaning that only certain wavelength ranges – known as transmission windows – allow the wavelengths to pass through the atmosphere to the Earth's surface and return to the sensor. Remote sensing satellites are designed to operate within these windows (Figure 2.15).

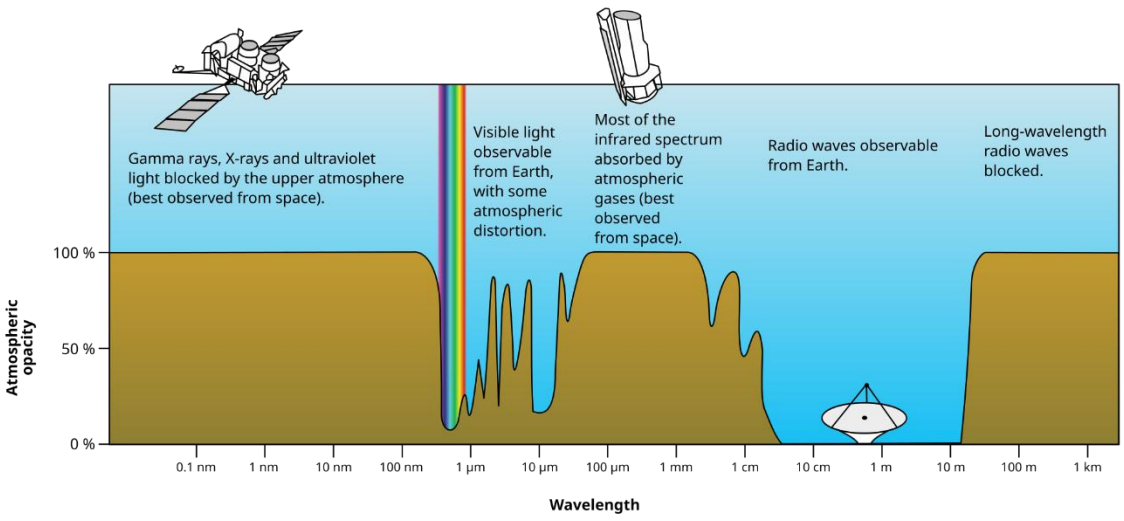


Figure 2.15: Transmission windows of the electromagnetic spectrum (image credit: Wikimedia Commons User: Mysid).

In the visible band, absorption by ice is weak and multiple scattering within the snow grains and air pockets mixes the visible light colours together, giving snow its high reflectance and bright white appearance. Water absorbs red light wavelengths and scatters

blue light within the water column, giving oceans and lakes their characteristic blue colour. Near-infrared wavelengths are absorbed more rapidly by ice and liquid water than visible wavelengths. In the thermal infrared, absorption levels are strong and ice and snow behave almost as black-body emitters which enable surface temperature retrievals. Snow and ice become relatively transparent under microwave and radio wavelengths which allows active and passive microwave sensors to penetrate the surface and detect subsurface features such as liquid water (Warren, 1982, 2019).

#### 2.2.2.2 Current methods of determining supraglacial lake depth

Determining supraglacial lake depth can be done in multiple ways. However, the techniques for doing so rely on different theoretical and technical foundations and can be split into; remotely sensed methods (radiative transfer-based, radar-based, SfM- and DEM-based), field-based and in situ methods, and theoretical methods.

Radiative transfer-based methods estimate lake depth by analysing how light interacts with the water column. The RTE (Philpot, 1987) uses the absorption and scattering properties of light in water to estimate depth and requires knowledge of ice surface reflectance and water optical properties. The equation is as follows:

$$z = \frac{\ln(A_d - R_\infty) - \ln(R_w - R_\infty)}{g} \tag{2.1}$$

where $z$ is the lake depth, $A_d$ represents the lake bottom albedo/reflectance, $R_\infty$ is the reflectance of optically deep water, $R_w$ is the reflectance value of the pixel of interest, and $g$ is the coefficient for spectral radiance loss in the water column.

The principles of the RTE rely on how easily certain wavelengths of light are absorbed and refracted within the water column. The level of spectral radiance loss is used to determine the water depth. This method works best for lakes with minimal surface contamination and clear water and can be used at scale (Sneed and Hamilton, 2007).

Due to its applicability at scale, the RTE offers an automatable approach to ice sheet-wide lake depth measurement from remotely sensed optical satellite imagery. However, prior to the study outlined in Chapter 4, there had been little to no validation of the RTE against other lake depth detection methods, meaning that depth results from this method carry an unconstrained degree of uncertainty. Despite this, depths derived from this method have extensive use in previous research because no alternative method has been developed that

enables lake depth measurement at a comparable scale (e.g. Georgiou et al., 2009; Pope et al., 2016; Sneed and Hamilton, 2007). The spatial resolution of the RTE is limited by the spatial resolution of the input optical satellite imagery. Although the spatial resolution of freely available optical satellite imagery is on the order of tens of metres (e.g. Sentinel-2 at 10 m (Drusch et al., 2012) and Landsat 8 at 30 m (Roy et al., 2014)) this still represents a limitation on the RTE. This is because the pixel size of an optical satellite with a 10 m resolution – the highest possible from freely available satellite data – is 100 $m^2$. Hence, the pixel represents an average reflectance of the area contained within that 100 $m^2$ area. If a lake was smaller than the pixel size of the input satellite, any attempt to determine its depth with the RTE would result in an underestimation even if the RTE was able to perfectly define depth, because the ice area around the lake would brighten the pixel, causing the lake to appear shallower than in reality.

A similar confounding effect is seen in areas of high cryoconite. Cryoconite is a dark, granular sediment composed of dust, soot, organic matter, and microbial communities that accumulates on the surface of glaciers and ice sheets. Due to its dark colour, it has a lower albedo than the surrounding ice and absorbs more incoming solar radiation, making it warmer. This melts the underlying ice and forms small depressions known as cryoconite holes (Figure 2.16) (Onuma et al., 2023; Sneed and Hamilton, 2011). These holes can further melt into the ice due to the positive feedback caused by low albedo. In areas with high cryoconite, a lake that is smaller than the pixel size of the input satellite would appear deeper when calculated using the RTE because the cryoconite around the lake would darken the pixel.

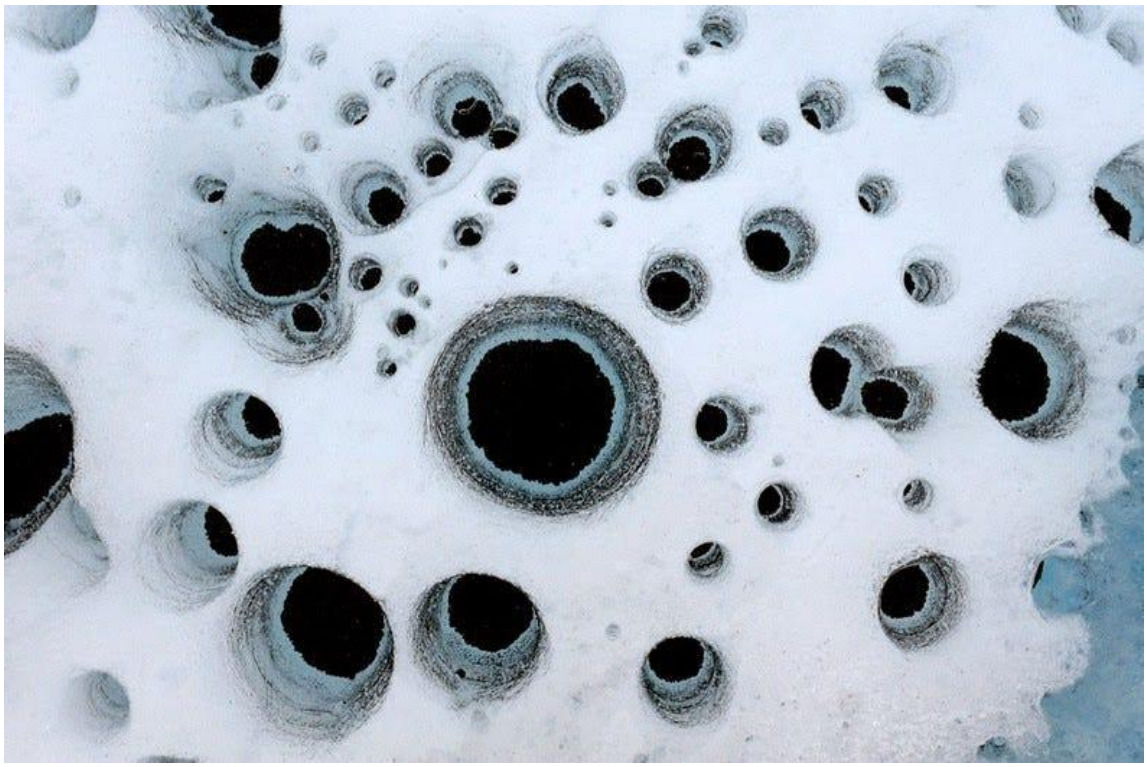

Figure 2.16: Cryoconite deposits on the surface of a glacier (image credit: J. Balog).

When surface lakes drain from areas of high cryoconite, the lake basin appears brighter than the surrounding ice. This suggests that the cryoconite holes have been washed out by the lake water which raises further issues surrounding the use of the RTE to determine lake depth. The RTE relies on several assumptions as determined by Sneed and Hamilton (2007). These assumptions are:

- The lake substrate (i.e. bottom) is homogeneous,
- Suspended or dissolved (in)organic particulate matter is minimal,
- There is no wind to cause waves on the lake surface,
- The lake surface and bed are parallel.

These assumptions describe an idealised pure water lake with a surface and uniformly absorbing bed of the same area thus allowing for vertical sides and a consistent parallel relationship. Not only this, but it also idealises the environmental conditions under which the geometric lake exists whereby there is no wind to cause waves. Supraglacial lakes do not conform to these assumptions. Cryoconite deposits may cause the bed to be non-uniformly absorbing (Figure 2.17). The bathymetry of a natural supraglacial lake will never offer a parallel surface and bed across its entire area with most exhibiting a smoothed shape to the lake bathymetry (Krawczynski et al., 2009). Similarly, the

environmental conditions during both the growth and maintenance of a lake cannot be ignored. The presence of cryoconite in the area will lead to ‘suspended or dissolved (in)organic particulate matter’ in the water column (Leidman et al., 2021). Even if this cryoconite were to settle at the bottom of the lake, it would still lower the overall albedo of the lake bottom, and its apparent removal when observing a drained lake basin suggests that it must have existed in the lake prior to drainage (e.g. Miles et al., 2017).

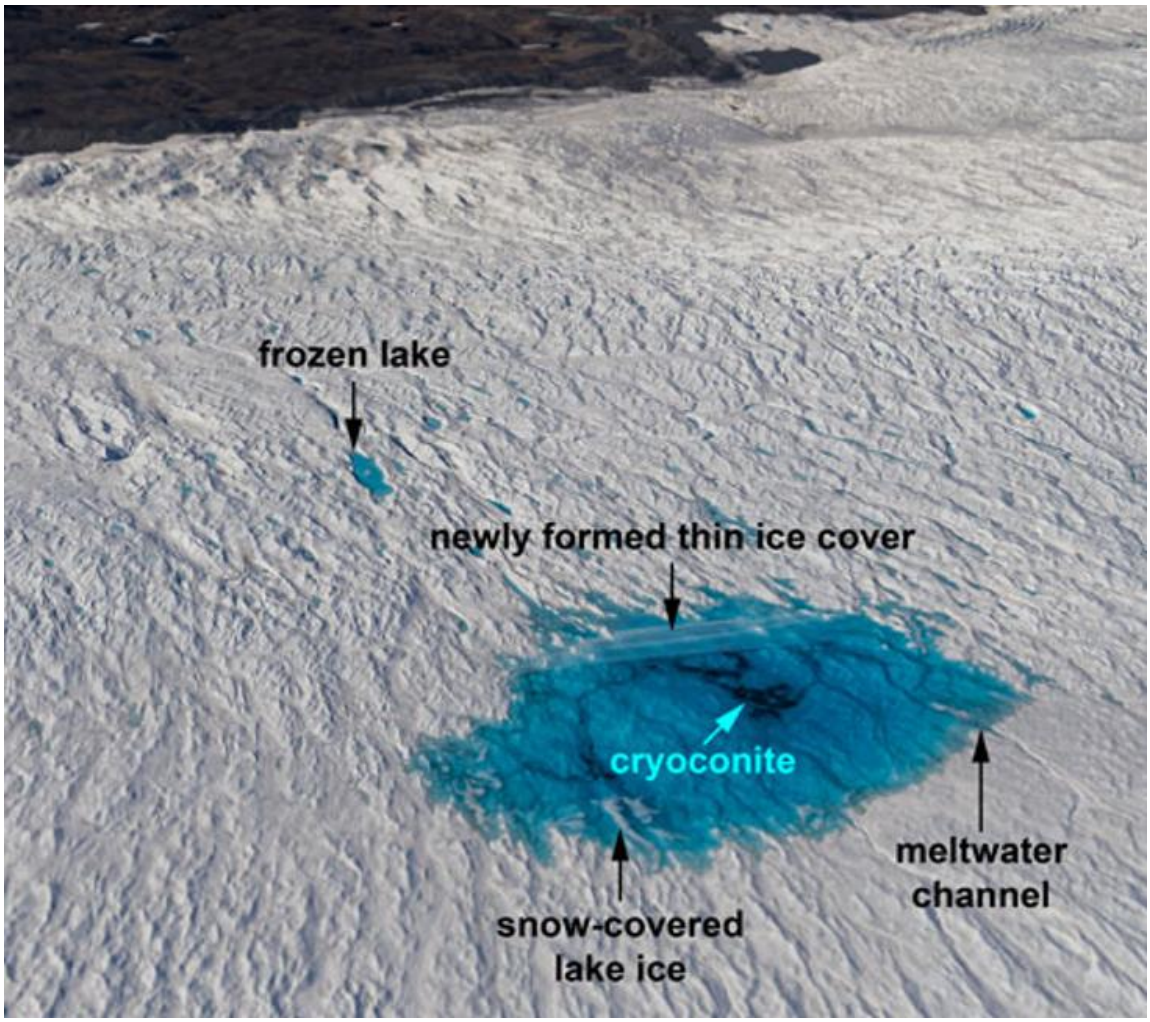


Figure 2.17: Supraglacial lake with cryoconite deposits in its bed, these mean the bed cannot be a uniform reflector (Studinger et al., 2022).

Empirical band-ratio methods rely on the principles of radiative transfer and may be used at scale due to their reliance on remotely sensed data (Banwell et al., 2014; Moussavi et al., 2016). This group of methods uses multispectral satellite imagery to derive relationships between spectral bands and lake depth. Commonly, studies use the ratio of blue light (which has high penetration and low absorption in the water column) to red light/near infrared wavelengths (which have low penetration and strong absorption). These ratio-based methods are simpler than full radiative transfer-based models but require calibration against in situ measurements (Moussavi et al., 2020).

Photon counting LiDAR methods using satellite missions such as ICESat-2 measure laser pulse reflections from both the lake surface and the lakebed (Datta and Wouters, 2021). ICESat-2 was launched in 2018 by NASA and is the successor satellite to the ICESat mission. With a nominal along-track resolution of 0.7 m, six acquisition beams, and a 91-

day revisit time (Markus et al., 2017), ICESat-2 provides very high-resolution photon returns of the atmosphere-water and water-ice interfaces. Due to these characteristics, ICESat-2 has also been used in previous studies to calculate lake depths (e.g. Datta and Wouters, 2021; Fair et al., 2020). LiDAR methods can provide direct depth estimates but the accuracy of these measurements depends on water clarity. These methods work best for relatively shallow lakes (< 7 m) where the photons can penetrate the water column down to the lakebed (Fair et al., 2020).

Radar-based methods use microwave signals to penetrate the ice and water (Lampkin and VanderBerg, 2011). Although SAR methods are mostly used to detect changes in surface properties rather than directly measuring depth, they can sometimes provide indirect information if liquid water is present beneath an ice cover (Johansson and Brown, 2012).

Radar sounding methods, including ice-penetrating radar missions such as Operation IceBridge, can sometimes detect lake bottoms if the water is not too deep and if radar attenuation is low (Datta and Wouters, 2021; Fair et al., 2020). SfM photogrammetry and DEM-based methods use high-resolution aerial or UAV imagery to generate 3-D surface reconstructions (e.g. Bash et al., 2018; Benoit et al., 2019; Rossini et al., 2018). With these methods, we can estimate changes in lake depth over time provided the bed topography is known. However, this requires high-quality imagery for accurate results.

Historically, field-based and in situ methods were the only way to determine lake depth on ice sheets due to the lack of remotely sensed data (Box and Ski, 2007; Tedesco and Steiner, 2011). Although these methods provide direct measurements, they are logistically challenging due to the isolated locations of supraglacial lakes. Advances in field equipment have increased the ability of field researchers to take in situ measurements of lake depths. Pressure sensors can be deployed at the bottom of the lake to measure hydrostatic pressure and infer depth. However, due to their nature as deployed instruments in water, the sensors are subject to potential drift, freezing adhesion to the lake bottom, and failure (Alexander et al., 2020). Acoustic echo sounding methods use sonar pings to determine lake depths (Box and Ski, 2007). This works well in clear, unfrozen water and is resultingly ideal for supraglacial lakes if focusing solely on its theoretical application.

However, all in situ measurement techniques rely on field deployment of personnel and instruments. There are significant dangers associated with field-based methods due to capsizing and the potential for rapid lake drainage events (Figure 2.18), where a lake may

drain in as little as two hours (Das et al., 2008). Resultingly, few in situ measurements of supraglacial lake depths exist with only three geographically limited studies available of the GrIS since 2010 (Brodský et al., 2022; Lutz et al., 2024; Tedesco and Steiner, 2011).

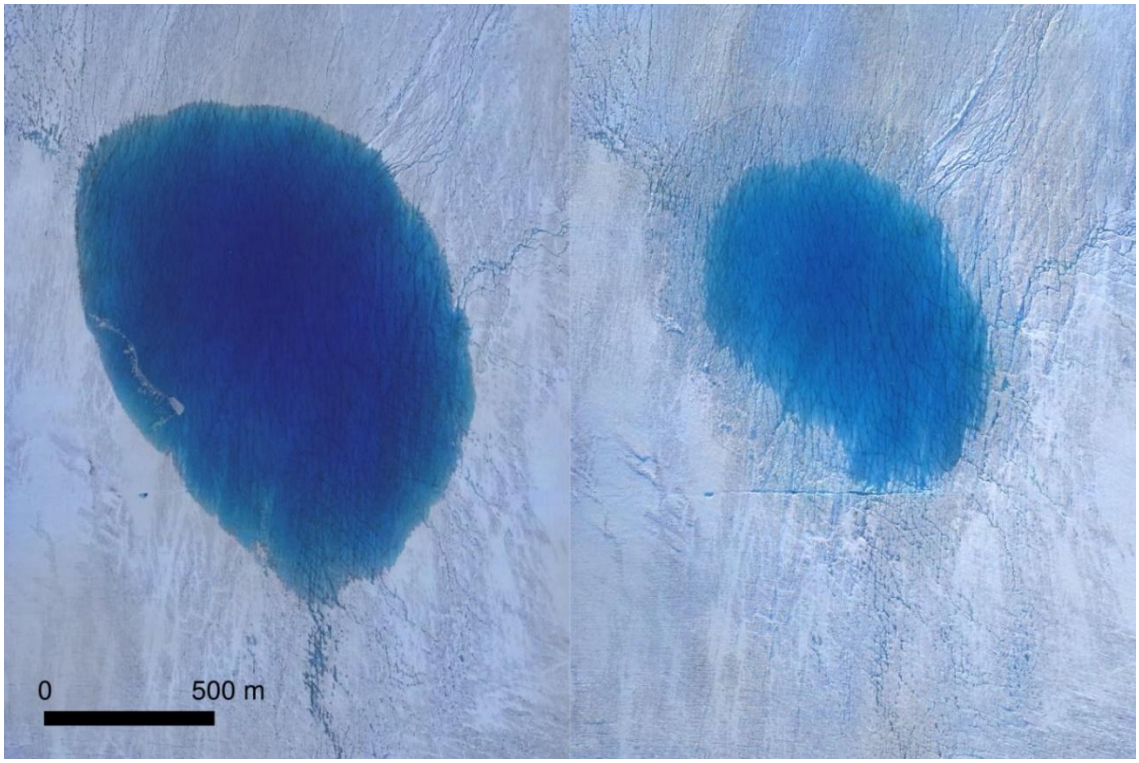


Figure 2.18: Aerial photographs of a supraglacial lake on the GrIS before (left) and after (right) partial drainage (image credit: T. Chudley).

Theoretical methods of determining supraglacial lake depth are inherently limited due to their reliance on simplifying assumptions. One such method, pioneered by Krawczynski et al. (2009), is the inverse cone method. This assumes that the lake basin has an inverted conical shape. Under this assumption, the maximum depth is approximated as one-hundredth of the lake diameter. Krawczynski et al. (2009) found that this approximation worked reasonably well for many surface lakes. However, some lake bathymetries deviate from a simple conical shape due to complex bed topography and differential melting, so the method cannot accurately predict maximum depth in these cases.

#### 2.2.2.3 Existing supraglacial lake depth products

Although many Greenland-based inventories of supraglacial lakes exist (Hu et al., 2021; Schröder et al., 2020; Dunmire et al., 2025), only one offers an ice sheet-wide inventory of lake depth, Corr (2023). This study represents the first decadal-based study of

Greenlandic supraglacial lakes and provides monthly and yearly estimates of lake extent and volume, with lake depths based on the RTE.

The unconstrained uncertainty of the RTE makes an intercomparison between it and other remote sensing methods essential for accurately determining lake depths on the GrIS. Without understanding this uncertainty, we cannot constrain the accuracy of RTE-based water volume calculations, limiting our confidence in future ice sheet predictions.

### 2.2.3 Locating grounding lines

Understanding the grounding line's behaviour is essential for assessing the stability of marine-terminating glaciers and their contribution to sea level rise. This section provides an overview of the key physical principles governing grounding line dynamics, including its role in ice sheet stability, interactions with oceanic and atmospheric forces, and the influence of tidal flexure. Following this, I review the current methods used to determine grounding line positions, distinguishing between dynamic and static approaches. Finally, I outline the primary datasets that support grounding line identification, highlighting their historical use and potential for advancing our understanding of Greenland's floating ice tongues.

#### 2.2.3.1 Background

The grounding line marks the transition between the grounded ice sheet (in contact with the bedrock at its base) and a floating ice shelf or ice tongue. Floating ice shelves are wider than they are long, leading to a 'shelf-like' appearance, whereas ice tongues are longer than they are wide, resulting in a 'tongue-like' appearance. Ice shelves typically form in embayments and are more common on the AIS (where embayments are a more common feature), whereas ice tongues typically form in valley fjords and are more common on the GrIS (where fjords are a more common feature). In similar environmental conditions, the geography of the land mass's fringes are the determining factor of if an ice tongue or ice shelf will form. The grounding line plays a key role in ice sheet stability, with its position determining the extent of the glacier which is in hydrostatic equilibrium and the level of interaction between the glacier and the ocean (Li et al., 2023c; Möller et al., 2022). Grounding line movement influences mass balance and contributes to sea level changes through basal melting, calving, and ice flow dynamics (Millan et al., 2023; Hill et al., 2024).

Grounding line position is governed by ice thickness, bed topography, and ocean interactions. When oceanic or atmospheric conditions increase basal melting, the grounding line can retreat inland, potentially destabilising the inland ice (e.g. Millan et al., 2022a; Reese et al., 2023). Conversely, in colder conditions or during a surge, the grounding line can advance into the ocean (Hill et al., 2018b; Mouginot et al., 2018). The response of the grounding line to external forcing is important for assessing the stability of marine-terminating glaciers, particularly in regions where bed topography slopes downward towards the inland ice (known as a retrograde bed). Grounding lines positioned on a retrograde bed make the ice sheet more susceptible to rapid retreat; this is known as MISI (Figure 2.19) (Schoof, 2007).

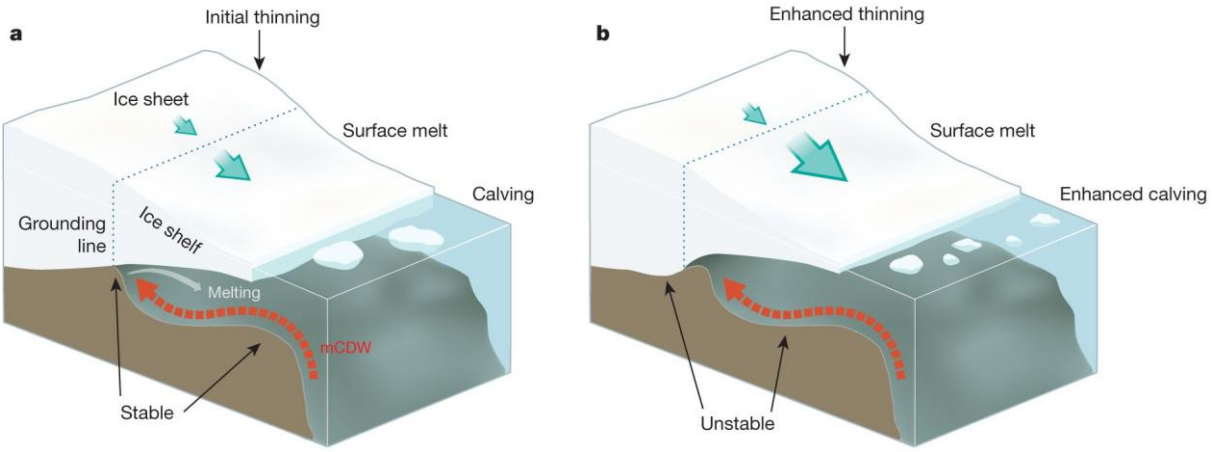


Figure 2.19: The MISI hypothesis (Hanna et al., 2013).

The floating portion of an ice tongue experiences bending and flexure due to tidal forcing and ocean pressure variations. The governing equation for the elastic bending of ice shelves under tidal forcing is derived from the Kirchhoff-Love plate theory, a two-dimensional mathematical model used to determine stresses and deformations in thin plates subject to forces and moments. With this theoretical model, an ice shelf/tongue can be modelled as a thin plate due to the significant disparity between its thickness and length/width (Holdsworth, 1969; Vaughan, 1995).

Flexural waves propagate through the ice shelf leading to localised bending stresses near the grounding line. Over time, repeated tidal flexure can contribute to fracture development, potentially affecting ice shelf stability and precipitating calving events (Vaughan, 1995; Hulbe et al., 2016).

Hydrostatic equilibrium is a condition met when a floating glacier extension maintains equilibrium by balancing its weight against the buoyant force exerted by seawater. The hydrostatic equilibrium condition is given by:

$$h_f = h_i \frac{\rho_i}{\rho_w} \tag{2.2}$$

where $h_f$ is the submerged ice thickness, $h_i$ is the ice thickness, $p_i$ is the density of ice, and $p_w$ is the density of seawater. This relationship governs flotation, determining the grounding line position.

The interactions between grounding line migration, tidal flexure, and hydrostatic equilibrium affect ice shelf stability and mass balance. Increased melting beneath floating ice tongues can reduce ice thickness, causing a retreat of the grounding line (Konrad et al., 2018; Li et al., 2015). This process can trigger positive feedback mechanisms such as reduced basal friction, increased fracturing and calving, and heightened sensitivity to sea level variation (Millan et al., 2022a). These mechanisms can cause increased ice velocity and mass loss, leading to further changes in the grounding line position and shelf thickness (Hill et al., 2018b). Understanding these fundamental principles is essential for predicting the response of ice tongues to climate change and improving ice sheet models used in sea level rise projections.

#### 2.2.3.2 IceBridge BedMachine Greenland bed elevation and ice thickness

IceBridge BedMachine Greenland version 5 (Morlighem et al., 2022) is a bed topography and bathymetry map of Greenland based on mass conservation, multi-beam data, and various other methods. In addition to the bed topography layer, BedMachine is packaged with surface elevation, ice thickness, and bed topography/ice thickness error layers in addition to an ice/ocean/land mask.

In this dataset, the mass conservation approach is used to calculate ice thickness from a combination of sparse, airborne radar-derived ice thickness data and high-resolution ice motion derived from InSAR. This method solves the mass conservation equation of deriving ice thickness whilst reducing the difference to the original radar-derived ice thickness data. It works best in areas of fast ice flow where the errors in the flow direction are smaller, and the glaciers slide on the bedrock. In the interior regions of the ice sheet, errors in the flow direction are larger, so the ice thickness is interpolated via kriging for

data up to 2016. Data post-2016 is interpolated with streamline diffusion as opposed to kriging.

There are multiple sources of error in the BedMachine dataset. Some sources include error in the ice velocity direction and magnitude (which is larger for slower ice flow areas), error in the SMB, and error in ice thinning rates. In areas that are less well constrained by radar-derived thickness data, or which rely on only one track of data, errors in the mass-conservation-inferred ice thickness exceed 50 m (Morlighem et al., 2013). In fact, the bed topography/ice thickness error layer shows significantly higher errors than this estimate for areas of every glacier researched within this thesis. In Figure 2.20 I show the example of Petermann Gletsjer, a large fast-flowing glacier in the north of Greenland. Further examples of the BedMachine bed elevation/ice thickness error can be found in Appendix B.3.

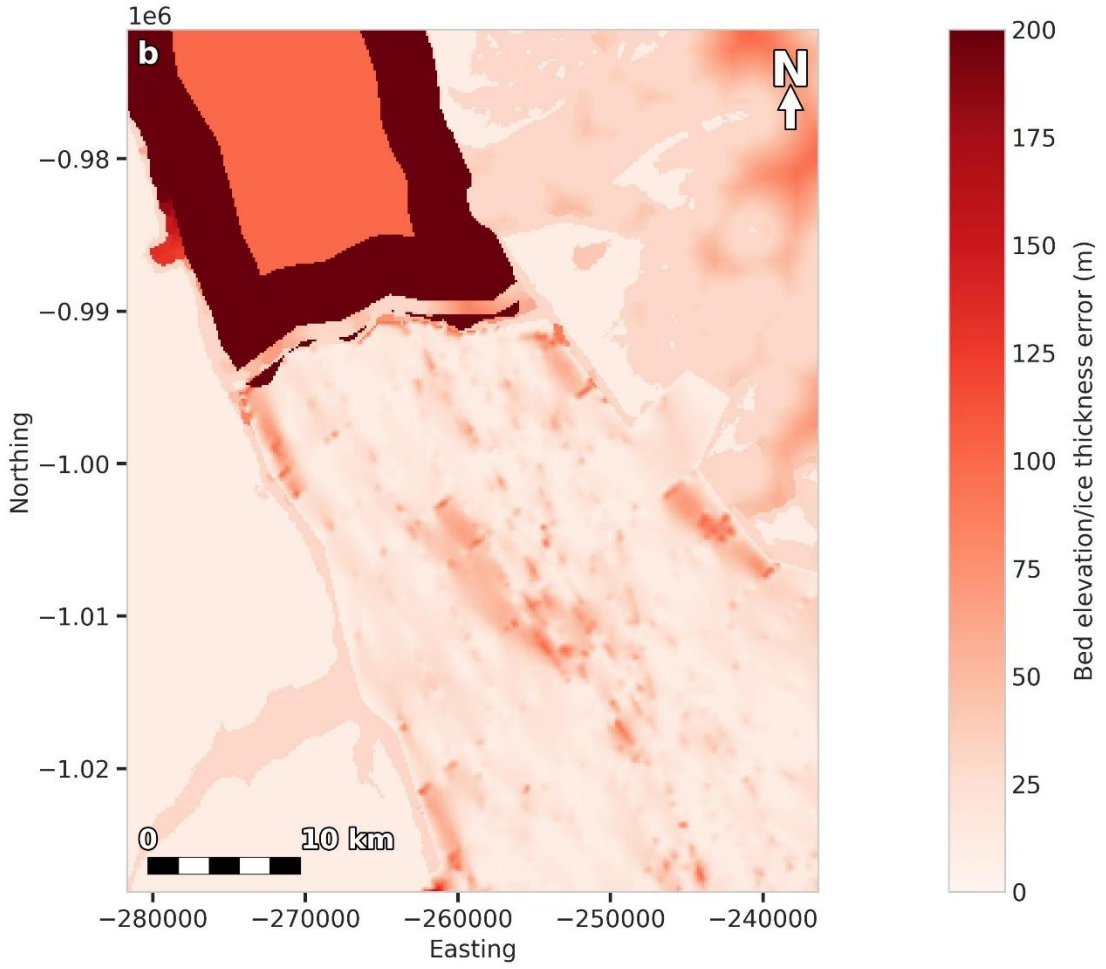


Figure 2.20: The BedMachine version 5 bed elevation/ice thickness error for Petermann Gletsjer in north Greenland.

The limitations on this dataset imposed by its source data mean that its error is not robust. However, other methods, such as quantile regression forests (QRFs), can result in more physically plausible and better constrained bed topography. Palmer et al. (2025) found that their QRF approach reduced the root mean square error of ice depth predictions by 18% compared to BedMachine version 3, and that it significantly improved uncertainty calibration. For BedMachine version 3, 68% of new observations fall within the Palmer et al. (2025) 90% prediction interval, whereas for the QRF model, this rose to ~90%. This QRF approach improves the balance between accuracy and uncertainty while offering a more computationally efficient, accessible method for deriving subglacial topography from radio-echo sounding data than the method of derivation for BedMachine.

#### 2.2.3.3 Finite Element Solution (2022) tidal prediction model

Global and regional tidal models provide the information required for understanding sea level variability, coastal dynamics, and ocean–ice interactions. The Finite Element Solution (2022) (FES2022) model (Lyard et al., in prep.) calculates tidal heights by combining an unstructured mesh, high-resolution bathymetry, and data assimilation of multi-mission satellite altimetry to solve the depth-integrated shallow-water equations for all major tidal constituents.

Key assumptions of the FES2022 tidal model include the barotropic approximation, stationary tidal dynamics, and simplified friction and self-attraction/loading representations. Consequently, model performance is less accurate in very shallow, friction-dominated, or estuarine environments, regions with strong internal tides, and in areas without satellite altimetry observations.

While this model performs well compared to other tidal models in shallow water regions and in coast and polar seas, several uncertainties remain. Errors in bathymetry, unresolved coastal complexity, limitations in altimetry near land and ice, and parameterisations of nonlinear processes all contribute to model uncertainty. Although the FES2022 tidal model is more accurate than many of its counterparts, it still exhibits limitations inherent to the physics, data availability, and computational constraints of its approach.

The FES2022 model achieves centimetre-level accuracy in the open ocean, representing a substantial improvement compared to earlier versions such as FES2014 (Lyard et al., 2021). However, regional validation studies indicate that while model errors in the open ocean are on the order of 1–2 cm for major constituents, larger discrepancies (up to tens

of centimetres) can occur in complex coastal zones, with FES2022 performing similarly to previous solutions in tide-gauge fits (Wang and He, 2025).

#### 2.2.3.4 Current methods

The grounding line position cannot be directly observed using satellite remote sensing. Instead, we rely on proxy indicators to infer its position. The current methods used fall into two categories, dynamic methods, and static methods.

Dynamic approaches detect vertical ice movement caused by tidal and atmospheric pressure variations, using techniques that exploit tidal signatures. These include:

- InSAR which measures differential ice displacement over time (e.g. Milillo et al., 2022; Millan et al., 2023; Mouginot et al., 2018; Rignot et al., 2001),
- SAR differential range offset tracking (SAR DROT) which uses sequential radar images to detect horizontal displacement (e.g. Joughin et al., 2016; Marsh et al., 2013),
- Tidal motion offset correlation (TMOC) which tracks small-scale tidal movements to determine the grounding line location (Wallis et al., 2024),
- Repeat-track laser altimetry (RTLA) which monitors surface elevation changes from spaceborne laser altimeters (e.g. Freer et al., 2023; Fricker and Padman, 2006; Li et al., 2022),
- Pseudo crossover radar altimetry (PCRA) which uses radar altimetry to compare elevation differences at crossover points (Dawson and Bamber, 2017, 2020).

These methods primarily identify the landward limit of tidal flexure, often referred to as the hinge line (Figure 1.10). However, due to the elastic properties of ice, deformation can extend inland from the true grounding line (Padman et al., 2018; Vaughan, 1994). This typically results in an overestimation of floating ice extent. Nevertheless, the discrepancy is often small, usually on the order of a few hundred meters, which is minor relative to the extent of floating ice (Rignot et al., 2011).

Static methods rely on single-time observations rather than temporal changes and can be divided into hydrostatic equilibrium methods and surface slope methods.

- Hydrostatic equilibrium methods are based on Archimedes' principle of buoyancy. These methods infer the grounding line from ice thickness and elevation data (e.g.

Friedl et al., 2018; Le Meur et al., 2014). The aim is to locate the landward limit of stable hydrostatic equilibrium, where ice is freely floating (Figure 1.10). However, deviations from hydrostatic balance often occur near the surface slope break, causing grounding line estimates to align more closely with this transition rather than the true equilibrium point. Horizontal uncertainties in these methods can reach up to 350 meters on slopes of at least 1° (Friedl et al., 2018).

- Surface slope methods identify the break in glacier slope which is a key characteristic of grounding line transitions. These methods use elevation profiles, radar altimetry-derived DEMs (e.g. Herzfeld et al., 2008; Herzfeld and Wallin, 2014; Hogg et al., 2018), and optical imagery (e.g. Bindschadler et al., 2011). Defining a singular slope break is challenging in ice plains due to the presence of multiple breaks (Alley et al., 1989; Christie et al., 2018). Optical satellite images can aid in slope break identification through shading contrasts, a technique which is leveraged in numerous studies (e.g. Christie et al., 2018; Möller et al., 2022).

While both dynamic and static methods have been extensively applied on the AIS, their use on the GrIS remains comparatively limited. Notable studies include Rignot et al. (2001), Climate Change Initiative (2023) and Millan et al. (2023) (InSAR), and Möller et al. (2022) (InSAR, hydrostatic equilibrium, surface slope). All these studies use InSAR, with only one, Möller et al. (2022), using a combination of dynamic and static methods. Although Rignot et al. (2001) proffers temporal snapshots of the grounding lines of northern Greenland, each of the other studies provides a temporal evolution of their studied glaciers' grounding lines. These datasets specifically focus on the late 2010s, likely due to the higher availability of freely accessible SAR data for this period. As such, there are temporal gaps left in the grounding line record in the early 2010s.

#### 2.2.3.5 Previous products and estimates

Antarctic ice shelf grounding lines are extensively studied, since the large size of Antarctic ice shelves makes them a higher priority than Greenland's floating ice tongues in terms of potential contribution to global sea level rise. Whilst the floating extensions of Greenland are smaller, they contribute significantly to ice sheet stability, mediating the ice sheet's dynamics and thus its contribution to global sea level rise. Of the 208 marine-terminating glaciers on the GrIS (Kochtitzky and Copland, 2022), fewer than 14 (6.7%)

have had a floating extension monitored in the past few decades (Millan et al., 2023; Rignot et al., 2001).

Using InSAR data from ERS-1 and ERS-2, Rignot et al. (2001) mapped the 1992 and 1996 grounding lines of ten northern Greenland marine-terminating glaciers (where data permitted). Table 2.1 details the glaciers studied, and Figure 2.21 shows the mapped grounding lines. The grounding lines from this study have been used in other products including the BedMachine version 3 dataset published some two decades later (Morlighem et al., 2017). Since grounding lines are dynamic features, it is likely that their ability to usefully contribute to such products will decrease with time if records are not updated.

More recent datasets include Mouginot et al. (2018) which contains grounding lines defined from InSAR data. This study defined the grounding lines of Storstrømmen and L. Bistrup Bræ which are detailed in Table 2.1. Möller et al. (2022) used the shade method and InSAR data to define the grounding lines of the floating extensions of Flade Isblink (Table 2.1).

Millan et al. (2023) represents one of the most comprehensive Greenland grounding line studies in recent literature, with eight glaciers surveyed. This research also used InSAR data to map the grounding lines, taking data from ERS-1, ERS-2, and Sentinel-1. The glaciers studied are detailed in Table 2.1.

The final available grounding line dataset for the Greenland glaciers was produced by the Climate Change Initiative (CCI) and is also derived from InSAR data (Climate Change Initiative, 2023). The years to which this dataset pertains are detailed in Table 2.1.

Table 2.1 elucidates the need for a method which relies on non-SAR data. There are significant gaps in the historical record before the mid-2010s for most of the glaciers when SAR data was not available. Grounding lines are an essential climate variable, which means that they have been defined as a key measure for monitoring and understanding the Earth's climate system (WMO et al., 2022). The recommended temporal resolution for grounding lines is annual (WMO et al., 2022), meaning that continuous monitoring and augmentation of temporal gaps is important; DEM-based methods could offer the solution to this issue.

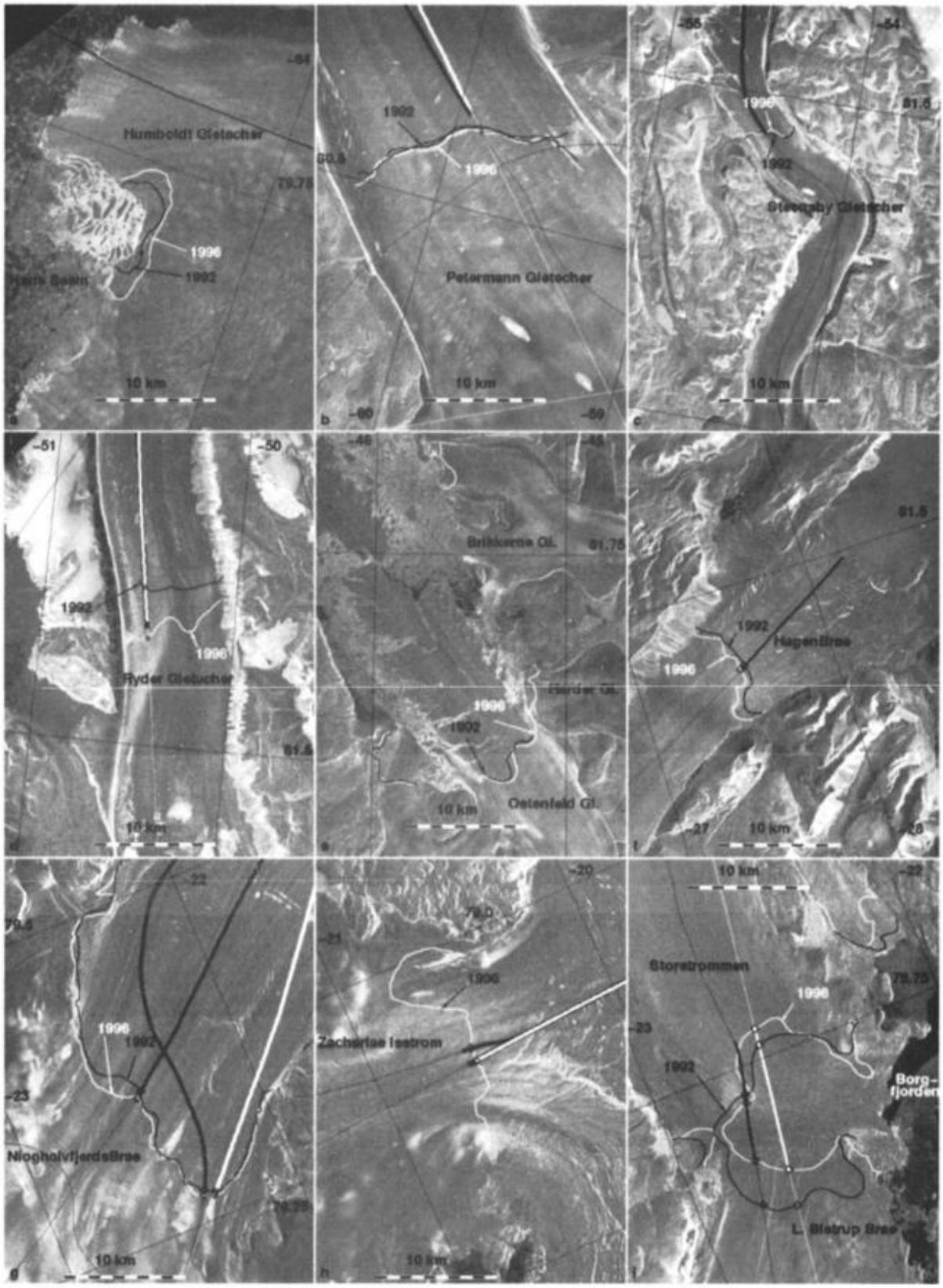


Figure 2.21: The grounding lines of northern Greenlandic glaciers as determined by Rignot et al. (2001).

Table 2.1: The sources of historical Greenlandic grounding lines. Key: CCI = Climate Change Initiative (2023), Mi = Millan et al. (2023), Mö = Möller et al. (2022), Mou = Mouginot et al. (2018), Ri = Rignot et al. (2001), and cross-hatched cells = no data.

| Glacier name | Grounding line margin | | | | | | | | | | | | | | | | |
|---|---|---|---|---|---|---|---|---|---|---|---|---|---|---|---|---|---|
| | ‘78 | ‘92 | ‘93 | ‘94 | ‘95 | ‘96 | ‘99 | 2006 | 2011 | 2014 | 2015 | 2016 | 2017 | 2018 | 2019 | 2020 | 2021 |
| Petermann | | Mi | | | CCI | Mi | | | Mi | Mi | Mi | Mi | Mi | Mi | Mi | Mi | Mi |
| Steensby | | Mi | | | | | | | | | | Mi | Mi | Mi | Mi | Mi | |
| Ryder | | Mi | | | | CCI | | | Mi | | Mi | Mi | Mi | Mi | Mi | Mi | |
| C. H. Ostenfeld | | Ri | | | | Ri | | | | | | | | | | | |
| Harder | | | | | | Ri | | | | | | | | | | | |
| Brikkerne | | | | | | Ri | | | | | | | | | | | |
| Hagen Bræ | | | | | | CCI | | | | | | | CCI | | | | |
| Flade Isblink | | | Mö | | | | Mö | Mö | | Mö | | | | Mö | Mö | | Mö |
| Nioghalvfjerdsbræ | | Mi | | Mi | CCI | Mi | | | Mi | | | Mi | Mi | Mi | Mi | Mi | |
| Zachariæ Isstrøm | | | | | CCI | Mi | | | Mi | Mi | | | Mi | | | Mi | |
| Storstrømmen | Mou | Mi, Mou | | | | Mi, Mou | | | | | Mou | Mi | Mi, Mou | Mi | Mi | Mi | |
| L. Bistrup Bræ | Mou | Mou | | | | Mi, Mou | | | | | Mou | Mi | Mi, Mou | Mi | Mi | Mi | |

# 3 Introduction – Summaries

## 3.1 Introduction summary

Accurately measuring ice sheet surface and subsurface features is important for understanding ice sheet dynamics, hydrology, and stability. This section summarises our current understanding, the context of this thesis, and the overall thesis objectives and scope. I first outline the role of DEMs in glaciology, highlighting their established and emerging uses in monitoring surface elevation, supraglacial lakes, and grounding line positions. I then review the primary methods for estimating supraglacial lake depth and detecting grounding lines, assessing their strengths, limitations, and relevance to ice sheet stability. By contextualising these approaches, I lay the foundations for my research, which aims to refine existing methodologies and advance new techniques for improving our understanding of ice sheet processes. Finally, I outline the specific goals and structure of this thesis.

### 3.1.1 The importance of DEMs

DEMs are essential tools in glaciology, providing high-resolution data on ice sheet topography, surface changes, and ice-ocean interactions. They have been widely used to monitor ice sheet mass balance (e.g. Otosaka et al., 2023; Winstrup et al., 2024), surface melt (e.g. Winstrup et al., 2024), and ice surface and subsurface characteristics (e.g. Bowling et al., 2019, 2021; Palmer et al., 2015), with applications ranging from ice velocity mapping to detecting elevation changes due to thinning or thickening (Palmer et al., 2010; Rivera et al., 2005; Shean et al., 2019). Satellite-derived DEMs such as those from ICESat-2, CryoSat-2, and WorldView stereo imagery have been used to measure surface elevation changes over time, providing insights into short-term seasonal fluctuations and long-term ice loss trends (Dai et al., 2018; Slater et al., 2018; Shen et al., 2022).

One important but still developing application of DEMs is determining supraglacial lake depth. Pope et al. (2016) demonstrated the potential of DEM differencing to estimate lake volume changes, but this method relied on bespoke DEMs because datasets like ArcticDEM did not yet exist. Given the increasing availability of high-resolution DEMs, there is potential to expand this approach to broader spatial and temporal scales, improving our understanding of meltwater storage and its influence on ice dynamics.

DEMs also have the potential for refining grounding line detection, a key factor in understanding ice sheet stability and ocean-driven ice loss. While grounding lines have traditionally been mapped using techniques such as InSAR (Rignot et al., 2001; Mouginot et al., 2018; Milillo et al., 2022; Millan et al., 2023), there is potential to use DEM stacks to identify grounding lines based on the stack's deviations in given locations. Additionally, coupling DEM time series with tidal models could allow for high-low tide DEM pair identification, providing further constraints on grounding line migration and ice-ocean interactions. These approaches could complement existing methods and enhance our ability to track grounding line movement in response to climate-driven changes.

Despite these promising applications, many potential uses of DEMs in glaciology remain unexplored, including the estimation of calving volumes and calculation of basal melt rates. As satellite technology advances and computational techniques improve, DEMs will continue to offer exciting opportunities for revealing new aspects of ice sheet behaviour and improving predictions of future change.

### 3.1.2 Summary of current understanding

Understanding supraglacial lake depth and grounding line locations is essential for assessing ice sheet hydrology, ice-ocean interactions, and overall ice sheet stability. Remote sensing techniques provide valuable tools for these measurements, though current methods have inherent limitations. Here, I summarise the primary techniques used for supraglacial lake depth estimation and grounding line detection and establish the context of this thesis.

#### 3.1.2.1 Measuring supraglacial lake depth from remotely sensed data

Supraglacial lakes are essential for ice sheet hydrology and dynamics, with their depths indicating the potential for hydrofracture events affecting ice sheet stability (Das et al., 2008; Krawczynski et al., 2009). Several remote sensing methods, each with advantages and limitations, have been developed to measure lake depth.

Optical and multispectral techniques, such as empirical band ratios (e.g. Pope et al., 2016) and radiative transfer models (e.g. Philpot, 1987), rely on light penetration and wavelength reflectance but require cloud-free conditions and assume uniform lakebed reflectance (Sneed and Hamilton, 2007, 2011). Microwave and radar methods, including SAR, can detect lake extent but struggle with depth estimation due to signal attenuation

and surface roughness (Lampkin and VanderBerg, 2011). Satellite altimetry uses changes in photon return to infer depth but is limited by its along-track data sampling and long revisit intervals (Datta and Wouters, 2021; Fair et al., 2020; Markus et al., 2017). DEM differencing, based on surface elevation changes post-drainage (Pope et al., 2016), requires cloud-free optical or radar acquisitions and is limited by satellite revisit intervals. Common limitations across all methods include spatial gaps due to fixed orbital tracks, cloud cover interference for optical methods, and temporal gaps from repeat-pass intervals, restricting the ability to track rapid depth changes.

#### 3.1.2.2 Locating grounding lines using remotely sensed data

Accurately locating grounding lines is important for assessing ice mass loss and ice-ocean interactions. Current methods mainly rely on InSAR (e.g. Milillo et al., 2022; Millan et al., 2023; Mouginot et al., 2018; Rignot et al., 2001), while DEMs and optical imagery offer alternative approaches with specific limitations (e.g. Bindschadler et al., 2011; Herzfeld et al., 2008; Herzfeld and Wallin, 2014; Hogg et al., 2018).

InSAR detects tidal flexure at the grounding line using differential radar phase measurements, but accurate interpretation requires precise tidal models, and its temporal resolution is constrained by satellite revisit cycles. InSAR is less reliable in areas with low tidal range or complex surface roughness (Chatterjee et al., 2009). DEM-based methods infer the grounding line location from surface topography, but the break-in-slope method only provides a proxy, and accuracy depends on DEM resolution and data quality. Optical imagery techniques detect slope breaks through changes in surface shading (Bindschadler et al., 2011), but these rely on subjective interpretation and favourable lighting conditions.

Each method has constraints, with many dependent on satellite revisit intervals, limiting the ability to track rapid grounding line migration. Additionally, meteorological factors and surface roughness complicate grounding line detection, and while DEMs are often used for slope break detection, they are less commonly employed for direct grounding line identification, with InSAR preferred.

#### 3.1.2.3 The context of this thesis

The limitations of current remote sensing techniques highlight the need for improved methodologies. The vast availability of high-resolution DEMs offers a promising opportunity to overcome some of these limitations. The research I present in this thesis

addresses these gaps by using a high-resolution DEM, ArcticDEM, as a comparative methodology for defining lake depth against the RTE and ICESat-2 laser altimetry. This extends the use of DEMs for lake depth detection beyond previous applications such as those employed by Pope et al. (2016). Additionally, I present a method to determine the extent of floating ice via DEM stack deviations and a novel method that differences DEMs coupled with a tidal model to determine the location of the grounding line. By expanding the utility of DEM-based approaches to use as a comparative dataset for lake depths, and beyond simple slope break detection for grounding lines, this research contributes to advancing the field and improving our ability to monitor ice sheet dynamics. With this research, I aim to refine existing methodologies and provide new insights into our understanding of supraglacial lake depth, floating ice tongue extents, and grounding lines, contributing to a more comprehensive understanding of ice sheet processes.

## 3.2 Thesis objectives and scope

This research aims to explore and refine DEM-based methods to study the dynamic processes of the GrIS. Understanding these processes is critical for improving projections of future ice sheet evolution and its contribution to sea level rise.

The primary objective of this study is to develop and refine methodological approaches that leverage DEMs. By improving the accuracy and applicability of these methods, this research seeks to enhance our ability to monitor ice sheet processes.

### 3.2.1 Specific goals

To achieve this overarching objective, the research focuses on the following specific goals:

1. Develop and evaluate methods to measure supraglacial lake depth from space. No study yet intercompares supraglacial lake depth measurements made with the RTE, LiDAR bathymetry, and DEMs, and we do not yet have constraints on the uncertainty of the RTE approach. This study intercompares these depth measurements and constrains uncertainty in the RTE approach.

2. Develop and validate a novel DEM deviation approach for floating ice tongue identification on marine-terminating glaciers. Although previous methods have used static DEM methods to identify floating ice extents, e.g. the break in slope method, none have used DEMs as the input data to a dynamic method aimed at identifying tidal movement (and thus floating ice). This study provides a proof of concept that DEMs can be used dynamically to identify floating ice.

3. Investigate the application of tidal modelling and DEM differencing for grounding line detection. Although DEM differencing offers a potential approach to exploiting the tidal-induced ice flexure characteristic of floating glacier extensions, no studies have yet exploited DEM datasets by coupling the individual DEMs with tidal data. This study proves that tidally coupled high-low DEM pairs can be differenced to locate the grounding line.

### 3.2.2 Thesis structure

In the following three chapters, I present the results of this thesis. Chapter 4 presents an intercomparison of three satellite methods for determining supraglacial lake depth, highlighting their respective strengths and limitations. In Chapter 5, I provide an

inventory of floating ice tongues in northern Greenland derived from DEMs, offering insights into its distribution and dynamics. Chapter 6 introduces a new method for determining grounding line locations using DEMs and a tidal model, providing a novel approach to ice sheet boundary detection.

In the final chapter of the main body, Chapter 7, I synthesise the findings from the three research chapters, discussing their broader implications and contributions to the field. Within this chapter, I also consider the implications of my research within a broader context and propose potential directions for future studies. The appendices, located after the main body of the thesis, contain additional information relevant to Chapters 4 and 5, including supplementary data, figures, and methodologies.

# Chapter 4

# 4 Evaluation of satellite methods for estimating supraglacial lake depth in southwest Greenland

Laura Melling[1], Amber Leeson[1], Malcolm McMillan[1], Jennifer Maddalena[1], Jade Bowling[1], Emily Glen[1], Louise Sandberg Sørensen[2], Mai Winstrup[2], and Rasmus Lørup Arildsen[2]

[1] Lancaster Environment Centre, Lancaster University, Lancaster, LA1 4YQ, United Kingdom

[2] DTU Space, Danmarks Tekniske Universitet, 2800 Lyngby, Denmark

**Correspondence:**

Laura Melling (lauraisobelmelling@gmail.com, l.melling@lancaster.ac.uk)

While this research builds upon the foundation established in my master's thesis, it represents a significant advancement in both scope and methodology. This study incorporates an additional wavelength band (green light) alongside a more in-depth analysis of the original red light wavelengths. Furthermore, I have conducted extensive intercomparison between these two bands, providing a more comprehensive evaluation than was possible in my previous research. These enhancements, along with the broader analytical framework applied in this study, ensure that this work is distinct and meets the expectations of doctoral-level research.

The following study was published in The Cryosphere on 8th February 2024 (citation: Melling et al., 2024). This paper has been formatted for consistency within the thesis, but otherwise appears as published.

This chapter directly contributed to the supraglacial hydrological assessment section of the European Space Agency-funded project, 4DGreenland. This paper was edited by

Joseph MacGregor and reviewed by two anonymous referees. LM and AL conceptualised the research. LM, AL, MM, and JM designed the study. JB wrote and supplied the DEM stacking script detailed in Sect. 4.3.3. EG provided the 2019 lake inventory shapefiles. MW, LSS, and RLA processed the ICESat-2 ATL03 data. LM obtained the data, performed the analyses, created all figures, and wrote the paper. All the co-authors contributed to manuscript editing.

## 4.1 Abstract

Supraglacial lakes form on the Greenland ice sheet in the melt season (May to October) when meltwater collects in surface depressions on the ice. Supraglacial lakes can act as a control on ice dynamics since, given a large enough volume of water and a favourable stress regime, hydrofracture of the lake can occur, which enables water transfer from the ice surface to the bedrock, where it can lubricate the base. The depth (and thus volume) of these lakes is typically estimated by applying a radiative transfer equation (RTE) to optical satellite imagery. This method can be used at scale across entire ice sheets but is poorly validated due to a paucity of in situ depth data. Here we intercompare supraglacial lake depth detection by means of ArcticDEM digital elevation models, ICESat-2 photon refraction, and the RTE applied to Sentinel-2 images across five lakes in southwest Greenland. We found good agreement between the ArcticDEM and ICESat-2 approaches (Pearson's $r = 0.98$) but found that the RTE overestimates lake depth by up to 153% using the green band (543–578 nm) and underestimates lake depth by up to 63% using the red band (650–680 nm). Parametric uncertainty in the RTE estimates is substantial and is dominated by uncertainty in estimates of reflectance at the lakebed, which are derived empirically. Uncertainty in lake depth estimates translates into a poor understanding of total lake volume, which could mean that hydrofracture likelihood is poorly constrained, in turn affecting ice velocity predictions. Further laboratory studies to constrain spectral radiance loss in the water column and investigation of the potential effects of cryoconite on lakebed reflectance could improve the RTE in its current format. However, we also suggest that future work should explore multi-sensor approaches to deriving lake depth from optical satellite imagery, which may improve depth estimates and will certainly result in better-constrained uncertainties.

## 4.2 Introduction

Supraglacial lakes form when meltwater collects in surface depressions on glaciers and ice sheets. On the Greenland ice sheet, lakes form in approximately the same locations each melt season from May to October (Sundal et al., 2009) as their positions are controlled by bedrock topography (Echelmeyer et al., 1991; Krawczynski et al., 2009). Alongside rivers and streams, supraglacial lakes form a complex hydrological system of water storage and transport on the ice sheet surface. As the melt season progresses, supraglacial lakes grow in size through the accumulation of meltwater. These lakes either drain or refreeze, with ~34% of lakes at lower elevations draining slowly, ~14% draining rapidly, and ~50% refreezing. At higher elevations, lakes tend to refreeze (Selmes et al., 2013). Drainage can occur slowly over the ice surface through supraglacial channels or rapidly through the ice if the weight of the water is sufficient to drive a crevasse through the full ice thickness to the bed. This process is known as hydrofracture, and related drainage events can occur in as little as 2 h (Das et al., 2008). In these events, the water is routed to the base of the ice sheet, where it can cause a hydraulic pressure increase that temporarily lifts the ice off the bed. This process can enhance basal sliding and increase ice flow rates (Fitzpatrick et al., 2013; Tedesco et al., 2013; Christoffersen et al., 2018; Tuckett et al., 2019; Maier et al., 2023). Short-term increases in meltwater input cause temporary spikes in water pressure, leading to ice acceleration. However, an increase in mean melt supply does not necessarily cause an increase in ice sheet velocity (Schoof, 2010). Ergo, knowing the volume of water held on the ice sheet at any one time – and thus the potential for temporary spikes in water pressure through hydrofracture – is important for modelling ice sheet dynamics.

Our understanding of ice sheet behaviour assumes that we have an understanding of meltwater delivery (Parizek and Alley, 2004; Zwally et al., 2002). If the calculated depth of supraglacial lakes is inaccurate, the volume of the lake is inaccurate, thus meaning our calculations of injected meltwater to the ice sheet bed are also inaccurate. As a result, under- or overestimating the volume of meltwater holds consequences for the models on which we base our understanding of ice dynamics (e.g. Christoffersen et al., 2018; Tedesco et al., 2013).

To understand the amount and rate of meltwater delivery to the ice sheet bed, we require spatially and temporally continuous observations of lake volume. Our study area, located

in the southwest Greenland ice sheet (Figure 4.1), includes the lower Watson River basin (5800 $km^2$). This basin has a meltwater coverage (including supraglacial lakes, streams, and rivers) of 250 $km^2$ (Emily Glen, personal communication, 22 July 2022), meaning it is not feasible to acquire spatially and temporally continuous lake volume data from field surveys. Instead, several satellite-based methods can be used to estimate supraglacial lake depths remotely, potentially providing high spatial and temporal coverage. These methods are as follows: physics-based modelling, such as the application of the radiative transfer equation (RTE) proposed by Philpot (1987) to optical satellite imagery (Moussavi et al., 2020); laser altimetry, which is used to measure lake depths directly from photon refraction (Fair et al., 2020); the use of digital elevation models (DEMs) to ascertain lake depth from the underlying ice surface topography (Yang et al., 2019); and empirical models derived from regression of in situ depth measurements with remotely sensed data (Pope et al., 2016).

These methods each have known advantages and limitations for deriving lake depths. Physics-based models applied to optical satellite data (e.g. Sentinel-2) provide continuous spatial coverage at high-resolution temporal sampling (i.e. every 5 d), and they can be used at scale. ICESat-2 can directly measure lake depths but is limited to 1-D profiles along discrete satellite tracks which are spatially distant (4.1 km between acquisition beams of neighbouring satellite tracks at 67° N) and have coarse temporal sampling, inhibiting an assessment of lake dynamics as supraglacial hydrology evolves on sub-daily timescales (Das et al., 2008). ArcticDEM data is even more sporadic in space and time, with periods of months between acquisitions and missing data caused by cloud cover. Notably, this dataset only contains data from the summer months (March–October) as the input data is from optical satellites which depend on the presence of visible light. ArcticDEM offers a spatial resolution (2 m) of 1 order of magnitude higher than Sentinel-2 and thus enables a more detailed assessment of lake bathymetry – for example, to assess whether a lake basin contains open or healed crevasses that may promote lake drainage by hydrofracture. Although empirical models derived through the regression of in situ depth measurements with remotely sensed data have been shown to define reasonable lake depth (Pope et al., 2016), their coefficients are spatially constrained to the area in which the original in situ measurements were taken and are, therefore, unreasonable to apply on the ice sheet scale. Intercomparing multiple depth detection methods increases our confidence in the depths calculated at locations where there is agreement between

methods. This is especially important in the absence of ground truth data. Here, we examine and intercompare the performance of three satellite-based methods – a physics-based model that uses a radiative transfer equation (RTE), ICESat-2 laser altimetry, and ArcticDEM strip DEMs – in determining the depth of a test dataset of supraglacial lakes in the southwest Greenland ice sheet, where Greenlandic supraglacial lakes are extensive and numerous (Hu et al., 2021).

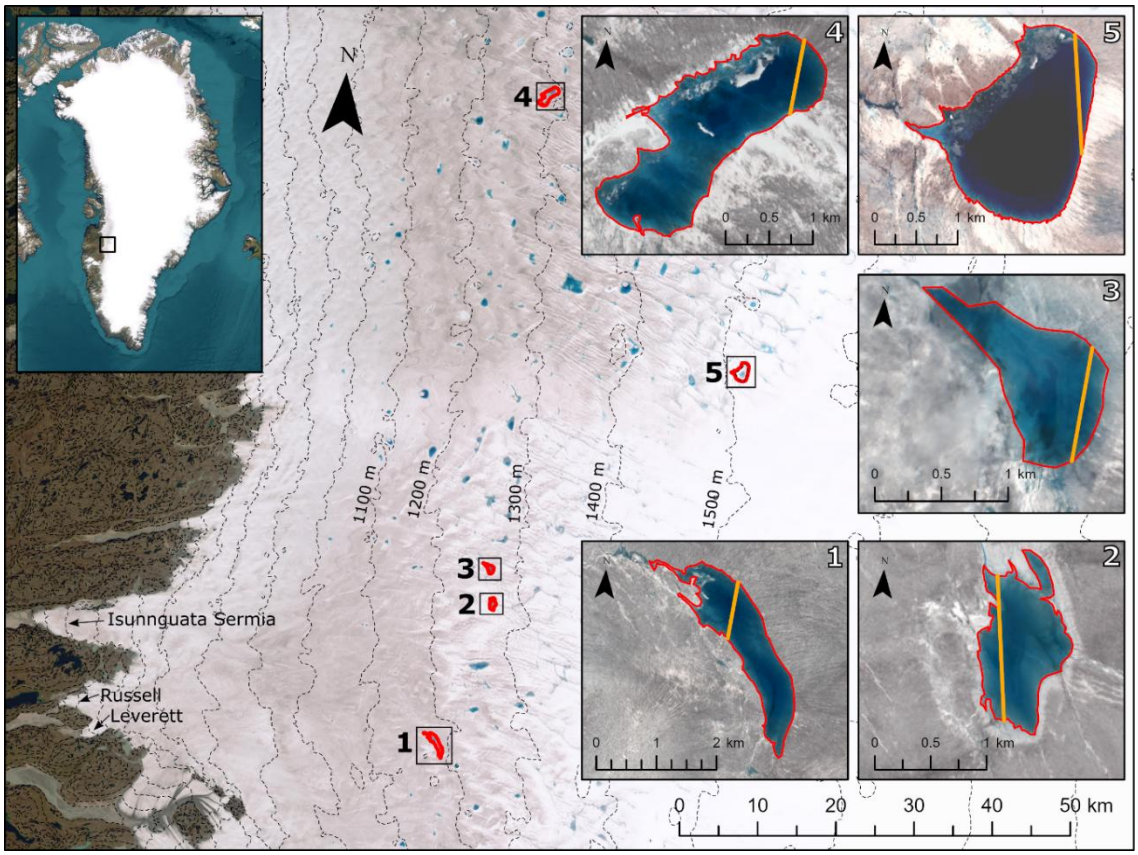


Figure 4.1: The locations of the five supraglacial lakes in relation to the study region. Contour lines calculated from the ArcticDEM 100 m mosaic are visible on the base map as dashed grey lines. The inset map indicates the location of the study area within Greenland. Panels (1)–(5) show Lake 1 to Lake 5 in detail, where the background is a true-colour image acquired on the date shown in Table A.2.1 for each lake. The manually delineated lake outline is given in red, and the ICESat-2 transect is given in orange. The ICESat-2 ground tracks were cropped to the lake edges. The background images in panels (1)–(5) are the Sentinel-2 tiles detailed in Table A.2.1 The base map data are courtesy of Earthstar Geographics via Esri.

## 4.3 Data and methods

### 4.3.1 Study region and supraglacial lakes

Our study region (Figure 4.1) is located in western Greenland and contains part of the Watson River basin, known for abundant supraglacial lake coverage. This region contains both active (repeatedly filling and draining) and non-active lakes and is known to respond dynamically to hydrological perturbations (e.g. Chudley et al., 2019; Das et al., 2008). Five lakes in this region were found to be suitable for depth retrieval from all three of the datasets (with the availability of ICESat-2 data being the main limitation; see Appendix A.1). Each of the five supraglacial lakes are active, are crossed by an ICESat-2 reference ground track (RGT), and have both concurrent optical imagery and a corresponding DEM showing an empty lake basin. These five lakes span a range of sizes (0.8–3.1 $km^2$) and appear at a range of elevations (1150–1500 m a.s.l.), as shown in Figure 4.1. We apply three different methods to measure the depth of each of our five lakes. These methods are described in detail below.

### 4.3.2 Method 1: radiative transfer equation applied to optical satellite imagery

Here, we apply the RTE (Eq. 4.1) first presented in Philpot (1987) to both red (0.65–0.68 μm) and green (0.54–0.58 μm) bands of level-1C Sentinel-2 optical satellite imageries which are temporally (±10 d) concurrent with the ICESat-2 data for each of our five case study lakes (Table A.2.1). To confirm that the lakes had not changed in size between the ICESat-2 and Sentinel-2 acquisition dates, we undertook a visual appraisal of optical satellite imagery acquired approximately 15 d either side of the ICESat-2 acquisition date. Sentinel-2 has a spatial resolution of 10 m and a revisit period in this region of about 5 d (Drusch et al., 2012). The RTE method is commonly applied to optical satellite data in order to determine lake depth on the Greenland ice sheet (e.g. Datta and Wouters, 2021; Moussavi et al., 2020; Williamson et al., 2018). We chose to use Sentinel-2 level-1C products which are pre-packaged as orthorectified, map-projected imageries of scaled top-of-atmosphere data, in keeping with these previous studies. We converted these values to unscaled top-of-atmosphere reflectance using standard methods (Datta and Wouters, 2021; Moussavi et al., 2020; Williamson et al., 2018). Although previous studies have averaged the depths retrieved from the red-band RTE and the panchromatic band of Landsat 8 (Pope et al., 2016; Williamson et al., 2018), we do not do so within this study

as Sentinel-2 does not have a panchromatic band. Additionally, this study specifically aims to understand the uncertainties associated with applying the physically based RTE to data acquired at a single band, and so an empirical averaging without a clear physical justification does not serve the purposes of this research.

The radiative transfer approach to modelling lake depth is based on the assumptions of the Bouguer–Lambert–Beer law. Equation 4.1 gives the formulation of the equation presented by Philpot (1987), written in terms of reflectance and inverted into the logarithmic form:

$$z = \frac{\ln(A_d - R_\infty) - \ln(R_w - R_\infty)}{g} \tag{4.1}$$

where $A_d$ represents the lake bottom albedo or reflectance, $R_\infty$ indicates the reflectance of optically deep water, $R_w$ is the recorded reflectance of a given pixel, $g$ is the coefficient for spectral radiance loss in the water column, and $z$ represents lake depth in metres. $A_d$, $R_\infty$, and $g$ can each take a range of plausible values, and so here we consider them to be tuneable parameters.

Here we take $A_d$ to be the average reflectance value in a 30 m wide ring (three pixels in Sentinel-2, after Moussavi et al. (2020)) around each of the five lakes to provide a unique $A_d$ value for each lake. This is the same way that $A_d$ is estimated in previous studies. $R_\infty$ represents reflection from the water column and is commonly taken as the reflectance of optically deep, clear, and still water, i.e. where it is reasonable to assume that there is no bed reflectance or sediment contamination (Sneed and Hamilton, 2007). Ideally, this would be done using ocean water pixels in the same satellite image from which lake depth is acquired. However, here we find that no ocean water was visible in the images we used, and so we substituted the image acquired closest in time and space in which ocean water was visible (Appendix A.2). To estimate $R_\infty$, we averaged the reflectance of the 10 darkest pixels in each substitute image after manually filtering out pixels obviously associated with sediment traces or sensor-related scanning issues. This is slightly different to the way that $R_\infty$ has been calculated in previous studies but does not produce values that are appreciably different.

We calculate $g$ using Eq. 4.2, which accounts for the scattering of both downwelling ($K_d$) and upwelling ($K_u$) light:

$$g = K_d + K_u \tag{4.2}$$

$K_d$ is calculated using Eq. 4.3 and is wavelength specific:

$$K_d = a_w + \frac{1}{2} b_m^{fw} \tag{4.3}$$

where $a_w$ is the absorption coefficient for pure water, and $b_m^{fw}$ is the backscattering coefficient for molecular scattering in freshwater. These are laboratory-derived values and are taken from Smith and Baker (1981). Very few laboratory estimates exist of $K_u$ (Philpot, 1989), and so previous studies have typically taken $K_u$ to be equal to $K_d$ (e.g. Maritorena et al., 1994; Sneed and Hamilton, 2007). We argue, however, that $K_u$ must be larger than $K_d$ because upwelling photons are more rapidly attenuated than downwelling photons in water (Kirk, 1989). In fact, experimental studies suggest that $K_u$ could be as high as $2.5K_d$ (Kirk, 1989). Here, we use an average of these two values and take $K_u$ to be $1.75K_d$. This will naturally lead to a higher value of $g$ than commonly used in supraglacial lake depth studies, and we note that it has been recently suggested that this would lead to more accurate lake depths (Brodský et al., 2022).

We estimate uncertainty by first assigning a range of plausible values to each tuneable parameter (Appendix A.3) and then applying the RTE to every permutation of the combination of these values. The standard deviation of depths calculated using these permutations was taken to represent the uncertainty of the depth measurement.

We find it helpful to compare our estimates to those given using previously published methods of estimating our tuneable parameters. We calculate these literature values of the parameters as follows: $g = 2K_d$ (Sneed and Hamilton, 2007), where $K_d$ is as described in Eq. 4.3, and $R_\infty$ is the reflectance of the single darkest pixel in the deep-sea scene (e.g. Georgiou et al., 2009; Pope et al., 2016).

In our modelling we assume the lake substrate is homogenous, suspended or dissolved particles are minimal, there is no inelastic scattering or fluorescence, the effects of wind are minimal, and lake bottom pixels are parallel to the lake surface, following Sneed and Hamilton (2011). We do not average band-specific depth estimates here for the reasons

outlined previously; however, we do note that this has been done in previous studies (e.g. Pope et al., 2016; Williamson et al., 2018).

### 4.3.3 Method 2: ArcticDEM

ArcticDEM is an open-access collection of high-resolution DEMs produced by the Polar Geospatial Center (Porter et al., 2022). The dataset is assembled from individual stereoscopic DEMs that are derived from pairs of high-resolution optical imagery acquired by the WorldView-1, WorldView-2, WorldView-3, and GeoEye-1 satellites (Porter et al., 2022). The DEMs are generated by applying the Surface Extraction from TIN-based Searchspace Minimization (SETSM) software to stereoscopic image pairs (Noh and Howat, 2017). We note that ArcticDEM's absolute elevation accuracy is less than 5 m in the vertical plane (Noh and Howat, 2015). This refers to the absolute accuracy when referenced to a geodetic datum. Therefore, if compared to another elevation dataset, the ArcticDEM data should not be considered as providing the 'true' elevation but as a relative measurement against that other dataset. Here, we use the most recent version of ArcticDEM data (version s2s041, release 8). The tile reference numbers of the DEMs used in this study are detailed in Table A.2.1; all available ArcticDEM DEMs of the study region were acquired from the Polar Geospatial Center.

In ArcticDEM, full lakes are represented by flat surfaces. To measure their depth, we need to examine the shape of the basin before it has filled or after it has drained. As drained lakes have similar characteristics to perpetually dry surface depressions, we had to first identify which depressions in the DEMs were associated with active lakes. To identify lakes that drain in our study region, we followed the approach outlined in Bowling et al. (2019). This takes all DEMs covering our study area in the ArcticDEM dataset and stacks them then interrogates the variance of the stack, with areas of high standard deviation indicating potentially active lakes. We filter to identify pixels where the standard deviation lies in the range of 2–7 m (below this threshold, variation in elevation can arise from artefacts in the DEM), and ICESat-2 depth detection is limited to lakes up to 7 m deep (Fair et al., 2020). We then cross-referenced these areas with the locations of known supraglacial lakes and the availability of ICESat-2 data to generate our sample (Appendix A.1).

We set the lake level in the empty DEM to be consistent with the ICESat-2 data under the assumption that the ICESat-2 and ArcticDEM data are spatially coregistered; i.e. we

identified the DEM elevation value at either end of the ICESat-2 transects where ICESat-2 depths are zero, averaged these values, and subtracted the average from the entire DEM.

Due to the sparse temporal sampling of ArcticDEM and the need to resolve empty basins, the DEMs are not temporally concurrent with the ICESat-2 and Sentinel-2 data. As a result, the smallest period between the ArcticDEM and ICESat-2 acquisition dates was approximately 2 months (Lake 4), and the largest period was approximately 11 months (Lake 5) (Table A.2.1). As the location and shape of supraglacial lakes are determined by bedrock topography (Echelmeyer et al., 1991), we assume there should be little change in the bathymetry of the lake basins between the data acquisition dates (see Sect. 4.4.1 for further details).

### 4.3.4 Method 3: ICESat-2

ICESat-2 data were used to derive depths delineated along the altimeter tracks which intersected supraglacial lakes. ICESat-2 was launched in 2018 and has a 91-d repeat period, six acquisition beams, and a nominal along-track resolution of 0.7 m (Markus et al., 2017), but it has non-continuous spatial coverage due to its instrumental and orbital characteristics. At 67° N, for example, the across-track spacing between RGTs is ~10.7 km, with ~4.1 km between the right acquisition beam of one RGT and the left acquisition beam of the neighbouring RGT. The spacing between ICESat-2 beam pairs at all latitudes is ~3.3 km, which limits the coverage of individual lakes.

After limiting the potential lake inventory by the availability of ArcticDEM (Appendix A.1), we considered the quality of the available ICESat-2 data, where the highest quality translates to the basins which can be most easily delineated from ICESat-2 photon refraction; i.e. we can see both the lake surface and bed returns of the photons. In doing so, we limited our lake selection to the five study lakes. We estimate the lake bathymetry of the supraglacial lakes using the ICESat-2 Advanced Topographic Laser Altimeter System (ATLAS) ATL03 (version 3) data product (Table A.2.1) (Neumann et al., 2019) based on the distinct photon returns received from the lake surface (air–water) and bed (water–ice) interfaces. The ATL03 data product provides geolocated photons but does not account for the refraction of photons in the air–water interface resulting from the change in refractive index between the two media. This change in photon speed and paths gives rise to horizontal and vertical errors in the geolocation record, causing the photon

locations to appear deeper in the lake and further off-nadir. We corrected the photon locations using the method described in (Parrish et al., 2019).

We invited 10 altimetry experts to manually digitise the lake bathymetry from the refraction-corrected ATLAS ATL03 photon data plots using an online digitisation tool (https://apps.automeris.io/wpd/, last access: 15 July 2021). We took the average of these manual delineations at 100 equidistant points along each transect to be the best estimate of lake bathymetry and used the standard deviation of these estimates as an indication of the bathymetry uncertainty.

## 4.4 Results

### 4.4.1 Supraglacial lake depths from ArcticDEM, ICESat-2, and the RTE

We calculated depths along the ICESat-2 transects over the five lakes using ArcticDEM, ICESat-2, and the RTE (Figure 4.2). The ArcticDEM, red-band RTE, and green-band RTE are sampled approximately every 0.7 m along the transect, whereas the ICESat-2 data are sampled at 100 equally spaced points along the transect. We attribute the noise in the RTE transects to differences in spatial resolution (where Sentinel-2 has the coarsest sampling of the three datasets). Here, we choose to evaluate at each sensors' native resolution in keeping with previous studies. However, we note that the application of low-pass filters to smooth the optical solutions could be explored in future work.

The red-band RTE depths plateau between 1 and 3 m, reaching their deepest depths at 2.87, 2.46, 2.04, 2.81, and 1.44 m for lakes 1, 2, 3, 4, and 5 respectively. This plateau typically results in an underestimation of maximum depth. In contrast, the green-band RTE depths show a systematic over-estimation compared to ArcticDEM and ICESat-2. The RTE depths are deeper when literature values (Georgiou et al., 2009; Pope et al., 2016; Sneed and Hamilton, 2007) are used as opposed to our parameter values.

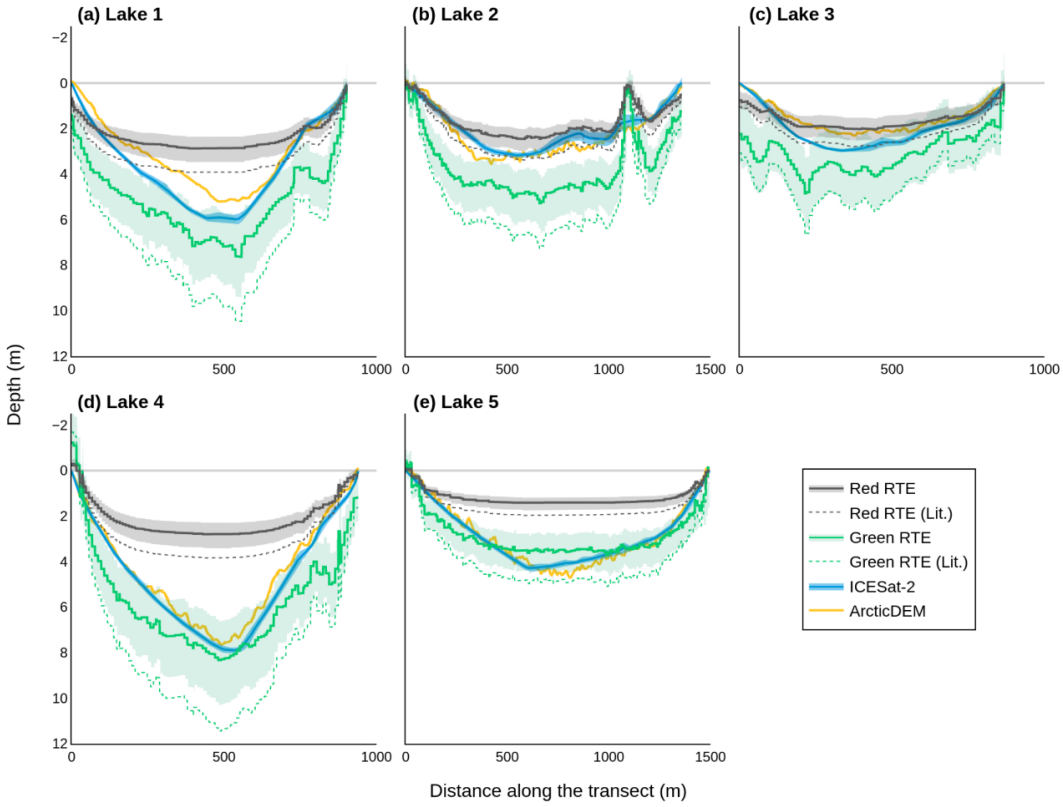


Figure 4.2: Supraglacial lake depth from the band-specific RTE, with both literature values and the values used for this study, ArcticDEM, and ICESat-2 along ICESat-2 transects. Depths achieved using the RTE with the literature values (red RTE (lit.), green RTE (lit.)) are shown for contextual reference. The uncertainties for each lake's band-specific RTE are calculated by co-varying all permutations of the RTE tuneable parameters. All uncertainties are calculated as 1 standard deviation. ArcticDEM absolute elevation accuracy is less than 5 m in the vertical plane (Noh and Howat, 2015). Lake 2 (b) exhibits a spike in both red-band RTE and green-band RTE depths at approximately 1200 m along the transect, which we attribute to a slight ice covering in the Sentinel-2 imagery. Transect locations are detailed in Figure 4.1.

Table 4.1: The maximum depths achieved by each method for the five lakes.

| Lake number | Green band RTE (m) | Red band RTE (m) | ArcticDEM (m) | ICESat-2 (m) | Maximum depth method |
|---|---|---|---|---|---|
| 1 | 7.63 | 2.87 | 5.22 | 5.98 | Green band RTE |
| 2 | 5.28 | 2.46 | 3.55 | 3.17 | Green band RTE |
| 3 | 4.85 | 2.04 | 2.33 | 2.96 | Green band RTE |
| 4 | 8.33 | 2.81 | 7.65 | 7.90 | Green band RTE |
| 5 | 3.70 | 1.44 | 4.71 | 4.30 | ArcticDEM |

The maximum depths achieved by each method differ for each lake (Table 4.1). Here, we disregard the RTE depths retrieved using the literature values as these are shown only for contextual reference. For each of the five lakes, except Lake 5, the green-band RTE is the method which achieves the maximum depth for the lake. This is likely due to the observed overestimation of the green-band RTE.

To explore the agreement between the different methods, we calculated the root mean square deviation (RMSD) and Pearson's correlation coefficient for each method pairing at each of the 100 equally spaced points along which the ICESat-2 data were sampled (Figure 4.3).

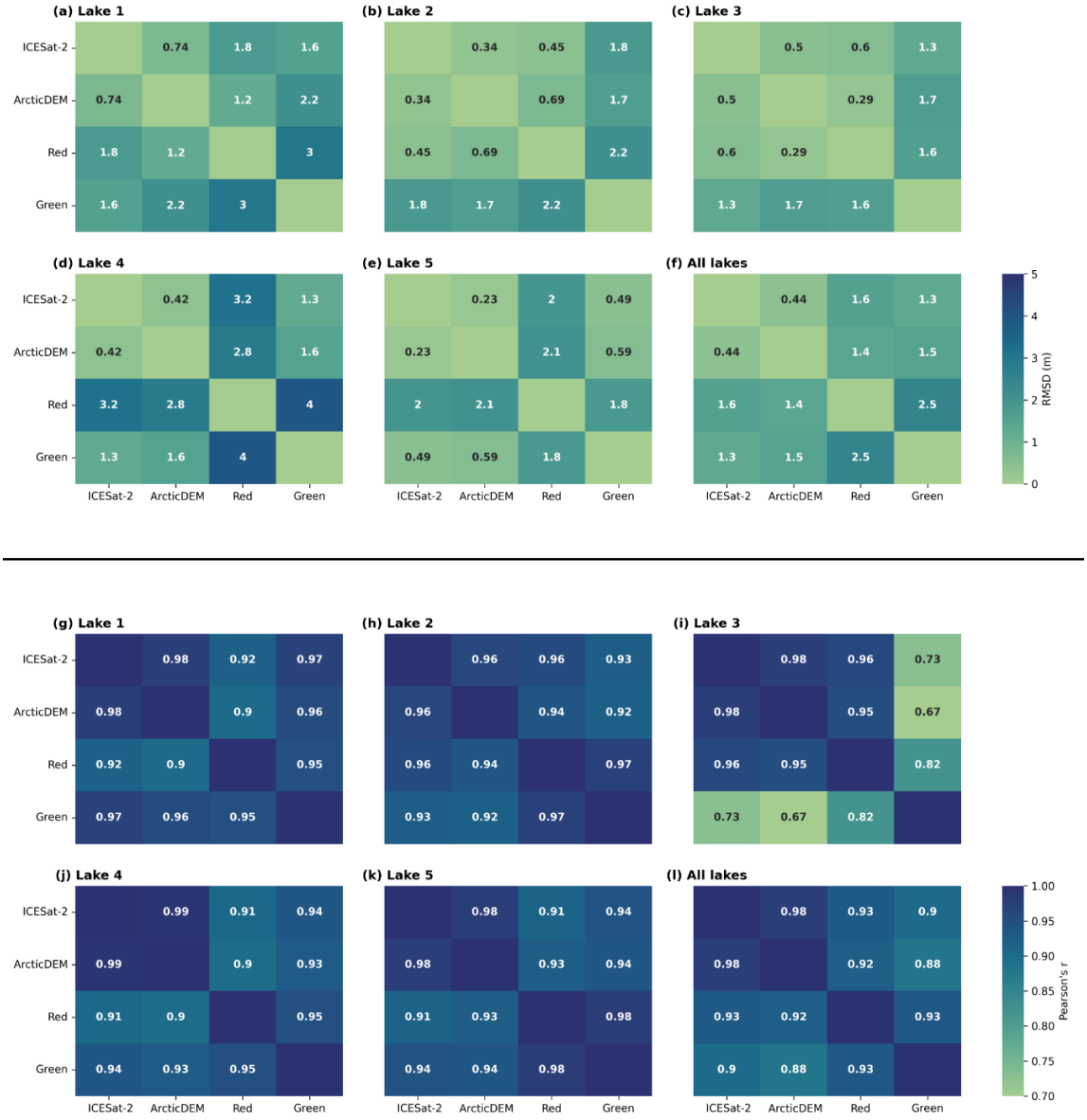


Figure 4.3: The root mean square deviation (RMSD) and Pearson's correlation coefficients for each paired combination of depths derived from ICESat-2, ArcticDEM, red-band RTE, and green-band RTE. Panels (a)–(e) show the RMSD for Lake 1 to Lake 5, and panel (f) shows the average RMSD for all five lakes. Panels (g)–(k) show the Pearson's correlation coefficient for Lake 1 to Lake 5, and panel (l) shows the average Pearson's correlation coefficient for all five lakes.

From Figure 4.3, the method pairing with the lowest RMSD is ICESat-2 and ArcticDEM for all lakes except Lake 3. For Lake 3, the method pairing with the lowest RMSD is the red-band RTE and ArcticDEM. On average, the ICESat-2 and ArcticDEM pairing has an RMSD of 0.44 m, and the method pairing with the highest average RMSD is the red-band RTE with the green-band RTE at an RMSD of 2.5 m. Additionally, our results indicate a high degree of agreement between the ArcticDEM depths and the ICESat-2 depths for

Lake 5 (RMSD = 0.23, $r$ = 0.98), enhancing our confidence in the lack of bathymetry change over the 11-month period between data acquisitions.

The Pearson's correlation coefficient of each of the method pairings is significant at $p < 0.001$. However, some of the method pairings have stronger correlations than others. The method pairing with the strongest correlation for all of the lakes is ICESat-2 and ArcticDEM with an average $r$ value of 0.98. The method pairing with the weakest correlation is different for each lake. For Lake 1 and Lake 4, the method pair with the lowest Pearson's $r$ value is the red-band RTE and ArcticDEM ($r$ = 0.90 for both). For Lake 2 and Lake 3, the pair with the lowest $r$ value is the green-band RTE and ArcticDEM ($r$ = 0.92 and 0.67 respectively). For Lake 5, the weakest correlation is for the pairing of the red-band RTE and ICESat-2 ($r$ = 0.91). The method pair with the weakest average Pearson's correlation is the green-band RTE and ArcticDEM ($r$ = 0.88), though this value is heavily impacted by the results from Lake 3.

### 4.4.2 ArcticDEM versus RTE: 2-D comparison of supraglacial lake depths

Next, we extend the 1-D analysis to two dimensions in a comparison between ArcticDEM and the RTE over the entire area of each lake (Figure 4.4). Again, we find that the red-band RTE depths plateau at depths consistent with Figure 4.2. Consistently with the findings from Figure 4.2, the lakes exhibit a relationship between the green-band RTE depths and the ArcticDEM depths, where the green-band RTE overestimates depth in the deepest portions of the lakes. This is particularly evident in Lake 5 as its bathymetry is simpler than that of the other lakes. Additionally, there are notable depth underestimations of the green-band RTE in Lake 4 and Lake 5. These underestimations correspond to floating ice on the lake surface, which is not present in the ArcticDEM data. The green-band RTE depths do not have visible plateau depths for these lakes. Instead, this method again overestimates depths compared to ArcticDEM. Table 4.2 details the average difference in the green-band RTE and red-band RTE in comparison to ArcticDEM.

Table 4.2: The average overestimation by the green-band RTE and red-band RTE depths and volumes when compared to ArcticDEM DEMs for each of the five lakes. All volume estimates are shown to 3 significant figures.

| Lake number | Average depth difference (red) (m) | Average volume difference (red) ($m^3$) | Average depth difference (green) (m) | Average volume difference (green) ($m^3$) | Volume estimated by ArcticDEM ($m^3$) |
|---|---|---|---|---|---|
| 1 | -0.06 | -133 000 (-3 %) | +2.05 | +4 230 000 (+106 %) | 4 000 000 |
| 2 | +0.13 | +111 000 (+9 %) | +2.26 | +1 870 000 (+153 %) | 1 230 000 |
| 3 | -0.01 | -10 900 (-1 %) | +1.22 | +997 000 (+89 %) | 1 130 000 |
| 4 | -1.96 | -5 210 000 (-50 %) | +0.94 | +2 500 000 (+24 %) | 10 400 000 |
| 5 | -2.16 | -5 870 000 (-63 %) | +0.52 | +1 420 000 (+15 %) | 9 260 000 |

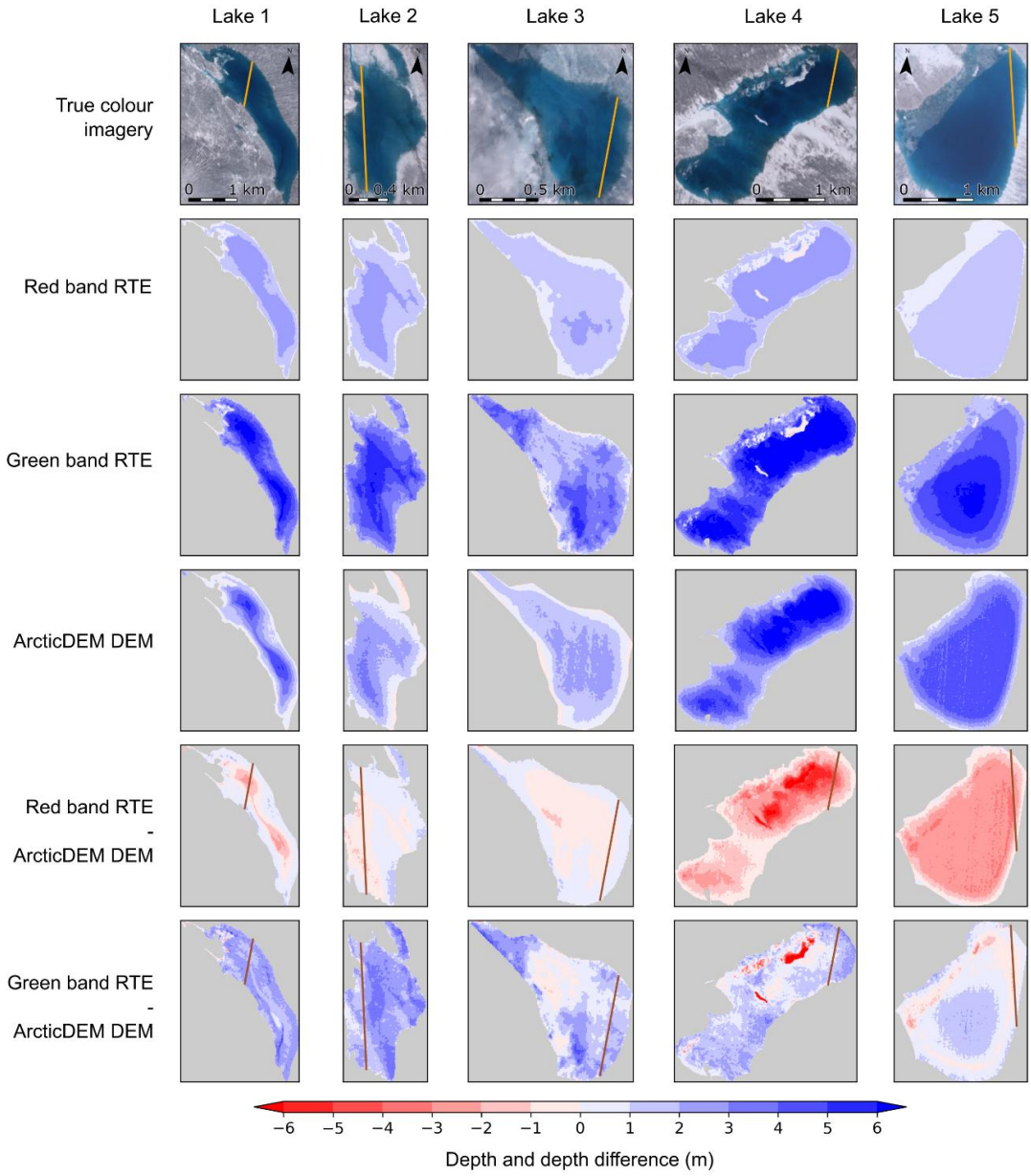


Figure 4.4: A comparison of red- and green-band RTE depths versus ArcticDEM depths in two dimensions. Each column shows results from one of our five study lakes, and each row shows information relating to a different retrieval method. The true-colour imagery is from Sentinel-2 (Table A.2.1). ICESat-2 transects are shown in orange on the true-colour imagery and the depth difference plots.

To further explore the red-band RTE depth plateauing effect and to identify any noteworthy patterns in the relationship between green-band RTE depths and ArcticDEM depths, we compared the red- and green-band RTE depths versus the ArcticDEM depths for all ArcticDEM pixels across the five lakes (Figure 4.5).

Figure 4.5 shows the relationship between the depth values of ArcticDEM, the red-band RTE, and the green-band RTE for every pixel of all five lakes. We find that the red-band RTE depth plateauing effect is clearly evident, with each of the lakes having a different plateau depth, as suggested in Figure 4.2 and Figure 4.4 (see dashed lines in Figure 4.5a). This variance in red-band RTE depth saturation between lakes can be seen in the dense, elongated clusters of the red-band RTE cloud, each of which can be attributed to a different lake. We attribute the difference in plateau depth to the varying $A_d$ values of the lakes, with red $A_d$ values of 0.42, 0.46, 0.35, 0.58, and 0.57 for lakes 1, 2, 3, 4, and 5 respectively. Shallower depths (typically towards the lake edges, as seen in Figure 4.4) agree relatively well when derived from the red-band RTE and ArcticDEM. However, as the lake gets deeper (towards the centre in most cases, as seen in Figure 4.4), the agreement between the red-band RTE depths and the ArcticDEM depths decreases as a consequence of red-band saturation. The green-band RTE shows a different pattern to that of the red-band RTE. From the location of the cloud in relation to the XY line, we see that the green-band RTE typically overestimates depth compared to ArcticDEM. The plateau depths of the green-band RTE for these lakes are not visible, but the size of the cloud gives an indication of the larger spread of values compared to the red-band RTE.

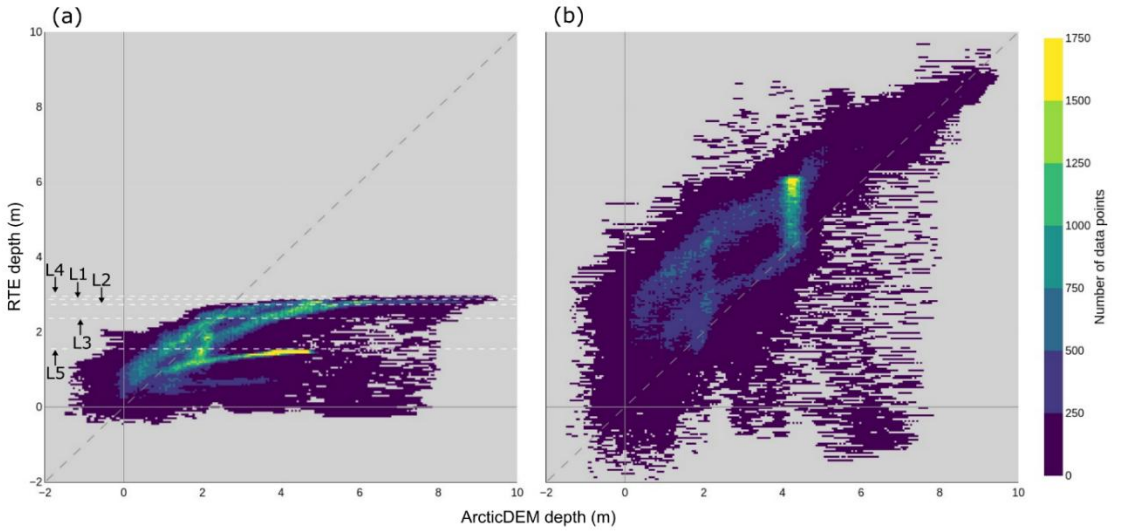


Figure 4.5: Density scatter plots of the depths derived from the red (a) and green (b) RTEs versus ArcticDEM depths for every pixel of the five lakes. The diagonal long-dashed lines represent one-to-one agreements between the depth datasets. The red-band RTE plateau depths are indicated by the labelled short-dash white lines in (a).

### 4.4.3 RTE sensitivity analysis

To investigate the sensitivity of the RTE to the tuneable parameters in the equation, we computed the relationship between depth and $R_w$ across the range of $R_w$ values recorded over supraglacial lakes in our imagery (Figure 4.6). We establish that, for the $R_w$ values we observe in the 2019 lake inventory (Emily Glen, personal communication, 22 July 2022), the red-band RTE depths have a theoretical range of −1.66 to 2.68 m, whereas the green-band RTE depths have a much larger range of −7.23 to 11.76 m. This variation in range helps to explain why the red-band RTE plateaus. The maximum depth that could be achieved by the red-band RTE on 8 July 2019 from our study region was 2.68 m. The maximum depth retrieved by the red-band RTE for any of the five lakes was 2.87 m (Lake 1), which is due to the difference in date and thus the glaciological conditions of the ice sheet.

Figure 4.6 is an indication of the limits to the green- and red-band RTEs on a specific date and not the absolute limits of the RTE. However, this analysis demonstrates that an empirical limit exists with regard to the depths achievable using both RTE approaches, which is shallower for the red band than it is for the green. Both the red- and green-band RTEs produce negative depths when the value of $R_w$ is larger than the value of $A_d$. Physically, this means that the lake bottom albedo is lower than the reflectance of the pixel of interest. In practice, this only occurs (a) when the pixel of interest represents misclassified floating ice, such as in the green-band RTE plots for Lake 4 and Lake 5 (Figure 4.4), or (b) as a result of uncertainty in $A_d$.

The distribution of green-band RTE depths is broader than the distribution of depths for the red-band RTE in Figure 4.5. We mainly attribute this to the variation in the range of possible depth values given in Figure 4.6a, where the green-band RTE depth range is larger than that for the red-band RTE. The green-band RTE range is larger because of the $A_d$ ranges of the lakes in the 2019 inventory, where $A_d$ takes the range of 0.13–0.77 for red and 0.21–0.80 for green. When combined with the difference in band-dependent values of $R_w$ and $g$, this results in a larger depth range.

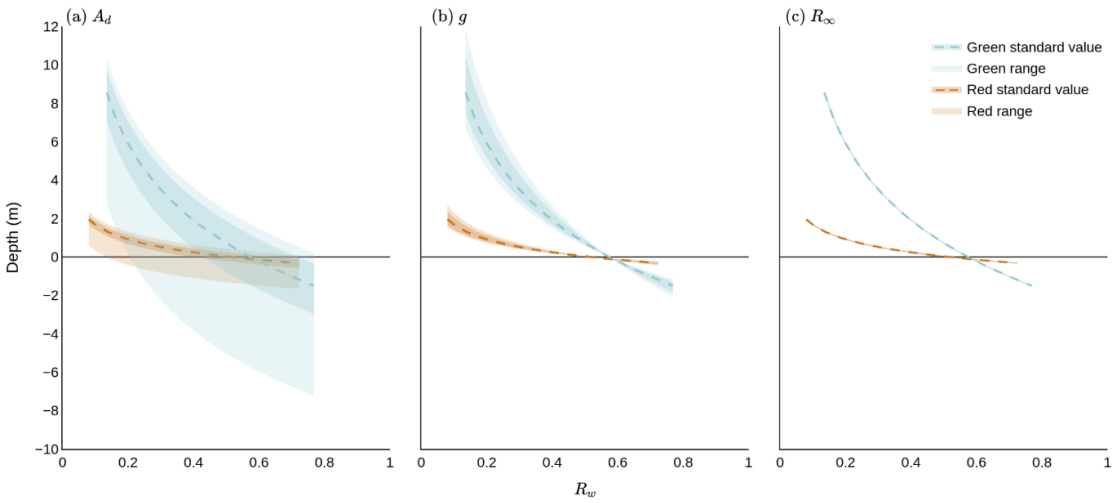


Figure 4.6: Sensitivity analysis of the RTE parameters within plausible ranges identified for each parameter (Appendix A.3). Each panel shows the variability of lake depth, as given by Eq. 4.1, with measured surface reflectance: (a) when $A_d$ is altered only, (b) when $g$ is altered only, and (c) when $R_\infty$ is altered only. When one parameter is altered, the other tuneable parameters are set to their literature value (see Sect. 4.3.2). $R_w$ is varied over its observed range on 8 July 2019, where reflectance values were extracted using a lake inventory not generated explicitly for this study (Emily Glen, personal communication, 22 July 2022). Red standard value and green standard value are calculated using our approach to calculating $A_d$, $g$, and $R_\infty$ (see Sect. 4.3.2). The darker-coloured shading indicates the uncertainty of these values. Red range and green range correspond to the possible depths achieved when upper and lower bounds are used for the parameter being varied. We note that in (c), the range and uncertainty of the depths are small and so appear as thin lines along the standard value lines.

## 4.5 Discussion

The RTE is the most common method applied at scale over the Greenland and Antarctic ice sheets to determine supraglacial lake depth (Banwell et al., 2014; Georgiou et al., 2009; Moussavi et al., 2020; Moussavi et al., 2016; Pope et al., 2016; Sneed and Hamilton, 2007, 2011; Williamson et al., 2018). The RTE is widely used because the high volume of optical satellite imagery in the polar regions means locations that are lacking in other types of remotely sensed data can be studied. However, our analysis has shown that use of the RTE, in its current form, has some limitations. Due to the rapid attenuation of red light in water, the red-band RTE cannot sense deeper than approximately 3 m, with the precise saturation depths of the lakes being dictated by the $A_d$ value. Therefore, evaluating the RTE with information from the red band means that depths from the portions of the lakes which are deeper than the red saturation point are being underestimated. As a result, when the red-band RTE is used to calculate lake depth, the total volume of water stored in lakes at the regional ice sheet scale is also underestimated.

Contrastingly, the use of the green band to evaluate the RTE leads to an overestimation of depth in the deepest portions of the lakes compared to ICESat-2 and ArcticDEM. From Figure 4.6 we can see that the saturation depth of the green-band RTE is approximately 8–11 m. This depth is dependent upon the values of $A_d$ and thus will be different for every lake. The saturation depths of the green-band RTE are not visible in Figure 4.5 because the lakes are not deep enough for the physically constrained range of the green-band RTE to plateau. However, there are two distinctive patches of ArcticDEM depth saturation in the green-band RTE cloud of Figure 4.5. These patches are portions of Lake 3 and Lake 5 which exhibit some noise within the DEM. Other spatiotemporally contiguous ArcticDEM data are unavailable for these lakes due to the sampling frequency of the dataset.

The average overestimations of the green-band RTE depths are typically larger than the average underestimations of the red-band RTE depths (Table 4.2), initially lending support to the use of the red-band RTE as opposed to the green-band RTE. However, the large variances in volume estimation between the green and red RTE depths and the ArcticDEM DEMs have contrasting implications with regard to both this assertion and one another. Use of the green-band RTE can lead to lake volume overestimations of 153% relative to ArcticDEM, with similar overestimations expected at larger scales. This has

further implications for our understanding of the role of meltwater in ice sheet dynamics and introduces a potential for exaggeration of the contribution of meltwater to localised ice velocities, which impacts our ability to predict ice-calving rates at marine-terminating glaciers (Melton et al., 2022). Conversely, use of the red-band RTE can lead to underestimations of 63% of the lake volume compared to ArcticDEM, which would potentially yield contrasting implications for our understanding of ice sheet dynamics.

Due to the plateauing effect of the red-band RTE and the systematic overestimation of the green-band RTE, neither parameter selection (ours nor the literature's) results in good agreement with either ArcticDEM or ICESat-2 for deep lakes. Although previous studies have employed a band-averaging method (Pope et al., 2016; Williamson et al., 2018), our results show that there are effects present in different bands which may be masked in a band-averaging approach, such as the plateauing effect observed within the red-band RTE and consistent overestimations in the green-band RTE. Therefore, it is not appropriate to average the green-band RTE depths and the red-band RTE depths.

It is inconclusive which parameter selection is best for shallow lakes, highlighting the importance of parameter selection in the use of the RTE. With our parameter value choices, the green-band RTE appears to predict lake bathymetry in closer agreement with ArcticDEM and ICESat-2 than the red-band RTE. Conversely, using the methods reported in previous literature (Banwell et al., 2014; Sneed and Hamilton, 2007) to calculate each of the parameters leads to the conclusion that the red-band RTE, at depths lower than its saturation depth, is more accurate in gauging lake depth than the green-band RTE. It is clear from Figure 4.6 that depth is largely insensitive to the choice of $R_\infty$. Since our calculation of $A_d$ is the same as that which is commonly used within existing literature (Moussavi et al., 2020; Sneed and Hamilton, 2007), we suggest that there is disagreement with respect to the best-performing band at depths lower than the saturation point of the red-band RTE because we use a different value of $g$. Specifically, a low coefficient of $K_d$ leads to a low $g$ value, which, as found in recent literature (e.g. Pope et al., 2016; Williamson et al., 2017), leads to larger lake depths. When this is combined with the green band in the RTE, it leads to a significant overestimation of depth, which can exceed 5 m, compared to the ICESat-2 and ArcticDEM depths (Figure 4.2).

Using the parameter values commonly found in the literature (Banwell et al., 2014; Sneed and Hamilton, 2007), the red-band RTE predicts depth relatively accurately until it

plateaus. This attribute makes it well suited for use with shallower lakes, such as those found on Antarctic ice shelves (Banwell et al., 2014). However, the calculation of $A_d$ needs to be carefully considered. Specifically, if $A_d$ is estimated from a ring of pixels around the edge of the lake (e.g. Moussavi et al., 2020; Sneed and Hamilton, 2007), then the presence of slush may adversely impact the derivation of a representative value. The differentiation of blue ice from slush on the Antarctic ice sheet is particularly difficult due to their structural and spectral similarities in satellite imagery (Moussavi et al., 2020; Dell et al., 2022). This makes the derivation of $A_d$ even more complicated, and care should be taken when calculating $A_d$ in the presence of blue ice due to the potential misidentification of slush (Dell et al., 2020). Figure 4.6 elucidates the importance of the choice of $A_d$ within the RTE, wherein a small change in $A_d$ translates into a large difference in estimated depth. Dell et al. (2020) estimated $A_d$ from the sixth concentric ring of pixels around Antarctic lakes to reduce the potential impacts of slush on the RTE. In future work, methods of estimating $A_d$ in both Greenland and Antarctica should be tested due to the importance of $A_d$ in the RTE.

Although generally in closer agreement with one another than with the red- or green-band RTEs, ICESat-2 and ArcticDEM cannot be used to track surface water volumes at scale across the ice sheet because of limitations in their spatial and temporal sampling. For example, ICESat-2 acquires elevation measurements along 1-D satellite tracks, and lakes are 2-D features; furthermore, whilst ArcticDEM acquisitions are 2-D, they are sparsely sampled in space and time. Methods which exploit regularly acquired 2-D satellite imagery – such as the application of the RTE to optical satellite imagery – are thus needed to monitor the total volume of water held within lakes on the ice sheet surface and its evolution through time. ArcticDEM and ICESat-2 data are of most value for their potential to constrain these methods. For example, Datta and Wouters (2021) used ICESat-2 to constrain empirically derived estimates of lake bathymetry from Sentinel-2 scenes in western Greenland. With a larger amount of ArcticDEM and/or ICESat-2 data, we suggest that future research could combine multiple satellite bands (Adegun et al., 2023) and data sources as inputs to a machine learning model and generate a well-constrained depth detection product using a data-driven approach as opposed to the model-derived approach we use here.

The relatively weaker correlation between the RTE datasets and the observational datasets of ArcticDEM and ICESat-2 is likely a result of the uncertainty introduced by each of the

RTE's tuneable parameters (Figure 4.6). $A_d$, in particular, is affected by the potentially incorrect assumption that suspended or particulate matter in the lake is minimal (Sneed and Hamilton, 2011). This raises the issue of cryoconite holes on the ice sheet surface, which are known to lower the albedo (Hotaling et al., 2021). Cryoconite holes are formed when aeolian dust settles on the ice sheet. The albedo of the dust-covered area is lower than the surrounding ice so it heats up and melts the underlying ice, forming vertical shafts. The ponding of surface water partially cleans these cryoconite holes, resulting in the disbursement of the particulate matter into the lake. However, the method currently used to estimate $A_d$ is assumed to accommodate this potential lowering of lake albedo. Therefore, if cryoconite was present in the lake basin, the ring of pixels used to estimate the lake bottom albedo would likely also contain cryoconite holes.

If the water column is affected by particulate matter, this would also affect the value of $g$ (Brodský et al., 2022). Currently, $g$ is calculated from $K_d$, the coefficient for the scattering of downwelling light in the water column. The $K_d$ value is laboratory-derived from optically clear water, i.e. water that does not contain particulate matter. Consequently, the value of $g$ would be incorrect for lakes which contain particulate matter, further limiting the generalisability of the RTE when it is used in such a scenario.

Currently, the limitations associated with red- and green-band RTE calculations have wider implications for other areas of cryospheric research, such as calculating hydrofracture likelihood and understanding fluctuations in local ice velocities. Lake volume is not the only control on the probability of lake hydrofracture, though it is reasonable to assume that the two things should be correlated. However, observational evidence of this correlation remains elusive despite large-scale studies of the phenomena (Williamson et al., 2018). It is possible that these large-scale studies found no evidence of a correlation between hydrofracture and lake volume, at least in part because of uncertainties in the RTE approach used to derive lake depth.

## 4.6 Conclusions

The Greenland ice sheet accommodates thousands of supraglacial lakes which form and reform every melt season. Current methods to estimate the volume of these lakes have either relatively poor spatio-temporal sampling or limitations in the accuracy with which they can retrieve lake depth. This study gives a detailed intercomparison of three methods which can be used to estimate lake depth – an integral component in the calculation of lake volume. Tracking the volume of water storage on the surface of the ice sheet is important for quantifying hydrofracture likelihood and determining the impacts of lake drainage on ice sheet velocities and requires ice-sheet-wide coverage and high temporal sampling to resolve seasonal dynamics.

Within this study, we found that two of the three methods considered, namely the ArcticDEM DEMs and the ICESat-2 laser altimetry approaches, have close agreement. However, these methods are spatially and temporally restricted, meaning they cannot be used to derive comprehensive estimates of surface water storage at the ice sheet scale. Our third method, which uses the Philpot (1987) RTE to derive depth from optical imagery, has relatively poor agreement with the other two methods, especially for deeper supraglacial lakes. We detected a plateauing effect in the red-band RTE which is caused by the rapid attenuation of light in the red band, suggesting that the use of this method will consistently underestimate the depths of lakes which are deeper than the lake-specific saturation limit. Within this study, the use of our RTE parameter values improved the ability of the green-band RTE to sense lake depth, and a comprehensive sensitivity analysis of the RTE's tuneable parameters leads us to believe that further alterations to the parameter calculation and/or equation could be undertaken to improve the method. Interestingly, the methods currently used within the literature to determine the parameter values appear to limit the accuracy of lake depth calculation using the green-band RTE within our five-lake sample. However, this is a case study of five lakes on the southwest Greenland ice sheet, and further work is required to understand whether this conclusion is generalisable to the whole ice sheet.

Nonetheless, the RTE is the only method which can currently be deployed at an ice sheet scale due to data availability constraints, meaning improvements to the method are paramount to its potential use as an accurate method for calculating lake depth. We suggest that future improvements to the current equation should focus on the calculation

of $A_d$, which has been shown to have the greatest influence on the derived depths. However, the calculation of $A_d$ also poses significant technical difficulties due to the issues in differentiating between water and ice in satellite imagery so care must be taken to ensure that new methods are robust and replicable at the ice sheet scale.

# Chapter 5

# 5 An inventory of northern Greenland's floating ice tongues using high-resolution digital elevation models

Laura Melling[1], Malcolm McMillan[1], Jennifer Maddalena[1], Amber Leeson[1], and Marco Möller[2]

[1] Lancaster Environment Centre, Lancaster University, Lancaster, LA1 4YQ, United Kingdom

[2] Department of Geodesy and Glaciology, Bavarian Academy of Sciences and Humanities, Munich, Germany

**Correspondence:**

Laura Melling (lauraisobelmelling@gmail.com, l.melling@lancaster.ac.uk)

The following work is prepared as a manuscript to be submitted as, "An inventory of northern Greenland's floating ice tongues using high-resolution digital elevation models".

For the following study, LM, M. McMillan, JM and AL conceptualised the research. LM, M. McMillan, and JM designed the study. M. Möller provided data pertaining to Flade Isblink. LM obtained the data, performed the analyses, created all figures, and wrote the paper. LM, M. McMillan, JM, and M. Möller contributed to manuscript editing.

## 5.1 Abstract

Grounding lines mark the transition between floating and grounded ice of marine-terminating glaciers. They are dynamic, often moving laterally with the tides and migrating over longer timescales due to ice thinning and thickening. The extent of floating ice is an indicator of a glacier's stability, meaning that finding accurate ways to determine an ice tongue's size is an important task. As subglacial features, the grounding line cannot be directly observed using satellite remote sensing; instead, proxies are used to determine their locations. Traditional methods for mapping the grounding lines and floating ice extents of Greenland's marine-terminating glaciers have primarily relied on synthetic aperture radar (SAR) interferometry. The launch of Sentinel-1B in 2016 significantly increased the availability of SAR data, leading to a substantial improvement in grounding line coverage and our understanding of the extent of Greenland's floating ice tongues. In contrast, SAR data from earlier years are more sporadic, limiting the temporal continuity of these observations.

We introduce a novel method that exploits high-resolution ArcticDEM digital elevation models (DEMs) from 2009-2021 to determine the extent of floating ice for fifteen northern Greenland glaciers with the potential for floating ice tongues. By analysing the temporal variance of elevations within a DEM stack, we identify the floating ice extent of Steensby Gletsjer, Ryder Gletsjer, Nioghalvfjerdsbræ (79 North or 79N), Storstrømmen, and L. Bistrup Bræ. We also confirm the absence of floating ice on Newman Bugt, C. H. Ostenfeld, Harder Gletsjer, the two southern lobes of Brikkerne Gletsjer, Jungersen Gletsjer, Henson Gletsjer, Hagen Bræ, and Zachariæ Isstrøm. Our method provides a proof of concept for using DEM height variations to determine high-resolution information relating to the floating ice extent of a glacier. This provides important geometric information about this key region at the spatial scale required for detailed process-based study of ice-ocean interactions, laying the foundation for new DEM-based approaches to grounding line and floating ice tongue mapping.

# 5.2 Introduction

## 5.2.1 Context and importance

The Greenland ice sheet (GrIS) is losing mass because enhanced surface melt and runoff, combined with increased ice discharge from outlet glaciers, outweigh the annual gains from snowfall. Approximately 14 mm of global sea level rise between 1992 and 2020 is attributed to ice lost from the ice sheet (Otosaka et al., 2023). Ice flows from the central ice sheet through outlet glaciers, and where these glaciers are marine-terminating, they calve or melt into the ocean. Due to calving front retreat, the GrIS has likely lost 20% more ice since 1985 than previously calculated (Fox-Kemper et al., 2021; Otosaka et al., 2023; Greene et al., 2024), making our understanding of the GrIS margins increasingly vital.

Although there are 208 marine-terminating glaciers on the GrIS (Kochtitzky and Copland, 2022), fewer than ten (~5%) have contemporary observations demonstrating that they terminate in floating ice tongues (see Table 5.1 for definitions) (Hill et al., 2017; Reeh, 2017; Wekerle et al., 2024; Zeising et al., 2024). Over the past century, many GrIS ice tongues have collapsed or considerably shortened due to environmental factors, such as increased air and ocean temperatures causing greater surface and basal melting (Christoffersen et al., 2011; Holland et al., 2008; Rignot et al., 2012; Straneo et al., 2010; Vermassen et al., 2020). Conversely, models suggest that ice tongues would thicken and elongate with cooler ocean temperatures and reduced calving, potentially leading to an advance in the position of the grounding line, grounding zone, and tidal flexure zone (Table 5.1) (Åkesson et al., 2022). Currently, the remaining ice tongues buttress ~18% of the total GrIS ice volume, making them a potentially significant control upon Greenlandic ice discharge and, consequently, mass loss (Millan et al., 2022a).

Table 5.1: Definitions of the grounding line-related parameters used within this manuscript.

| Keyword | Definition |
|---|---|
| Ice tongue | The floating extension of a marine-terminating glacier. Longer than they are wide, these extensions typically form in fjords. |
| Grounded ice | Ice that is in contact with the bedrock at its base. |
| Grounding line | The point where ice transitions from grounded to floating at its base. |
| Grounding zone | The area over which the grounding line migrates during a tidal cycle. |
| Tidal flexure | The flexure of ice caused by the difference in tidal movement between a floating ice tongue and the adjacent grounded ice. |
| Tidal flexure zone | The area of ice that experiences tidal flexure over the timespan of our dataset (2009-2021). |

Understanding the behaviour of Greenland's ice tongues is important as their weakening or collapse may destabilise the upstream ice which their presence had previously buttressed. This has the potential to significantly increase GrIS contributions to global sea level rise (Mouginot et al., 2015). In this regard, monitoring the location and migration of their grounding lines – and the extents of their floating ice tongues – provides insights into both glacier stability and the area of ice exposed to ocean-driven melt. For example, accelerated grounding line retreat is often linked to ice tongue collapse (Hill et al., 2023; Mitcham et al., 2022). Over years or decades, the grounding line may move due to basal melt, surface melt, dynamic thinning, glacial isostatic adjustment, elastic bedrock uplift, and changes in global sea level. At shorter timescales, the grounding line may move due to tidal movement and atmospheric pressure changes (the inverse barometer effect). Surging glaciers like Brikkerne, Storstrømmen, and L. Bistrup Bræ exhibit grounding line advancements during surges (Mouginot et al., 2018). Likewise, the grounding zone and tidal flexure zone also migrate with the grounding line. For instance, Petermann Gletsjer, with its ~50 km long ice tongue (Nick et al., 2013), has a grounding zone up to 6.5 km

wide (Ciracì et al., 2023). However, the range of sizes exhibited by Greenland's grounding zones is largely unknown.

Grounding lines are among the 55 essential climate variables (ECVs), which have been defined as critical for characterising Earth's climate. To ensure grounding line estimates are meaningful, the Global Climate Observing System (GCOS) specifies a minimum temporal resolution target of one year (WMO et al., 2022). For the 15 glaciers in Greenland that we determine to either have supported, or currently support, a floating extension (see Sect. 5.3 for more detail), 40% meet this target for 2016 to 2020 (Millan et al., 2023). However, only one glacier meets the GCOS target for 2014–2021, while just one other glacier has a grounding line estimate for 2015, with sporadic coverage across other years. These gaps are primarily due to the lack of free and open synthetic aperture radar data used by current grounding line delineation methods. As a result, enhancements to existing methods and the introduction of novel approaches are necessary to consistently meet the temporal resolution target, even when data gaps arise due to satellite decommissioning.

To date, no method has used stacks of timestamped stereoscopic digital elevation models (DEMs) derived from optical satellite imagery to define a point between the landward limit of tidal flexure (*F* in Figure 5.1) and the first point of hydrostatic equilibrium (*J* in Figure 5.1), despite stereoscopic optical satellite imagery offering extensive temporal coverage (2009-2021) with very high resolution (2 m) across all of Greenland. As such, leveraging these data to delineate an approximation of the floating ice extent has the potential to address historical data gaps and aid in achieving the GCOS temporal resolution target. Within this study, we present a DEM stacking method which incorporates DEM data over the course of approximately a decade to determine the decadal floating extent of northern Greenland's ice tongues. In doing so, we provide inland flotation limits for some glaciers but note that these are not temporally stamped and only represent an *indication* of the grounding line over the entire temporal range of the glacier's DEM stack.

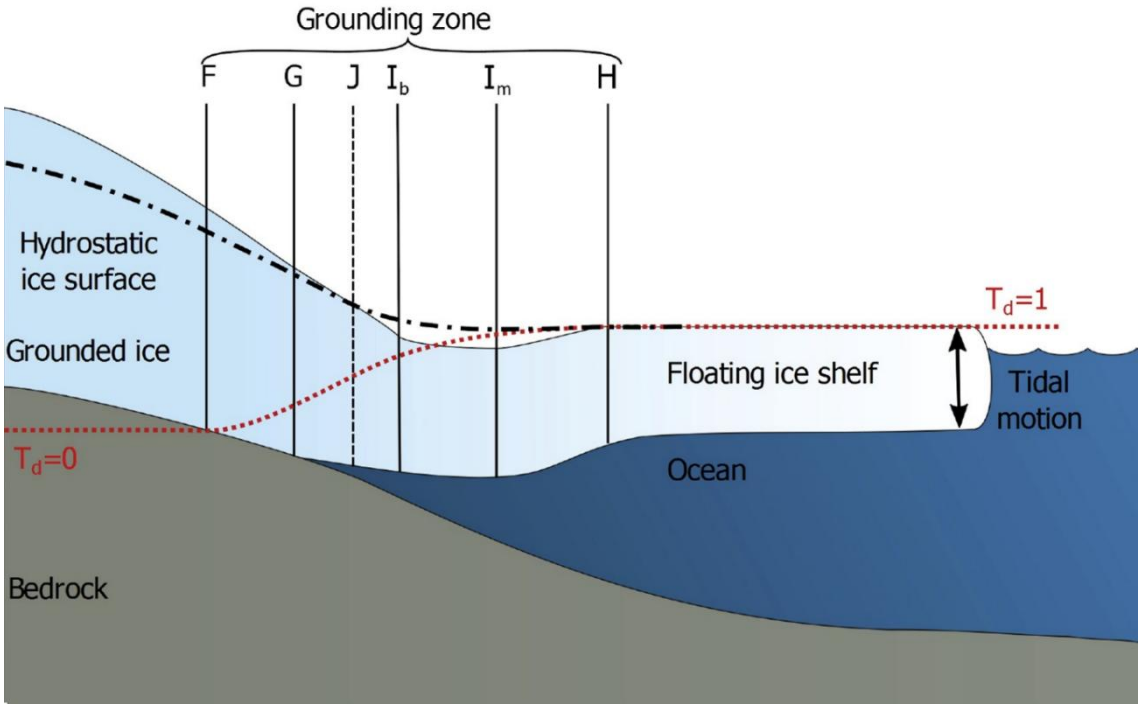


Figure 5.1: A representation of the structure of a floating ice shelf, reproduced from Friedl et al. (2020). Where, F: true landward limit of tidal ice flexure (hinge line), G: true grounding line, J: Point of first hydrostatic equilibrium, Ib: break in slope, Im: local elevation minimum, H: landward limit of stable hydrostatic equilibrium (freely floating ice), black dashed dotted line: hydrostatic ice surface (i.e. the hypothetical elevation of the ice in hydrostatic equilibrium), red dotted line: a dimensionless amplitude of tidal flexure (Td = 0 on grounded ice and Td = 1 on freely floating ice).

### 5.2.2 Past methods and our method

As the grounding line is a subglacial feature, it cannot be directly observed by satellite remote sensing methods, making it more difficult to identify and track than features on the ice surface. Instead, current remote sensing methods detect proxies for the location of grounding lines. Typically, these methods can be split into dynamic methods and static methods.

Dynamic methods detect vertical ice motion caused by tidal- or atmospheric pressure-induced variations. This group of methods focuses largely on exploiting tidal signatures and includes:

- interferometric SAR (InSAR) methods (e.g. Rignot et al., 2001; Milillo et al., 2022; Millan et al., 2023),

- SAR differential range offset tracking (SAR DROT) (e.g. Joughin et al., 2016; Marsh et al., 2013),
- tidal motion offset correlation (TMOC) (Wallis et al., 2024),
- repeat-track laser altimetry (RTLA) (e.g. Freer et al., 2023; Li et al., 2022; Fricker and Padman, 2006),
- pseudo crossover radar altimetry (PCRA) (Dawson and Bamber, 2017, 2020).

Dynamic methods primarily detect the landward limit of tidal flexure (*F* in Figure 5.1). Ice exhibits elastic properties that result in ice deformation inland of the true grounding line (*G* in Figure 5.1) (Padman et al., 2018; Vaughan, 1994), so these methods typically overestimate the area of floating ice. However, the distances between *G* and *F* are on the order of a few hundred metres, which is small compared to the scale of most of Greenland's floating ice tongues (Rignot et al., 2011).

Static methods derive grounding lines from mono-temporal datasets. This group of methods may be further split into hydrostatic and surface slope methods.

Hydrostatic methods apply Archimedes' principle of buoyancy to bedrock and ice elevation data (e.g. Friedl et al., 2018; Le Meur et al., 2014). Typically, these methods aim to locate the landward limit of stable hydrostatic equilibrium (*H* in Figure 5.1) where the ice freely floats on the ocean. However, the first major positive deviation from hydrostatic equilibrium – where the ice is thicker and no longer in hydrostatic equilibrium – occurs close to the break in surface slope ($I_b$ in Figure 5.1). As a result, hydrostatic methods approximate the grounding line as closer to either the point of first hydrostatic equilibrium (*J* in Figure 5.1) or $I_b$, rather than *H*. Both *J* and $I_b$ are typically closer to the true grounding line than *H*, but it has been estimated that this method has a horizontal uncertainty of 350 m in locating the transition from grounded to freely floating ice on a minimum 1° slope (Friedl et al., 2018).

In contrast, surface slope methods identify the break in glacier slope, which is characteristic of the transition from grounded to floating ice. This can be done using either single elevation profiles or radar altimetry-derived DEMs (e.g. Herzfeld et al., 2008; Herzfeld and Wallin, 2014; Hogg et al., 2018) as well as from optical satellite and airborne imagery (e.g. Stearns, 2011). A singular break in glacier slope can be difficult to define on ice plains – areas of slightly grounded ice which are sometimes present at the mouth

of ice streams – due to the presence of multiple breaks (Alley et al., 1989; Christie et al., 2018). The break in the glacier slope may also be located through shading on optical satellite images. A well-developed break presents as a distinct boundary between the levels of brightness within an image and has been used in multiple studies due to the high availability of optical satellite imagery (e.g. Christie et al., 2018; Möller et al., 2022).

Table 5.2: The data sources and methodologies of Greenland grounding line studies.

| **Study** | **Data source** | **Methodologies** |
|---|---|---|
| Climate Change Initiative (2023) | ERS-1/-2, Sentinel-1 | InSAR |
| Millan et al. (2023) | ERS-1/-2, Sentinel-1 | InSAR |
| Möller et al. (2022) | Sentinel-1<br>Operation IceBridge<br>Landsat 5/7/8 | InSAR<br>Hydrostatic equilibrium,<br>Surface slope (shadow) |
| Rignot et al. (2001) | ERS-1/-2 | InSAR |

Although the application of these methods is widespread in Antarctica, their use to map Greenland's grounding lines is far more limited, with notable studies including Climate Change Initiative (2023), Millan et al. (2023), Möller et al. (2022), and Rignot et al. (2001), all of which use InSAR data (Table 5.2). In this study, we therefore develop and deploy a novel, dynamic approach that instead uses high-resolution, timestamped DEMs (ArcticDEM) to identify a proxy for the inland limit of floating ice, which we define between the landward limit of tidal flexure and the point of hydrostatic equilibrium.

## 5.3 Study locations

For this study, we selected glaciers in northern Greenland that a) had supported floating portions in 1996 and/or b) currently supported a floating portion as recorded in recent literature. Our dataset of target glaciers thus consisted of (from west to east, see Figure 5.2): Petermann Gletsjer, Newman Bugt Gletsjer, Steensby Gletsjer, Ryder Gletsjer, C. H. Ostenfeld Gletsjer, Harder Gletsjer, Brikkerne Gletsjer, Jungersen Gletsjer, Henson Gletsjer, Hagen Bræ, Nioghalvfjerdsbræ (79N), Flade Isblink, Zachariæ Isstrøm, Storstrømmen and L. Bistrup Bræ. Below, we detail summaries of each of these glaciers, their grounding lines, and characteristics which make their study valuable. Although other glaciers further south in Greenland have intermittent tongues, these tend to be short and ephemeral and so are not considered within the context of the current study.

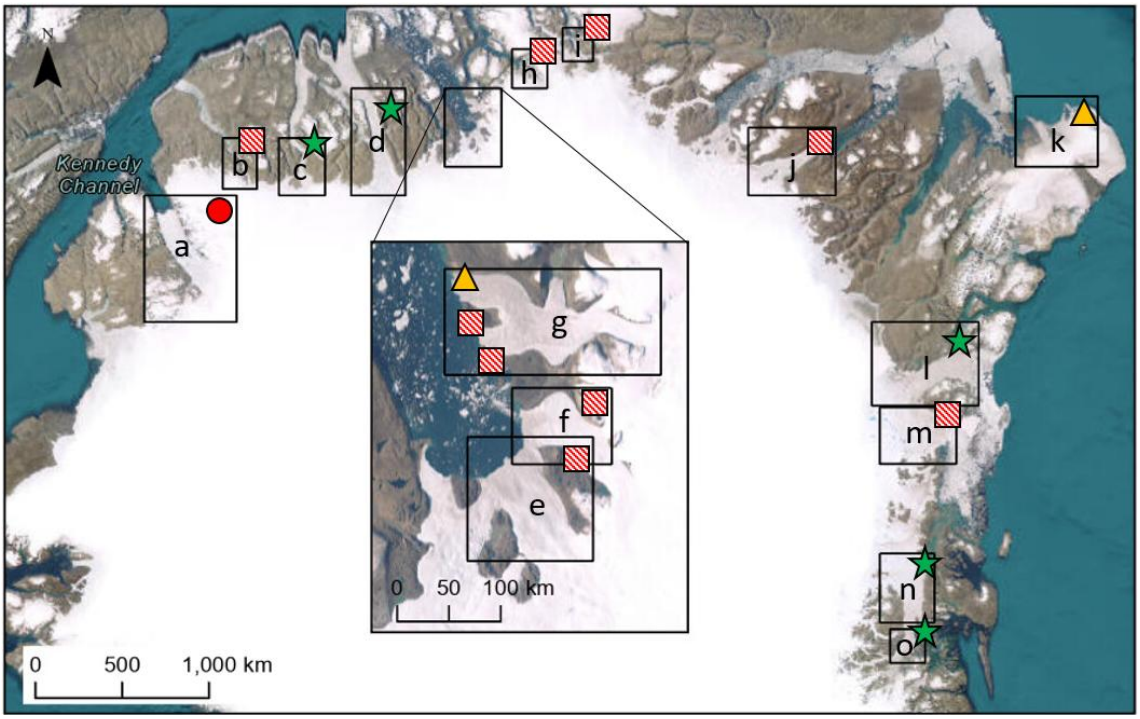


Figure 5.2: The locations and classifications of our studied glaciers in northern Greenland. The glaciers studied are indicated by the letters as follows; (a) Petermann, (b) Newman Bugt, (c) Steensby, (d) Ryder, (e) C. H. Ostenfeld, (f) Harder, (g) Brikkerne, (h) Jungersen, (i) Henson, (j) Hagen Bræ, (k) Flade Isblink, (l) Nioghalvfjerdsbræ (79N), (m) Zachariæ Isstrøm, (n) Storstrømmen, and (o) L. Bistrup Bræ. The green stars indicate a glacier/lobe where our method suggests the existence of a floating ice tongue, the orange triangles indicate that our method is ambiguous, the red circle indicates that our method fails to map a known grounding line, and the red hatched squares indicate an absence of a floating portion. The base map data are courtesy of Earthstar Geographics via Esri.

### 5.3.1 Petermann Gletsjer

Situated between Washington Land (Petermann Halvø) and Hall Land, Petermann Gletsjer flows northwards into Petermann Fjord and has one of the highest measured velocities of any of the northern Greenland glaciers (~1 km/yr) which has remained relatively constant for the last ~40 years (Higgins, 1991; Millan et al., 2022a). Petermann supports the longest ice tongue (70 km long and 20 km wide) in the northern hemisphere and has the second-largest ice tongue by area after Nioghalvfjerdsbræ (79N) (Rignot and Steffen, 2008; Wilson et al., 2017; Millan et al., 2022a). Petermann's discharge combines the inputs of multiple smaller glaciers, five of which descend from Kane Plateau on the east side to merge with the main ice stream. The largest of these tributary glaciers are Porsild Gletsjer (6 km wide) and Sigurd Berg Gletsjer (3 km wide). Large tabular icebergs

calve relatively frequently from the front of Petermann, with notable calving events occurring in 2010, 2012 and 2016 (Hill et al., 2018b; Humbert et al., 2023). These icebergs are transported into the Robeson Channel and the Kennedy Channel (Higgins, 1988). Following this, those within the Kennedy Channel may migrate southward through Nares Strait to Baffin Bay (Dunbar, 1978), increasing the likelihood of entering shipping routes through the Northwest Passages.

Petermann's floating tongue is laterally constrained by the fjord walls, which provides some stabilising effect across its width. While most Greenlandic floating tongues exhibit some degree of lateral confinement, glaciers such as Ryder are even more strongly constrained. Petermann is therefore relatively typical of Greenlandic floating tongues in terms of lateral stresses, but its confinement still influences the flow and surface expression of flotation. This is a consideration when using DEMs to identify floating areas, as surface elevation signals may be affected by the interaction of lateral and basal stresses.

Of the total ice lost from Petermann's ice tongue, 70% results from basal melting, 25% from surface melting, and 5% from calving (Rignot et al., 2001). Models suggest that these ratios could change given rising sea level and air temperatures (Åkesson et al., 2021; Ehrenfeucht et al., 2023). Notably, it has been hypothesised that once calving has begun to remove ice within 12 km of the grounding line, loss of the thicker sections of the ice tongue could alter the grounding line stresses enough to substantially increase the inland flow speeds, thus increasing Petermann's ice discharge and contribution to global sea level rise (Hill et al., 2018b). Observations suggest the grounding line is currently retreating, which may be due to enhanced basal melting close to the grounding line (Washam et al., 2018). The average basal slipperiness is approximately two orders of magnitude greater within 10 km upstream of the grounding line than the rest of Petermann's grounded ice (Hill et al., 2018b). Due to this, the rate of grounding line retreat and mass loss from Petermann is likely to increase once this increased basal slipperiness is combined with calving events which will further diminish the ice tongue's buttressing forces (Hill et al., 2018b).

Prior to 2017, Petermann's ice was thicker in the centre of the glacier compared to the edges, so the grounding line extended further seaward in its centre. This is commonly the case with fast-flowing ice streams (Hogg et al., 2016). However, Petermann may have

subsequently entered a phase of destabilisation and weakening of its ice shelf. Since 2017, Petermann's grounding line has experienced a significant retreat in its central section. Currently, the central portion of the glacier is stabilised on a sill at the top of a retrograde bed, whereas its eastern and western sides sit on prograde beds (Millan et al., 2022a). However, the eastern portion is close to the top of a retrograde bed, which has the potential to accentuate the glacier's retreat in the future (Millan et al., 2022a).

### 5.3.2 Newman Bugt

Located between Hall Land and Nyeboe Land, lies a fjord named Newman Bugt. Four tributary glaciers flow from the inland ice into this fjord to form a 2 km wide and 20 km long unnamed glacier, which we refer to within this study as Newman Bugt. The glacier flows from south to north within the fjord and reaches the sea as a slow-moving (~45 m/yr) mass with minimal ice discharge (Higgins, 1991; Rignot et al., 2001). In 1996, this glacier was observed to be fully grounded and likely retreating (Rignot et al., 2001). However, Higgins (1991) details that the frontal 1 km was afloat in 1978. As such, although a floating section is not expected, we include this glacier for completeness, and to confirm that is has maintained its grounded status.

### 5.3.3 Steensby Gletsjer

Between southern Nyeboe Land and Warming Land, a 5 km wide and 45 km long glacier drains from south to north into Sankt George Fjord. This glacier is known as Steensby Gletsjer and has, since 1992, had a relatively stable grounding line, which is located approximately 5 km inland of the calving front as of 2020 (Millan et al., 2023). Steensby's floating portion partially collapsed in 2014 due to high basal melt values, which resulted in a more than 60% velocity increase at the grounding line (Millan et al., 2023). As such, the ice velocity at the grounding line had reached ~450 m/yr by 2020. Consequently, glacier discharge rates increased by 28% between 2000 and 2020, which was likely a response by the glacier to the large loss in ice shelf buttressing (Millan et al., 2023). Although semi-permanent fjord ice once stabilised the ice front in a roughly constant position and hindered the migration of calved ice out of the Sankt George Fjord (Higgins, 1988, 1991), this sea ice is rarely multi-year in the 21$^{st}$ Century (Stroeve et al., 2012) and its seasonal melt-out allows for the easier removal of calved icebergs from the fjord.

### 5.3.4 Ryder Gletsjer

Ryder Gletsjer flows south to north between Permin Land and Wulff Land into Sherard Osborn Fjord. At 25 km long and 10 km wide, the floating extension of Ryder is one of the longer tongues in Greenland. Ryder is an episodically surging glacier that experienced a supraglacial lake drainage-induced miniature surge (lasting ~7 weeks) in 1995 (Joughin et al., 1996) and a suspected calving-induced surge in 2016 (Holmes et al., 2021). It has also been suggested that the surge behaviour may be caused by the unusual bed configuration of Ryder, which has transverse ridges leading to ponding of basal meltwater upstream of the grounding line (Rignot et al., 2001). As is the case for most glaciers with floating extensions, the highest basal melt rates for Ryder are found near the grounding line and can exceed 50 m/yr (Wilson et al., 2017). Although grounding line retreat for a simplified, theoretical floating glacier tongue occurs faster in the centre of the grounding line than the edges due to the lack of pinning points and comparatively higher stresses at the fjord edges (e.g. Millan et al., 2022a; Schwans et al., 2023), Ryder's grounding line has preferentially retreated on its eastern side since 1992 (Millan et al., 2023). This is likely a result of the bed configuration, which exhibits a deep (~1000 m) trench running along the eastern side of the fjord (Morlighem et al., 2022).

Ice-free summers were considered exceptional events within this fjord during the 1900s due to its high latitude (Higgins, 1991), but contemporary optical imagery from Landsat 8 and Sentinel-2 show the fjord was ice-free during the late summers of 2014, 2015, 2016, 2018 and 2019. As any sea ice buttressing reduces, the rate of calving from Ryder's terminus may increase due to a reduction in the restrictive forces at the ice front.

### 5.3.5 C. H. Ostenfeld Gletsjer

In Victoria Fjord, flowing south to north, lies a 20 km long and 7 km wide glacier named C. H. Ostenfeld Gletsjer. By the early 2010s, C. H. Ostenfeld was thought to have lost its floating extension, which once stretched ~25 km into Victoria Fjord (Higgins, 1991; Joughin et al., 2010; Hill et al., 2018a). The grounding line retreated ~500 m between 1992 and 1996, implying 1.2 m/yr of ice thinning during the same period (Rignot et al., 2001). Combined, these observations suggest that the glacier was in a state of dynamic imbalance.

At its calving front, C. H. Ostenfeld meets two marine-terminating glaciers: an unnamed glacier to the west, and Harder Gletsjer to the east. C. H. Ostenfeld exhibits a significantly

higher velocity than either of these two glaciers (~800 m/yr versus ~100 m/yr) (Higgins, 1991). Since the inferred collapse of the glacier's ice tongue, the glacier appears to calve at relatively equal rates across the entire width of its calving front (Hill et al., 2018a). The most recent estimations of C. H. Ostenfeld's grounding lines are from 1992 and 1996 (Rignot et al., 2001). These grounding line locations are now seaward of the calving front for this glacier and some datasets still present this glacier as having a floating portion (e.g. Morlighem et al., 2017). We have included this glacier within our study to update the location of the grounding line to either a) the 2024 calving front or b) a new location inland of this current calving front.

### 5.3.6 Harder Gletsjer

Directly northeast of C. H. Ostenfeld Gletsjer lies Harder Gletsjer. This glacier flows east to west and is bordered in the north by Th. Pedersen Land, separating it from Brikkerne Gletsjer. Nourished by a local ice dome rather than the inland ice, Harder measures ~17 km long and has a ~5 km-wide calving front (Rignot et al., 2001). It has a relatively low velocity (~100 m/yr) and merges with C. H. Ostenfeld on its southern side (Higgins, 1991). Having previously shared a merged grounding line with C. H. Ostenfeld in 1996, there have been no subsequent estimations of the grounding line location of Harder (Rignot et al., 2001). Similar to C. H. Ostenfeld, the calving front of Harder is now further inland than the most recent grounding line (1996, from Rignot et al. (2001)) used within any literature referencing the floating portion, implying the need for an updated grounding line or calving front mapping.

### 5.3.7 Brikkerne Gletsjer

North of Harder Gletsjer is another east-west flowing glacier. Although officially unnamed, this glacier acquired the name Brikkerne Gletsjer from a series of nunataks south of Nares Land. Meaning 'the pieces' in Danish, this series of nunataks was likely named for its appearance to ground researchers (Ineson and Peel, 1997). At ~28 km long, Brikkerne supports three lobes, all of which terminate in Victoria Fjord. From north to south, these lobes have ~4 km-, ~3 km-, and ~2 km-wide fronts respectively. Brikkerne is understood to be a surging glacier (Higgins and Weidick, 1990). Similarly to Harder Gletsjer, Brikkerne Gletsjer is nourished from a local ice dome instead of the inland ice (Rignot et al., 2001).

### 5.3.8 Jungersen Gletsjer

From the inland ice south of Freuchen Land, a relatively minor (~22 km long and 2 km wide) glacier named Jungersen Gletsjer drains south to north into Nordenskiöld Fjord. Prior to the 2010s, Jungersen merged near its front with less active tributaries of the Freuchen Land ice cap. However, a series of calving events occurred between 2018 and 2021 to remove the area of floating ice connecting Jungersen to these tributary glaciers. As of 2024, the Jungersen front is separated from the other Freuchen Land glaciers. In 1996, Jungersen supported a floating section with minimal iceberg discharge (Rignot et al., 2001). This floating section does not appear in any subsequent datasets. Hence, we include Jungersen to determine if it has supported an ice tongue in the last decade.

### 5.3.9 Henson Gletsjer

Henson Gletsjer is a south-to-north flowing minor glacier which drains into J. P. Koch Fjord between Lauge Koch Land to the west and the Hans Tausen Ice Cap to the east. It is a relatively slow glacier with a velocity of 170 m/yr (Rignot et al., 2001) and, as of 2021, measures ~11 km long and ~3 km wide. Several significant calving events removed ~6.4 $km^2$ of ice from the front of Henson between 2015 and 2021, resulting in a frontal retreat of ~3.7 km. Henson was recorded as having a floating section with minimal discharge in 1996 (Rignot et al., 2001). Similarly to Jungersen, Rignot et al. (2001) indicated the presence of a floating section but did not indicate the location of the grounding line, and hence we include Henson to assess whether it has more recently sustained an ice tongue.

### 5.3.10 Hagen Bræ

Located in Hagen Fjord between J. C. Christensen Land and Mylius-Erichsen Land, Hagen Bræ is a major southwest-northeast flowing glacier which drains ~6% of north Greenland and measures 60 km long with an 8 km-wide front (Hill et al., 2018a). Observations of Hagen Bræ indicate that the glacier may be a surging glacier with possible surges occurring in the 1970s/80s and the early 2000s, with ice velocity measurements derived from ERS-1/-2, Envisat, and Sentinel-1 providing evidence that Hagen Bræ has both Alaskan- and Svalbard-type surge characteristics (Rignot et al., 2001; Solgaard et al., 2020). As of 2020, the glacier was transitioning between active surge and quiescence (Solgaard et al., 2020).

Hagen Bræ has previously supported a floating tongue whose grounding line retreated 400 m between 1992 and 1996, translating to 1.6 m/yr of thinning (Rignot et al., 2001). Estimates from 1996 place the location of the grounding line seaward of the present-day calving front (Rignot et al., 2001; Millan et al., 2023), sited on a large transverse ridge in the bed elevation. From 2001-2005, the floating extension of Hagen Bræ started to dislocate at the shear margins, resulting in the collapse of either the whole ice tongue or a significant portion between 2008 and 2009 (Millan et al., 2023). However, estimates from 2017 place the grounding line ~46 km further inland, south of the two islands which partially dam the glacier (Climate Change Initiative, 2023; Higgins, 1988).

### 5.3.11 Flade Isblink

Flade Isblink is the largest independent ice cap in Greenland. It has an area of 8,500 $km^2$ and is situated in Northern Kronprins Christian Land on the Princess Dagmar Peninsula in northeast Greenland (Kelly and Lowell, 2009; Palmer et al., 2010). The ice cap has only one significant outlet glacier, which is in the north, to the east of Station Nord (Higgins, 1991). This outlet flows south to north and is 20 km long with a 25 km-wide front. Consisting of two separate basins, this outlet has a grounding line 4-8 km inland of the calving front, with an estimated floating area of ~220 $km^2$ (Möller et al., 2022).

Satellite data suggests that the outlet surges (Joughin et al., 2010), and that it surged between 1996 and 2001, with rapid thickening and increased ice flux (Möller et al., 2022). The events have been characterised as Svalbard-type surges modified by ice-shelf buttressing (Möller et al., 2022).

### 5.3.12 Nioghalvfjerdsbræ (79N)

Nioghalvfjerdsfjorden, located between Kronprins Christian Land and Lamberts Land, is filled by the floating tongue of a glacier known as Nioghalvfjerdsbræ or 79 North Glacier. We refer to this glacier as 79N. This glacier is one of the main outlets of the Northeast Greenland Ice Stream (NEGIS). The NEGIS drains ~17% of the GrIS (Roberts et al., 2024), and also drains into 79N's southerly neighbour, Zachariæ Isstrøm, meaning these two outlet glaciers play critically important roles in the mass-loss dynamics of the GrIS.

The floating extension of 79N flows southwest to northeast, is 60 km long and supports a 30 km-wide front which abuts a series of small islands. This floating tongue is the largest in Greenland (Wilson et al., 2017). Pre-2020, an 8 km-wide northern branch of 79N, known as Spalte Gletsjer, occupied the Dijmphna Sund fjord to the north of the main

tongue (Higgins, 1988). This branch of 79N completely disintegrated in 2020 (Humbert et al., 2023).

The grounding line of 79N is near the ice-dammed lake known as Blåsø and has retreated ~4.5 km in its central section since 1996 (Millan et al., 2023), as 79N's floating ice tongue has thinned (Wilson et al., 2017). Currently, the total melt flux of 79N exceeds the inflow of ice, with submarine melting accounting for approximately 80% of the annual non-calving mass loss.

### 5.3.13 Zachariæ Isstrøm

Jökelbugten is a fjord between Lamberts Land to the north and Hertugen af Orléans Land to the south. A 25 km long floating tongue, 60 km wide at its grounding line, narrows to a 20 km-wide front within this fjord and presents as the floating extension of the west-to-east flowing Zachariæ Isstrøm. The NEGIS drains into this glacier, making it an important glacier in terms of mass-loss dynamics on the GrIS. A number of published studies have concluded that Zachariæ Isstrøm lost its ice shelf between 2012 and 2013 with subsequent studies confirming the glacier as grounded (Münchow et al., 2014; Mouginot et al., 2015; Millan et al., 2023). However, InSAR estimates of the grounding line location from 2017 place it ~25 km inland of the calving front, on a transverse ridge (Climate Change Initiative, 2023).

### 5.3.14 Storstrømmen

Between Dronning Louise Land and Germania Land lies Storstrømmen, a north-south flowing surging glacier (Mouginot et al., 2018). The floating extension of this glacier is 15 km long and 15 km wide at its grounding line. Storstrømmen merges with L. Bistrup Bræ in the south to flow into Borgfjorden. On satellite imagery, a convergence line is visible at the meeting of Storstrømmen and L. Bistrup Bræ. To the west of this convergence line lies the proglacial lake, Randsøen, which exhibits melange along the convergence line. The convergence of Storstrømmen and L. Bistrup Bræ may cause the glaciers to exert back forces on one another (Mouginot et al., 2018).

From 1913 to 1978, the front of Storstrømmen retreated 9-12 km and then suddenly advanced between 1978 and 1982 (Weidick et al., 1996). This surge advanced the front by 8 km as the speed peaked at 3 km/yr (Reeh et al., 1994; Mouginot et al., 2018). Since 1982, Storstrømmen has stayed quiescent with a slowly retreating front (Weidick et al., 1996; Mouginot et al., 2018). Between 1992 and 2017, the grounding line retreated 10

km, equivalent to an average rate of 400 m/yr (Mouginot et al., 2018). With a likely surge periodicity of ~50 years, and with current rates of melt and grounding line retreat, Storstrømmen is predicted to meet presurge conditions between 2027 and 2030 (Mouginot et al., 2018).

### 5.3.15L. Bistrup Bræ

L. Bistrup Bræ flows south to north between Dronning Louise Land and Hochstetter Land south of Storstrømmen. L. Bistrup Bræ terminates in a 12 km wide front which flows into Borgfjorden alongside Storstrømmen. Although also a surging glacier, L. Bistrup Bræ surges at a much slower velocity than Storstrømmen and is also expected to be in quiescence (Rignot et al., 2001). Reaching a maximum of 1.35 km/yr at the height of its surge in 1993 (during the 1988-1996 surge), compared to Storstrømmen's 3 km/yr between 1978 and 1982, L. Bistrup Bræ likely experiences significant back forces from Storstrømmen during its surge cycle (Mouginot et al., 2018). The most inland position of the grounding line for L. Bistrup Bræ is from 1978. Between 1978 and 1996 – encompassing the most recent recorded surge of L. Bistrup Bræ – the grounding line position advanced by 5 km. Since 1996, the grounding line has retreated by 3.5 km to reoccupy its 1992 position (Mouginot et al., 2018). Like Storstrømmen, L. Bistrup Bræ has a surge cycle of 30-50 years, albeit with a cycle phased ~10 years later (Mouginot et al., 2018).

## 5.4 Data

To delineate the extent of floating ice on the selected glaciers, we required digital elevation modelling datasets and auxiliary contextual datasets. In this section, we describe the datasets used in our method.

### 5.4.1 Principal datasets

We used two DEM datasets provided by the Polar Geospatial Centre (PGC) as our principal datasets. These were:

- ArcticDEM strip DEMs at 2 m resolution; and,
- ArcticDEM mosaic DEM at 100 m resolution.

ArcticDEM strip DEMs are time-stamped, indicating the earliest acquisition date within the stereoscopic pair (see Sect. 2.2.1), and come from an open-access collection of high-resolution (2 m) DEM data produced by the PGC (Porter et al., 2022). This dataset is assembled from individual stereoscopic DEMs, which are derived from high-resolution (0.32 to 0.5 m) satellite imagery pairs. ArcticDEM strip DEMs are generated by applying the Surface Extraction from TIN-based Searchspace Minimization (SETSM) software to these stereo pair images (Noh and Howat, 2015). All ArcticDEM strip DEM data used in this study were produced from stereo pairs acquired between 2009 and 2021 during the summer months. Although the dataset has full spatial coverage of the GrIS, the coverage is uneven through time, with some regions having significantly more data than others (Figure 5.3, Figure 5.4).

The strip DEMs preserve the original temporal resolution of the stereoscopic DEMs and provide a temporal snapshot of the surface height. These DEMs vary in size from tens to thousands of square kilometres and have an average area of approximately 800 $km^2$ across the GrIS. Strips are produced for a range of different research purposes. For this reason, the margins of the GrIS have substantially more data than the interior, with regions of high interest such as Petermann Gletsjer having the highest quantities of data. Additionally, satellite convergence means that the northern GrIS has more strip DEMs than the southern regions. The timestamps of the strips allow for comparison of topographic data acquired in different seasons or years (Figure 5.3, Figure 5.4).

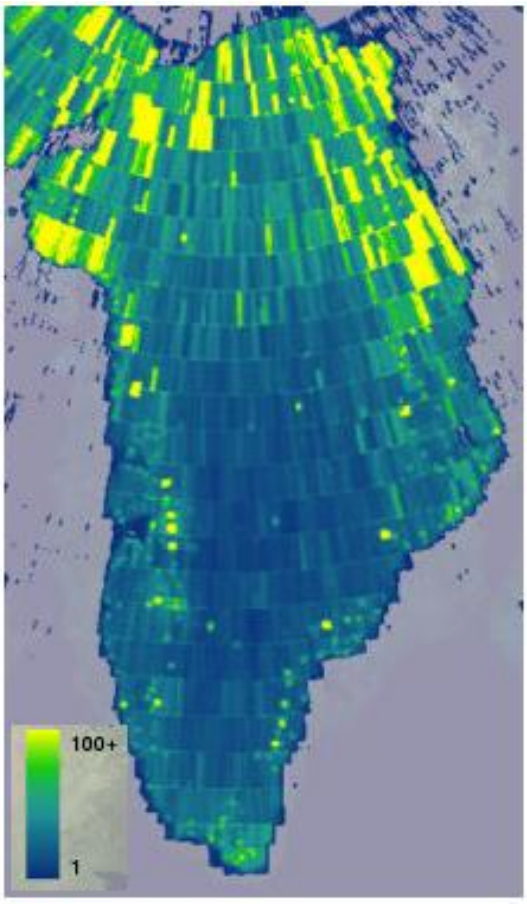


Figure 5.3: The number of ArcticDEM strip DEMs available over the GrIS as of the April 2025 data release. Image courtesy of the Polar Geospatial Centre (https://www.pgc.umn.edu/data/arcticdem/, date accessed: 29th October 2025).

In addition to the strip DEMs, the PGC produces DEM mosaics of varying spatial resolutions (2 m, 10 m, 32 m, 50 m, 100 m, 500 m, and 1 km) (Porter et al., 2023). The DEM mosaics are assembled from multiple strip DEMs which have been co-registered, blended, and feathered to reduce edge-matching artefacts. This provides a more consistent and comprehensive DEM product over larger areas. The PGC uses a median-mosaicking approach to produce the DEM mosaics. This provides the median value of all strip elevations at each pixel (for the strip DEM stack, dated 2009–2021), with outlier filtering applied. As a result, a specific date cannot be assigned to a mosaic pixel as the value of said pixel is a median average of all overlying strip DEMs. Quality control factors such as the number of strips, median absolute deviation, and the time range of DEM acquisitions for each mosaic pixel are provided in the metadata to identify areas of poor-quality data and rapidly changing regions. We use the DEM mosaic as a reference dataset against which to mask our strip DEMs.

Although the PGC produces 2 m resolution DEM mosaics, these are provided as 50 km x 50 km tiles, so we instead chose to use the non-tiled ArcticDEM 100 m mosaic which meant we could avoid introducing edge effects caused by merging. Additionally, this ensured spatial consistency and limited the potential introduction of artefacts during data processing. The mosaics cover the full ArcticDEM domain and have been used as reference datasets in many other studies (e.g. Seehaus et al., 2020; Shiggins et al., 2023; Dai et al., 2024; Grimes et al., 2024).

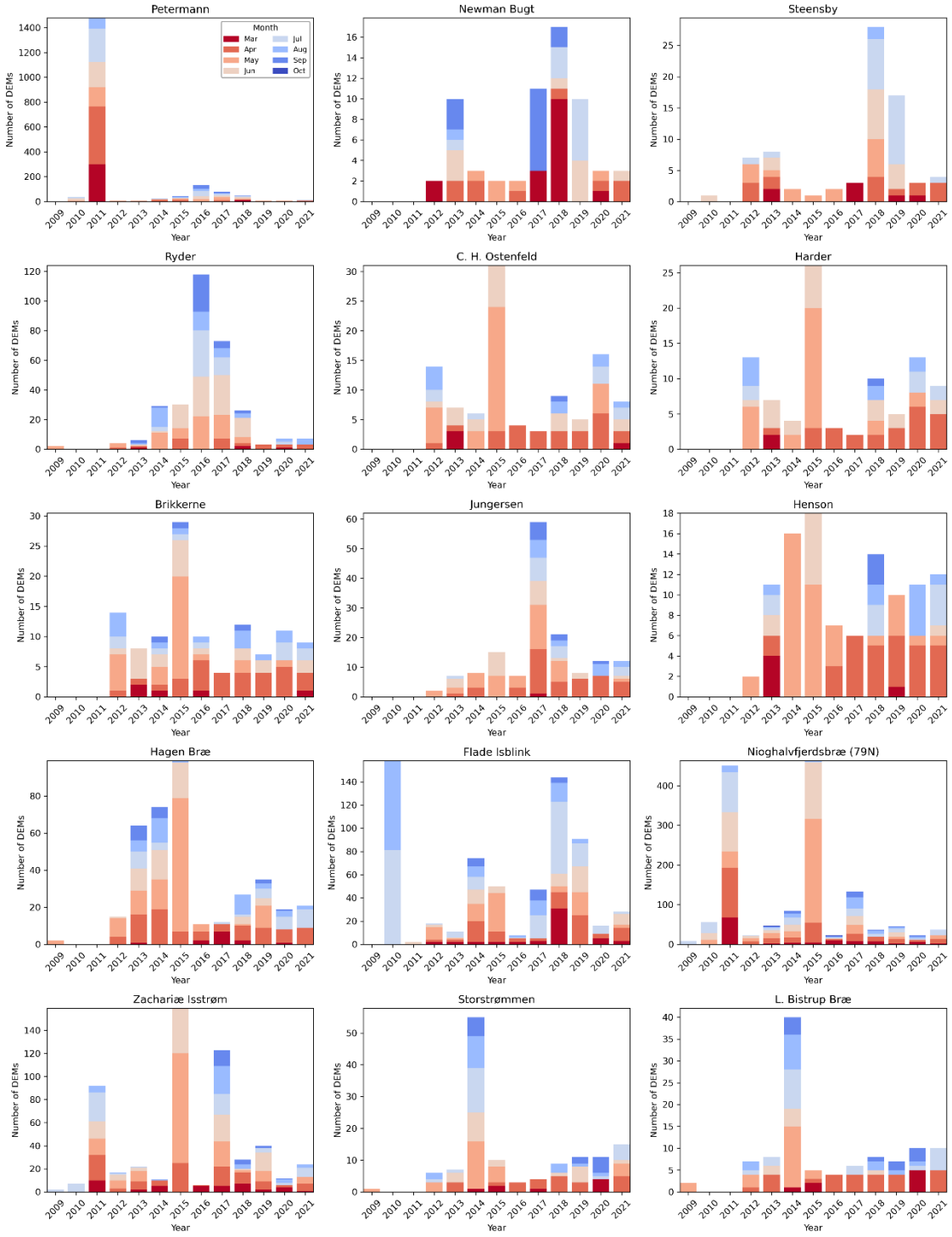


Figure 5.4: The number of DEMs available monthly and annually for our grounding line processing chain once all filtering steps detailed in Sect. 5.5 have been applied. Glaciers are presented in their west-to-east configuration from top-to-bottom, left-to-right.

### 5.4.2 Ancillary datasets

To determine if each of our glaciers had supported an ice tongue in the past decade, we compiled contextual data from several ancillary datasets. These data included:

- Landsat 8 and Sentinel-2 optical satellite imagery.
- Historical calving front locations (Climate Change Initiative, 2023; Hill et al., 2018a).
- Historical grounding line locations (Rignot et al., 2001; Climate Change Initiative, 2023; Mouginot et al., 2018; Millan et al., 2023).
- Bed elevation, ice surface elevation, ice thickness, and ice mask from BedMachine version 5 (Morlighem et al., 2022).

These ancillary datasets gave us a wider understanding of each glacier's behaviour and ability to support an ice tongue.

For each glacier, we used a combination of Landsat 8 and Sentinel-2 optical satellite imagery to visually confirm calving events during the date range we studied for each glacier, which typically spanned between 2009 and 2021. This information is required to ensure that our method (see Sect. 5.5) does not mistakenly identify calving events as tidal fluctuations. The date range differed from glacier to glacier due to the availability of our DEM data. Depending on the calving front dataset, calving front locations were available until 2015 for six glaciers and until 2020 for one glacier (Climate Change Initiative, 2023; Hill et al., 2018a). For glaciers where a) we did not have previous calving front locations from the literature and/or b) the calving front was within a few kilometres of the historical grounding line, we delineated reference calving fronts using the Google Earth Engine Digitisation Tool (GEEDiT) (Lea, 2018). We detail the sources of each calving front in Table 5.3. Each calving front we delineated using GEEDiT was taken from the end of August, a few weeks before the annual sea ice minimum (Meier et al., 2021) to maximise the likelihood of capturing the most retreated, heavily calved state of the glacier for that year. Additionally, we used optical satellite imagery to identify surface features, such as streams and crevassing, to help evaluate the performance of our method.

We compiled grounding line datasets from the literature for all the target glaciers (Table 5.3) and used these grounding lines for contextual reference of the grounding lines' past locations and trajectories over the last decade. We used this data to validate the results of our method.

Our final ancillary dataset was BedMachine version 5 (Morlighem et al., 2022). BedMachine is a bed topography/bathymetry map of the GrIS based on multi-beam echo-sounding data and a mass conservation approach. This dataset has a nominal timestamp of 2007 (Morlighem et al., 2022). Along with the bed elevation data, BedMachine is packaged with an ice/ocean/land mask that contains historical grounding line information. We used the bed elevation dataset to improve our understanding of where and why the tidal flexure zone would likely migrate over time. Additionally, we used the ice surface elevation and ice thickness layers to determine the height above flotation and the height at flotation for each glacier which gave us an independent estimate of the grounding line to help evaluate the performance of our method. We detail our method for calculating the height above flotation and height at flotation in Sect. 5.5.6.

The spatial resolution of this dataset is 150 m and the uncertainty on the bed elevation data may be > 50 m in some areas of Greenland. The ice mask details the floating and grounded portions of the ice sheet, albeit using data from Rignot et al. (2001), which may not be representative of present-day conditions. Together, these ancillary datasets provided us with a basic context for our target glaciers.

Table 5.3: The number of DEMs, and sources of the margins and historical grounding lines used within this study. For the margin and grounding line data, each year column is split into two columns for each glacier, the left shows the source of the margin data, and the right shows the source of the grounding line data. Glacier abbreviations are as follows: Petermann (PG), Newman Bugt (NB), Steensby (Ste), Ryder (R), C. H. Ostenfeld (CHO), Harder (Ha), Brikkerne (B), Jungersen (J), Henson (He), Hagen Bræ (HB), Flade Isblink (FI), 79 North (79N), Zachariæ Isstrøm (ZI), Storstrømmen (Stor), L. Bistrup Bræ (LBB). Key: A = Author-delineated data, C = Climate Change Initiative (2023) data, H = Hill et al. (2018a) data, Mi = Millan et al. (2023) data, Mö = Möller et al. (2022) data, R = Rignot et al. (2001) data, and cross-hatched cells = no data. See Table 5.2 for methodologies and data sources of grounding line citations. The number of DEMs for each glacier is calculated as the number of DEMs that contain valid (i.e. non-NaN) data after the pre-processing stages detailed in Sect. 5.5.1 to Sect. 5.5.3 and has valid data in the grounded polygon (see Sect. 5.5.4). The asterisk on Hagen Bræ's number of DEMs indicates the reduced number (Appendix B.1).

| Glacier (Abbrev.) | No° of DEMs | Year [Margin \| Grounding Line] | | | | | | | | | | | | | | | | | | | | | | | | | | | | | | | | | |
|---|---|---|---|---|---|---|---|---|---|---|---|---|---|---|---|---|---|---|---|---|---|---|---|---|---|---|---|---|---|---|---|---|---|---|---|
| | | 1992 | | 1993 | | 1994 | | 1995 | | 1996 | | 1999 | | 2006 | | 2009 | | 2010 | | 2011 | | 2012 | | 2013 | | 2014 | | 2015 | | 2016 | | 2017 | | 2018 | | 2019 | | 2020 | | 2021 | |
| PG | 1889 | | Mi | | | | | | C | | Mi | | | | | | | | | | Mi | | | | | | Mi | | Mi | | Mi | | Mi | | Mi | | Mi | | Mi |
| NB | 63 | | | | | | | | | | | | | | | | | | | | | A | | A | | A | | A | | A | | A | | A | | A | | | |
| Ste | 76 | | Mi | | | | | | | | | | | | | | | A | | H | | | | H | | A | | A | | A | Mi | A | Mi | A | Mi | A | Mi | | |
| R | 305 | | Mi | | | | | | | | C | | | | | H | | H | | H | Mi | H | | H | | H | | H | Mi | C | Mi | | Mi | | Mi | | Mi | | |
| CHO | 103 | | R | | | | | | | | R | | | | | H | | H | | H | | H | | H | | H | | H | | C | | A | | A | | A | | A | |
| Ha | 92 | | | | | | | | | | R | | | | | | | | | | | H | | H | | H | | H | | A | | A | | A | | A | | | |
| B | 114 | | | | | | | | | | R | | | | | | | | | | | H | | H | | H | | H | | A | | A | | A | | A | | A | |
| J | 151 | | | | | | | | | | | | | | | | | | | | | | | | | | | A | | A | | A | | A | | A | | A | |
| He | 107 | | | | | | | | | | | | | | | | | | | | | | | | | | | A | | A | | A | | A | | A | | A | |
| HB | 38* | | | | | | | | | | C | | | | | H | | H | | H | | H | | H | | H | | H | | C | | | C | | | C | | C | | |
| FI | 647 | | | | Mö | | | | | | | | Mö | | Mö | | | | | | | | | | | | Mö | | | A | | A | | A | Mö | A | Mö | A | | A | Mö |
| 79N | 1431 | | Mi | | | | Mi | | C | | Mi | | | | | | | | | | Mi | | | | | | | | Mi | | Mi | | Mi | | Mi | | Mi | | |
| ZI | 543 | | | | | | | | C | | Mi | | | | | H | | H | | H | Mi | H | | H | | H | Mi | C | | C | | | Mi | | | | Mi | | |
| Stor | 132 | | Mi | | | | | | | | Mi | | | | | H | | H | | H | | H | | H | | H | | H | | | Mi | | Mi | | Mi | | Mi | | |
| LBB | 107 | | | | | | | | | | Mi | | | | | H | | H | | H | | H | | H | | H | | H | | A | Mi | A | Mi | A | Mi | A | Mi | A | Mi | | |

## 5.5 Methodology

The method that we present here is a dynamic tidal method which identifies a point between the landward limit of tidal flexure and the hydrostatic equilibrium line. We use this as a proxy for an estimate of the true grounding line over the date range of our DEM stacks but emphasise that the method described herein does not identify the true grounding line. In our study, we use all available strip DEMs for all glaciers except for Hagen Bræ, where we restrict the number of DEMs used to ensure a balanced spatial distribution (Appendix B.1). Our method involves the following steps described below.

### 5.5.1 Step 1) Masking – pre-packaged mask

During DEM processing, only edge artefacts are removed by the PGC's in-house filtering method. The PGC therefore packages their raw strip DEMs with an additional quality control mask, which aims to identify any errors in the DEMs resulting from cloud or water contamination. These bitmasks can be optionally applied to the DEMs to remove regions of the DEM that the PGC deem to represent potentially erroneous data, such as edge effects, open water and cloud pixels. These quality control masks are provided as 8-bit unsigned integer rasters which are unique to each DEM. We applied the PGC official Python script to filter each DEM of interest using the associated mask (Husby, 2023). This script selectively masks pixels exhibiting cloud, water, or edge effects.

After we had applied the masks to the DEMs, we clipped all the DEMs to the extent of each glacier. We defined each glacier's extent by manually delineating a polygon encompassing the area around the suspected tidal flexure zone and extending inland onto the main ice sheet or ice cap. We used all available historical locations of the glacier grounding lines to ensure that we analysed the appropriate area of the glacier.

### 5.5.2 Step 2) Masking – thresholding

After applying the pre-packaged mask, some anomalous values were still present in the DEMs. We understand these to represent unrealistic elevation values originating from unfiltered cloud pixels or other artefacts. To filter out the invalid DEM pixels that were not filtered by either the PGC in-house filtering method or the DEM masking script, we compared the heights of each DEM to the height of the ArcticDEM 100 m mosaic (version 4). To do this, we clipped the mosaic to the glacier polygon and resampled the mosaic to 2 m resolution using bilinear interpolation. We then differenced the two rasters and removed any pixels from the source strip that deviated by more 10 metres from the

mosaic. In developing the method, we also tested a range of other thresholds and selected a 10 m threshold as a reasonable balance between removing unrealistic elevation values and filtering out valid data. The output DEMs which were passed to the next stage of processing thus only included pixels whose values were within a 10 m vertical difference of the ArcticDEM 100 m mosaic.

### 5.5.3 Step 3) Smoothing

Surface ice velocities can exceed 3 m/day (~1 km/year) on some glaciers in northern Greenland (Li et al., 2023a). Small-scale topographic features on the glaciers primarily consist of ridges and crevassing caused by spatial variability in ice surface velocities (Rea and Evans, 2011). Surface ridges and crevasses on glaciers are advected with ice flow, leading to high-frequency variability in elevation through time at fixed locations, particularly in regions of rapid flow (Li et al., 2023a; Rea and Evans, 2011).

To reduce this short-wavelength noise while preserving the high-resolution raster for further analysis, we computed the blockwise median elevation over 100 x 100 m cells of each 2 m DEM. The coarsened grid was then linearly interpolated back to the original 2 m posting, producing a smoothed DEM that retained larger-scale elevation patterns while mitigating artefacts from advected features. This differs from standard aggregation, where the raster would remain at 100 m resolution and fine-scale pixel-based operations would no longer be possible. Although we explored the use of velocity-field based corrections, these proved unreliable in regions of complex, non-linear flow near fjords, where surface features cannot be tracked accurately. Edge effects introduced by the smoothing are minimal due to the blockwise median and interpolation procedure. This smoothing method reduces artefacts caused by the advection of surface features in regions of high velocity, whilst maintaining the larger-scale elevation variance which is the focus of this study.

### 5.5.4 Step 4) Vertical alignment

Typically, each strip DEM is vertically offset relative to the other strip DEMs. As our method aims to identify spatial changes in the stacked deviation associated with moving from grounded to floating ice, we needed to correct this offset. To do so, we first needed to identify an area of the glacier upstream of the grounding line. As such, we defined a polygon inland of each glacier terminus which we had strong reason to believe was

grounded. Specifically, we defined the grounded areas as meeting the following requirements:

- Suitably far inland to account for potential grounding line retreat
- Excludes surface hydrological features
- Within the original glacier polygon defined in Sect. 5.5.1

To ensure the areas were suitably far inland, we determined the most inland grounding line estimates for each glacier and delineated a parallel line approximately 2 km further inland to account for any additional grounding line retreat. This bounded the seaward edge of our grounded area. We placed this line 2 km inland of the most inland grounding line estimations based on the relative rate of retreat exhibited by Petermann Gletsjer. This fast-flowing glacier had an average retreat rate of 1 km/year between 2016 and 2021 (Millan et al., 2022a), and we expect that the smaller and slower glaciers would likely exhibit a slower retreat rate, in comparison. Additionally, our fastest glaciers had more recent grounding line estimations (Table 5.3) with which to base the location of our 2 km-further-inland line, increasing our confidence in the validity of our grounded area. Although applying this relatively conservative assumption may have reduced the total area over which we vertically align our DEMs, it allowed us to have relative certainty that the entire area was indeed grounded at the time of our DEM acquisitions.

Next, we excluded surface hydrological features from our grounded polygon, on the basis that lakes and streams may fill and empty over time, causing unwanted additional variance in our stacked DEMs, which would complicate the vertical alignment procedure. To do so, we masked the DEMs with an amalgamated supraglacial hydrology raster that represented the maximum surface water depth from 2012-2021 (Corr, 2023). We limited this raster to areas where surface water was predicted to be more than 1 m deep, as this was indicative of ponded water where the elevation variance was expected to be most significant. The grounded area was entirely within the original glacier polygon, and the lateral and upstream edges of the grounded area were defined to match to the original glacier polygon geometry defined in Sect. 5.5.1.

To perform the vertical alignment, we sampled each glacier's grounded area polygon at 100 m intervals (i.e. one sampling point (SP) for every 0.01 $km^2$). If a DEM did not cover $\geq$ 25 SPs (i.e. 0.25 $km^2$ of grounded area), we considered the DEM's grounded coverage to be insufficient and did not include it in any further calculations. Once we had extracted

the height of each DEM for each SP, we calculated the median height for each SP from the stacked DEMs.

To vertically align each strip DEM, we then differenced the height of the DEM at each SP and the median height of that SP for the SPs that the DEM covered. We then applied the average value of these differences as a constant vertical correction to the DEM. We did not correct for potential tilt or skew effects in our method as the purpose of this step was to apply a simple, vertical alignment, and visual inspections of the DEMs suggested that these higher order factors had minimal impact on the results. We focused on correcting for vertical offsets, as these have the most direct impact on elevation change estimates. Although both horizontal and vertical uncertainties are of similar magnitude in ArcticDEM strip data, correcting for horizontal misalignments typically requires more computationally intensive coregistration approaches, whereas vertical bias can be more efficiently reduced through relative referencing. Given the large number of DEMs in this study, addressing horizontal offsets was prohibitively time-consuming, and we therefore limited correction efforts to the vertical dimension. Once applied, this vertical offset of each DEM allowed us to effectively remove the combined effects of grounded ice thinning and vertical misalignment, in order to isolate the spatial variance in the residual signal. Specifically, this allowed us to exploit the differing signals of elevation change exhibited by floating and grounding ice, due to the effects of buoyancy and tidal processes.

### 5.5.5 Step 5) Stacking, statistics and manual delineation

After vertically aligning the DEMs, we calculated the median absolute deviation from the median (hereafter referred to as the median absolute deviation), the standard deviation of elevation, and the number of DEMs by stacking the processed DEMs and calculating the statistics for each 4 $m^2$ pixel.

To determine if and where each glacier reached flotation, we defined a longitudinal transect down the centreline of each glacier, and sampled the heights of the processed DEMs, along with the median absolute deviation and the standard deviation of the stack along the transect. Where there was evidence of downstream divergence amongst the processed DEMs, and the median absolute deviation and the standard deviation estimates increased, we posit that the glacier is in a state of flotation. Where visual inspection of

the median absolute deviation map implied a floating portion, we delineated the inland limit of the floating ice tongue manually from this deviation data.

### 5.5.6 Step 6) Height above/at flotation

We determined the height above flotation, $h_f$, from the BedMachine version 5 ice thickness, $H$, and BedMachine version 5 ice surface elevation, $h$, layers using Eq. 5.1 (adapted from Milillo et al. (2019) with alterations respecting the densities of ice, $\rho_i$, and seawater, $\rho_w$, as used in the BedMachine version 5 product) as

$$h_f = h - H\left(1 - \frac{\rho_i}{\rho_w}\right) \tag{5.1}$$

where the densities of ice, $\rho_i$, and seawater, $\rho_w$, are 917 kg/m$^3$ and 1023 kg/m$^3$, respectively. We present the results of these calculations in Appendix B.2. We also calculated the height at flotation, $h_{af}$, using

$$h_{af} = h - h_f \tag{5.2}$$

where $h$ is the BedMachine version 5 ice surface elevation layer and $h_f$ is height above flotation as defined in Eq. 5.1. The height at flotation is useful because it defines the hypothetical surface at which the ice will detach from the bed and enter a state of flotation. We present the results of these calculations in panel c of each figure in Section 5.6.

We calculated the height at flotation uncertainty, $\sigma h_{af}$, as

$$\sigma h_{af} = \sigma H\left(1 - \frac{\rho_i}{\rho_w}\right) \tag{5.3}$$

where $\sigma H$ is the BedMachine version 5 bed topography and ice thickness error layer and the densities of ice, $\rho_i$, and seawater, $\rho_w$, are 917 kg/m$^3$ and 1023 kg/m$^3$, respectively. We present the uncertainty of our height at flotation calculations on panel c of each figure in Section 5.6.

## 5.6 Results

Our results vary by study site. As such, we have categorised the results into subsections defined by the confidence associated with our inland flotation limit identification (where our inland flotation limit indicates the inland location of floating ice over the duration of the DEM stack). Although we categorise our glaciers by confidence level, we reiterate that these results elucidate the proof of concept for using DEMs to find floating ice. Ergo, even our most confident results are not without ambiguity, and these interpretations should be considered indicative rather than definitive.

For most glaciers, we present our results in a three-panel format. In the top left panel is a contextual map of the glacier showing any previous grounding lines and calving fronts detailed within the literature, as well as the location of the central transect. In the top right panel, we show our median absolute deviation results from our method and, where applicable, our estimation of the inland flotation limit location. The bottom panel shows the average annual heights of the stacked and aligned DEMs along the central transect, with vertical lines to indicate the locations of the literature-derived grounding and calving zones, together with our inland flotation limit estimation, where applicable. For some glaciers, we have added extra panels for context which we explain in full in their relevant sections. We present our results for each glacier in turn.

### 5.6.1 Glaciers with apparent flotation signatures

#### 5.6.1.1 Storstrømmen

The median absolute deviation map (Figure 5.5b) for Storstrømmen shows a defined and abrupt change between regions of high (floating) and low (grounded) elevation variance. The transition between these regions occurs close the recent (2016-2022) grounding lines delineated by Millan et al. (2023). Additionally, the ice velocity data from the NASA MEaSUREs ITS_LIVE project (Gardner et al., 2025) shows a velocity increase around the locations of these grounding lines. This is expected around the grounding line as the ice lifts off the bed, removing the effect of basal friction, and allowing the ice to flow faster. The velocity increases from these grounding lines towards the calving front with the general pattern of ice flow trending towards the lateral margins of the glacier from the centre flowline.

We note that the deviation pattern allows us to observe more detailed geometry of the grounding line compared to previous estimations, suggesting that Storstrømmen's

grounding line exhibits small inlets and promontories across its width, likely reflecting the underlying bed topography (Figure B.2.1a). The pattern of the height above flotation data (Figure B.2.1b) indicates a low gradient on the ice tongue up to the approximate location of the inland flotation limit that increases upstream, independently indicating potential flotation.

We also observe patterns associated with iceberg movement of the minor northern lobe, as calved ice is transported away from the glacier margin. The floating ice on Storstrømmen exhibits a striated pattern, which we suggest may be caused by the presence of meltwater channels and longitudinal ridges within the ice surface. These meltwater channels are also visible on the grounded ice portion, and we indicate an example of this feature with a yellow star in Figure 5.5b.

Figure 5.5c confirms the retreating nature of Storstrømmen where the average annual elevation signals begin to plateau, indicating flotation, between ~9,000 and ~12,500 m along the transect. The later years transition from high to low gradient further inland than the earlier years, implying a gradual retreat of the grounding line. It is important to note here that the artificial alignment against an upstream grounded area means that if the upstream area is thickening, e.g. in the characteristic way that a surging glacier such as Storstrømmen may thicken, the artificial alignment could exaggerate the thinning trend downstream, which is responsible for the apparent change in sea level in Figure 5.5c.

We also note that the height at flotation line shown in Figure 5.5c indicates flotation around the same location as the plateau of the average 2021 DEM elevations. The uncertainty on the height at flotation is relatively small and stable until ~500 m inland of the 1992 grounding line where it increases. This is due to the change in bed elevation source type from kriging to interpolation (Figure B.3.1a). Figure 5.5a indicates greater grounding line retreat across the central portion of the glacier versus in the lateral margins. The area of relatively high deviation immediately upstream of the central grounding line, indicated by a black triangle in Figure 5.5b, exhibits a strong thinning signal which may indicate a future preference for further retreat in the grounding line's central portion. This analysis may concur with Storstrømmen's nature as a surging glacier (Higgins and Weidick, 1990; Mouginot et al., 2018) which experiences surface thickening in the upper reaches of the glacier and thinning in the lower reaches during pre-surge quiescence.

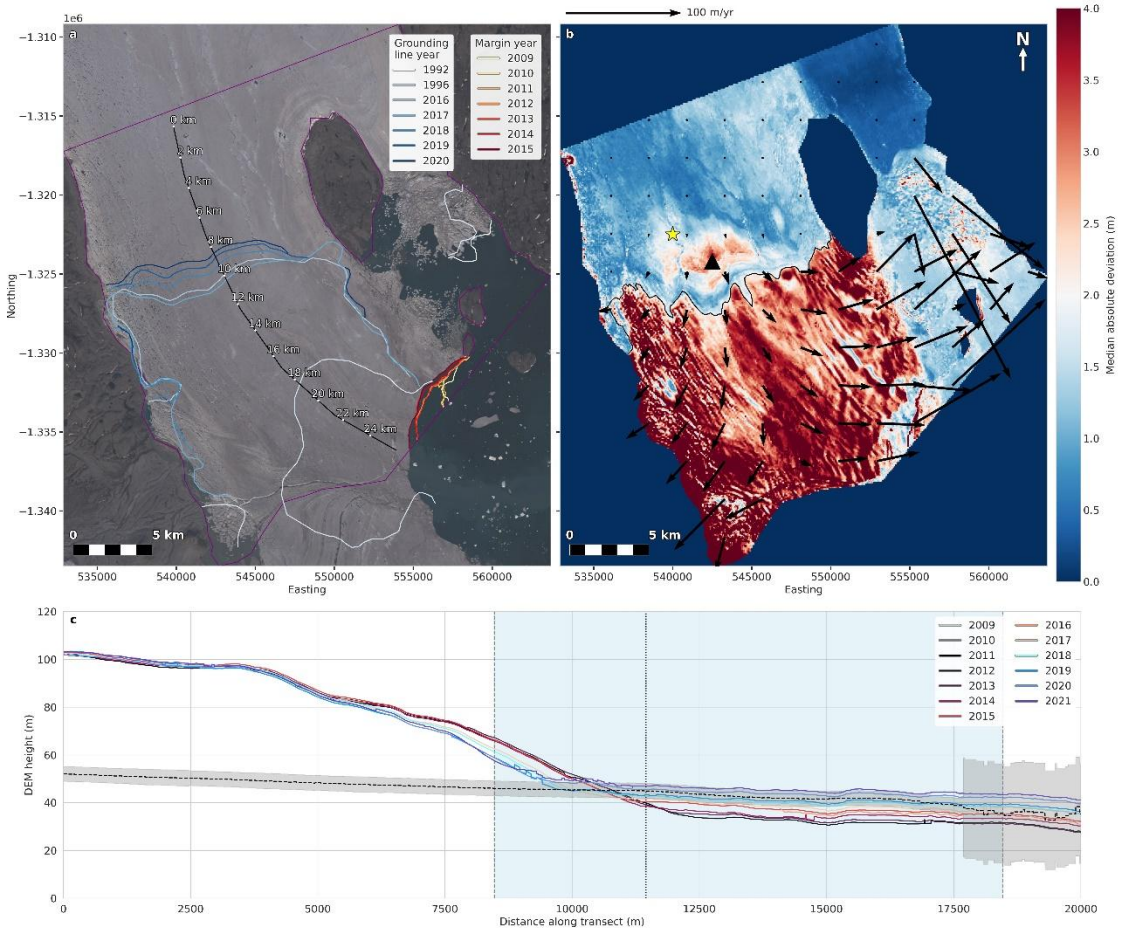


Figure 5.5: DEM variance and grounding line information for Storstrømmen. Panel a presents an overview of the study site (outlined in purple), including the calving front and grounding line locations detailed in Table 5.3, and the location of the longitudinal transect shown in panel c. The base map of this panel is a Landsat 8 natural colour composite from 6th August 2015. Panel b presents the median absolute deviation map produced by our method with our inland flotation limit delineated in black. The yellow star on panel b indicates a meltwater channel, and the black triangle indicates the area which exhibits a strong thinning signal. The black arrows on this panel indicate the ice velocity provided by the NASA MEaSUREs ITS_LIVE project (Gardner et al., 2025). Panel c shows the aligned stacked DEM elevations, averaged per year, along the transect shown in panel a, with the dashed black line indicating the height at flotation of the glacier calculated using Eq. 5.2 with grey shading indicating the uncertainty calculated using Eq. 5.3. The light blue vertical area bordered by dashed black lines indicates the range over which grounding lines have been located in previous studies. The dotted black vertical line on this panel indicates the location where our inland flotation limit, as shown in panel b, intersects the longitudinal transect.

#### 5.6.1.2 Steensby

Figure 5.6 shows the median absolute deviation and aligned DEM heights for Steensby Gletsjer. We observe a generally low median absolute deviation across the south of the glacier, which transitions to a pattern of high median absolute deviation in the north. At the approximate location of the Millan et al. (2023) grounding lines, we find a distinct transition from low to high deviation, thus supporting the inference that ice first transitions from grounded to floating at this location. Noting this feature – and the height above flotation as shown in Figure B.2.2b which independently indicates grounding at this location – we place our estimation of the inland flotation limit at this transition (Figure 5.6b). The signal becomes less clear to the west of the glacier which means that we only provide a portion of the inland flotation limit instead of an estimation across the full glacier width.

Figure 5.6b also shows ice flow speeds from the NASA MEaSUREs ITS_LIVE project (Gardner et al., 2025) which depict a relatively fast but stable pattern across the glacier with slightly faster flow in the central portions. This is presumably due to lateral drag from the fjord walls. Unlike Storstrømmen, there is no indication of speed up post-grounding line which could be due to the narrow nature of the fjord and its lateral drag stresses. The height at flotation shown in Figure 5.6c shows a gradual increase in uncertainty from ~6 km along the transect to ~9.5 km along the transect where it stabilises at approximately ±10 m. This uncertainty increases to approximately ±16 m where the bed elevation source data changes from mass conservation to interpolation (Figure B.3.2a).

Further downstream of our inland flotation limit location, we find a discontinuous band of lower median absolute deviation which we interpret as possibly indicating a region of light or ephemeral grounding caused by localised rises in the bed elevation which we indicate with a yellow star on Figure 5.6a and Figure B.2.2a. The alternating high-low deviation pattern across the width of the glacier upstream of the (Millan et al., 2023) grounding lines is likely the result of longitudinal crevassing or supraglacial hydrological features (see the black triangles in Figure 5.6b).

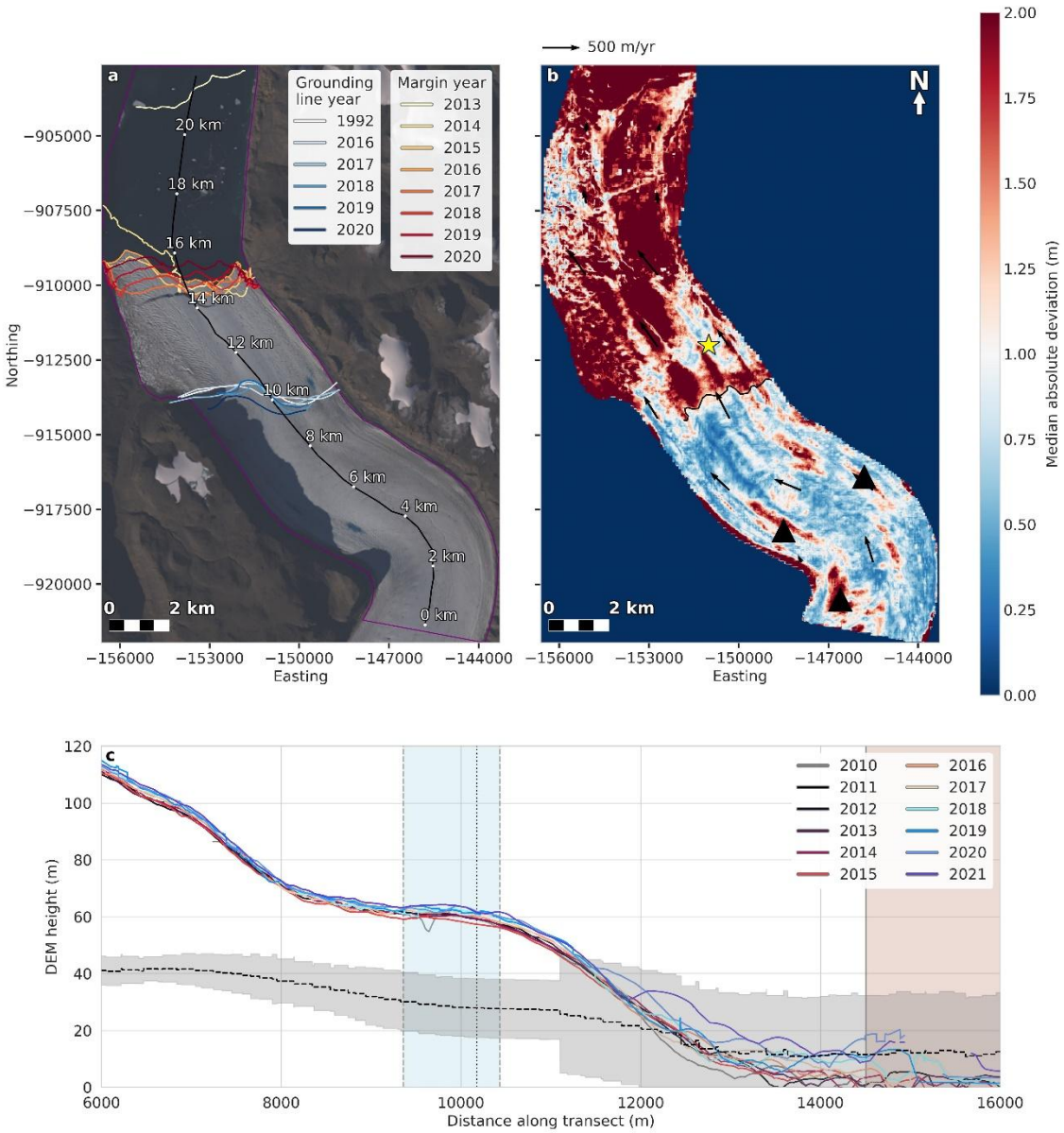


Figure 5.6: DEM variance and grounding line information for Steensby Gletsjer. Panel a presents an overview of the study site (outlined in purple), including the calving front and grounding line locations detailed in Table 5.3, and the location of the longitudinal transect shown in panel c. The base map of this panel is a Landsat 8 natural colour composite from 16th August 2016. Panel b presents the median absolute deviation map produced by our method with our inland flotation limit delineated in black. The yellow star on panel b indicates a region of light or ephemeral grounding, and the black triangles represent areas of longitudinal crevassing and/or supraglacial hydrological features. The black arrows on this panel indicate the ice velocity provided by the NASA MEaSUREs ITS_LIVE project (Gardner et al., 2025). Panel c shows the aligned stacked DEM elevations, averaged per year, along the transect shown in panel a, with the dashed black line indicating the height at flotation of the glacier calculated using Eq. 5.2 with grey shading indicating the uncertainty calculated using Eq. 5.3. The light blue vertical area bordered by dashed

black lines indicates the range over which grounding lines have been located in previous studies. Similarly, the solid black vertical line delineating the pink region represents the most inland location mapped for the glacier's calving front. The dotted black vertical line on this panel indicates the location where our inland flotation limit, as shown in panel b, intersects the longitudinal transect.

#### 5.6.1.3 Ryder

In Figure 5.7, we see a difference between the deviation signals up- and downstream of the grounding area. Our estimation of the inland flotation limit (Figure 5.7b), which we place at the inland limit of the region of high median absolute deviation present on the ice tongue, largely agrees with the grounding lines delineated by Millan et al. (2023) and we attribute the difference in the western portion of the inland flotation limit to be caused by a rise in the bedrock elevation which may cause the tongue to be ephemerally grounded (see Figure B.2.3a).

The SAR-based method used by Millan et al. (2023) derives grounding lines from pairs of SAR images, capturing grounding conditions at specific moments in time. As a result, it may indicate periods when this region was temporarily afloat. In contrast, our approach integrates DEMs over multiple years rather than relying on single-image pairs. This means that if the region is intermittently grounded by the bedrock rise, its transient grounding could reduce the deviation signal, making it less likely to be identified as floating. In Figure 5.7c, we see a ripple pattern indicative of the downstream migration of crevasses and ridges affecting the median absolute deviation.

Figure 5.7b also shows the ice velocity from the NASA MEaSUREs ITS_LIVE project (Gardner et al., 2025). The velocity is faster on the western side of the glacier than the east, tending towards faster flow in the centre seaward of the grounding lines. Although there is no significant speed up after the grounding line locations, the pattern across the glacier width shows that the lateral margins have slower speeds than the centre, indicating a potential restrictive drag from the fjord walls. Velocities are slower in the southeast of the glacier and correspond to a lower median absolute deviation from our method which likely results from the slower movement of surface features.

In Figure 5.7c, we observe a very small uncertainty over the majority of the grounding line-occupied area with a large increase at ~47 km along the transect. This is likely due to the change in bed elevation source from mass conservation to interpolation (Figure

B.3.3a). We note that the height at flotation abruptly decreases at this bed elevation source boundary. The height at flotation crosses the annual average DEM lines at almost the same location where we have located our inland flotation limit, lending credence to our method.

This glacier accommodates large hydrological surface features, namely supraglacial lakes (Otto et al., 2022), which again present as localised regions of high elevation variance in our median absolute deviation maps. The locations of two lakes, as observed in Sentinel-2 imagery from August 2019, are denoted by yellow stars in Figure 5.7b.

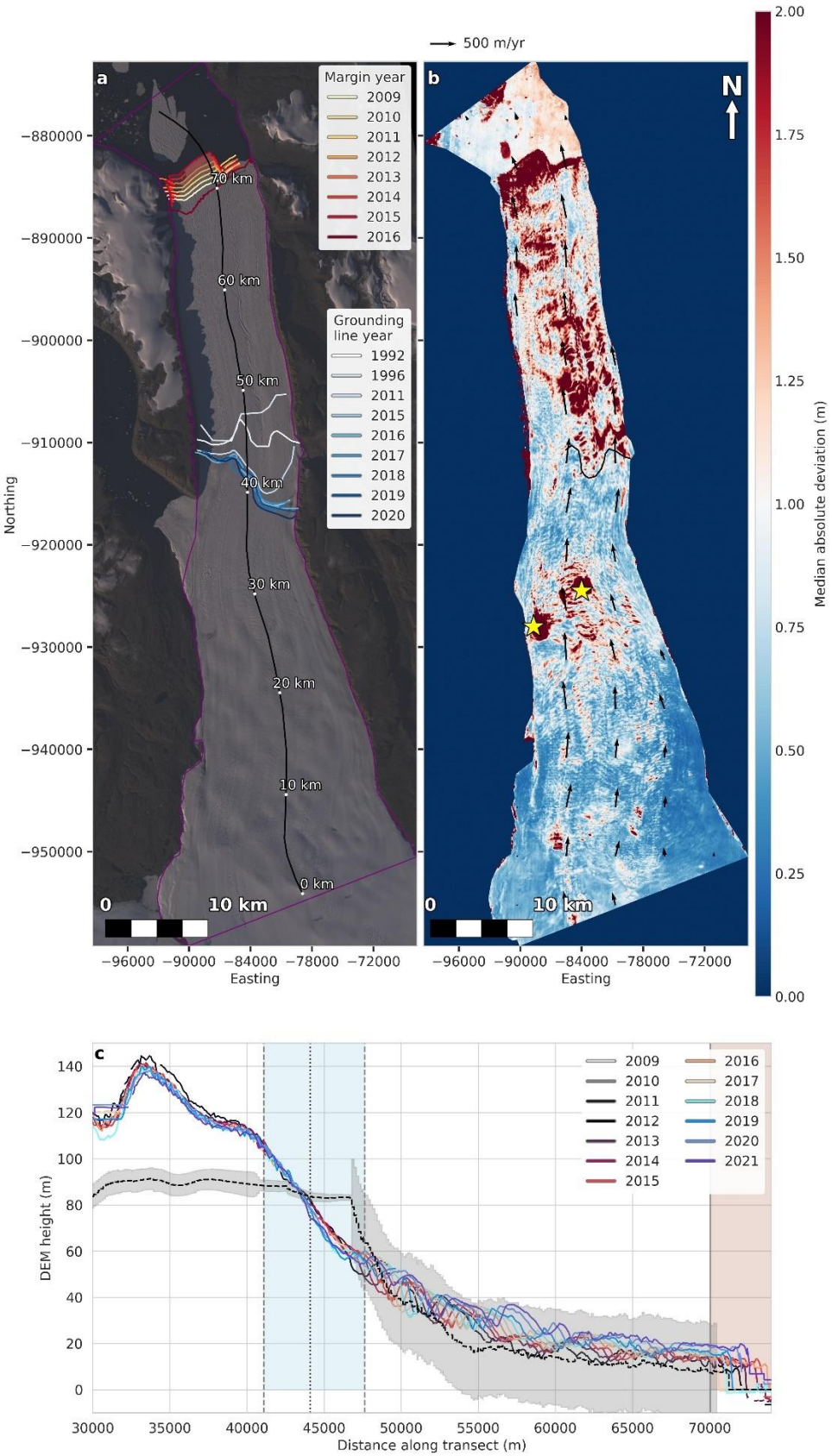


Figure 5.7: DEM variance and grounding line information for Ryder Gletsjer. Panel a presents an overview of the study site (outlined in purple), including the calving front and grounding line locations detailed in Table 5.3, and the location of the longitudinal transect shown in panel c. The

base map of this panel is a Landsat 8 natural colour composite from 28th August 2015. Panel b presents the median absolute deviation map produced by our method with our inland flotation limit delineated in black. The two yellow stars on panel b indicate supraglacial ponding. The black arrows on this panel indicate the ice velocity provided by the NASA MEaSUREs ITS_LIVE project (Gardner et al., 2025). Panel c shows the aligned stacked DEM elevations, averaged per year, along the transect shown in panel a, with the dashed black line indicating the height at flotation of the glacier calculated using Eq. 5.2 with grey shading indicating the uncertainty calculated using Eq. 5.3. The light blue vertical area bordered by dashed black lines indicates the range over which grounding lines have been located in previous studies. Similarly, the solid black vertical line delineating the pink region represents the most inland location mapped for the glacier's calving front. The dotted black vertical line on this panel indicates the location where our inland flotation limit, as shown in panel b, intersects the longitudinal transect.

#### 5.6.1.4 Nioghalvfjerdsbræ (79N)

The median absolute deviation signature of 79N is less distinct than other glaciers in this study, with a more gradual low-to-high pattern from the inland ice to the sea. This may be indicative of an extensive region of lightly grounded ice which mostly follows the pattern of the bed elevation – as indicated by the height above flotation in Figure B.2.4b – or it may represent a higher level of ablation relative to the upstream grounded area. Further inland we observe patches of high deviation corresponding to supraglacial hydrological features which we indicate with yellow stars in Figure 5.8b. We observe a distinct rectilinear polygon of low deviation in the south of the glacier which we attribute to the relatively high count of DEMs available in this region of the glacier (Figure B.2.4c).

Our estimation of the inland flotation limit concurs with both the Millan et al. (2023) and Climate Change Initiative (2023) grounding lines (Figure 5.8b, Table 5.3). Additionally, our calculations of height above flotation agree with the likelihood of ice flotation in this area. Although this glacier has a relatively high velocity, its surface is not very rough, meaning that, unlike other fast-flowing glaciers such as Petermann and Ryder, the movement of crevasses and ridges is not as apparent in the deviation signatures. The velocity of this glacier (from the NASA MEaSUREs ITS_LIVE project (Gardner et al., 2025)) is shown in Figure 5.8b as a scaled field of black arrows. There is a significant speed up pre-grounding lines that becomes faster post-grounding lines. The flow is faster in the centre than at the edges of the fjord which is likely due to lateral drag.

The height at flotation of this glacier, as shown in Figure 5.8c, has a very small uncertainty and crosses the annual average DEM lines closer to the most seaward grounding line than to our inland flotation limit line. The bed elevation source briefly swaps from mass conservation to interpolation before changing to gravity inversion (Figure B.3.4a). The uncertainty associated with the mass conservation and gravity inversion methods are relatively low, meaning that the interpolation uncertainty is also low as it is only interpolating over a small distance.

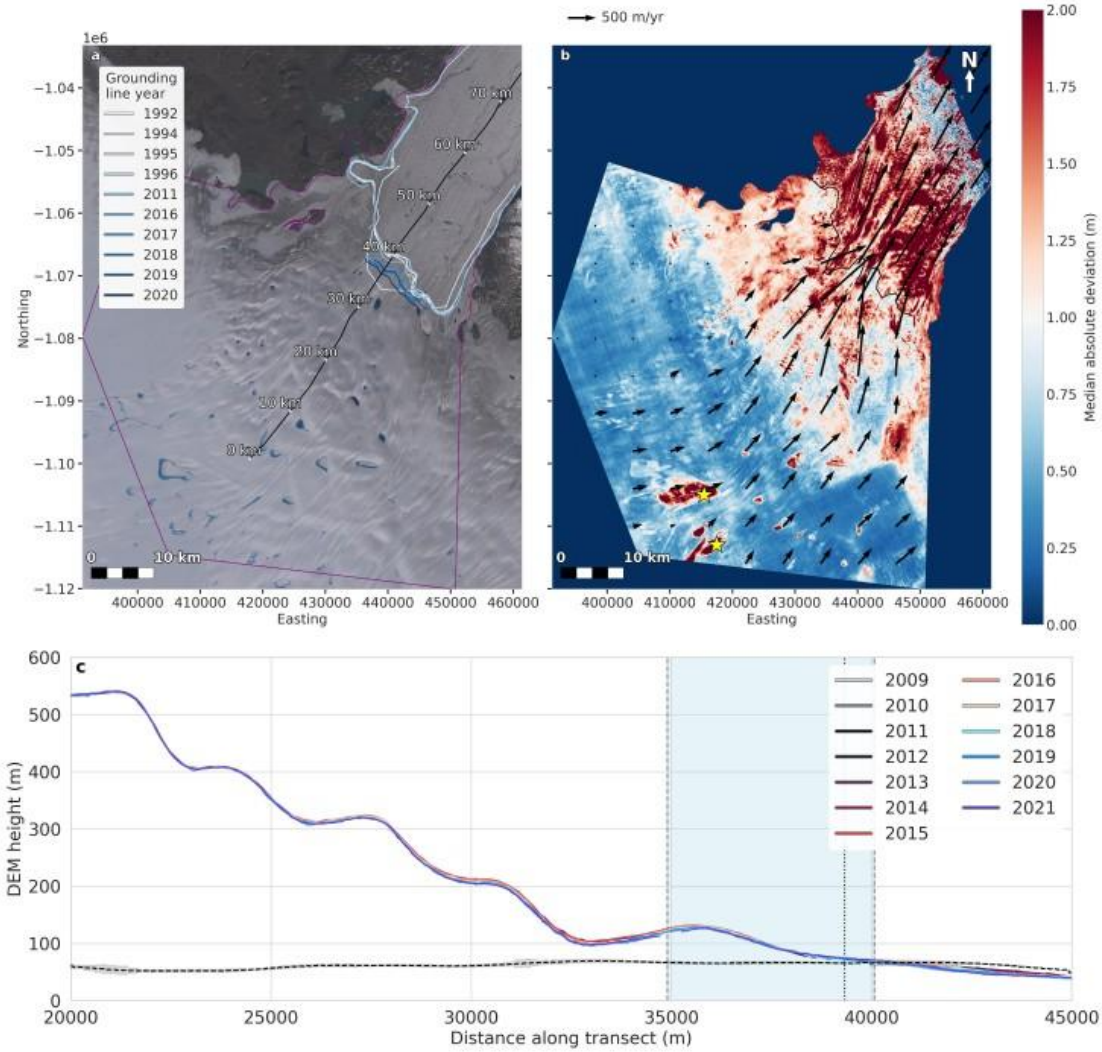


Figure 5.8: DEM variance and grounding line information for 79N. Panel a presents an overview of the study site (outlined in purple), including the grounding line locations detailed in Table 5.3, and the location of the longitudinal transect shown in panel c. The base map of this panel is a Landsat 8 natural colour composite from 7th August 2015. Panel b presents the median absolute deviation map produced by our method with our inland flotation limit delineated in black. The two yellow stars on panel b indicate supraglacial ponding. The black arrows on this panel indicate the ice velocity provided by the NASA MEaSUREs ITS_LIVE project (Gardner et al., 2025). Panel c shows the aligned stacked DEM elevations, averaged per year, along the transect shown in panel a, with the dashed black line indicating the height at flotation of the glacier calculated using Eq. 5.2 with grey shading indicating the uncertainty calculated using Eq. 5.3. The light blue vertical area bordered by dashed black lines indicates the range over which grounding lines have been located in previous studies. The dotted black vertical line on this panel indicates the location where our inland flotation limit, as shown in panel b, intersects the longitudinal transect.

#### 5.6.1.5 L. Bistrup Bræ

The deviation pattern of L. Bistrup Bræ is more complicated than that of its northern neighbour, Storstrømmen (Figure 5.9b). L. Bistrup Bræ appears to have an inverted pattern in the median absolute deviation signal at its inland flotation limit as compared to the other floating glaciers, with high deviation on a portion of the grounded ice and lower deviations on the floating ice. We suggest this is due to a strong thinning signal in the lower regions of the glacier, as seen between 13,000 m and 21,500 m along the transect in Figure 5.9c. The thinning of the floating tongue is less evident in the surface elevations because of the buoyant nature of ice.

Thinning signals on floating and grounded ice present differently, with floating ice rising to balance the thinning signal, whereas grounded ice is unable to do this as it is stuck to the bedrock. This results in a higher elevation deviation in the thinning portion of the grounded ice compared to the floating section. The height above flotation map in Figure B.2.5b independently implies the floating nature of the downstream region of ice. Similarly, the height at flotation data shown in Figure 5.9c imply that the glacier could be in flotation past our inland flotation limit. However, the annual average DEM heights and the height at flotation are very close in elevation from ~22 km along the transect, so the glacier may be lightly grounded further seaward of this transect distance.

The height at flotation uncertainty is relatively small and stable up to ~23.5 km along the transect where it suddenly increases and then similarly decreases at ~25 km along the transect. This is likely due to the bed elevation sources changing from kriging briefly into the less certain method of interpolation, and then into bathymetry data which has a very low uncertainty (Figure B.3.5a).

The velocity profile of this glacier, as shown in Figure 5.9b is slow compared to our other glaciers and slows to almost 0 m/yr towards the inland flotation limit. The velocity then abruptly increases after the inland flotation limit which corresponds to the expected velocity behaviour of floating ice under the removal of basal drag.

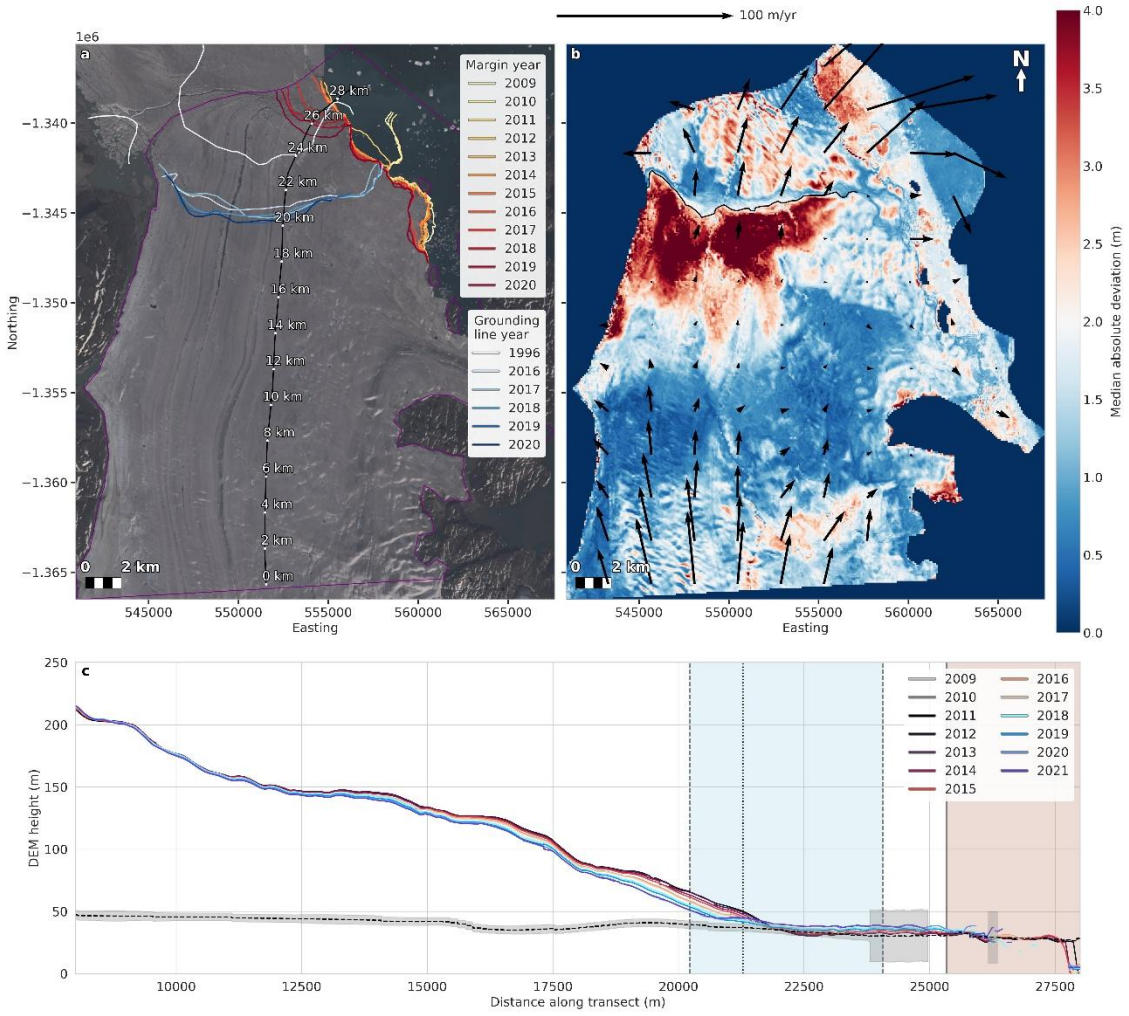


Figure 5.9: DEM variance and grounding line information for L. Bistrup Bræ. Panel a presents an overview of the study site (outlined in purple), including the calving front and grounding line locations detailed in Table 5.3, and the location of the longitudinal transect shown in panel c. The base map of this panel is a Landsat 8 natural colour composite from 6th August 2015. Panel b presents the median absolute deviation map produced by our method with our inland flotation limit delineated in black. The black arrows on this panel indicate the ice velocity provided by the NASA MEaSUREs ITS_LIVE project (Gardner et al., 2025). Panel c shows the aligned stacked DEM elevations, averaged per year, along the transect shown in panel a, with the dashed black line indicating the height at flotation of the glacier calculated using Eq. 5.2 with grey shading indicating the uncertainty calculated using Eq. 5.3. The light blue vertical area bordered by dashed black lines indicates the range over which grounding lines have been located in previous studies. Similarly, the solid black vertical line delineating the pink region represents the most inland location mapped for the glacier's calving front. The dotted black vertical line on this panel indicates the location where our inland flotation limit, as shown in panel b, intersects the longitudinal transect.

### 5.6.2 Glaciers with possible flotation signatures

#### 5.6.2.1 Brikkerne

Unlike lobes 2 and 3, lobe 1 has a historical grounding line from 1996 (Rignot et al., 2001) and our data suggests that this lobe may still support a ~1 km long floating portion, ~20 years later. Additionally, this lobe is the fastest of the three, meaning that most of the ice mass from the glacier will travel through this terminus (Figure 5.10b). The use of auxiliary data to calculate height above flotation (Figure B.2.6b) allows us to independently confirm the likely floating nature of this region. In Figure 5.10c, we show the height at flotation and its uncertainty and see that the increase in uncertainty corresponds with the change in bed elevation source data from mass conservation to interpolation (Figure B.3.6a).

Also in Figure 5.10c, we see that the later years appear at higher elevations than the earlier years, which is indicative that the median absolute deviation signal is likely one that is caused by floating ice, rather than longer-term thinning. However, the signal is obscured by the short length of the suspected floating portion. As such, we delineate an area of higher deviation inland of the calving fronts which partially agrees with the 1996 grounding line and update this inland flotation limit to reflect the 2010s changes in the location of the calving front.

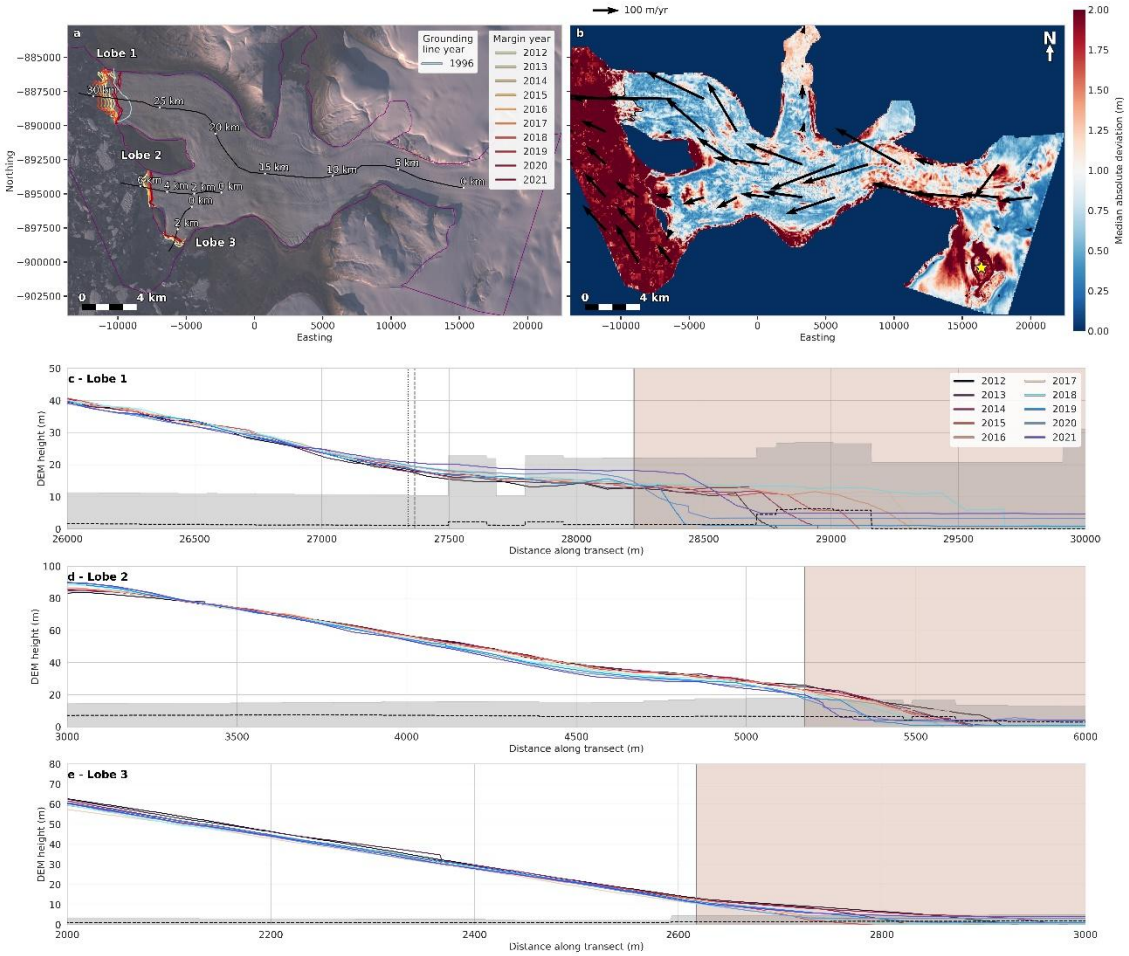


Figure 5.10: DEM variance and grounding line information for Brikkerne Gletsjer. Panel a presents an overview of the study site (outlined in purple), including the calving front and grounding line locations detailed in Table 5.3, and the location of the longitudinal transects shown in panels c, d, and e. The base map of this panel is a Landsat 8 natural colour composite from 14th September 2016. Panel b presents the median absolute deviation map produced by our method with our inland flotation limit delineated in black. The yellow star on panel b indicates the location of a subglacial lake drainage event which occurred in summer 2014 (Bowling et al., 2021). The black arrows on this panel indicate the ice velocity provided by the NASA MEaSUREs ITS_LIVE project (Gardner et al., 2025). Panels c, d, and e represent lobes 1, 2, and 3, respectively, and each shows the aligned stacked DEM elevations for their respective lobe, averaged per year, along the transects shown in panel a, with the dashed black line indicating the height at flotation of the glacier calculated using Eq. 5.2 with grey shading indicating the uncertainty calculated using Eq. 5.3. The solid black vertical line delineating the pink region represents the most inland location mapped for the lobe's calving front. On panel c, the dashed black vertical line indicates the location of the grounding line that was located by Rignot et al. (2001). Similarly, the dotted black vertical line on this panel indicates the location where our inland flotation limit, as shown in panel b, intersects the longitudinal transect.

#### 5.6.2.2 Flade Isblink

Flade Isblink exhibits an extremely variable pattern of elevation deviation across its entire surface with patches of high deviation located both at higher elevations and at locations close to previously reported grounding lines (Möller et al., 2022). In agreement with Möller et al. (2022) and Kappelsberger et al. (2021), we believe that the northern basin (lobe 1) has high deviations along the region of grounding line retreat due to the surface lowering induced by this retreat. This can be seen by the progressive thinning and the inland migration of the steep slope feeding into the ice shelf, which is apparent in Figure 5.11c. The high deviation patch surrounded by the area of low deviation in the upper part of the northern basin concurs with a similar pattern of surface elevation increase observed by Kappelsberger et al. (2021). This pattern can be explained by thickening in the accumulation area of the ice cap resulting from ongoing dynamic recovery from previous surge-related ice mass losses (Möller et al., 2022).

The southern basin (lobe 2) shows an across-glacier pattern in its marine-terminating area with high deviations in the north and low deviations in the south. The northern area of high deviation is situated in the lowest part of the ablation zone and is prone to more intense surface melting (Möller et al., 2022). This leads to surface lowering and the observed high deviations, as can be seen in Figure 5.11b and Figure B.2.7d. The southern area of low deviation is situated in the main ice flow which allows for more rapid delivery of new ice mass, partly compensating for the mass loss by surface melting and leading to less elevation change than the northern area of this lobe (Möller et al., 2022). The area of high deviation surrounded by the area of low deviation in the upper part of this basin is explained in the same way as for the northern basin and was also observed by Kappelsberger et al. (2021).

The velocity field shows that the fastest area of ice flow on Flade Isblink is lobe 2, with lobe 1 only showing movement in its upper reaches (from the ice dome out to the terminus). Lobe 1 does not exhibit much velocity change post-historical grounding lines, but it does show a slight across-glacier pattern where the south is slower than the rest of the lobe. This is likely caused by lateral drag from the exposed bedrock area. Lobe 1 exhibits very low velocities both pre- and post-historical grounding lines.

There are patches of high deviation on the floating ice. From the bed topography (Figure B.2.7a), we determine that these are bedrock highs which reflect pinning points on the ice

shelf, where the ice may become temporarily grounded and thus experience greater rates of elevation change relative to the surrounding ice that is floating in hydrostatic equilibrium. When thinned, the surface of the floating ice would not appear to have lowered as much as areas of the ice that were temporarily grounded because the surface would float up to balance out the elevation change. This means that the areas which were temporarily grounded by the pinning points would exhibit higher deviations in their elevation because the thinning signal would not be balanced by the floating ice.

In Figure 5.11c, we see that the height at flotation of lobe 1 suggests that the glacier should be floating at ~17 km along the transect. This briefly re-grounds ~20–21.5 km along the transect whereafter it recommences flotation. The height at flotation of lobe 2 also shows variation from our inland flotation limit location. From ~17 km along the transect, the height at flotation is higher than the annual average DEM elevations, suggesting that the glacier may be in flotation. This corresponds to the high deviation patch seen in our method's median absolute deviation (Figure 5.11b) and highlights our method's subjectivity in the final placement of the inland flotation limit. The uncertainty of the height at flotation (Figure 5.11c) is comparably large and stable for both lobes across the lengths of their transects which is likely because the bed elevation data source does not change (Figure B.3.7a).

Although this glacier presents possible flotation signatures, the data does not allow for a clear understanding of the glacier's floating status, and we place our inland flotation limit as a guiding line as opposed to a definitive estimate.

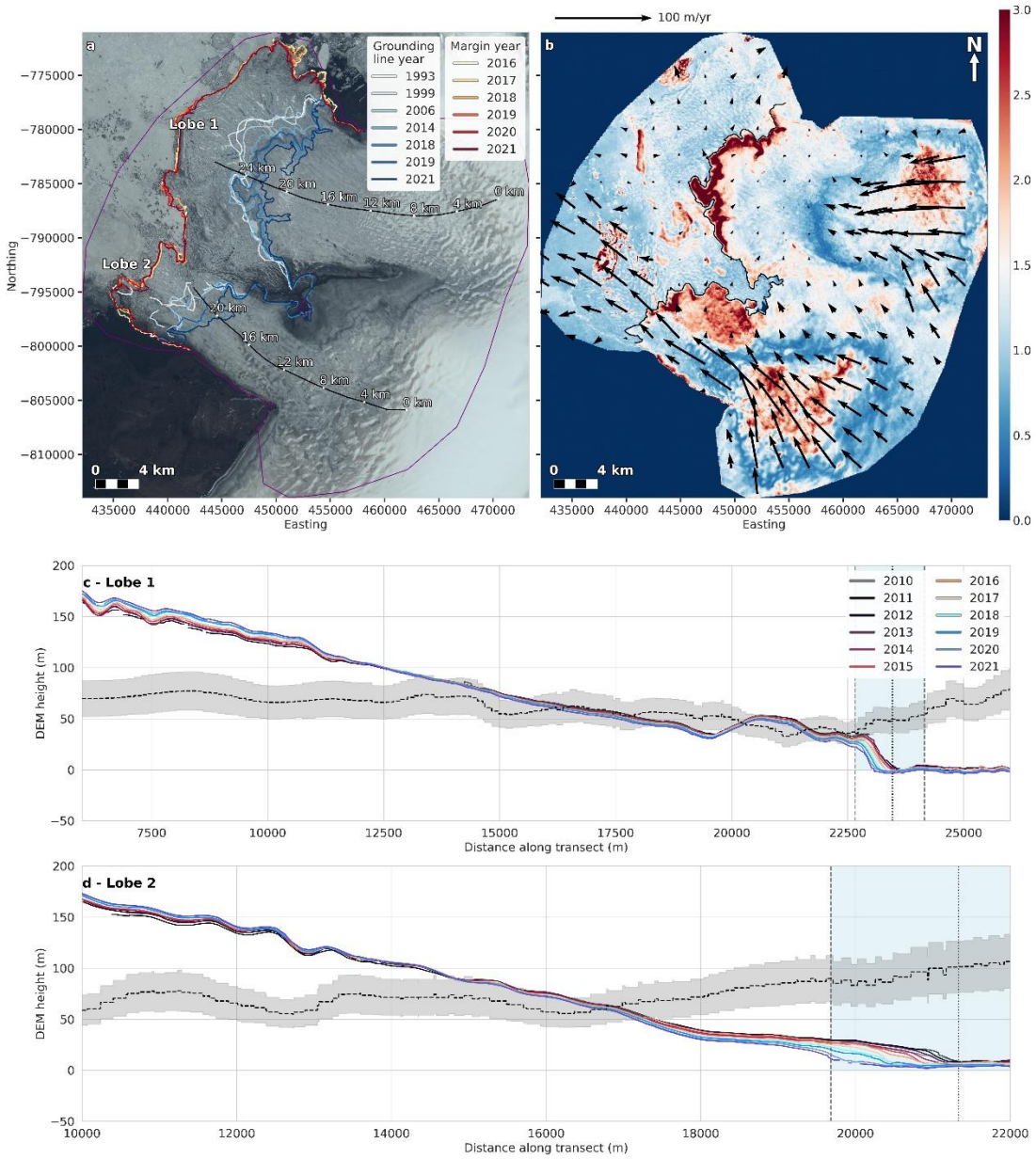


Figure 5.11: DEM variance and grounding line information for Flade Isblink. Panel a presents an overview of the study site (outlined in purple), including the calving front and grounding line locations detailed in Table 5.3, and the location of the longitudinal transects shown in panels c and d. The base map of this panel is a Landsat 8 natural colour composite from 2nd August 2016. Panel b presents the median absolute deviation map produced by our method with our inland flotation limit delineated in black. The black arrows on this panel indicate the ice velocity provided by the NASA MEaSUREs ITS_LIVE project (Gardner et al., 2025). Panel c and d represent lobes 1 and 2, respectively, and each shows the aligned stacked DEM elevations for their respective lobe, averaged per year, along the transect shown in panel a, with the dashed black line indicating the height at flotation of the glacier calculated using Eq. 5.2 with grey shading indicating the uncertainty calculated using Eq. 5.3. The light blue vertical area bordered by dashed black lines indicates the range over which grounding lines have been located in previous studies.

The dotted black vertical line on each panel indicates the location where our inland flotation limit, as shown in panel b, intersects the lobe's longitudinal transect.

### 5.6.3 Glaciers with no detectable flotation signatures (ice not floating)

#### 5.6.3.1 Newman Bugt

From Figure 5.12, we see no evidence of a floating tongue and therefore conclude that Newman Bugt is completely grounded at its terminus. This is consistent with the absence of any mention in the recent literature of a floating section of Newman Bugt (reflected in the lack of historical grounding lines in Figure 5.12a). The median absolute deviation of Newman Bugt is relatively stable along the transect until the margin where we see a peak in deviation caused by calving events (Figure 5.12b.1). Although patches of higher deviation do exist before Newman Bugt's margin, we attribute these to the slight x and y misalignment of the DEMs over a longitudinal ridge marked by a yellow star in Figure 5.12a.1. Newman Bugt's velocity is low and stable along the length of the glacier with slightly smaller velocities towards the lateral margins – this is likely caused by lateral drag.

The height above flotation map in Figure B.2.8b independently confirms that this glacier is unlikely to support a floating extension. Additionally, the height at flotation (Figure 5.12c) does not show elevation large than the annual average DEM elevations until distances along the transect which are seaward of the calving front. The uncertainty of the height at flotation is relatively low pre-calving front and its bed elevation source data is calculated using interpolation (Figure B.3.8a).

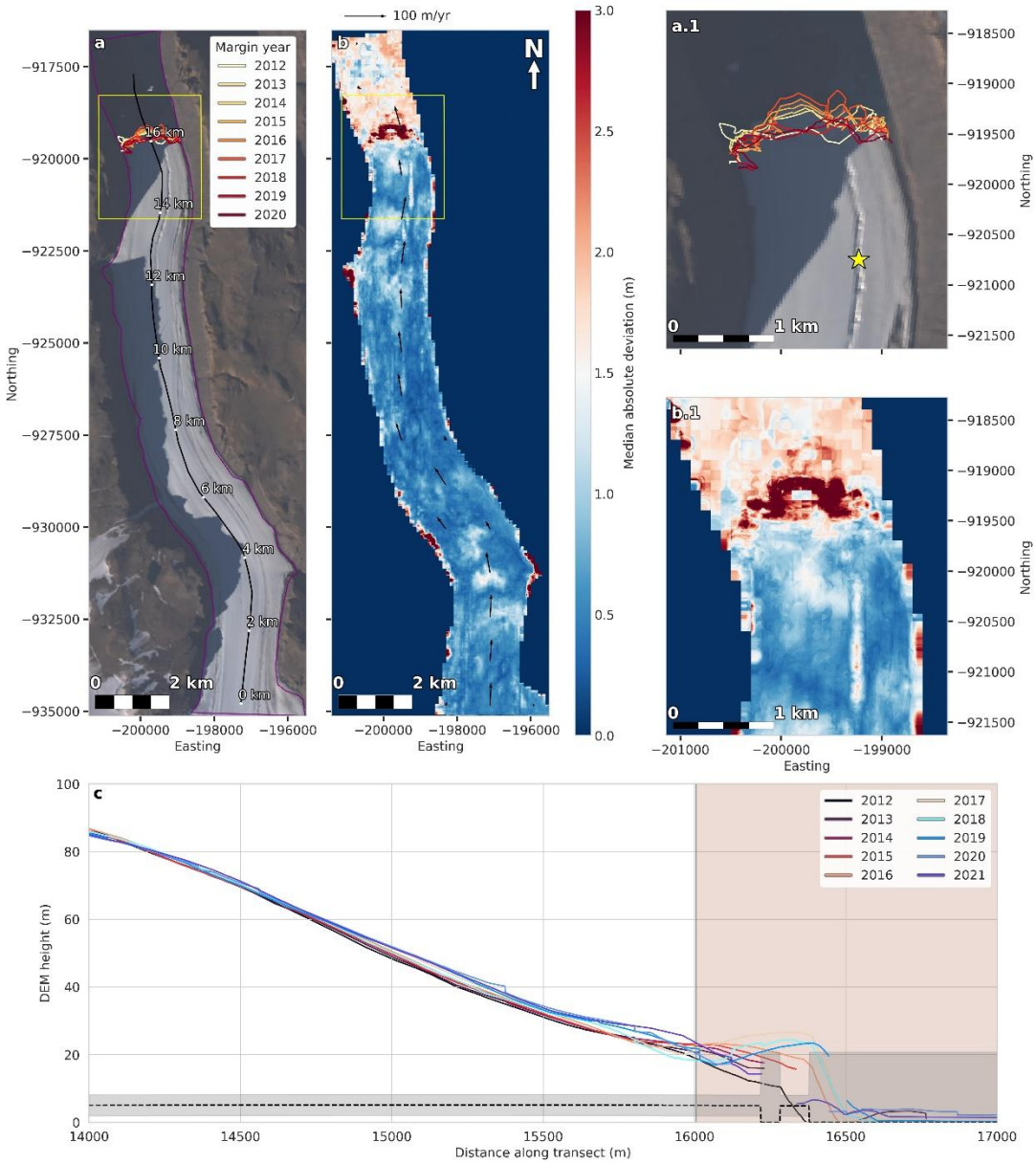


Figure 5.12: DEM variance for Newman Bugt. Panel a presents an overview of the study site (outlined in purple), including the calving front locations detailed in Table 5.3, and the location of the longitudinal transect shown in panel c. The yellow box in this panel outlines the focus of panel a.1, where a yellow star indicates a longitudinal ridge. The base map of panels a and a.1 is a Landsat 8 natural colour composite from 16th August 2016. Panel b presents the median absolute deviation map produced by our method. The yellow box on this panel outlines the focus of panel b.1. The black arrows on panel b indicate the ice velocity provided by the NASA MEaSUREs ITS_LIVE project (Gardner et al., 2025). Panel c shows the aligned stacked DEM elevations, averaged per year, along the transect shown in panel a, with the dashed black line indicating the height at flotation of the glacier calculated using Eq. 5.2 with grey shading indicating the uncertainty calculated using Eq. 5.3. The solid black vertical line delineating the pink region represents the most inland location mapped for the glacier's calving front.

#### 5.6.3.2 C. H. Ostenfeld

From Figure 5.13, we see that the only grounding lines for C. H. Ostenfeld are from 1992 and 1996 (Rignot et al., 2001). These grounding lines are now seaward of the current glacier terminus across much of the ice front, indicating that the calving front has now retreated beyond these historical grounding line positions. From the deviation patterns exhibited by C. H. Ostenfeld, there is no conclusive evidence to suggest that any part of it is floating. Figure 5.13c exhibits a reversed pattern to glaciers which we know to have floating portions where the later years (e.g. 2018, 2019, 2020) show lower elevations than the earlier years at approximately 20,000 m along the transect, implying a thinning trend.

The height at flotation of this glacier (Figure 5.13c) shows a low level of uncertainty until seaward of the calving front where the bed elevation data source swaps from mass conservation to interpolation (Figure B.3.9a). The surface velocity of this glacier is fast and gets faster towards the calving front. Similar to some of our other glaciers, the lateral margins of this glacier exhibit slower velocities, likely due to lateral drag.

Comparing the BedMachine version 5 bed elevation and the ArcticDEM version 4 mosaic, we see that only a small portion of C. H. Ostenfeld can be in hydrostatic equilibrium (Figure B.2.9b), supporting our conclusion that there is no significant floating tongue. However, this low-lying region is only just above sea level and, combined with the thinning signal upstream, this section might be expected to unground imminently. We see potential evidence to support this theory in the bedrock trough visible in Figure B.2.9a which indicates potential for significant retreat in the future.

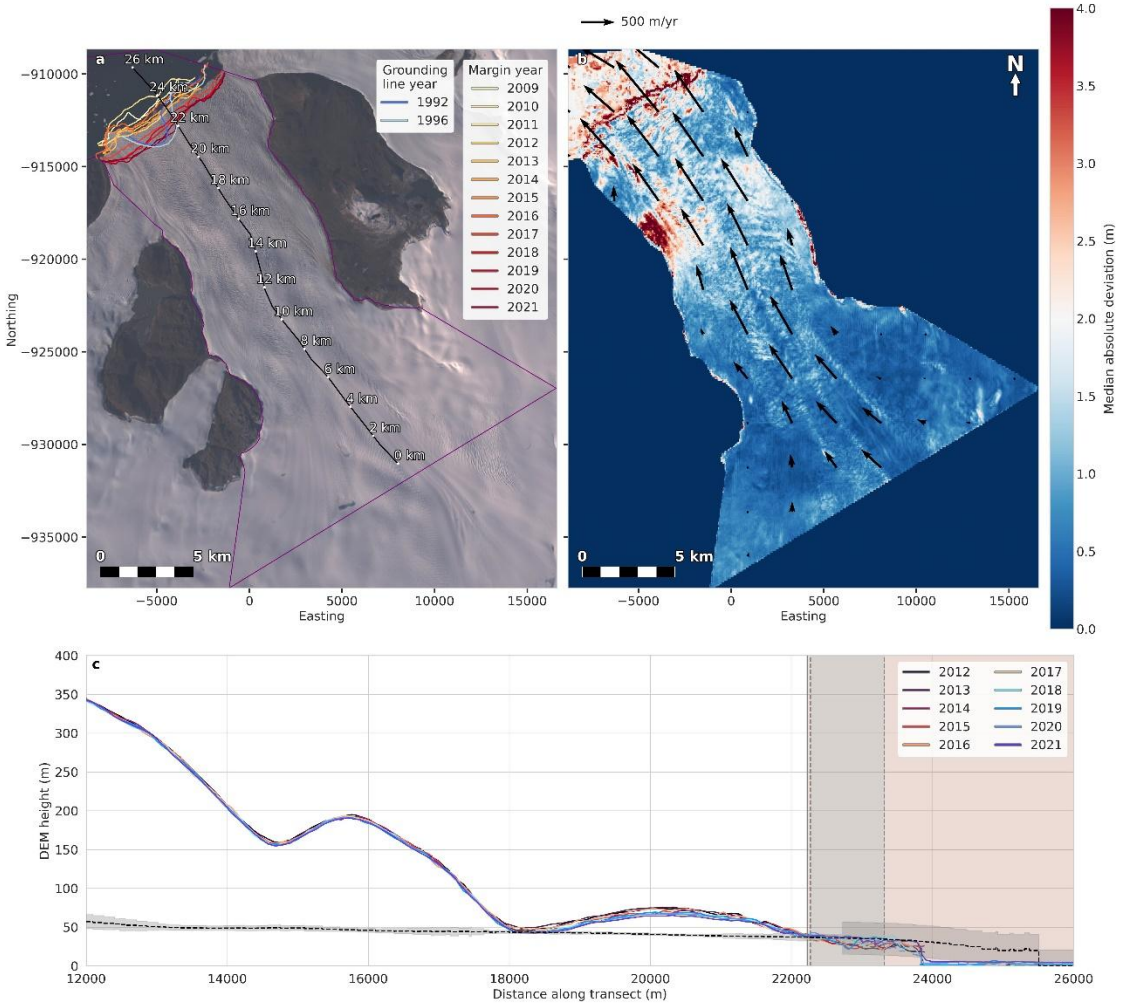


Figure 5.13: DEM variance and grounding line information for C. H. Ostenfeld Gletsjer. Panel a presents an overview of the study site (outlined in purple), including the calving front and grounding line locations detailed in Table 5.3, and the location of the longitudinal transect shown in panel c. The base map of this panel is a Landsat 8 natural colour composite from 28th August 2015. Panel b presents the median absolute deviation map produced by our method. The black arrows on this panel indicate the ice velocity provided by the NASA MEaSUREs ITS_LIVE project (Gardner et al., 2025). Panel c shows the aligned stacked DEM elevations, averaged per year, along the transect shown in panel a, with the dashed black line indicating the height at flotation of the glacier calculated using Eq. 5.2 with grey shading indicating the uncertainty calculated using Eq. 5.3. The darker vertical area bordered by dashed black lines within the pink area indicates the range over which grounding lines have been located in previous studies. Similarly, the solid black vertical line delineating the pink region represents the most inland location mapped for the glacier's calving front.

#### 5.6.3.3 Harder

The only grounding line in the literature for Harder is from 1996 (Rignot et al., 2001). As was the case for C. H. Ostenfeld, we again see that this grounding line is entirely seaward of the current glacier terminus position (Figure 5.14a). Therefore, this grounding line can no longer represent the point at which the glacier ice begins to float. Close inspection of Figure 5.14c suggests that there may be a thinning signal towards the glacier terminus akin to that observed on C. H. Ostenfeld. This area of high deviation is closely correlated with a bedrock trench visible in bed elevation data (Figure B.2.10a), but from its height above flotation (Figure B.2.10b), we can confirm that Harder is unlikely to support a floating tongue.

The velocity of this glacier is smaller than that of its southerly neighbour, C. H. Ostenfeld, but its velocity increases towards the terminus (Figure 5.14b). Similar to other fjord-constrained glaciers, the lateral margins of this glacier show smaller velocities due to the effects of drag. The height at flotation in Figure 5.14c shows a small uncertainty until after the calving front and the height at flotation is not at a higher elevation than the annual average DEM elevations until after the calving front, lending credence to its status as non-floating. The bed elevation for this glacier is calculated using the mass conservation approach (Figure B.3.10a). Additionally, our method has located a previously unknown subglacial lake. We indicate this with a yellow star in Figure 5.14b.

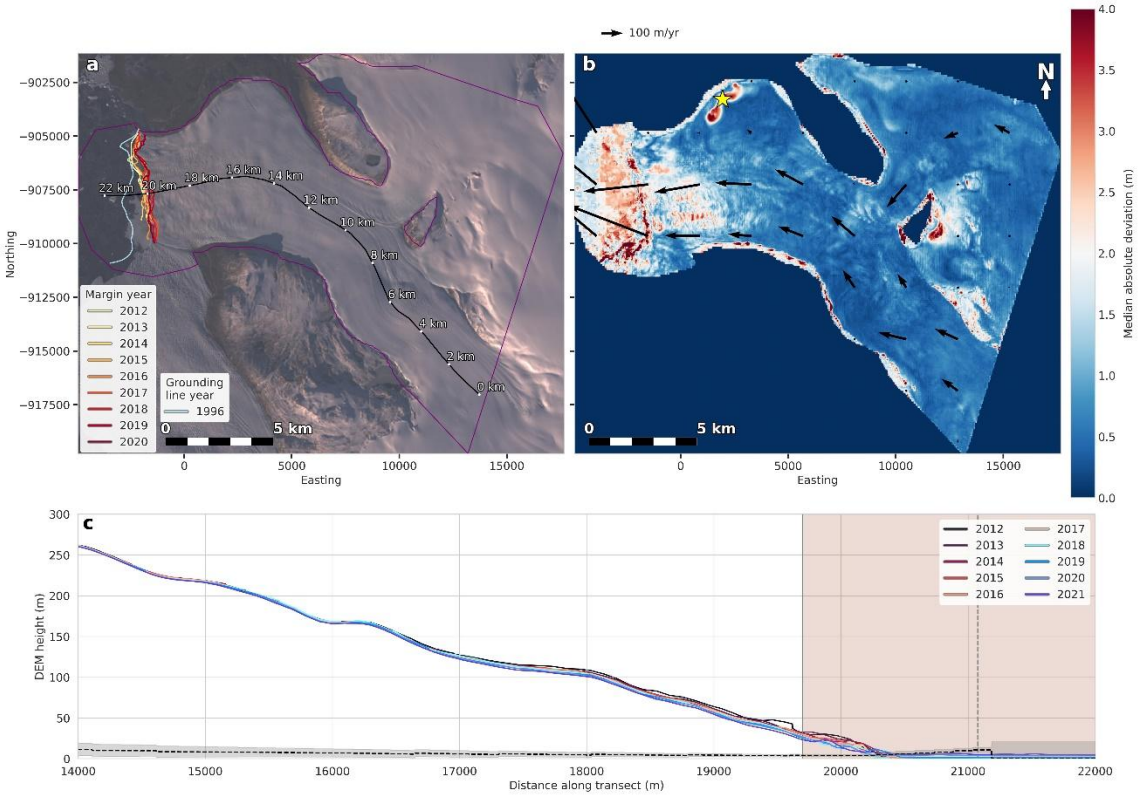


Figure 5.14: DEM variance and grounding line information for Harder Gletsjer. Panel a presents an overview of the study site (outlined in purple), including the calving front and grounding line locations detailed in Table 5.3, and the location of the longitudinal transect shown in panel c. The base map of this panel is a Landsat 8 natural colour composite from 14th September 2016. Panel b presents the median absolute deviation map produced by our method. The yellow star on panel b indicates a previously unknown subglacial lake. The black arrows on this panel indicate the ice velocity provided by the NASA MEaSUREs ITS_LIVE project (Gardner et al., 2025). Panel c shows the aligned stacked DEM elevations, averaged per year, along the transect shown in panel a, with the dashed black line indicating the height at flotation of the glacier calculated using Eq. 5.2 with grey shading indicating the uncertainty calculated using Eq. 5.3. The dashed black vertical line indicates the grounding line delineated by Rignot et al. (2001). The solid black vertical line delineating the pink region represents the most inland location mapped for the glacier's calving front.

#### 5.6.3.4 Brikkerne

Brikkerne has three marine-terminating lobes which we refer to as lobes 1, 2 and 3, respectively, from north to south. Neither lobe 2 nor lobe 3 of Brikkerne support a floating portion – which is supported by their lack of historical grounding lines within the literature – but it is important to note that lobe 2 has a similar thinning signature to that observed at both Harder and C. H. Ostenfeld. The deviation pattern of lobe 2 matches a trough in the bed topography but from the height above flotation calculations (Figure B.2.6b), it is very unlikely that this lobe could support a floating portion. We discuss lobe 1 in Sect. 5.6.2.1.

Although the velocity of lobe 1 is relatively fast, the velocities of lobe 2 and 3 are comparatively slower, meaning that these lobes have a smaller ice mass delivery. The heights at flotation in panels *d* and *e* of Figure 5.10 show a larger uncertainty on lobe 2 than lobe 3 and agree with our findings that neither lobe support a floating portion.

Additionally, our method has identified the signature of a large subglacial lake drainage event that occurred in summer 2014 (Bowling et al., 2021). This associated surface collapse basin is marked with a yellow star in Figure 5.10b.

#### 5.6.3.5 Jungersen

The median absolute deviation map of Jungersen (Figure 5.15b) shows an area of high elevation variance close to (within ~2 km) the glacier's calving front. However, it is clear from the surface and bed elevation profiles that the ice is too thick to be approaching flotation in this region (Figure B.2.11a). Rather, akin to Harder Gletsjer, the DEMs from earlier years show higher elevations than those acquired in later years, suggesting that the median absolute deviation signal reflects an enhanced long-term thinning trend near the glacier margin, relative to the polygon further inland that was used to align the DEMs. Therefore, we conclude that Jungersen does not currently support a floating ice tongue and is likely exhibiting a strong thinning signature instead.

This corresponds with the findings from the height at flotation calculation (Figure 5.15c) which does not show higher elevation than the annual average DEM elevations at any point along the transect. The height at flotation shows a very low uncertainty and is calculated using kriging down the centreline of the glacier. Interpolation is used to calculate the bed elevation at the glacier's lateral margins. Additionally, this glacier shows a velocity field (from the NASA MEaSUREs ITS_LIVE project (Gardner et al., 2025))

which is fast in the middle reaches of the glacier and slower in both the upper and lower reaches (Figure 5.15b).

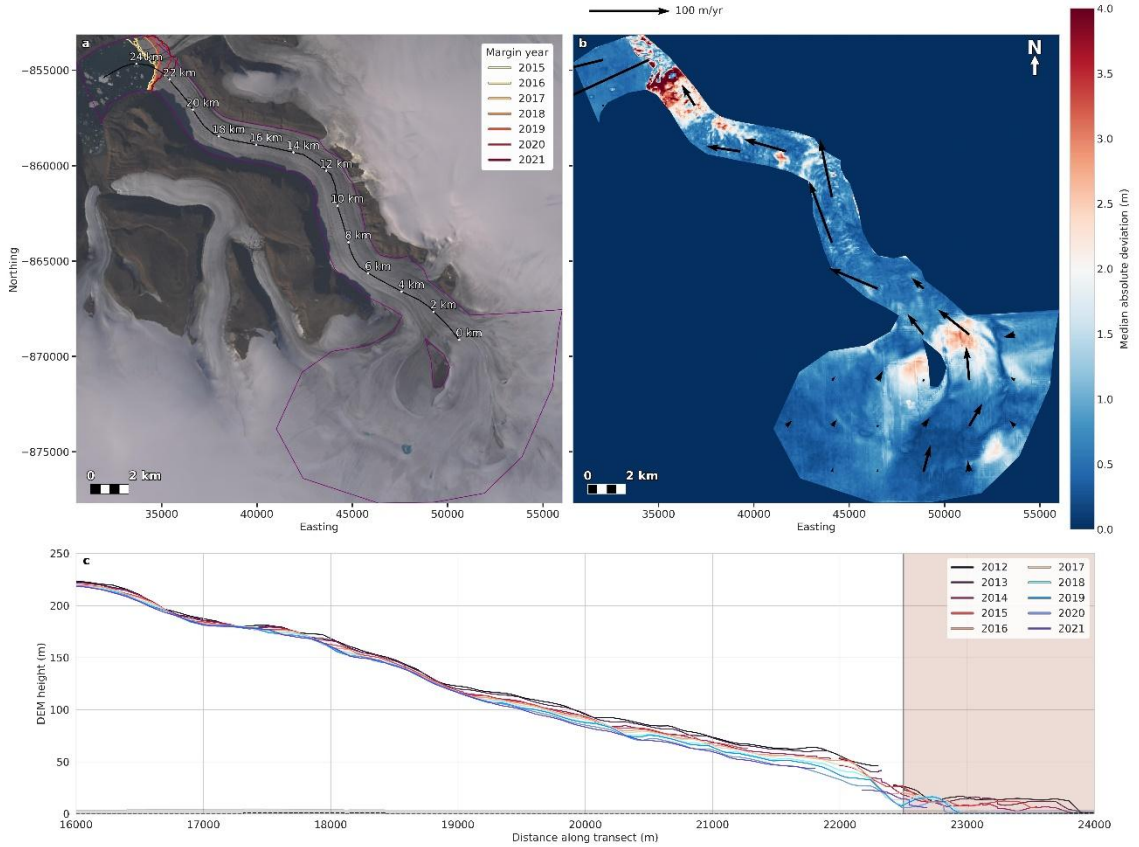


Figure 5.15: DEM variance for Jungersen Gletsjer. Panel a presents an overview of the study site (outlined in purple), including the calving front locations detailed in Table 5.3, and the location of the longitudinal transect shown in panel c. The base map of this panel is a Landsat 8 natural colour composite from 31st July 2016. Panel b presents the median absolute deviation map produced by our method. The black arrows on this panel indicate the ice velocity provided by the NASA MEaSUREs ITS_LIVE project (Gardner et al., 2025). Panel c shows the aligned stacked DEM elevations, averaged per year, along the transect shown in panel a, with the dashed black line indicating the height at flotation of the glacier calculated using Eq. 5.2 with grey shading indicating the uncertainty calculated using Eq. 5.3. The solid black vertical line delineating the pink region represents the most inland location mapped for the glacier's calving front.

#### 5.6.3.6 Henson

In Figure 5.16b, we see that Henson exhibits an undulating pattern in the median absolute deviation in elevation across the fjord-constrained area of the glacier. Near to the glacier terminus, the increased deviation is caused by a series of calving events, some of which notably removed ~4 $km^2$ of glacier ice between 2017 and 2018. Upstream of the calving front, there is no clear deviation pattern to suggest the presence of a floating portion or uniform thinning/thickening signal across the glacier. Additionally, the longitudinal surface gradient of Henson is relatively steep, meaning that, in combination with the bed topography, there is minimal scope for the ice to be in a state of flotation (Figure B.2.12c). The bed elevation is calculated from kriging down the central portion of the glacier, with interpolation nearer the lateral margins of the glacier and after the calving front (Figure B.3.12a). The height at flotation calculated using this bed elevation data (Figure 5.16c) never has a higher elevation than the annual average DEM elevations and it has a low uncertainty due to the kriging nature of its bed source data. Together, these data provide high certainty that Henson Gletsjer has been completely grounded for the past decade and is currently unable to support a floating tongue, even though it may have done so in the past (Rignot et al., 2001).

The velocity field of this glacier shows a glacier-length and -width pattern whereby the lower reaches of the glacier are faster compared to the upper, and the lateral margins of the glacier are slower than the central flow portions (Figure 5.16b). The difference across the glacier's width is likely due to the restrictive effect of lateral drag.

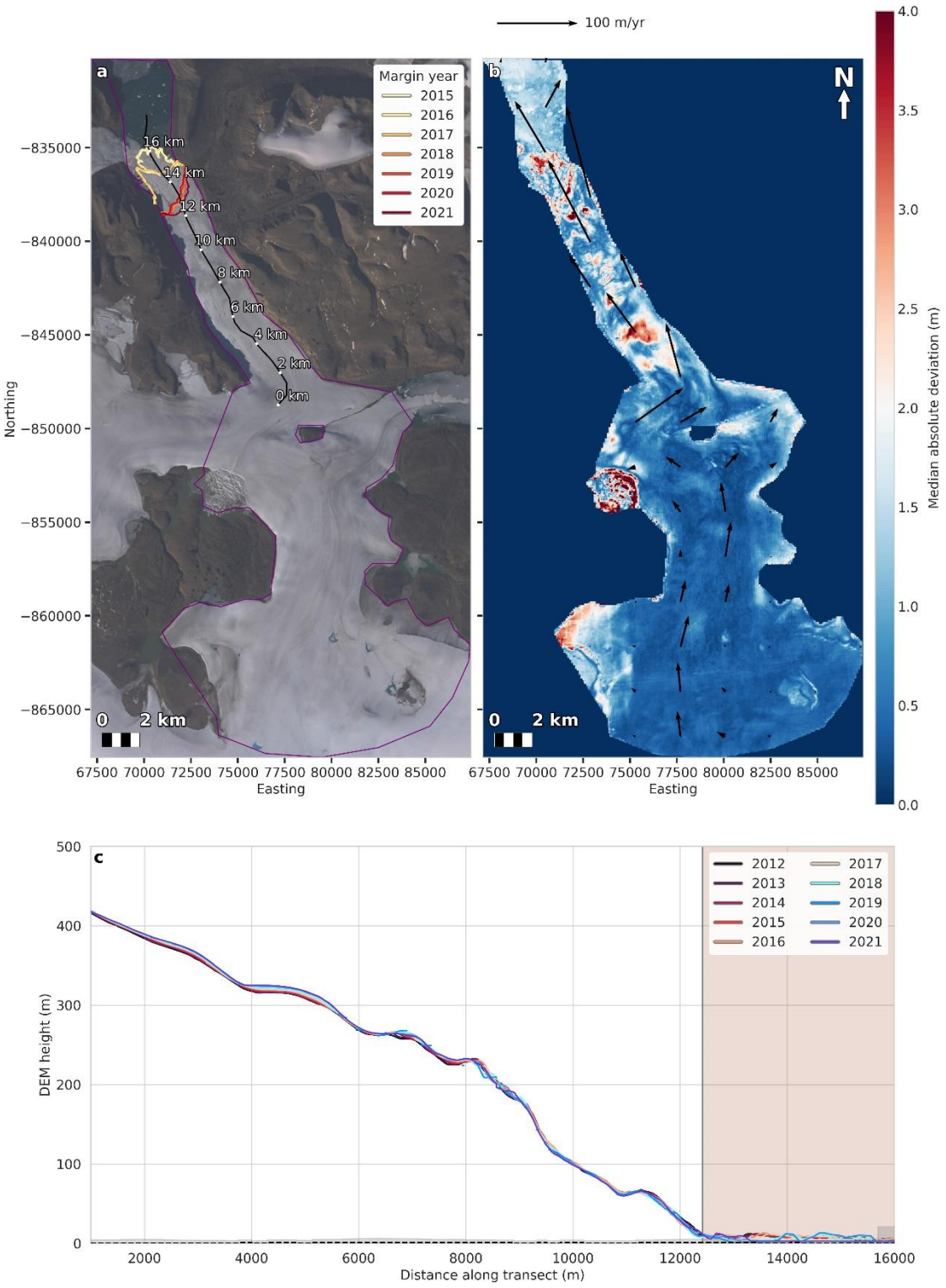


Figure 5.16: DEM variance for Henson Gletsjer. Panel a presents an overview of the study site (outlined in purple), including the calving front locations detailed in Table 5.3, and the location of the longitudinal transect shown in panel c. The base map of this panel is a Landsat 8 natural colour composite from 31st July 2016. Panel b presents the median absolute deviation map produced by our method. The black arrows on this panel indicate the ice velocity provided by the NASA MEaSUREs ITS_LIVE project (Gardner et al., 2025). Panel c shows the aligned stacked

DEM elevations, averaged per year, along the transect shown in panel a, with the dashed black line indicating the height at flotation of the glacier calculated using Eq. 5.2 with grey shading indicating the uncertainty calculated using Eq. 5.3. The solid black vertical line delineating the pink region represents the most inland location mapped for the glacier's calving front.

#### 5.6.3.7 Hagen Bræ

Hagen Bræ shows a generally complex and noisy pattern in the median absolute deviation which complicates its interpretation (Figure 5.17b). Although there appears to be a gradual tendency towards a higher pattern of elevation variance seaward of the 2017 grounding line defined by the Climate Change Initiative (CCI) project (Climate Change Initiative, 2023), our calculations suggest that Hagen Bræ was unlikely to have reached flotation at this location, given that the ice surface elevation is ~700 m above sea level (Figure B.2.13a). We believe that the stronger deviation signal apparent towards the terminus of the glacier is again likely caused by the glacier thinning at a faster rate than the upstream area where the DEM alignment is applied. The velocity of this glacier is fast down the central flow region to the north of the glacier and is substantially smaller in the southern flow region (Figure 5.17b). Additionally, the velocity is slightly smaller at the lateral margins due to lateral drag.

Unfortunately, all the DEMs which covered the glacier terminus were of poor quality, such that they were filtered out during the pre-processing stages. Nevertheless, and in agreement with Millan et al. (2023), we infer that Hagen Bræ is fully grounded, based upon our height at flotation calculations (Figure 5.17c). These are based on the bed elevation data from BedMachine version 5 which was calculated using the mass conservation method (Figure B.3.13a). The uncertainty of the height at flotation is very low along the length of the transect and we note that the height at flotation is never higher than the annual average DEM elevations, suggesting that this glacier cannot be in flotation over the area depicted by our results. This is further supported by previous work, which concluded that Hagen Bræ would need to thin by approximately 100 m to achieve flotation at its terminus (Solgaard et al., 2020).

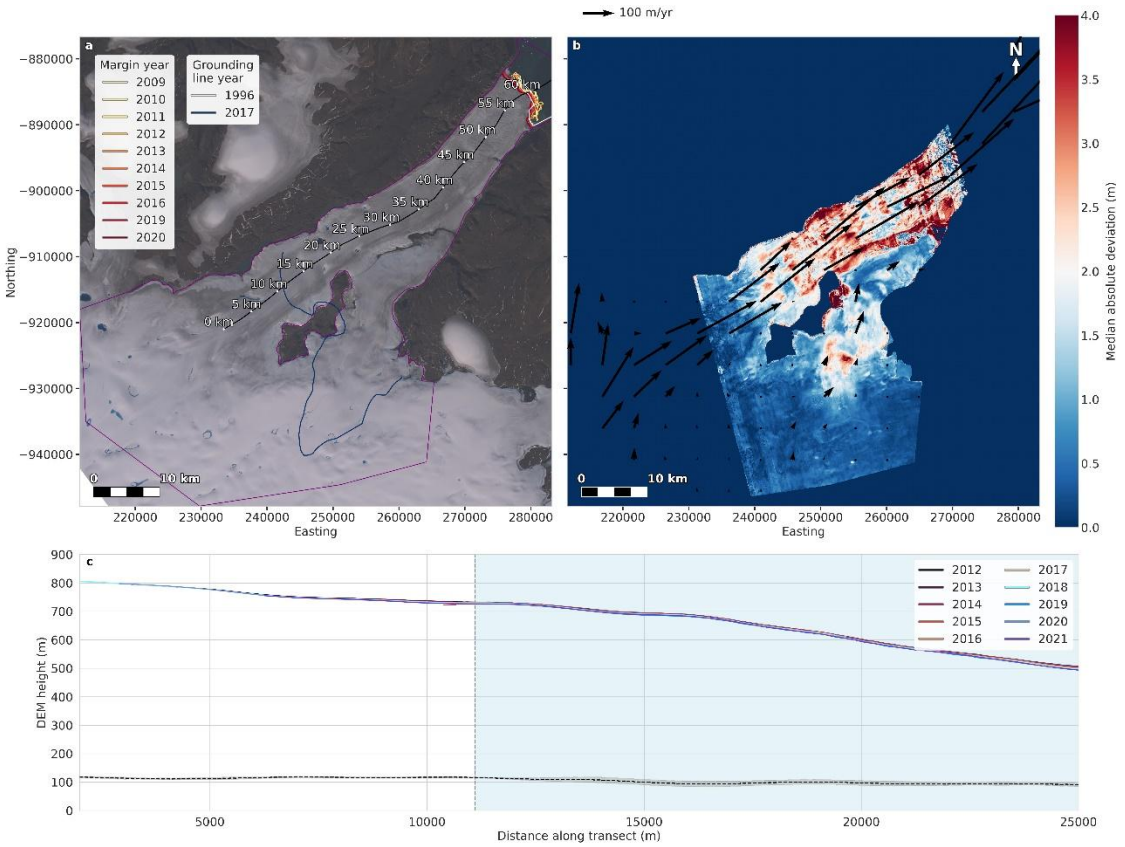


Figure 5.17: DEM variance and grounding line information for Hagen Bræ. Panel a presents an overview of the study site (outlined in purple), including the calving front and grounding line locations detailed in Table 5.3, and the location of the longitudinal transect shown in panel c. The base map of this panel is a Landsat 8 natural colour composite from 14th August 2015. Panel b presents the median absolute deviation map produced by our method. The black arrows on this panel indicate the ice velocity provided by the NASA MEaSUREs ITS_LIVE project (Gardner et al., 2025). Panel c shows the aligned stacked DEM elevations, averaged per year, along the transect shown in panel a, with the dashed black line indicating the height at flotation of the glacier calculated using Eq. 5.2 with grey shading indicating the uncertainty calculated using Eq. 5.3. The light blue vertical area bordered by a dashed black line indicates the range over which grounding lines have been located in previous studies.

#### 5.6.3.8 Zachariæ Isstrøm

Similar to Hagen Bræ, the deviation signal of Zachariæ Isstrøm is relatively complex, with a gradual transition from higher deviation near the calving front, to lower deviation inland (Figure 5.18). Although we find high deviation immediately downstream of the 2017 Climate Change Initiative (2023) grounding line, as was the case for Hagen Bræ, the ice appears to be too thick here to be approaching flotation (Figure B.2.14c). Our height at flotation in Figure 5.18c shows that the ice would have to thin by hundreds of metres to be at the height of flotation. The height at flotation is based on the bed elevation data from the NASA MEaSUREs ITS_LIVE project (Gardner et al., 2025) which used mass conservation to find bed elevation (Figure B.3.14a). The height at flotation uncertainty is low along the length of the transect. Rather, we infer that the high deviations that we observe on this glacier are likely again differential signals of ice thinning. The velocity of this glacier is even across its width, with an increase towards the glacier terminus (Figure 5.18b). Unfortunately, the scarcity of sufficient quality DEM data covering the ice front means that we cannot compute the deviation signal – and hence assess flotation – at the terminus of the glacier.

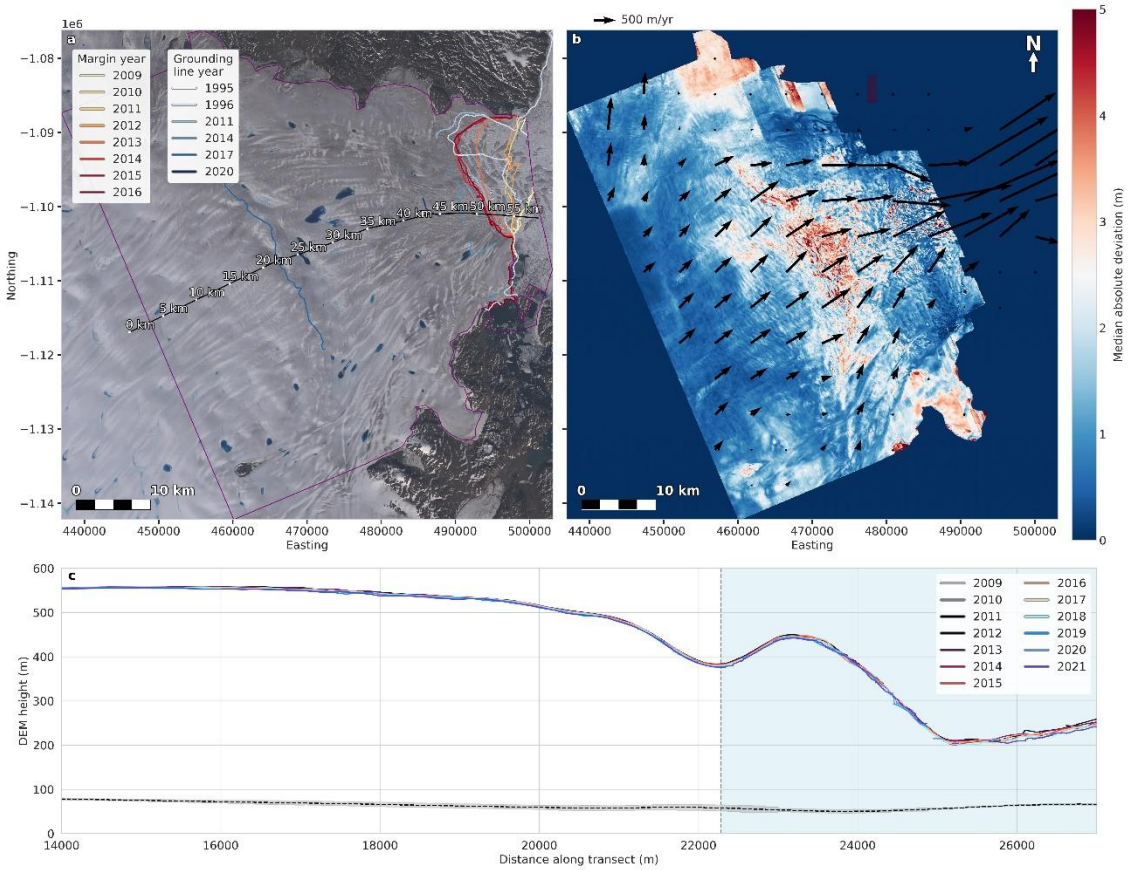


Figure 5.18: DEM variance and grounding line information for Zachariæ Isstrøm. Panel a presents an overview of the study site (outlined in purple), including the calving front and grounding line locations detailed in Table 5.3, and the location of the longitudinal transect shown in panel c. The base map of this panel is a Landsat 8 natural colour composite from 7th August 2015. Panel b presents the median absolute deviation map produced by our method. The black arrows on this panel indicate the ice velocity provided by the NASA MEaSUREs ITS_LIVE project (Gardner et al., 2025). Panel c shows the aligned stacked DEM elevations, averaged per year, along the transect shown in panel a, with the dashed black line indicating the height at flotation of the glacier calculated using Eq. 5.2 with grey shading indicating the uncertainty calculated using Eq. 5.3. The light blue vertical area bordered by a dashed black line indicates the range over which grounding lines have been located in previous studies.

### 5.6.4 Glaciers with no detectable flotation signatures (method failure)

#### 5.6.4.1 Petermann

Although in the previous sections we have demonstrated that our new method can detect signatures of floating ice, there are cases where this approach, as it is currently implemented, has been unable to identify known floating ice tongues. Notably, this is the case for Petermann (Figure 5.19b). Here, the deviation signature exhibits a complicated pattern which arises from the downstream advection of surface crevasses and ridges.

Although our method attempts to mitigate the high deviations caused by crevasse and ridge migration through the smoothing step, the surface variations on Petermann are often too wide, and move too rapidly, for our smoothing step to reduce their impact. On Petermann, these irregular surfaces are not confined to the areas near the fjord walls as they are on other glaciers; instead, the irregularities exist across the entire width of the glacier. Resultingly, our method is unable to identify a inland flotation limit on this glacier due to the limitations imposed by the high surface velocity.

The velocity field of this glacier shows length and width patterns where the faster velocities are in the centre of the glacier width and seaward of the grounding line area (Figure 5.19b). The velocities are smaller at the lateral margins of the glacier due to lateral drag. In Figure 5.19c, we show that the height at flotation of this glacier does not show higher elevations than the annual average DEM elevations until the seaward edge of the grounding line area. The uncertainty on the height at flotation values are small until ~35.75km along the transect where the bed elevation source data swaps from mass conservation to interpolation (Figure B.3.15a)

We note that Figure 5.19c shows a divergence of elevations at the intersection between the DEM elevations and the height above flotation line, which may suggest that improvements to the method could identify a inland flotation limit for this glacier. We consider possible future improvements that could be made to the method to address this in the next section.

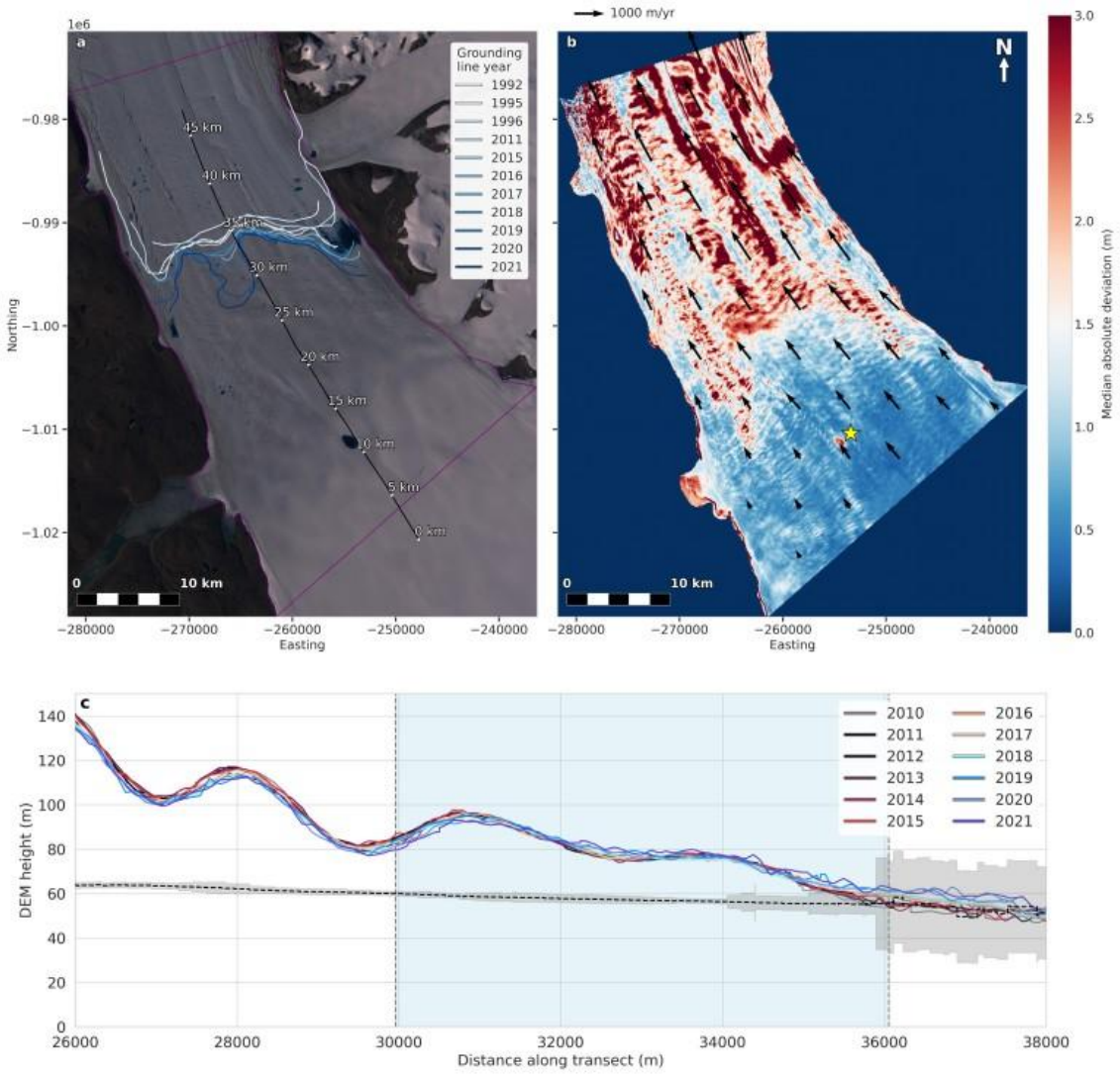


Figure 5.19: DEM variance and grounding line information for Petermann Gletsjer. Panel a presents an overview of the study site (outlined in purple), including the grounding line locations detailed in Table 5.3, and the location of the longitudinal transect shown in panel c. The base map of this panel is a Landsat 8 natural colour composite from 7th August 2016. Panel b presents the median absolute deviation map produced by our method. The yellow star on panel b indicates supraglacial ponding visible in panel a. The black arrows on this panel indicate the ice velocity provided by the NASA MEaSUREs ITS_LIVE project (Gardner et al., 2025). Panel c shows the aligned stacked DEM elevations, averaged per year, along the transect shown in panel a, with the dashed black line indicating the height at flotation of the glacier calculated using Eq. 5.2 with grey shading indicating the uncertainty calculated using Eq. 5.3. The light blue vertical area bordered by dashed black lines indicates the range over which grounding lines have been located in previous studies.

## 5.7 Discussion

Our assessment of temporal elevation variance (Sect. 5.6), combined with the heights of the processed DEMs, has allowed us to make a first-order evaluation of the grounded/floating status of 15 of Greenland's most northerly marine-terminating glaciers over the last decade. Within the limits of our approach, we identified approximate inland limits of floating ice on five glaciers, found no evidence to suggest the presence of a floating extension (due to a real lack of floating ice) on eight, and identified two glaciers with ambiguous flotation signatures on at least one lobe. Our results illustrate that DEM-derived elevation changes can offer a proof of concept for detecting the inland limit of flotation at decadal scale, rather than providing definitive grounding line positions.

Where previous estimates of grounding lines exist from other sources (Climate Change Initiative, 2023; Millan et al., 2023; Möller et al., 2022; Rignot et al., 2001), our results show broad visual agreement. However, because these datasets were known to us during interpretation, they may have influenced our placement and therefore the results cannot be regarded as entirely independent. The method we present here should therefore be viewed as having potential as a complementary approach, rather than as a replacement for established techniques such as SAR, potentially allowing for temporal and spatial gap-filling within the SAR-dominated grounding line datasets.

The high spatial resolution of ArcticDEM (2 m) allows for the delineation of small features, such as the detailed pattern of the inland flotation limit across the glacier width, which likely reflects the underlying bed topography. Beyond the inland flotation limit itself, additional glaciological features can also be identified, such as the subglacial lake visible in Figure 5.14b, which adds context to the glacier that may otherwise be overlooked with traditional methods. Our dataset thus resolves fine detail at the key ice-ocean interface (the grounding line), which ultimately is important for efforts to better understand how the ice sheet responds to environmental forcing. Nonetheless, the decade-scale sampling limits our ability to track shorter-term grounding line migration. This approach therefore represents an initial demonstration of how DEMs may be used in this context, with scope for method refinement.

Despite the promising aspects of the method, it does not consistently succeed in resolving the inland flotation limit. Performance is particularly limited on glaciers with substantial surface roughness and high flow speeds such as Petermann, 79N and Zachariæ Isstrøm.

Crevassing is often more pronounced at the glaciers' lateral markings, due to the resistive force of the adjacent bedrock (Herzfeld et al., 2004). Therefore, whilst it might not always be possible to use this method to map the full inland flotation limit width due to the obscuring effect of crevasse movement, it may be possible to delineate an estimate in the central part of the glacier in cases where crevassing is less pronounced.

There are also methodological aspects that warrant further development. Incorporating surface velocity estimates could help account for deformation-related artefacts and improve cross-glacier consistency. Additional elevation datasets may assist in separating true flotation-related signals from background thinning or thickening, which the current vertical alignment step only partially addresses. Time constraints limited our ability to fully coregister the DEMs with independent elevation products, but future work should consider integration with datasets such as ICESat-2 to refine absolute height control and improve DEM intercomparability.

Overall, the method presented here should be viewed as an exploratory framework. It demonstrates that DEMs contain useful information for identifying potential flotation limits but also highlights clear challenges that need to be addressed before such an approach can be applied more routinely or with high confidence. Rather than offering definitive grounding line estimations, this study provides a baseline from which more robust, higher-resolution, and better-validated methods can be developed.

## 5.8 Conclusions

In this study, we developed a novel method for detecting the existence of Greenlandic floating ice tongues, using repeated timestamped ArcticDEM 2 m DEMs. Using historical calving front locations, historical grounding line locations, and bed elevations, we performed a comprehensive assessment of this new method, to evaluate its utility for detecting the floating extensions of 15 of Greenland's northerly, marine-terminating glaciers. Our method exploits the high spatial resolution ArcticDEM digital elevation modelling dataset and has successfully located floating ice tongues across five glaciers in Greenland. We have also used the method to confirm the lack of a floating extension on eight glaciers and have identified two glaciers where the presence of a floating extension is ambiguous on at least one of its lobes. Only on one glacier (Petermann) did the method fail to detect a known grounding line, which we attribute to the glacier's high velocity and surface roughness. As such, we conclude that our method is able to provide decadal-scale inland flotation limit information, in cases where the glacier has relatively smooth surface characteristics. Our study therefore provides definitive evidence that DEM height variations can be used to find the extent of floating ice, thereby serving as a complimentary data source to supplement SAR-derived grounding line datasets in the future.

# Chapter 6

# 6 A new grounding line detection method using high-resolution digital elevation models and a tide model

Laura Melling[1], Malcolm McMillan[1], Jennifer Maddalena[1], and Amber Leeson[1]

[1] Lancaster Environment Centre, Lancaster University, Lancaster, LA1 4YQ, United Kingdom

**Correspondence:**

Laura Melling (lauraisobelmelling@gmail.com, l.melling@lancaster.ac.uk)

The following work is prepared as a manuscript to be submitted as, “A new grounding line detection method using high-resolution digital elevation models and a tide model”.

For the following study, LM, MM, JM and AL conceptualised the research. LM, MM, and JM designed the study. LM obtained the data, performed the analyses, created all figures, and wrote the paper. LM, MM, and JM contributed to manuscript editing.

# 6.1 Abstract

Grounding lines mark the transition from grounded to floating ice and are crucial for understanding glacier dynamics and ice sheet stability. Traditional grounding line detection methods rely primarily on synthetic aperture radar interferometry, which is limited by data availability and temporal gaps. This study presents a novel approach using digital elevation model (DEM) differencing coupled with tidal modelling to identify grounding line locations in northern Greenland. We apply this method to three major glaciers – Petermann Gletsjer, Nioghalvfjerdsbræ (also known as 79 North Glacier or 79N), and Storstrømmen – coupling ArcticDEM 2-m resolution DEMs (Porter et al., 2022) with the FES2022 tidal model. Our results demonstrate the feasibility of this approach, providing 112 new partial grounding line estimates for Petermann Gletsjer between 2011 and 2018, and suggesting the presence of a floating tongue on Storstrømmen's minor northern lobe until at least 2018. While results for 79N were more limited due to data constraints, our findings help fill temporal gaps in the grounding line record. This method represents a significant advancement in grounding line detection, with potential applications extending to other marine-terminating glaciers in Greenland and to the ice shelves of the Antarctic ice sheet. By improving the temporal resolution of grounding line data, this study contributes to resolving grounding line dynamics over a range of timescales, which is important for monitoring grounding line migration and informing numerical ice sheet models.

## 6.2 Introduction

The precise delineation of grounding lines is important for understanding the dynamics of glaciers and ice sheets. The grounding line represents the transition from grounded ice, which is in direct contact with the bedrock, to floating ice. This boundary is dynamic, shifting with tidal cycles and evolving over longer timescales in response to ice thinning, thickening, and variations in bedrock topography. Tracking these changes is essential for predicting glacier surges, evaluating the stability of floating ice tongues, and modelling ice sheet contributions to global sea level rise. The Global Climate Observing System (GCOS) has recognised grounding lines as one of 55 essential climate variables (ECVs), with a recommended minimum temporal resolution of one year (WMO et al., 2022). Achieving this resolution requires improvements to existing methods or the development of new approaches for grounding line detection.

Current methods for delineating grounding lines in Greenland rely predominantly on interferometric synthetic aperture radar (InSAR), whereas methods to delineate the grounding lines of Antarctica also make use of altimetry (e.g. Brunt et al., 2010; Fricker and Padman, 2006; Hogg et al., 2018). The most comprehensive contemporary grounding line dataset for northern Greenland is based on synthetic aperture radar (SAR) data from European Remote-Sensing Satellite (ERS)-1, ERS-2 and Sentinel-1 (Millan et al., 2023). However, SAR-based methods are limited by limited data availability within the 2010s. ERS-2 ceased operations in 2011, while Sentinel-1 only began acquiring data in 2014, resulting in temporal gaps in the dataset, particularly for 2012 and 2013. This has left a spatiotemporal knowledge gap for Greenland's grounding lines between 2011 and 2014. Additionally, InSAR-based methods can suffer from loss of coherence in areas of fast-flowing ice, limiting their effectiveness.

Given that SAR alone cannot deliver the recommended temporal sampling (WMO et al., 2022) over the past decade – and altimetry methods often used in Antarctica have not been translated to Greenland due to the limited number and size of floating glacier extensions, and complex fjord geometry and surface roughness causing signal limitations and noise – there is a need to develop and test alternative methods that use other types of data. High-resolution commercial optical satellites, such as WorldView-1 and WorldView-2, have demonstrated their applicability to timestamped digital elevation model (DEM) production through datasets such as ArcticDEM (Porter et al., 2022). These

datasets offer a relatively high temporal resolution, potentially enabling targeted acquisition of optical imagery at tidal highs and lows, thereby facilitating grounding line detection through DEM differencing.

In Chapter 5, we developed a variance-based approach to locating floating ice from DEM stacks. Whilst this was effective at identifying the extent of floating ice for approximately half of the studied glaciers in northern Greenland, it lacked high temporal resolution and failed to identify the floating ice tongue of Petermann Gletsjer. In this study we therefore introduce a novel approach to grounding line detection that leverages DEM differencing in combination with tidal modelling. To our knowledge, this is the first method to use DEM differencing for this purpose and the first to pair DEMs with a tidal model to determine grounding line locations. Our approach is designed to provide timestamped grounding line locations, and thus to help address the temporal gaps present in SAR-based datasets, thereby enhancing the continuity of grounding line records. By improving our understanding of grounding line behaviour in northern Greenland, we can provide valuable information for models of ice sheet dynamics and, ultimately contribute to a better understanding of the impacts of sea level rise on coastal communities worldwide.

Our research focuses on three major glaciers in northern Greenland – Petermann Gletsjer, 79N, and Storstrømmen – each supporting a floating extension (Millan et al., 2023). The varying characteristics of these three glaciers allows for a comprehensive evaluation of the method's robustness and applicability across diverse glaciological conditions. This study investigates whether DEM differencing coupled with tidal modelling can effectively determine grounding line locations for these glaciers over the past decade.

## 6.3 Study locations

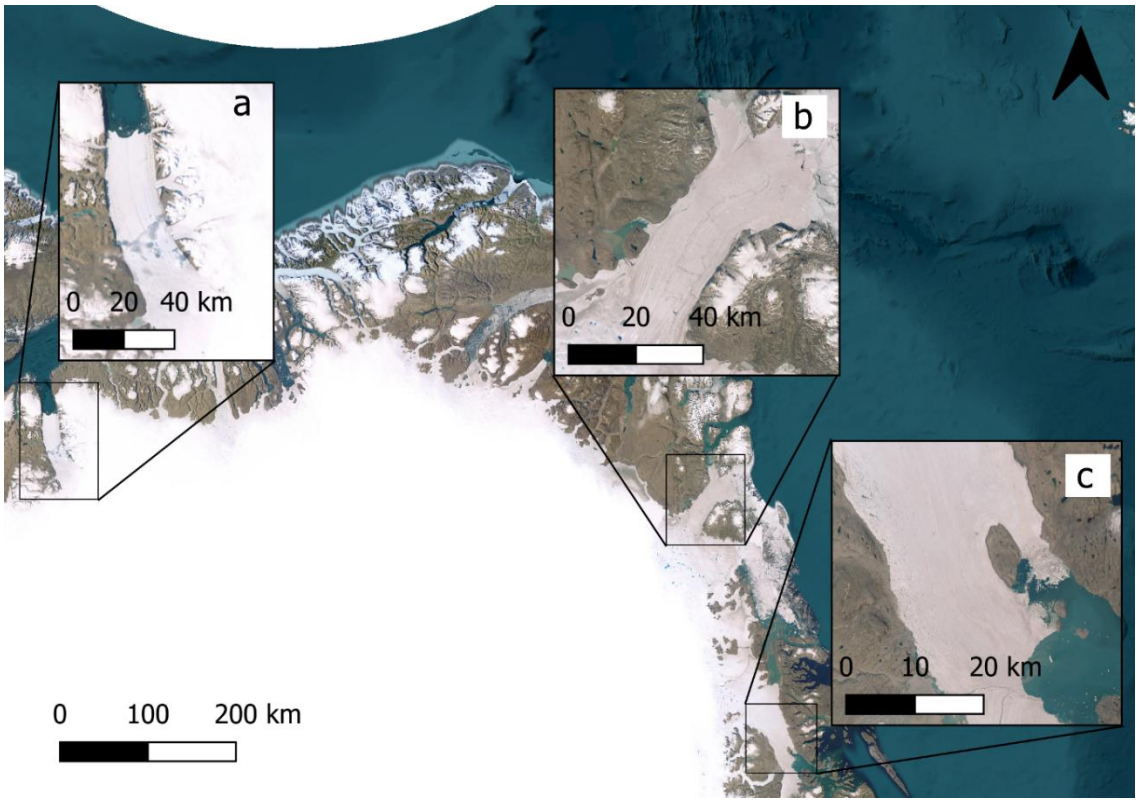


Figure 6.1: Map showing the locations of our study glaciers (a: Petermann Gletsjer, b: Nioghalvfjerdsbræ (79N), and c: Storstrømmen) within northern Greenland. The base map data are courtesy of Earthstar Geographics via Esri.

We chose three marine-terminating glaciers in northern Greenland for our study, with each location supporting an ice tongue and serving a different purpose in testing our novel method. The three study locations were Petermann Gletsjer, Nioghalvfjerdsbræ (79N), and Storstrømmen (see Figure 6.1). We chose Petermann Gletsjer for its high data volume and high velocity to test whether a DEM-based dynamic method could successfully determine its grounding line, as we were unable to identify an ice tongue for the glacier in Chapter 5. We selected 79N because it has an even higher velocity than Petermann Gletsjer, but we previously identified an ice tongue for it in Chapter 5. Finally, we chose Storstrømmen to test the method on a glacier with limited data availability. We provide a brief description of each study site in the following sections.

### 6.3.1 Petermann Gletsjer

Petermann Gletsjer is a north-flowing glacier with one of the highest measured velocities of any of the northern Greenland glaciers (~1 km/yr) (Higgins, 1991; Millan et al., 2022a).

These high speeds present challenges for our deviation-based method (see Chapter 5) of determining the presence of a floating extension due to the movement of crevasses and ridges on the glacier surface. At 70 km long and 20 km wide, Petermann Gletsjer supports the longest and second-largest ice tongue in the northern hemisphere (Rignot and Steffen, 2008; Wilson et al., 2017; Millan et al., 2022a).

Petermann Gletsjer is a major drainage conduit of the ice sheet, with 4% of Greenland's ice mass buttressed by its ice tongue (Rignot et al., 2001). Before 2017, the glacier's grounding line was more advanced along the central section (Hogg et al., 2016). However, since 2017, this section has experienced 5 km of retreat (Millan et al., 2022a). Additionally, some models suggest that future changes in calving could affect the grounding line dynamics (Hill et al., 2018b).

Petermann Gletsjer has the largest number of ArcticDEM DEMs of any of the glaciers in northern Greenland (5432 total) across a wide timespan (2010–2021) which increases the likelihood of capturing temporal changes in ice elevation. This extensive dataset allows for more flexibility in analysis and may help counteract challenges posed by the glacier's high velocity, making it easier to extract meaningful insights despite rapid ice motion.

### 6.3.2 Nioghalvfjerdsbræ (79 North/79N)

In the northeast of Greenland, 79N (Nioghalvfjerdsbræ), the largest ice tongue in Greenland (Wilson et al., 2017), fills Nioghalvfjerdsfjorden. Since 1996, 79N's grounding line has retreated ~4.5 km (Millan et al., 2023). In the 2010s, the ice tongue thinned, with basal melt contributing significantly to annual non-calving mass loss (Wilson et al., 2017).

79N has a high velocity (~1.4 km/yr) (Rignot and Kanagaratnam, 2006) and suffers from the crevasse- and ridge-induced issues experienced by elevation-derived methods of determining the presence of a floating extension (Chapter 5). Although 79N has fewer DEMs available than Petermann Gletsjer (1883 total), we identified apparent flotation signatures of an ice tongue using DEM deviation signals from 2009–2021 in Chapter 5.

### 6.3.3 Storstrømmen

Finally, we chose to test our method on Storstrømmen, a southeast flowing glacier with a floating extension of ~15 km (measured at the grounding line). This glacier has two lobes, one main lobe to the south which transports the majority of the glacier's ice towards the

ocean, and another smaller lobe to the north which is now considered fully grounded (Millan et al., 2023).

Storstrømmen is a surging glacier, and thus it experiences retreats and sudden advances of its grounding line and calving front (Mouginot et al., 2018). The glacier has a predicted surge periodicity of ~52 years and is expected to meet pre-surge conditions between 2027 and 2030. This means that understanding its recent grounding line behaviour is particularly important (Mouginot et al., 2018).

Storstrømmen has substantially fewer DEMs than either Petermann Gletsjer or 79N (132 total) but has been intensely studied using traditional methods (InSAR) for the period between 2016 and 2020 (Millan et al., 2023). Storstrømmen is therefore a good site for validating our method, allowing comparisons of grounding lines from InSAR and DEM differencing. In addition, the lower number of DEMs allows us to test the resilience of our method on glaciers with less data.

## 6.4 Data

### 6.4.1 DEM datasets

For our study, we required a DEM dataset with which to test our method, and a reference dataset against which to coregister the DEM dataset. For these, we downloaded the ArcticDEM timestamped strip DEMs at 2 m resolution (version 4.1) and the ArcticDEM mosaic DEM at 100 m resolution (version 4.1) from the Polar Geospatial Center (PGC). Both datasets are open-access and produced by the PGC (Porter et al., 2022, 2023). The strip DEM dataset is assembled from pairs of stereoscopic DEMs derived from 0.32-0.5 m resolution optical satellite imagery. They are generated by applying the Surface Extraction from TIN-based Searchspace Minimization (SETSM) software to each stereo-pair of images (Noh and Howat, 2015).

All ArcticDEM strip DEM data used in this study were produced from stereo pairs acquired in the summer months between 2010 and 2021. Although the dataset has full spatial coverage of Greenland, the coverage is uneven, with Petermann Gletsjer and 79N having significantly more data than Storstrømmen (Figure 6.2). The reason for the inequality between the number of DEMs available for each site is a combination of orbital convergence and the level of scientific interest. Petermann Gletsjer and 79N are substantially larger than Storstrømmen and buttress more of the inland ice meaning that they are more preferentially studied due to their higher relative importance (e.g. Li et al., 2023a; Macdonald et al., 2018; Millan et al., 2022a, 2023; Wekerle et al., 2024; Zeising et al., 2024). Resultingly, the PGC produces more DEMs for these glaciers than for smaller glaciers like Storstrømmen. The strip DEMs provide snapshots of the surface height with the timestamps of the strips allowing for comparison of topographic data acquired in different seasons or years.

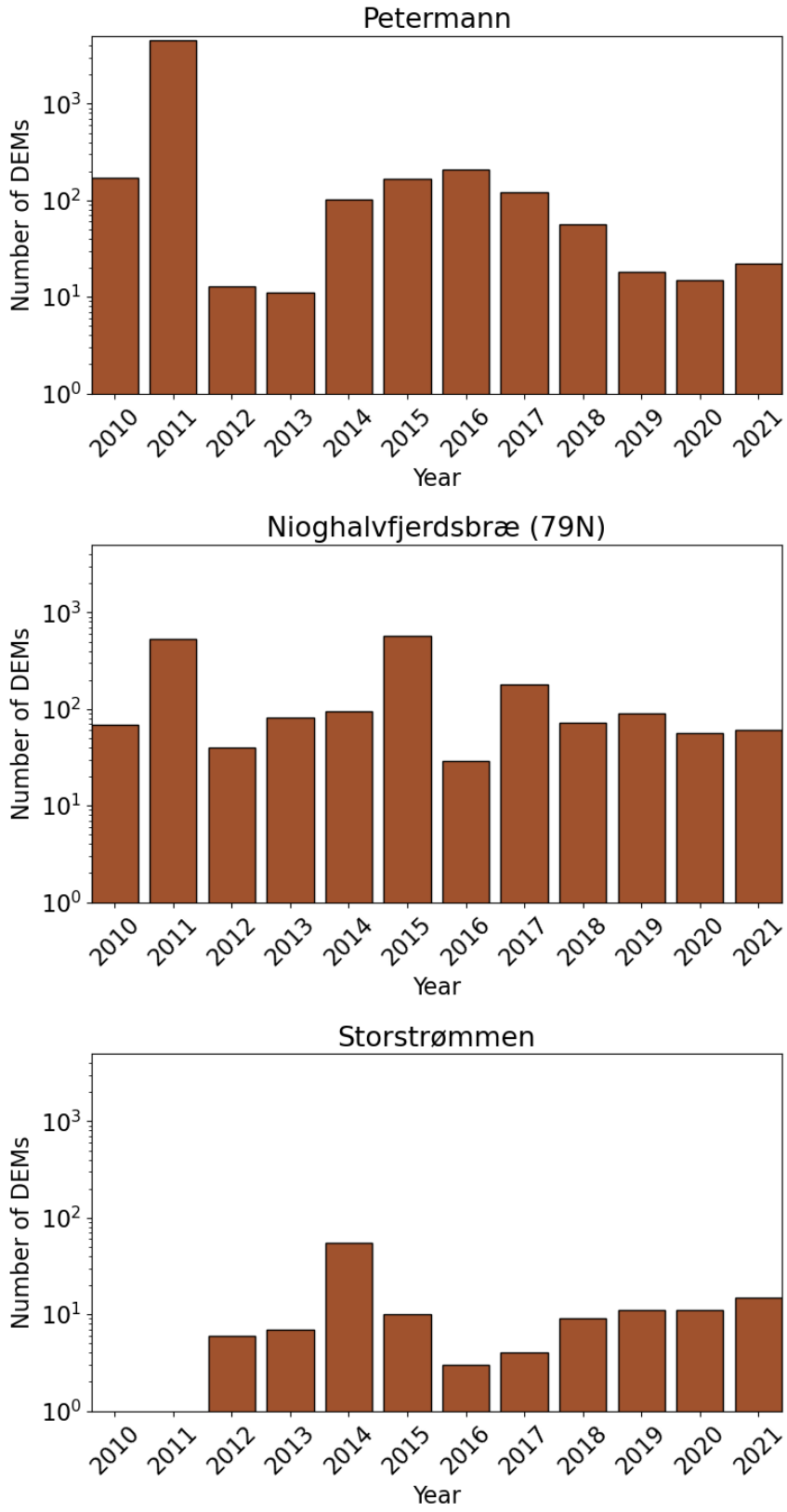


Figure 6.2: The number of DEMs available per year for each of our three study sites prior to any data processing.

We used the ArcticDEM mosaic DEM at 100 m resolution as our reference dataset against which to coregister the strip DEMs (Porter et al., 2023). Coregistration is the process of aligning datasets to a common spatial reference frame. It ensures that features match across different data sources or time points, reducing errors, improving change detection, and enhancing comparability between the two datasets. The mosaic is assembled from strip DEMs which have been blended and feathered to reduce edge-matching artefacts. This results in a more consistent and comprehensive DEM product over areas larger than the strip DEMs, although as a time-averaged product, it no longer boasts the temporal resolution of a single strip DEM. The PGC produces the DEM mosaics using a median-mosaicking style with outlier filtering which provides the median value of multiple strip elevations at each pixel (Porter et al., 2023).

### 6.4.2 Ancillary datasets

In addition to these core DEM datasets, we leveraged data from several ancillary sources to support our analysis. These datasets comprised:

- Sentinel-2, Landsat 7 and Landsat 8 optical satellite imagery
- The Millan et al. (2023) grounding lines from SAR interferometry
- BedMachine version 5 (Morlighem et al., 2022)

We used Sentinel-2, Landsat 7 and Landsat 8 optical satellite imagery to inspect the glacier surface for artefacts such as crevassing, ridging and/or supraglacial hydrology. The Millan et al. (2023) dataset provides the locations of grounding lines on Petermann Gletsjer (1992, 1996, 2011, 2015–2021), 79N (1992, 1994, 1996, 2011, 2016–2020), and Storstrømmen (1996, 2016–2020). We validated the results of our method against these grounding lines and used them for contextual reference of the grounding lines' trajectories over the last decade. Millan et al. (2023) is used as the comparison dataset because it provides the most spatially extensive grounding line product currently available for Greenland, rather than because it represents a definitive reference of truth.

BedMachine version 5 (Morlighem et al., 2022) was our final ancillary dataset. BedMachine is a 150 m resolution bed topography/bathymetry map of Greenland based on multi-beam echo-sounding data and a mass conservation approach. We used the ice/ocean/land mask within this dataset to identify the different surface types in Greenland for use during the coregistration step (Sect. 6.5.5). Additionally, we used the ice thickness

and ice surface elevation layers to calculate the height above flotation for each glacier. We detail this calculation in Sect. 6.5.8. These ancillary datasets provided us with context for our target glaciers.

## 6.5 Methodology

The method we present in this study is a dynamic tidal method which identifies the landward limit of tidal ice flexure (the hinge line). The tidal flexure limit is an accepted proxy for the grounding line as identified in previous studies (e.g. Freer et al., 2023; Li et al., 2022; Milillo et al., 2022; Millan et al., 2023) but we emphasise that the method described herein cannot identify the true grounding line due to the elastic properties of ice.

### 6.5.1 Step 1: Data acquisition and masking

First, we identified all DEMs which cover the target glacier. For this, we delineated a polygon of the region covered by previous grounding line estimates and extended it 2 km inland and 2 km seaward to ensure comprehensive coverage of potential grounding line positions. We used this polygon to select the appropriate DEMs from the PGC Strip DEM Extent Index. Once we had determined which DEMs we required for the analysis, we downloaded the relevant ArcticDEM 2m resolution DEMs and the ArcticDEM version 4 mosaic (100 m spatial resolution) from the PGC (Porter et al., 2022, 2023).

The in-house filtering method applied by the PGC during strip DEM production only removes edge artefacts. However, the strip DEMs are packaged with quality control masks specific to each strip DEM. Errors within the DEMs which result from clouds or water are identified within these masks and each mask is provided as an 8-bit unsigned integer raster. These masks represent regions of the strip DEM which the PGC believe represent poor quality data. As such, we applied these masks to each target DEM as part of our pre-processing, using the PGC Python script to apply these masks to each DEM of interest (Husby, 2023). This script masks pixels exhibiting cloud, water, or edge effects.

### 6.5.2 Step 2: Filtering

Some ArcticDEM strip DEMs are produced by combining pairs of stereoscopic images that were acquired at different dates and times. As our method requires the DEM to correspond to a specific time to ensure the validity of our tidal calculations, we removed any DEMs from our dataset whose constituent optical images were acquired more than three hours apart. We chose to restrict the optical acquisition time differences of our DEMs to three hours because a three-hour difference between the optical image acquisitions represents approximately one quarter of a 12-hour tidal cycle. This ensured that the tidal difference between image pairs was smaller than the tidal signal that we

were attempting to measure between DEMs. This resulted in the removal of ~87.5% of our DEMs for Petermann Gletsjer, with the vast majority removed from 2011. Of the original 4527 DEMs from 2011, 4346 were removed (96%). For 79N, we removed 62% of our total DEMs. Finally, for Storstrømmen, we removed 13% of the DEMs. While the removal rates for Petermann Gletsjer and 79N were high, this step was necessary to ensure the validity of our approach. However, due to the large number of available DEMs remaining at both sites, we still had a substantial dataset for input into our grounding line detection process (Figure 6.3).

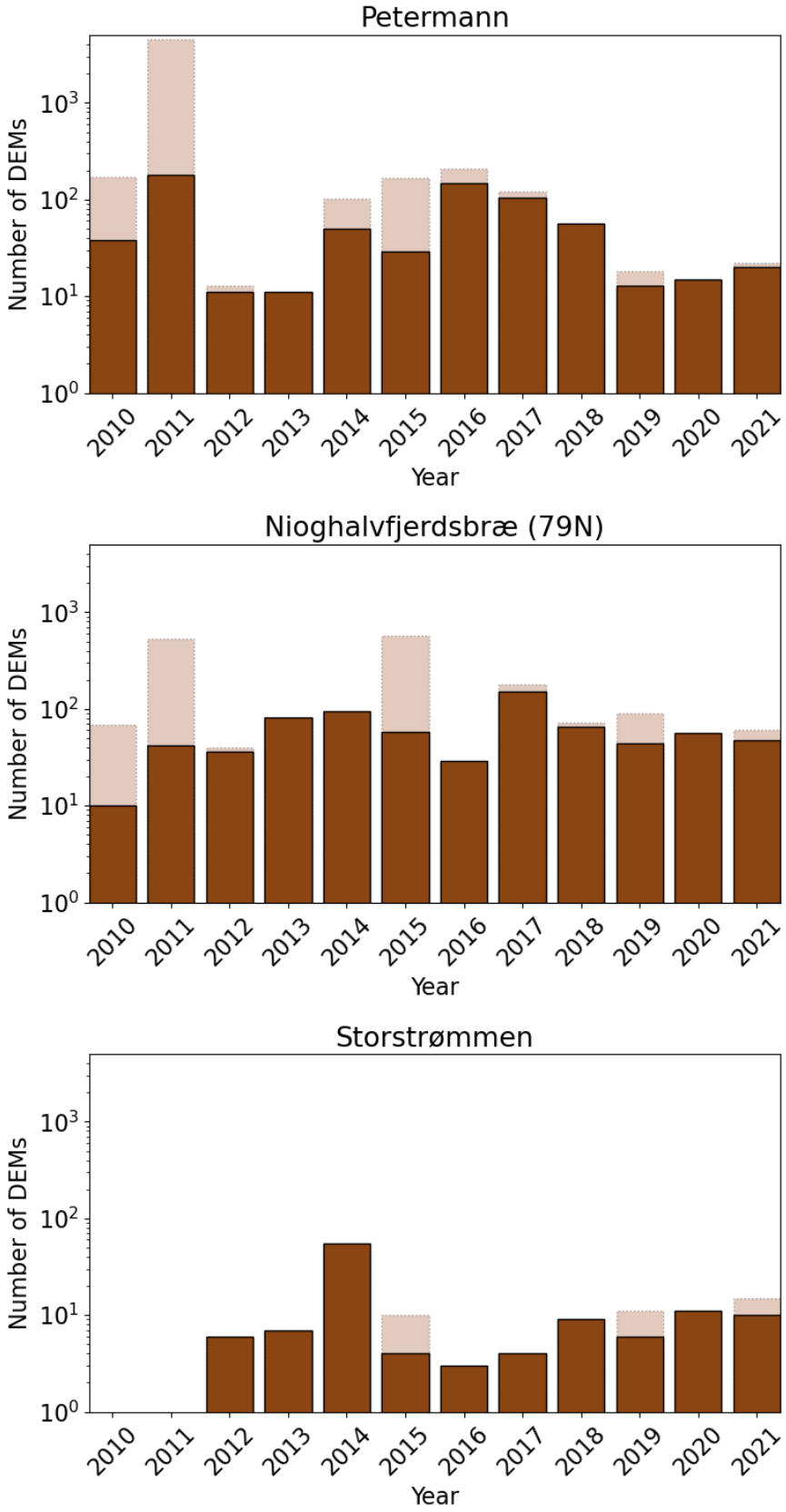


Figure 6.3: The number of DEMs available per year for each of our three study sites after processing described in Sect. 6.5.1 and Sect. 6.5.2. The original numbers of available DEMs are shown with faded bars.

### 6.5.3 Step 3: Tidal height calculation

Once we had filtered the DEMs according to the time difference between the stereoscopic image pair, we calculated the tidal height of each DEM at a coordinate close to the mouth of the glacier's fjord. To do this, we used tidal predictions from the Finite Element Solution Model (2022) (FES2022) tide model (Lyard et al., in prep.), implemented within the pyTMD Python package (Sutterley et al., 2017). More specifically, we used the pyTMD function compute.tide_elevations (Sutterley et al., 2017) with the following parameters: MODEL=FES2022, EPSG=3413, TYPE=grid, TIME=UTC, METHOD=bilinear, and FILL_VALUE=-9999. The FES2022 tide product was funded by the Centre National d'Études Spatiales (CNÉS) and made freely available by AVISO (CNÉS, 2024).

### 6.5.4 Step 4: Finding candidate DEM pairs

Next, we used the tide model predictions to determine DEM pairs that were well suited to the potential identification of grounding lines. To do this, we limited the difference in the number of days to <14 days, and the difference in tidal height to > 0.4 m. Although we explored different temporal and tidal height limits, these values achieved a compromise between stringency and ensuring a large number of DEM pairs for analysis. This step reduced the number of DEMs available for Petermann Gletsjer down to 840, 79N Gletsjer reduced to 168 DEMs, and Storstrømmen's number of DEMs was reduced to 96.

### 6.5.5 Step 5: Coregistration

Once we had a list of candidate DEM pairs from which we could potentially identify the grounding line, we coregistered all of the DEMs which were a member of at least one pair. We did this to ensure spatial consistency between the DEMs to better identify the floating and grounded areas. We coregistered our DEMs with the Python package XDEM and used the Nuth and Kääb coregistration algorithm contained within this package (Nuth and Kääb, 2011; XDEM Contributors, 2023). The Nuth and Kääb coregistration algorithm applies planar shifts to the DEMs, making it substantially faster to implement than other algorithms which apply skew and tilt corrections (Nuth and Kääb, 2011).

The Nuth and Kääb method in XDEM requires the identification of stable reference areas over which the coregistration can be performed. We therefore used the BedMachine

version 5 land type mask (Morlighem et al., 2022), to produce polygons of the ice-free bedrock areas which we assume to be relatively stable.

Although the PGC produces 2 m mosaics, these are provided as 50 km by 50 km tiles. To avoid introducing edge effects caused by merging these tiles, we bilinearly interpolated the ArcticDEM 100 m mosaic to 2 m resolution. Since this step aims to correct large-scale effects across the strip DEMs, we did not require the full 2 m resolution mosaic. Additionally, the 100 m mosaic covers the full ArcticDEM domain and has been used as a reference dataset in many other studies (e.g. Dai et al., 2024; Grimes et al., 2024; Seehaus et al., 2020; Shiggins et al., 2023). Once we had bilinearly interpolated the mosaic, we clipped it to the extent of our stable polygons. Once clipped, we coregistered each of our DEMs against the 2 m resolution ArcticDEM mosaic reference areas.

### 6.5.6 Step 6: Smoothing

After coregistration, we smoothed the DEMs to 100 m spatial resolution to reduce the impact of crevassing and ridging which could have caused problems during analysis on high-velocity glaciers (see Chapter 5). To do this, we calculated the median value of the original 2 m pixels within a 100 m pixel footprint and assigned this as the new value of the 100 m pixel. Once smoothed to 100 m, we bilinearly interpolated the DEM back to 2 m resolution. This gave us DEMs at 2 m sampling with lower surface roughness that reduced the impact of crevasse movement on fast-flowing glaciers.

### 6.5.7 Step 7: DEM differencing and grounding line delineation

When we had performed all the pre-processing steps, we differenced each DEM pair to determine a map of the surface elevation changes occurring over the intervening (<14 day) period. We then inspected each pair for evidence of a distinct transition in the height difference indicative of a tidal displacement signal and, where this was the case, manually delineated the grounding line based upon this height change signal.

### 6.5.8 Step 8: Height above flotation

To provide ourselves with an independent grounding line estimate against which to compare our results, we calculated the height above flotation, $h_f$, from the BedMachine version 5 (Morlighem et al., 2022) ice surface elevation layer, $h$, and the BedMachine version 5 (Morlighem et al., 2022) ice thickness layer, $H$, using Eq. 6.1 (adapted from Milillo et al. (2019) with alterations respecting the densities of ice, $\rho_i$, and seawater, $\rho_w$, from the BedMachine version 5 product) as

$$h_f = h - H\left(1 - \frac{\rho_i}{\rho_w}\right) \tag{6.1}$$

where the densities of ice, $\rho_i$, and seawater, $\rho_w$, are 917 kg/m$^3$ and 1023 kg/m$^3$, respectively (Morlighem et al., 2022).

## 6.6 Results

In this section, we present the results and analysis of our new method of grounding line detection for the Petermann Gletsjer, 79N, and Storstrømmen glaciers in northern Greenland. Due to the volume of data available, we present a selection of example plots to elucidate our key findings.

### 6.6.1 Petermann Gletsjer

We delineated 117 new grounding line segments for Petermann Gletsjer. In Figure 6.4, we present two examples of differenced DEMs from March and April 2013 (Figure 6.4b) and September 2016 (Figure 6.4d) with reference grounding lines (Millan et al., 2023) which bracket our grounding line dates, and our manually delineated grounding lines. In these examples, we see a clear transition in the DEM-pair elevation difference between the grounded and floating sections of the ice. Although our grounding lines do not agree exactly with the reference grounding lines (Millan et al., 2023), they are within 2-3 km, and it is important to note that these grounding lines do not depict the same years. In Figure 6.4b, the reference grounding lines are from April 2011 and September 2015, whereas our differenced DEM pair is made from DEMs dated from March and April 2013. Our grounding line thus represents a period of time for which we do not have data within the historical grounding line record.

The reference grounding lines in Figure 6.4d are dated from November 2016 and August 2017, with our differenced DEM pair dated September 2016. Although both our method and the method of Millan et al. (2023) aim to identify the inland limit of tidal flexure and would therefore be expected to produce closely aligned grounding line positions, the flexural transition is not a discrete boundary but instead is a zone that can span several kilometres (Ciracì et al., 2023). Both techniques identify a grounding line within this zone from inherently noisy data. The locations of these lines are visually determined and therefore subjective, potentially yielding grounding line positions that differ by several kilometres. We note that our grounding line extends further to the west than the Millan et al. (2023) grounding lines, further informing Petermann Gletsjer's spatial record.

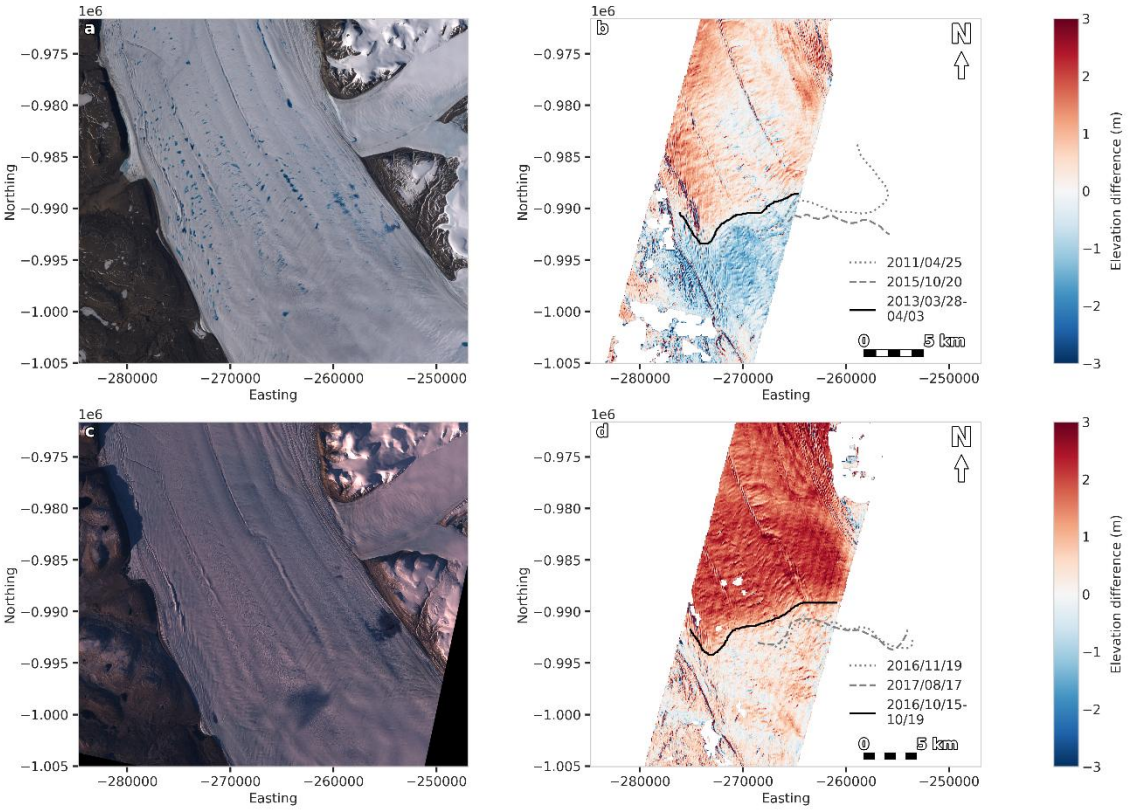


Figure 6.4: DEM elevation difference and grounding line information for Petermann Gletsjer. Panel a presents a Landsat 8 optical satellite image dated 27th June 2014 as contextual reference for the data in panel b. In panel b, we present the elevation difference between DEM 1 (28th March 2013) and DEM 2 (3rd April 2013) with a modelled tidal height difference of 1.27 m. Also on this panel, we show the Millan et al. (2023) grounding lines, dated 25th April 2011 and 20th September 2015, and our grounding line. Panel c presents a Sentinel-2 optical satellite image dated 16th September 2016 as contextual reference for the data in panel d. In panel d, we present the elevation difference between DEM 3 (15th September 2016) and DEM 4 (19th September 2016) with a modelled tidal height difference of 1.96 m. Also on this panel, we show the Millan et al. (2023) grounding lines, dated 19th November 2016 and 17th August 2017, and our grounding line.

In Figure 6.5 we present two examples of differenced DEMs from which we were unable to delineate a grounding line. It is important to note that the modelled tidal height difference for the result shown in Figure 6.4b is 1.27 m whereas the modelled tidal height difference for the result in Figure 6.5b is 1.25 m, suggesting that there are factors other than the tidal height difference affecting our ability to delineate the grounding line. This may be due to errors in the DEM such as jitter. We observe a minor along-track (parallel to the long side) jitter signal in Figure 6.5b which could limit our ability to delineate the

grounding line and a clear across-track (perpendicular to the long side) jitter signal which presents as striping artefacts in Figure 6.5c which may have a similar effect.

Overall, the 117 new grounding line segments that we identify follow approximately the same geometries and locations as the Millan et al. (2023) grounding lines (Figure 6.6). Notably, we do not observe a temporal retreat of the grounding line, as was found by Millan et al. (2023), who conclude that Petermann Gletsjer's grounding line is retreating, and instead we find bunching close to the Millan et al. (2023) 2011 grounding line position. This is further illustrated in Figure 6.7a where we delineate the areas spanned annually by all grounding lines mapped in 2011, 2016, and 2017. These polygons incorporate any sub annual variability in the grounding line (e.g. due to tidal oscillation) and any imprecision within the method. As such they provide indicators of the uncertainty of an annual grounding line position resulting from the combination of these factors. We observe that the 2011, 2016, and 2017 grounding area polygons cover largely the same areas. We note that the locations of these polygons agree with the height above flotation shown in Figure 6.7b.

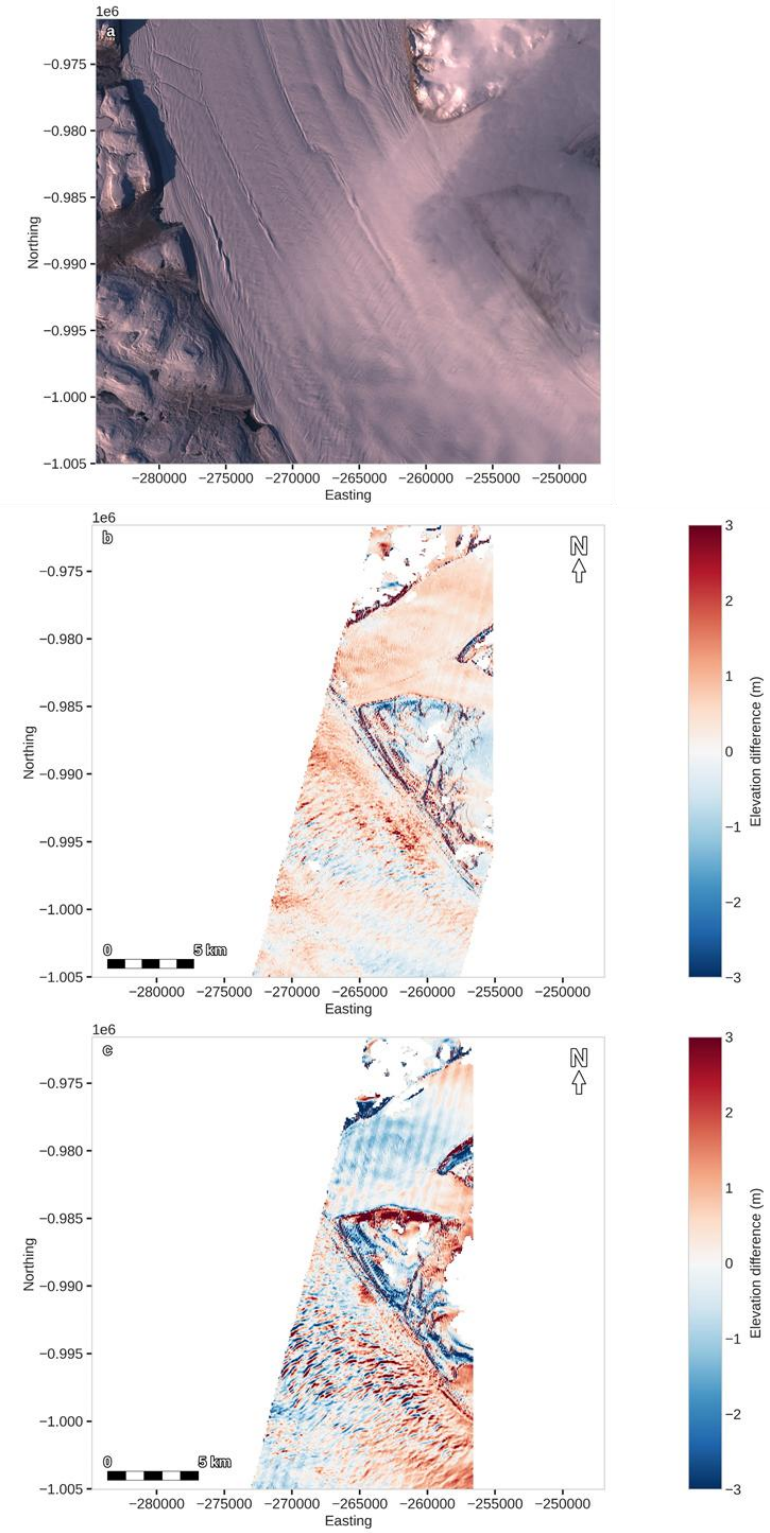


Figure 6.5: DEM elevation difference examples for Petermann Gletsjer. Panel a presents a Sentinel-2 optical satellite image dated 8th September 2017 as contextual reference for the data in panels b and c. In panel b, we present the elevation difference between DEM 1 (17th August 2017) and DEM 2 (20th August 2017) with a modelled tidal height difference of 1.25 m. In panel c, we present the elevation difference between DEM 3 (7th September 2017) and DEM 4 (21st September 2017) with a modelled tidal height difference of 0.86 m.

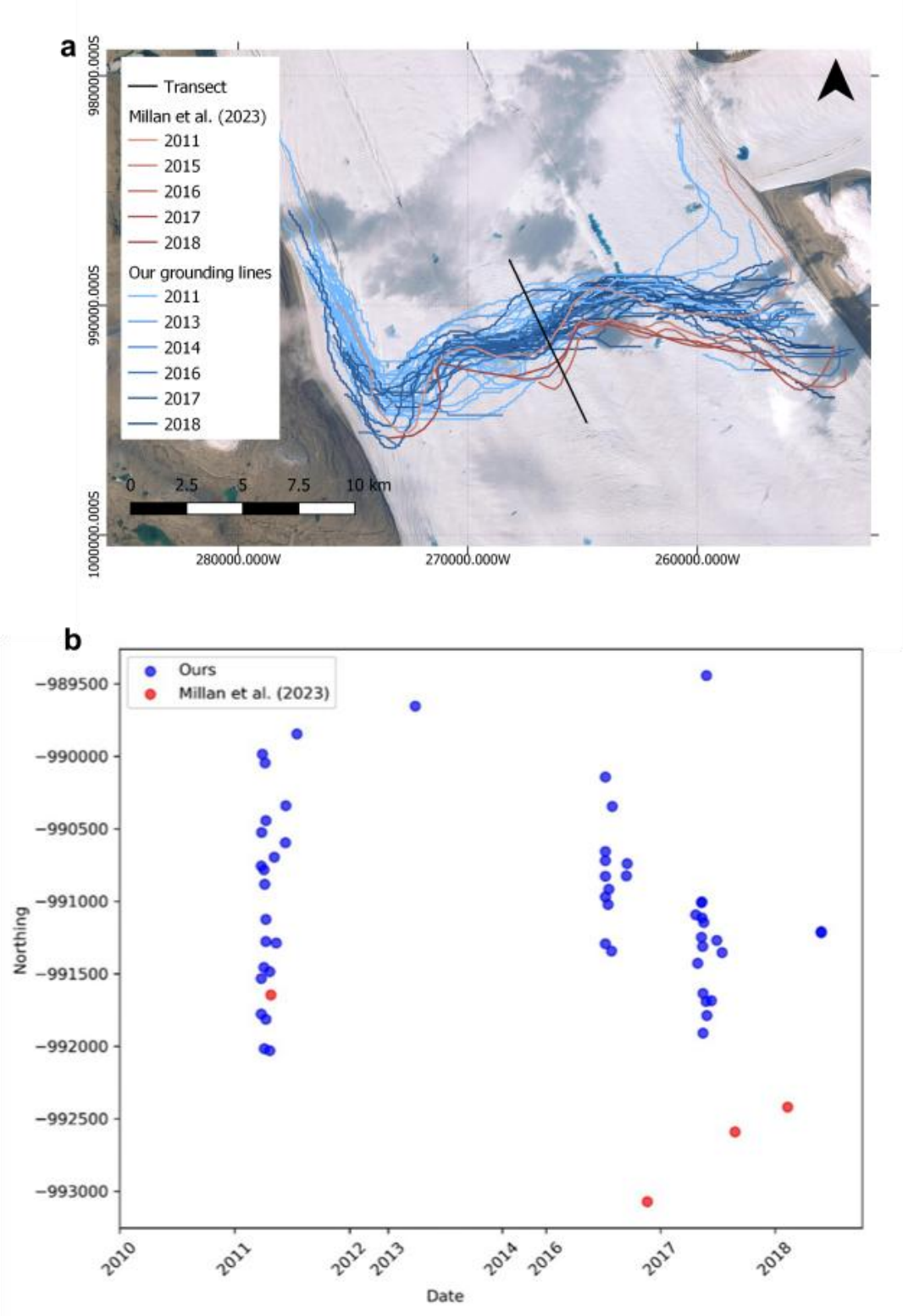


Figure 6.6: A comparison of the locations and geometries of the Millan et al. (2023) grounding lines between 2011 and 2018 and our grounding lines on Petermann Gletsjer. The data in panel b were sampled along the transect line in panel a. The base map data in panel a are courtesy of Earthstar Geographics via Esri.

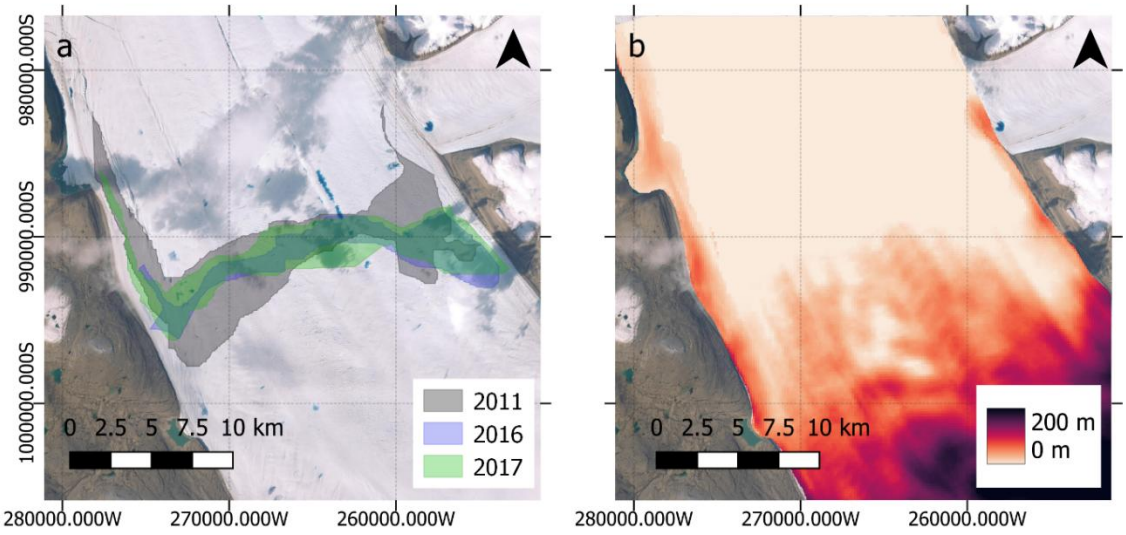


Figure 6.7: Envelopes of grounding lines and height above flotation for Petermann Gletsjer. Panel a presents polygons representing the envelopes of our 2011 (grey), 2016 (blue), and 2017 (green) grounding lines for Petermann Gletsjer. Panel b shows the height above flotation for Petermann Gletsjer, calculated per Eq. 6.1. The base map data in both panels are courtesy of Earthstar Geographics via Esri.

In Table 6.1, we present the temporal distribution of our new grounding line segments versus the number of DEM pairs available after filtering (Sect. 6.5.2) for Petermann Gletsjer. Of Petermann Gletsjer's 1371 DEM pairs, 1103 were from 2011, along with 51 of our new grounding line segments. We have also delineated several tens of new grounding line segments for 2016 and 2017.

Table 6.1: The temporal distribution of our new grounding line segments compared to the number of DEM pairs for Petermann Gletsjer.

| Year | Number of DEM pairs | Number of new grounding lines |
|---|---|---|
| 2010 | 7 | 0 |
| 2011 | 1103 | 51 |
| 2012 | 1 | 0 |
| 2013 | 3 | 1 |
| 2014 | 3 | 1 |
| 2015 | 0 | 0 |
| 2016 | 109 | 23 |
| 2017 | 90 | 30 |
| 2018 | 52 | 6 |

| | | |
|---|---|---|
| 2019 | 1 | 0 |
| 2020 | 1 | 0 |
| 2021 | 1 | 0 |
| Total | 1371 | 112 |

### 6.6.2 Storstrømmen

Storstrømmen consists of two lobes. The major southern lobe ('Lobe 1') was our initial focus of study following our understanding from Millan et al. (2023) that the minor northern lobe was completely grounded. However, our results suggest that this secondary lobe, which we will henceforth refer to as 'Lobe 2', may have also been floating between at least 2014 and 2018. In Figure 6.8, we present examples of DEM differences and associated grounding lines for Lobe 1 and Lobe 2 along with reference grounding lines from Millan et al. (2023) for Lobe 1.

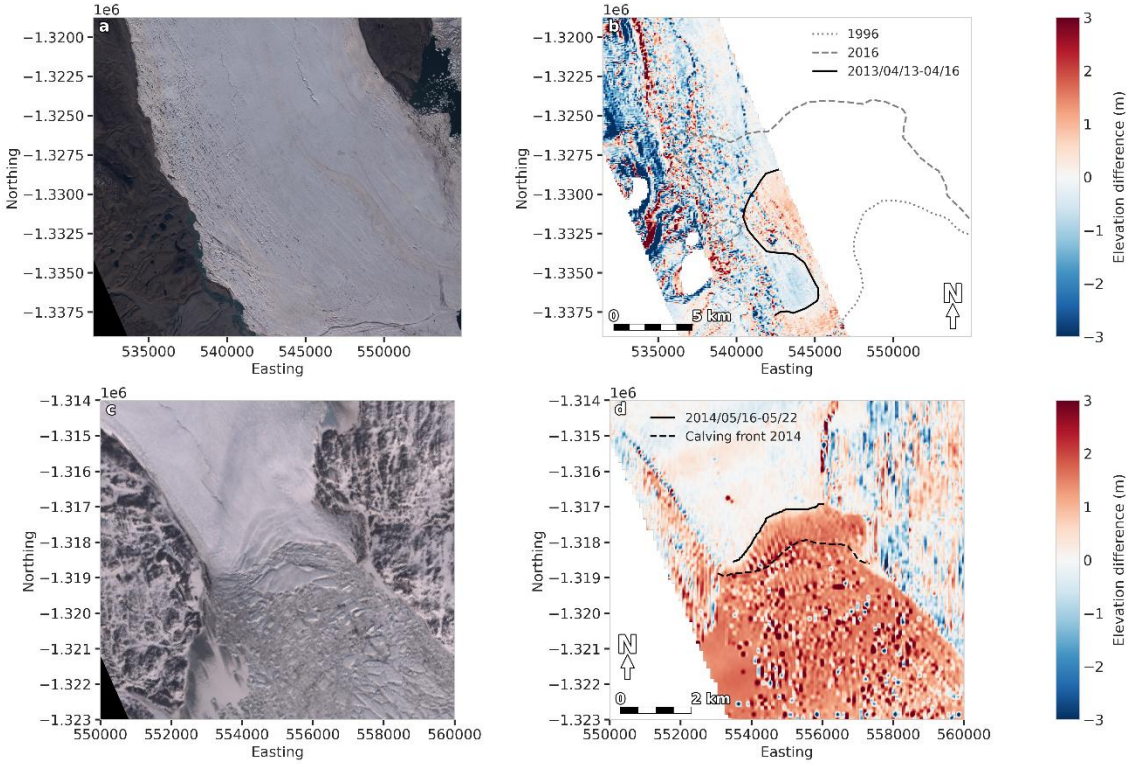


Figure 6.8: DEM elevation difference and grounding line information for Storstrømmen. Panel a presents a Landsat 8 optical satellite image dated 23rd August 2013 as contextual reference for the data in panel b. In panel b, we present the elevation difference between DEM 1 (13th April 2013) and DEM 2 (16th April 2013) with a modelled tidal height difference of 0.71 m. Also on this panel, we show the Millan et al. (2023) grounding lines, dated 1996 and 2016, and our

grounding line. Panel c presents a Landsat 8 optical satellite image dated 22nd May 2014 as contextual reference for the data in panel d. In panel d, we present the elevation difference between DEM 3 (16th May 2014) and DEM 4 (22nd May 2014) with a modelled tidal height difference of 1.08 m. Also on this panel, we show the calving front (14th May 2014) delineated using the Google Earth Engine Digitisation Tool (GEEDiT) (Lea, 2018), and our grounding line.

Figure 6.8b highlights a particularly interesting result from April 2013, revealing a distinct S-shaped grounding line on Lobe 1, in contrast to the more typical grounding line that runs approximately perpendicular to the direction of glacier flow. Our newly mapped grounding line from 2013 sits between the reference grounding lines (dated from 1996 and 2016) (Millan et al., 2023) and represents another example of the capability of our method to fill what would otherwise be gaps in the existing grounding line record. The noise on this subplot is caused by the movement of lateral crevasses and surface streams on the west side of the glacier. These features are visible in Figure 6.8a.

In Figure 6.9a, we present a comparison of the Millan et al. (2023) grounding lines between 2016 and 2020 versus our 12 new grounding line segments for Storstrømmen Lobe 1. For the central portion of the glacier, our grounding line segments and the Millan et al. (2023) grounding lines are located in approximately similar locations, with variation for our grounding lines dated from 2013 and 2014. In Figure 6.9b, we also present a plot of the height above flotation for Lobe 1, providing an independent measure of the likely grounding line position in 2007 (the nominal date of the BedMachine version 5 surface elevation data (Morlighem et al., 2022)). Figure 6.9b also suggests light grounding on the area close to the western flank of the glacier which agrees with the location of the S-shaped grounding line in Figure 6.8b.

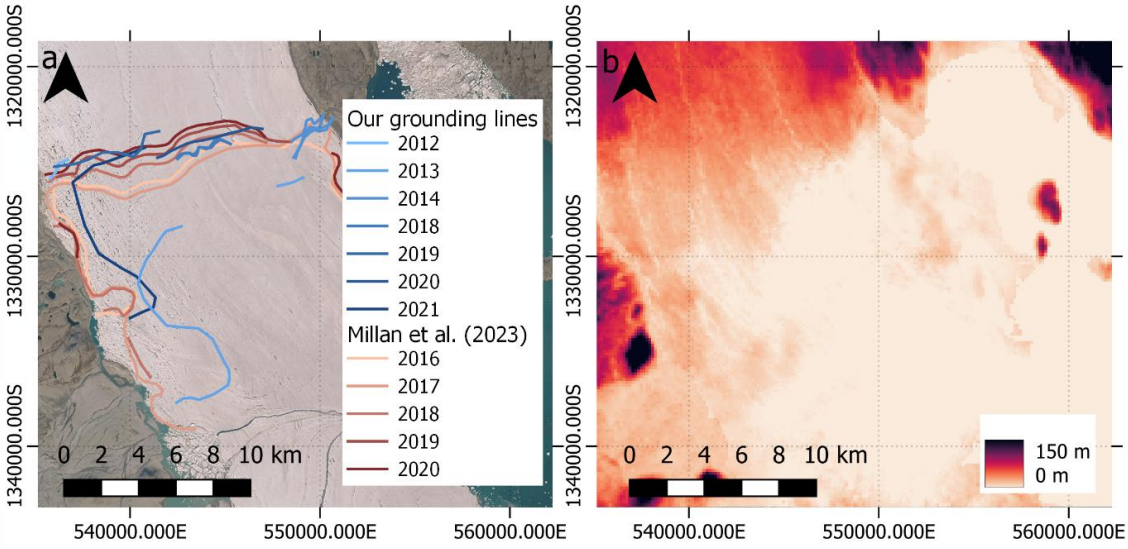


Figure 6.9: A comparison of the locations of our Storstrømmen Lobe 1 grounding lines versus the 2010s Millan et al. (2023) grounding lines (panel a), and the height above flotation for Storstrømmen Lobe 1, calculated per Eq. 6.1 (panel b). The base map data in panel a are courtesy of Earthstar Geographics via Esri.

Figure 6.8d also provides new insight into the terminus regime of this glacier. This difference map is comprised of DEMs dated from May 2014 and shows a clear signal between grounded and floating ice. The floating extension of the 2014 lobe is approximately 3.85 $km^2$ as determined by our delineation of the contemporary glacier margin using GEEDiT (Lea, 2018), making it ~0.4 $km^2$ larger than New York's Central Park. The noisy signals on the sea in Figure 6.8d are caused by the movement of floating ice within the fjord. In Figure 6.10a, we present our 80 new Storstrømmen Lobe 2 grounding line segments versus the Millan et al. (2023) 1992 and 1996 grounding lines. In Figure 6.10b, we also present the height above flotation for this lobe, independently suggesting its potential floating nature. In Table 6.2, we show the temporal distribution of the number of DEM pairs and the number of grounding lines available per lobe. We have delineated 92 new grounding line segments for Storstrømmen, of which 80 are located on Lobe 2 – a lobe previously considered to be fully grounded.

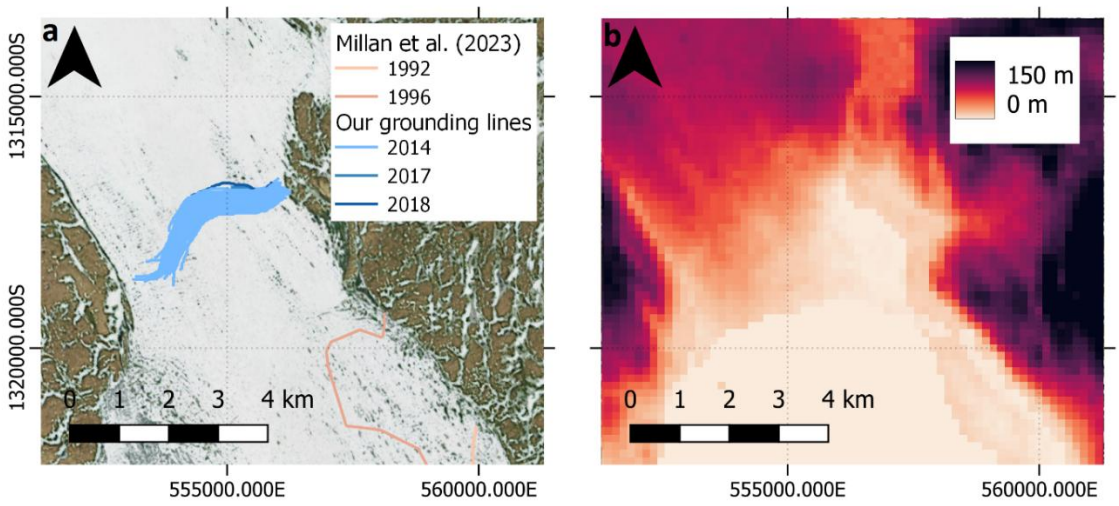


Figure 6.10: A comparison of the locations of our Storstrømmen Lobe 2 grounding line segments versus the Millan et al. (2023) grounding lines (panel a), and the height above flotation for Storstrømmen Lobe 2, calculated per Eq. 6.1 (panel b). The base map data in panel a are courtesy of Earthstar Geographics via Esri.

Table 6.2: The temporal distribution of our new grounding line segments compared to the number of DEM pairs for Storstrømmen.

| Year | Number of DEM pairs | | Number of new grounding lines | |
|---|---|---|---|---|
| | Lobe 1 | Lobe 2 | Lobe 1 | Lobe 2 |
| 2012 | 2 | 0 | 1 | 0 |
| 2013 | 2 | 0 | 2 | 0 |
| 2014 | 5 | 90 | 4 | 78 |
| 2015 | 0 | 0 | 0 | 0 |
| 2016 | 0 | 0 | 0 | 0 |
| 2017 | 1 | 1 | 0 | 1 |
| 2018 | 2 | 1 | 2 | 1 |
| 2019 | 1 | 0 | 1 | 0 |
| 2020 | 4 | 0 | 1 | 0 |
| 2021 | 2 | 0 | 1 | 0 |
| Total | 19 | 92 | 12 | 80 |

### 6.6.3 79N

Delineating the grounding lines of 79N using our new method proved more difficult than delineating either Petermann Gletsjer's or Storstrømmen's due to the more limited availability of DEMs. 79N had only 18 DEM pairs from which we could potentially extract grounding lines. From these 18 pairs, we were able to tentatively delineate seven grounding line segments, although these delineations were relatively uncertain.

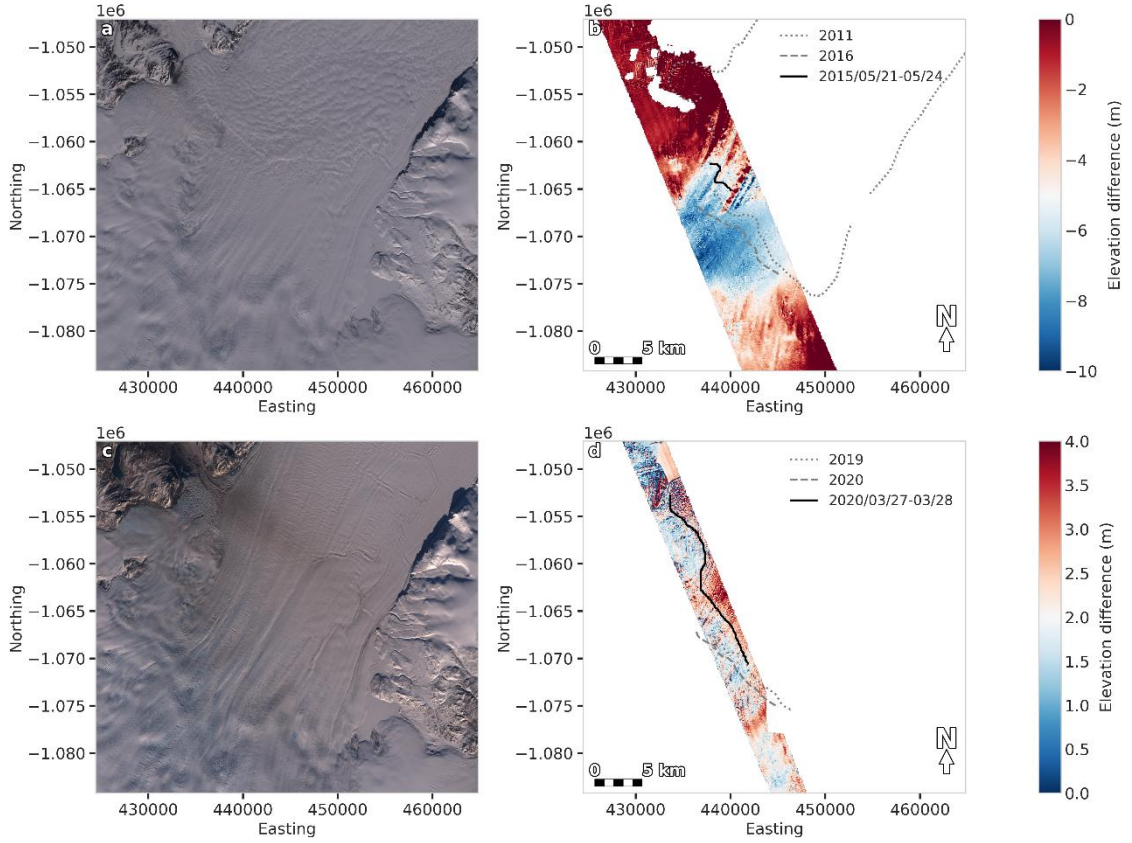


Figure 6.11: DEM elevation difference and grounding line information for 79N Gletsjer. Panel a presents a Landsat 8 optical satellite image dated 28th May 2015 as contextual reference for the data in panel b. In panel b, we present the elevation difference between DEM 1 (21st May 2015) and DEM 2 (24th May 2015) with a modelled tidal height difference of 0.52 m. Also on this panel, we show the Millan et al. (2023) grounding lines, dated 2011 and 2016, and our tentative grounding line. Panel c presents a Landsat 8 optical satellite image dated 16th April 2020 as contextual reference for the data in panel d. In panel d, we present the elevation difference between DEM 3 (27th March 2020) and DEM 4 (28th March 2020) with a modelled tidal height difference of 0.70 m. Also on this panel, we show the Millan et al. (2023) grounding lines, dated 2019 and 2020, and our tentative grounding line.

Figure 6.11 shows two examples of these grounding line segments. Although these examples are not as clear as those shown in Figure 6.4 or Figure 6.8, we show them to elucidate the difficulties posed by both poor data quality and satellite jitter. Jitter, in the case of satellites, refers to small, unintended movements or vibrations during imaging, which can cause blurring or misalignment in the captured data. The differenced DEM in Figure 6.11b was comprised of DEMs dated from May 2015 and the reference grounding lines (Millan et al., 2023) are dated from 2011 and 2016. In this panel, we choose to delineate only a portion of the grounding line due to the along-track (perpendicular to the long-side of the differenced DEM) jitter signal visible between E: 438,934 m, N: -1,067,738 m and E: 443,683 m, N: -1,065,885 m which meant we were unable to delineate the grounding line south of this area.

The differenced DEM in Figure 6.11d is comprised of DEMs dated from March 2020, with the reference grounding lines dated from 2019 and 2020. Across-track (parallel to the long-side of the differenced DEM) jitter is visible in this panel and our confidence in the grounding line location is limited by the along-track width of the differenced DEM. In Figure 6.12a, we present our seven new, tentative grounding line segments for 79N along with a comparison to the Millan et al. (2023) grounding lines. Figure 6.12b shows the height above flotation for 79N as contextual reference for the locations of the tentative grounding line segments in Figure 6.12a. This provides us with independent evidence of the location of the grounding area.

In Table 6.3, we show the temporal distribution of our new tentative grounding line segments for 79N, along with the number of DEM pairs available for study. We delineated four new, tentative grounding line segments for 2015, although we note that three of these were based on DEM pairs which comprised DEMs dated 2015-05-21 and 2015-05-24, meaning that these grounding lines will, in effect, delineate largely the same grounding line location, giving an indication of the precision of our method.

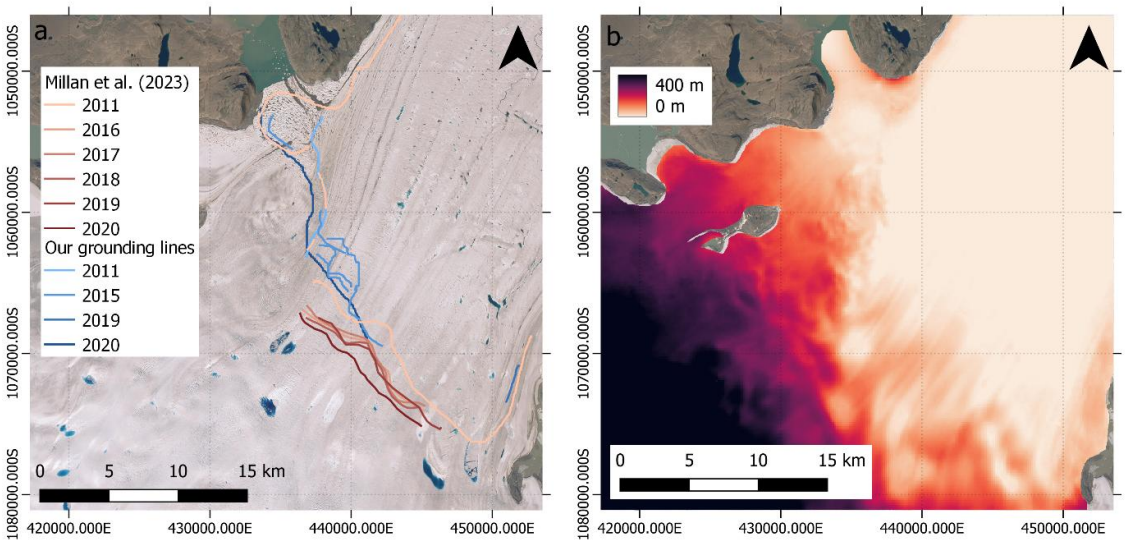


Figure 6.12: A comparison of the locations of our tentative 79N Gletsjer grounding line segments versus the Millan et al. (2023) grounding lines (panel a), and the height above flotation for 79N Gletsjer, calculated per Eq. 6.1 (panel b). The base map data in both panels are courtesy of Earthstar Geographics via Esri.

Table 6.3: The temporal distribution of our new, tentative grounding line segments compared to the number of DEM pairs for 79N.

| Year | Number of DEM pairs | Number of new grounding lines |
|---|---|---|
| 2011 | 1 | 1 |
| 2012 | 3 | 0 |
| 2013 | 3 | 0 |
| 2014 | 0 | 0 |
| 2015 | 5 | 4 |
| 2016 | 0 | 0 |
| 2017 | 1 | 0 |
| 2018 | 0 | 0 |
| 2019 | 4 | 1 |
| 2020 | 1 | 1 |
| Total | 18 | 7 |

## 6.7 Discussion

In this study, we present a novel method for delineating grounding lines using high-resolution DEM differencing. Our method couples DEMs with a tidal model to find high-low tidal pairs and we have shown that it is capable of determining the locations of grounding lines on two major ice tongues in northern Greenland, with possible success at one more. In the following sections, we discuss the benefits and limitations offered by this new method.

### 6.7.1 Benefits of the method

#### 6.7.1.1 Temporal gap-filling capabilities

Millan et al. (2023) provide the most comprehensive grounding line dataset for northern Greenland, with grounding lines mapped for Petermann Gletsjer in 1992, 1996, 2011, and 2015-2021. While this is an invaluable record, on its own it does not meet the GCOS recommendation of annual sampling (WMO et al., 2022). Our method provides the ability to delineate grounding lines from a non-SAR dataset and complements this record with a grounding line segment for 2013 and one for 2014. Additionally, we have delineated a large number of grounding line segments for 2011, 2016, 2017, and a further six for 2018. The locations of our grounding lines largely agree with the general placement and geometry of the Millan et al. (2023) dataset, and we suggest that deviations are likely due to the differences in acquisition dates and subjectivity of manual delineation from both InSAR and DEM data. Although radar data (e.g. from Operation IceBridge) could offer point validation of grounding line locations, coverage over our glaciers is limited both spatially and temporally. A systematic analysis using this dataset falls beyond the scope of this study which sought to demonstrate the feasibility of using tidally coupled DEMs to delineate grounding lines. However, future research could validate manually delineated grounding lines, such as those derived using this method and those derived by Millan et al. (2023), using other data such as Operation Icebridge to determine their relative agreement and accuracy.

Millan et al. (2023) mapped grounding lines for Storstrømmen's major southern lobe using data acquired in 1996, and 2016-2020. In this study, we have located grounding lines which help back-fill the historical record, with grounding line segments dated from 2012, 2013, 2014 and 2021 for the southern lobe, further extending the grounding line record for Storstrømmen. Overall, for this lobe, we have delineated 12 new grounding

line segments between 2012 and 2021 which aid in our understanding of the grounding line's migration. As mentioned previously, the migration patterns of Storstrømmen are indicative of surge behaviour, with major retreat preceding sudden advancement. While this method does not attempt to diagnose surge behaviour, more complete grounding line records could provide useful context for future studies on ice dynamics, making the exploitation of DEM differencing a particularly important avenue for filling temporal gaps left by the commonly used SAR datasets. Our method also provides data coverage for areas that are otherwise understudied or lacking direct observations from SAR, offering new insights into regions of the grounding line that have been difficult to analyse with existing approaches.

For 79N, Millan et al. (2023) produced grounding line estimates for 1992, 1994, 1996, 2011, and 2016-2020. We bolster this dataset with four tentative new grounding line segments from 2015, and one each from 2011, 2019 and 2020 – years covered by Millan et al. (2023). Our grounding lines agree with the general location of the Millan et al. (2023) dataset, but our analysis was limited by the availability and quality of suitable DEM pairs. Although there were 1883 DEMs available for study over 79N, there were only 18 DEM pairs that met all of our temporal and spatial data stipulations. Of these 18, we could tentatively delineate new grounding line segments from seven, making 79N our most limited result.

#### 6.7.1.2 Annual fluctuations in grounding line location

The spread of Petermann Gletsjer's grounding lines (Figure 6.6) between 2011 and 2018 shows a clustering of data around the Millan et al. (2023) 2011 grounding line. We see retreat trends to the west and east margins of the grounding line, with no real trend observable across most of the central portion except the very centre which shows a slight retreat. However, the volume of data available for 2011 has led to a large spread of grounding lines for this year, implying no significant change in grounding line location between 2011, 2016, and 2017, relative to the intra-annual variability (Figure 6.7). For the period between 1992 and 2016, Hogg et al. (2016) found that the west of Petermann Gletsjer's grounding line was stable, with the east of the grounding line being unusually variable. They attributed an average 18% of the observed grounding line movement to be due to tidal variations (Hogg et al., 2016). Our results support this assertion; that the observed retreat in previous grounding line records of Petermann Gletsjer may not solely reflect long-term retreat but could instead be influenced by the tidally induced migration

of the grounding line, i.e. whether individual grounding lines were mapped at high or low tide. This illustrates the value of high frequency sampling of grounding lines to distinguish between different periodicities of grounding line migration.

#### 6.7.1.3 Identification of a new floating extension

There are only two historical grounding line records for Storstrømmen's northern lobe. These are from 1992 and 1996, with the lobe now considered fully grounded as of the late 1990s (Millan et al., 2023). However, our research suggests that this minor northern lobe supported a 3.85 $km^2$ floating extension in 2014, reducing to a 3.25 $km^2$ area in 2018. Additionally, we have defined 80 new grounding line segments for this lobe – 78 of which are in 2014, with one each in 2017 and 2018. This illustrates the potential of our new method to identify previously unresolved floating portions of other glaciers that may have been missed by traditional approaches.

### 6.7.2 Limitations and opportunities for further research

#### 6.7.2.1 Jitter

Jitter caused major issues during the delineation of our grounding lines. In Figure 6.13 we present examples of differenced DEMs affected by along- and across-track jitter on Petermann Gletsjer. Both examples in this figure are from May 2011.

Table 6.4 shows the number of DEM pairs which were affected by jitter across each glacier, along with the number of DEM pairs where the jitter was so pronounced that we were unable to discern a grounding line signature. We classified these characteristics through visual inspection. Although jitter was a major issue for our grounding line delineation – affecting 100% of the DEMs for Storstrømmen Lobe 2 – it only prohibited the drawing of a grounding line for a maximum of 22% of the available DEM pairs for each glacier.

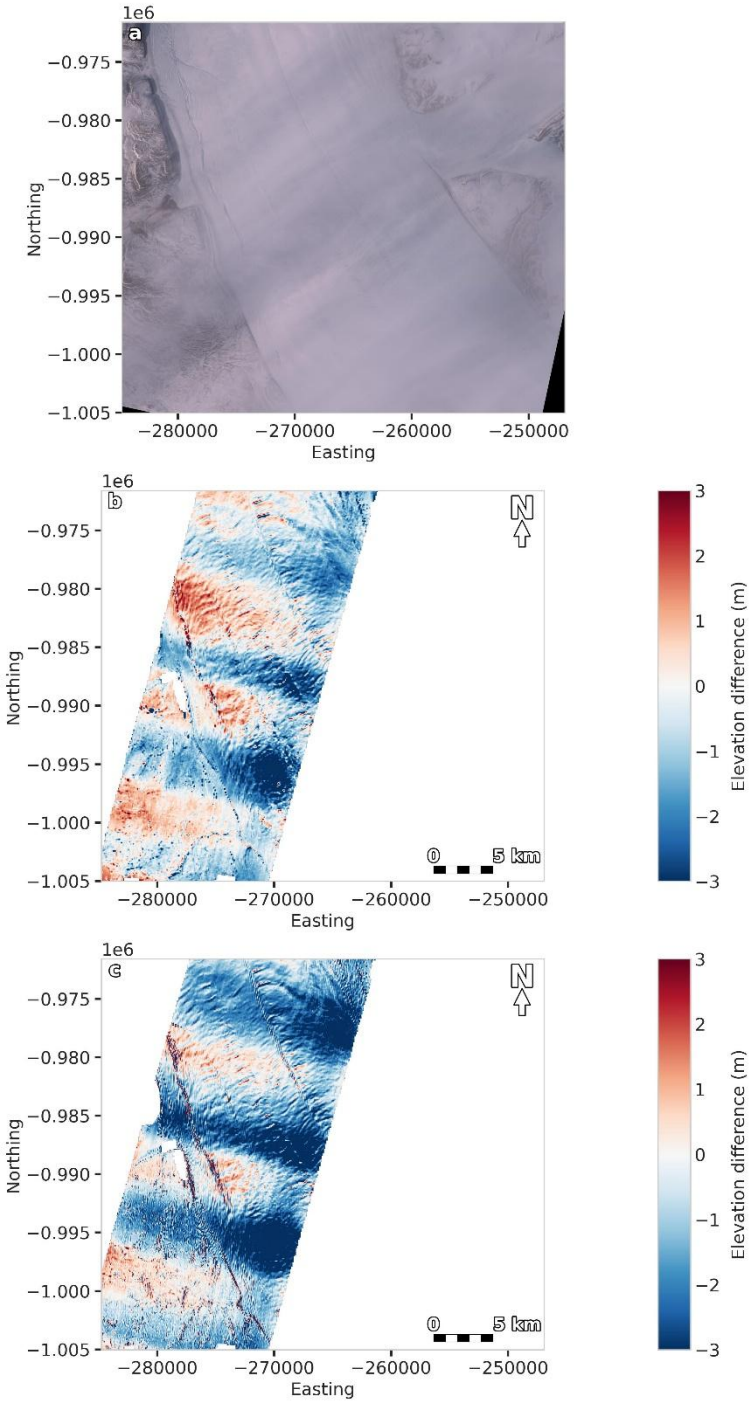


Figure 6.13: DEM elevation difference examples presenting jitter on Petermann Gletsjer. Panel a presents a Landsat 8 optical satellite image dated 23rd May 2013 as contextual reference for the data in panels b and c. In panel b, we present the elevation difference between DEM 1 (13th May 2011) and DEM 2 (26th May 2011) with a modelled tidal height difference of 0.88 m. In panel c, we present the elevation difference between DEM 3 (13th May 2011) and DEM 4 (26th May 2011) with a modelled tidal height difference of 0.88 m.

Table 6.4: For all three glaciers, the number of DEM pairs affected by jitter and the number of DEM pairs where jitter prohibited grounding line delineation.

| Glacier name | Number of DEM pairs affected by jitter out of total number of pairs | Number of DEM pairs where jitter prohibited grounding line delineation |
|---|---|---|
| Petermann Gletsjer | 408/1371 (30%) | 285 (21% of total) |
| 79N | 14/18 (78%) | 4 (22% of total) |
| Storstrømmen 1 | 13/19 (68%) | 2 (11% of total) |
| Storstrømmen 2 | 92/92 (100%) | 11 (12% of total) |

This posed a major challenge for our method, with over a third of the total 1500 DEM pairs affected by jitter to varying degrees. Approximately 20% of our DEM pairs were so badly affected by jitter that there were no visible grounding line signatures. There is a possibility that we could have delineated another ~300 grounding lines had jitter not affected our data. Jitter is a well-known issue that affects stereoscopic DEMs (Girod et al., 2015; Liu et al., 2016). However, correcting for this issue in full remains an unsolved challenge and, to date, no existing study has fully resolved it. Future work could address this issue by removing the jitter signal prior to differencing. This could be done by fitting a harmonic model (e.g. a sum of sine and cosine terms, as in harmonic regression or Fourier decomposition) to each DEM to estimate the spatially coherent jitter waveform and subtracting it to produce detrended DEMs before calculating elevation differences. While our method successfully achieves the goal of proving that DEM differencing may be used to determine grounding line location, it could be further improved if the effect of jitter was fully modelled and corrected.

#### 6.7.2.2 Future research potential

Here, we have focused on proving the capabilities of our method at three study sites in Greenland. In the future, this method could be further developed to increase its use in both space and time. Spatially, it could be applied to other Greenlandic glaciers (see Chapter 5) and also tested over the Antarctic ice shelves using the Reference Elevation Model of Antarctica (REMA) (Howat et al., 2022), which is the southern hemisphere's counterpart to ArcticDEM. Temporally, this method could be applied to other DEM

datasets such as the timestamped Advanced Spaceborne Thermal Emission and Reflection Radiometer (ASTER) dataset (e.g. Girod et al., 2015, 2017; Abrams et al., 2020) which would extend the duration of the scientific record.

The availability of more datasets which can be used to delineate grounding lines means that we can validate previous approaches and provide greater confidence in their validity, along with increasing temporal sampling, expanding the duration of the scientific record, and improving our understanding of grounding line migration and behaviour. Using methods which exploit previously underutilised data allows us to improve our confidence in the locations of these grounding lines and here we have successfully proved that this can be done with DEM differencing in combination with a tide model.

## 6.8 Conclusions

In this study, we have developed and visually appraised a new method for identifying Greenlandic grounding lines, using differenced DEMs in combination with a tide model. We exploit a high-resolution DEM dataset (ArcticDEM) which is historically underutilised in grounding line research. Our method has helped to fill gaps in the historical record for the Petermann Gletsjer, 79N and Storstrømmen glaciers, and additionally helped to determine the presence of 3.45 $km^2$ floating extension on the minor northern lobe of Storstrømmen as of 2018. The volume of data over Petermann Gletsjer has allowed us to produce estimates of the potential grounding areas for 2011, 2016, and 2017, and suggests that perceived retreat of the grounding line may have more uncertainty than previously assumed, due to the potential impact of short-term tidally induced oscillations. These findings enhance our ability to monitor ice sheet grounding line dynamics, which is critical for understanding its ongoing evolution and contribution to sea-level rise.

Our study represents a significant methodological advancement in grounding line detection. By demonstrating the viability of DEM differencing coupled with tidal modelling, we provide a new tool for monitoring grounding lines in Greenland and potentially Antarctica. The theories and methods presented here are transferable to REMA (Howat et al., 2022) allowing similar applications on the large floating ice shelves of the Antarctic ice sheet, and ASTER (Abrams et al., 2020), allowing for a temporal expansion of the scientific record. By enhancing our ability to track grounding line evolution, this research contributes to ongoing efforts to improve projections of ice sheet stability and sea level rise, with implications for climate change adaptation and coastal resilience planning. Our study advances the use of DEMs for ice sheet monitoring, providing a valuable tool for understanding cryospheric change in a warming climate.

# 7 Synthesis

## 7.1 Introduction

In this thesis, I have demonstrated how digital elevation modelling data can be used to map and measure a range of glaciologically important features of the Greenland ice sheet. In doing so, I have addressed my overarching aim, which was to develop and refine methodological approaches that leverage digital elevation models (DEMs). I primarily used two datasets to achieve this – ArcticDEM 2 m resolution strip DEMs (version s2s041) (Porter et al., 2022) and the ArcticDEM 100 m mosaic version 4 (Porter et al., 2023) – both of which were developed and distributed by the Polar Geospatial Center (PGC).

The research manuscripts which I presented in Chapters 4, 5, and 6 contributed to this aim in different ways. In Chapter 4, I validated the most commonly used method of determining supraglacial lake depth through the study of five supraglacial lakes in southwest Greenland using a DEM approach and a laser altimetry approach. This addressed a pressing gap in our current understanding of the accuracy of such methods, which had generally received little attention in terms of targeted validation activities and sensitivity analysis in the past. In Chapter 5, I presented a method for determining the decadal signature of a glacier's floating ice using a DEM stacking approach. Chapter 6 presented a novel method for determining grounding line location. In this study, I coupled a tidal model with DEMs to determine high-low tidal pairs and then differenced these pairs to find the location of the grounding lines of three major marine-terminating glaciers in northern Greenland.

This final chapter of my thesis provides a comprehensive overview of the key findings, synthesis, broader impact, and future directions of the research presented in this work. I begin with a summary of each of the main results chapters, each contributing to our understanding of ice sheet processes through the innovative use of ArcticDEM, from validating supraglacial lake depth estimation to refining grounding line detection methods. The synthesis section discusses the synergies and conceptual progression of the research, demonstrating how each chapter builds on the last to deepen our understanding of ice sheet processes. A section on broader impact follows, highlighting the contributions of this work to the wider field, particularly in enhancing the methodology and potential

applications for future glaciological studies and climate assessments. Next, I propose future research directions which consider the limitations of – and suggest opportunities for further improving and expanding – the methods presented within this thesis, paving the way for new applications in glaciology. Finally, I summarise the key conclusions of the thesis and reflect on its overall contribution to the field of ice sheet research.

## 7.2 Summary of key findings

This section introduces the three chapters that form the core of this thesis, each focusing on different aspects of ice sheet processes and the use of ArcticDEM for glaciological analysis. In the following subsections, I summarise the findings from each of these chapters in turn.

### 7.2.1 Chapter 2: Supraglacial lake depth validation

Chapter 4 presented a detailed intercomparison of three established approaches used to estimate supraglacial lake depth, a key parameter in determining lake volume. Knowing the water volume of lakes on ice sheets is essential for understanding their impact on ice dynamics, basal lubrication, and potential contributions to sea level rise, meaning that knowing a lake's depth is equally important. The methods I presented in this chapter were; (i) an optical remote sensing method based on the Philpot (1987) radiative transfer equation (RTE), (ii) a method based on the mapping of an empty lake basin from ArcticDEM, and (iii) ICESat-2 laser altimetry retrievals of water column depth.

The results demonstrated that depth estimates derived from ArcticDEM 2 m DEMs and ICESat-2 are in close agreement (Pearson's $r$ = 0.98), suggesting that these methods provide relatively reliable measurements. However, both approaches are constrained by limited spatial and temporal availability of the required input data, rendering them unsuitable for ice-sheet-wide depth estimation. In contrast, the RTE method, applied to optical satellite imagery, offers the potential for large-scale deployment but exhibits larger discrepancies in depth retrieval relative to the other methods, particularly for deeper lakes. We observed a systematic underestimation of depth using the red-band RTE (up to 63%) and a depth plateauing effect, both of which we attributed to the rapid attenuation of light in this wavelength range. While the green-band RTE provided improved depth estimates of shallow lakes and no evident depth plateau in the studied lakes, its accuracy remained sensitive to the choice of input parameters, and it overestimated depths by up to 153%.

A comprehensive sensitivity analysis of the RTE highlighted that the parameter $A_d$, which represents the reflectance of the lake bottom, has the strongest influence on derived depths. However, determining $A_d$ is inherently challenging as it is estimated as a ring of pixels around the lake, and the lake edge is often difficult to distinguish from the surrounding ice within optical satellite imagery. The methods currently used in the literature to calculate $A_d$ appear to limit the accuracy of the green-band RTE, at least

within the five-lake case study presented within this chapter. Further investigation is required to assess whether these findings are generalisable across the entire ice sheet. Despite its limitations, the RTE method currently remains the only viable option for ice-sheet-wide depth estimation, meaning improvements to its parameterisation are essential.

### 7.2.2 Chapter 3: Floating ice tongue detection via DEM deviation

Chapter 5 developed and assessed a novel method for detecting the floating ice extents of northern Greenland's marine-terminating glaciers using stacks of timestamped ArcticDEM 2 m DEMs. Traditional floating ice detection methods primarily rely on synthetic aperture radar (SAR) interferometry, which, while effective, is limited by temporal data availability and the need for relative stability in the surface backscattering characteristics. ArcticDEM has similar limitations, but its temporal coverage differs from that of SAR. For example, ArcticDEM provides data during the period between the cessation of ERS-2 operations and the start of Sentinel-1 (2012-2013 inclusive). This study explored the potential of using DEM elevation variations as an alternative or complementary approach to SAR-based floating ice detection.

The method involves analysing the temporal variance in elevation within a DEM stack to identify regions where vertical ice motion and tidal influences suggest the transition from floating to grounded ice. To assess its effectiveness, we incorporated historical calving front locations, historical grounding line positions, and bed elevation data into the analysis of 15 northern Greenlandic marine-terminating glaciers. With this DEM-based approach we detected apparent flotation signatures on five glaciers, found no evidence for a floating extension on eight (due to a lack of real floating ice signatures), and observed two cases where there are possible flotation signatures on at least one lobe. The only glacier where the method found no detectable flotation signatures due to method failure was Petermann Gletsjer, where high ice velocity and surface roughness likely obscured the detection of floating ice.

These findings demonstrate that DEM height variations have the potential to serve as a valuable proxy for floating ice extents, providing decadal-scale insight into glacier dynamics. However, several challenges affected the interpretation of our results, meaning that this study offers a proof of concept as opposed to a complete method of definitively locating floating ice. The advection of surface features with ice flow can introduce additional elevation variability at any fixed point in space, complicating the identification

of floating ice signals, while inconsistencies in DEM alignment may result in vertical offsets that impact accuracy.

Despite these challenges, this study provides strong evidence that ArcticDEM-derived elevation deviations can supplement existing SAR-based floating ice extent datasets. By expanding the range of tools available for floating ice monitoring, this method contributes to a more comprehensive understanding of the Greenland ice sheet's stability.

### 7.2.3 Chapter 4: Grounding line detection via DEM differencing coupled with a tidal model

The study in Chapter 6 developed a novel method for detecting Greenlandic grounding lines by combining ArcticDEM 2 m DEMs with the Finite Element Solution Model (2022) (FES2022) tide model. We chose this tidal model because it outperforms all other global tidal solutions for all tidal waves when compared to tidal gauges (Carrère et al., 2022). We applied the method to three major marine-terminating glaciers in Greenland: Petermann Gletsjer, Nioghalvfjerdsbræ (79 North or 79N), and Storstrømmen. By analysing DEM height differences across tidal cycles, we mapped 211 new partial grounding lines between 2011 and 2021 (Petermann Gletsjer: 112, 79N: 7, Storstrømmen: 12 (Lobe 1) and 80 (Lobe 2)), significantly expanding the historical record for these glaciers. Notably, the method identified a 3.45 km² floating extension on the minor northern lobe (Lobe 2) of Storstrømmen as of 2018, a lobe which was previously believed to be grounded as of the late 1990s (Millan et al., 2023). For Petermann Gletsjer, where data availability was particularly high, we estimated partial grounding line positions for 2011, 2013, 2014, 2016, 2017, and 2018. The results suggest that previously perceived grounding line retreat may be subject to greater uncertainty than assumed, due to the impact of short-term tidally induced oscillations that create transient changes in grounding position. This new approach enhances our ability to assess ice sheet grounding line dynamics, providing crucial insight into their stability and potential retreat under changing climate conditions.

By demonstrating that DEM differencing, when combined with tidal modelling, is a viable method for grounding line detection, this approach offers a complementary tool to SAR-based techniques, providing a means of expanding historical records and improving our understanding of grounding line evolution.

The ability to track grounding line changes with greater spatial and temporal resolution has significant implications for ice sheet stability assessments and sea level rise projections. By refining techniques for monitoring grounding lines, this research strengthens our capacity to predict future ice sheet behaviour and inform global efforts to mitigate and adapt to the impacts of cryospheric change.

## 7.3 Synthesis

In this section, I outline the synergies and conceptual progression of the research presented in this thesis, which moves from initial data validation to larger-scale applications and methodological refinements. Chapter 4 demonstrated strong agreement between ArcticDEM and ICESat-2 for supraglacial lake depth measurement, increasing our confidence in its reliability for broader ice sheet research applications. Chapter 5 extended the use of ArcticDEM to floating ice tongue detection, introducing a method for determining their decadal extents. Chapter 6 presented a new method for determining grounding line location, which overcame some of the surface velocity and artificial vertical offsets encountered in Chapter 5. These studies represent a range of different methods using high-resolution DEMs, each contributing to a deeper understanding of ice sheet processes and providing a foundation for future research in this field.

### 7.3.1 Conceptual progression of the research

ArcticDEM is a rich and underutilised high-resolution dataset, and I use it within this thesis to investigate and develop methods to better understand ice sheet processes. I have done this in a number of ways, from improving our confidence in other depth-retrieval methods (Chapter 4) through to broader scale applications of determining the floating extents and grounding lines of glaciers in northern Greenland (Chapter 5 and Chapter 6).

In Chapter 4, I used ArcticDEM to measure the depth of supraglacial lakes. While previous studies have used other DEM sources for this purpose, such as those derived from stereo satellite imagery (e.g. Pope et al., 2016), this work established ArcticDEM's utility as a dataset from which we can extract high-resolution topographical data. By demonstrating the accuracy and reliability of ArcticDEM in this context, Chapter 4 laid the foundation for its further application in broader ice sheet studies.

Chapter 5 extended the use of DEMs to a larger-scale feature: floating ice tongues. Using ArcticDEM, this study developed a novel method to identify floating ice extents by analysing the deviations in a DEM stack spanning approximately a decade. This research provided a proof-of-concept for using DEMs to identify the decadal extents of a glacier's floating ice with reasonable accuracy, expanding the spatial extent and scale beyond the five small-scale surface features (lakes) studied in Chapter 4, to instead focus on a larger-scale analysis of northern Greenland and processes that are critical to ice sheet dynamics. This chapter also extends the temporal use of ArcticDEM compared to Chapter 4 which

focused on instantaneous realisations of topography from single DEM acquisitions. Comparatively, Chapter 5 shows how geophysical information can be extracted from stacks of DEMs, extending the analysis into the temporal dimension.

Chapter 6 presents a novel approach that couples individual DEMs with a tide model to find high-low tidal pairs which can be differenced to determine the grounding line location. One major challenge in Chapter 5 was the difficulty in delineating the extent of floating ice for fast-flowing glaciers, particularly in areas with extensive crevassing and surface ridges. The movement of these surface features obscured the deviation signal used for floating ice detection, even after smoothing. To mitigate this effect within Chapter 6, we introduced a time interval constraint for the high-low tidal DEM pairs, limiting the maximum difference to 14 days. For reference, a glacier moving at 1.4 km/yr glacier (e.g. 79N Gletsjer (Rignot and Kanagaratnam, 2006)) would experience ~54 m of displacement over 14 days – approximately half the resolution of the smoothed DEMs (100 m) – therefore meaning that any elevation variation caused by the velocity-induced displacement of surface features should be reduced during the smoothing step. The use of tidal pairs within a maximum time difference of 14 days allowed for the identification of grounding line change at a relatively fine temporal scale, increasing the potential for more detailed observations of ice sheet dynamics. Grounding lines are an essential climate variable (ECV) as determined by the Global Climate Observing System (GCOS) and they have a recommended temporal resolution of at least one estimate per year (WMO et al., 2022). By increasing the frequency of grounding line detection, Chapter 6 proved the applicability of ArcticDEM for monitoring short-term ice sheet changes, offering a new method for helping meet the GCOS annual target.

Another key challenge in Chapter 5 was vertical offsets introduced by the method. We vertically adjusted all DEMs against the grounded area upstream of each glacier, assuming that the rate of thinning/thickening in this area was the same as the floating downstream area. However, this assumption proved incorrect for some glaciers that exhibited differences in the thinning/thickening rates of their upstream and downstream areas. This led to artificial misalignment in the z-axis, making it difficult to interpret the transition between floating and grounded ice. To ensure we did not encounter this issue in Chapter 6, we implemented a different coregistration approach. Instead of aligning DEMs against the upstream grounded ice, we used the Nuth and Kääb (2011) method to coregister each strip DEM against the ArcticDEM mosaic. This approach relied on stable

bedrock areas as reference points, ensuring consistent coreferencing across all DEMs. The limiting of temporal difference between the constituent DEMs in the DEM pairs to 14 days also ensured we could not observe a significant elevation change in the ice thickness due to long-term thinning or thickening. By addressing both the velocity-induced deviation signal issues and vertical offset challenges from Chapter 5, Chapter 6 presents a novel method to reliability locate grounding lines.

These iterative adjustments highlight the role of exploratory findings in shaping later research decisions, demonstrating how the methods developed in this thesis evolved in response to real-world data limitations and analytical challenges. Together, these chapters demonstrate a conceptual progression from data validation to large-scale application and methodological refinement, ultimately advancing the use of ArcticDEM in ice sheet research.

### 7.3.2 Similarities and differences between the studies

The three studies in this thesis share a common foundation in their use of ArcticDEM for ice sheet feature analysis, yet they diverge in their specific applications, methodological approaches, and the challenges they address.

A fundamental similarity across all three studies is their reliance on ArcticDEM as the primary dataset. ArcticDEM provided a high-resolution elevation dataset that enabled the identification of subtle surface variations that would be challenging to detect using coarser-resolution DEMs or alternative remote sensing techniques.

Another key similarity is the emphasis on developing novel methodologies. Chapter 4 used ArcticDEM to determine supraglacial lake depth. This is a novel application of the dataset, as is its use as a comparative dataset against other lake depth detection techniques. Chapter 5 introduced a new approach to detecting the extents of floating ice tongues, demonstrating the feasibility of using DEM-based deviation analysis to detect floating ice. However, for some glaciers the method encountered challenges related to surface velocity effects and vertical offsets, which complicated interpretation. Additionally, the method presented in Chapter 5 cannot track the dynamics of the grounding line over time. Chapter 6 addressed these issues and developed a method capable of detecting a grounding line from a single pair of DEMs.

Despite these similarities, the studies differ in their scale of analysis, methodological challenges, and intended applications. Chapter 4 focused on a small-scale case study of

five supraglacial lakes, where we compared ArcticDEM's accuracy against other satellite-based lake depth measurement methods. In contrast, Chapter 5 addressed the large-scale challenge of detecting the floating ice extents of marine-terminating glaciers of northern Greenland, requiring the integration of multiple DEMs over a larger temporal scale (decadal). The size of each glacier meant that we had to combine DEMs from different years to fully cover each glacier's grounding area. This shift in scale introduced new complexities, particularly computationally, with greater need for automation which necessitated a higher level of programming capability than previously required. Additionally, the temporal scale of Chapter 5 resulted in the analysis of fast-flowing ice whereas the research presented in Chapter 4 focused on single-epoch datasets and so did not have to contend with this issue.

Compared to Chapter 5, Chapter 6 predominantly focused on much smaller-scale time-varying signals. We avoided the velocity-induced issues in fast-flowing glacier regions where crevasses and ridges may have obscured the grounding line signal by implementing the 14-day temporal difference limitation between constituent DEMs in a DEM pair. The movement of these surface features, even after smoothing, disrupted the deviation signal within Chapter 5, and would have made it difficult to directly locate a grounding line from two differenced DEMs. However, another major issue in Chapter 5 was the presence of artificial vertical offsets, which resulted from the coregistration method used. We vertically adjusted all DEMs against the grounded ice upstream, under the assumption that the surface elevation change in these regions would match the surface elevation change downstream. However, this assumption proved incorrect for some glaciers, leading to artificial misalignment in the z-axis. We instead chose to coregister our DEMs with the Nuth and Kääb (2011) method in Chapter 6.

While the three studies share a unifying theme of using ArcticDEM for ice sheet feature analysis, their differences highlight an evolution from data validation on small-scale features to large-scale spatial application, with Chapter 6 focusing primarily on the temporal, as opposed to spatial, dimension. Collectively, these studies enhance the understanding of ice sheet dynamics and provide a foundation for future remote sensing-based research on supraglacial lakes and grounding lines.

## 7.4 Broader impact

This section outlines the key contributions of this thesis, focusing on the advancements in using high-resolution DEMs to study ice sheet processes. It highlights the evaluation of methods for supraglacial lake depth estimation, the introduction of floating ice tongue and grounding line detection techniques, and improvements in these methods for broader applications. I also discuss the practical implications of these contributions, emphasising their potential to enhance future glaciological studies and inform climate change assessments.

Chapter 4 provided a critical re-evaluation of a widely used method for estimating supraglacial lake depth. By demonstrating the accuracy and limitations of ArcticDEM for this purpose, this study showed how other topographic datasets can be used to assess the commonly used RTE approach.

Additionally, this chapter quantitatively determined the accuracy of the RTE approach. Our study questions the validity of findings using this method such as the ice-sheet-wide water volume measurements in Corr (2023) and more localised volume research such as Moussavi et al. (2016). These studies implicitly assume that the RTE provides an unbiased estimate of water depth. However, our validation results demonstrate that RTE errors are systematic and related to the input wavelength.

It is important to constrain methodological uncertainty because this affects the accuracy of large-scale depth estimates. These uncertainty estimates are used by many different groups, including Earth observation researchers creating datasets, hydrological modellers who use these datasets to validate their models, and ice sheet modellers who use the data to understand the distribution and movement of water, including lake drainage to the ice sheet bed.

The conical-structure assumption by Krawczynski et al. (2009) depicts supraglacial lakes as having a 1:100 depth–diameter relationship. Our results show that evaluating the RTE with the green band wavelengths can overestimate lake depth by up to 153%. The volume of a conical lake depends on both its depth and its radius, according to the formula $V = \frac{1}{3}\pi r^2 h$. Under a 1:100 depth–diameter relationship, the radius of the lake scales linearly with depth, so any overestimate in depth also increases the radius proportionally. Because volume scales with the depth multiplied by the square of the radius, the overall volume

scales with the cube of the depth factor. For example, the 153% overestimate in depth using the green band corresponds to a depth factor of 1.53. Cubing this gives $1.53^3 = 3.58$, meaning that the inferred volume would be overestimated by approximately 258% relative to the true volume. This demonstrates how errors in depth can dramatically inflate volume estimates and elucidates the need to re-evaluate these previous supraglacial lake volume estimates in light of our findings.

Our study encourages further refinement of the RTE method or the development of a new method which can be used at scale across the ice sheet.

Chapter 5 introduces an approach to floating ice detection using the decadal-scale deviation analysis of a DEM stack. This offers an alternative to traditional approaches and provides a proof-of-concept that DEMs can be used to determine the extent of floating ice on a glacier. Having multiple datasets on which to rely allows for more comprehensive analysis, as spatial and temporal gaps in one dataset can be filled by another, ensuring better coverage across different regions. This redundancy also helps verify the results, increasing confidence in the findings from each dataset. An example of this can be seen in the case of Hagen Bræ. Both the evidence presented in this study and the findings from Millan et al. (2023) suggest that Hagen Bræ is entirely grounded. However, the CCI (2023) project has defined a 2017 grounding line approximately 50 km inland from the calving front. Even when solely considering the height at flotation data presented in our study (see Figure 5.17c), it is clear that this location is highly unlikely to represent Hagen Bræ's actual grounding line, if indeed it supports a floating extension. Our study casts doubt on the validity of the grounding lines delineated by CCI (2023) and raises concerns about the accuracy of their method in locating grounding line positions.

The decadal-scale floating ice extents in this study provide a broad indication of where floating ice has been observed over the last decade, helping researchers identify regions of persistent or intermittent flotation. This is valuable for ice sheet modellers and climate scientists studying long-term ice sheet stability, as well as for improving models of ice-ocean interactions. It also provides useful baseline information for future studies assessing changes in ice extent and dynamics.

Chapter 6 introduces a novel method of determining grounding line location by differencing high-low tidal DEM pairs. We have produced new records of partial grounding lines for three key glaciers in Greenland, providing valuable data for future

research. These grounding lines have helped back-fill temporal and spatial gaps within the time series of Petermann Gletsjer and Storstrømmen which will aid future researchers of these glaciers. Our Storstrømmen Lobe 1 grounding line, delineated from the 2013-04-13/2013-04-16 DEM pair, displays a pronounced S-shape (Figure 6.8; Figure 6.9) that suggests a previously unrecognised area of grounding on the western flank. This interpretation is supported by the height above flotation derived from BedMachine version 5 (Figure 6.9) and by the underlying bed topography (Figure B.2.1a).

By mapping grounding line positions for 2012, 2013, and 2014, we fill part of the temporal gap between the published 1996 and 2016 grounding lines, which bracket our new delineations. These intermediate years reveal that Storstrømmen's grounding line did not retreat steadily during this period but instead underwent a marked shift in behaviour. Approximate distance–time estimates indicate a retreat rate of ~0.28 km $yr^{-1}$ between 1996 and 2012/2013 (a retreat of 4.5 km), followed by an acceleration to ~1 km $yr^{-1}$ between 2013 and 2016 (a retreat of 3 km).

This acceleration demonstrates that the grounding line's retreat was not uniformly stable, contrasting with the longer-term average of 0.4 km $yr^{-1}$ reported by Mouginot et al. (2018). The new grounding line geometries therefore reveal previously undocumented variability in Storstrømmen's retreat rate and highlight the potential for short-term, kilometre-scale grounding changes that were not captured in the sparse historical record.

Ensuring the temporal and spatial continuity of a time series is of particular importance to remote sensing researchers. They need to know the location of a grounding line concurrent with their data so that they can apply appropriate corrections to the grounded and floating ice extents. Without temporally concurrent knowledge of the grounding line, they may over- or under-correct parts of their data, leading to higher uncertainty within their results. As basal friction does not impact floating ice velocity to the same degree as it does the velocity of grounded ice, an accurate understanding of the grounding line location at specific timestamps is also important for ice sheet modellers who use it to help predict ice loss from the ice sheets, and therefore sea level rise.

For Storstrømmen, we have shown that the northern secondary lobe may have been floating pre-2018, with the implication that it could still be floating today. Some literature, such as Millan et al. (2023), assume that this lobe is grounded. However, upon review of Figure 1 in Millan et al. (2023), the potential floating nature of this lobe is evident within

their ice velocity data. This suggests that those glaciers which are not expected to terminate in a floating extension may be inadvertently excluded from floating ice inventories by current methods. As such, these inventories should not be considered definitive for identifying all floating glaciers.

Of particular interest is the data presented in Figure 6.7 which shows the envelopes of grounding line spatial spread derived from our method. These results align with Ciracì et al. (2023), who found that the grounding zone of Petermann Gletsjer was 3–6.5 km wide at the lateral margins in 2011, 2016, and 2017. Taken together, this raises questions about the assumed annually representative nature of published grounding lines. Instead, it suggests that producing an annual delineation of the grounding zone may be more informative for future work, particularly for glaciers with wide grounding zones where glacier dynamics differ inland, within, and seaward of the grounding zone.

Additionally, some studies treat sensor-induced artefacts (e.g. satellite jitter) as stable or negligible (e.g. Bessette-Kirton et al., 2018; Liu et al., 2023), yet the enhanced wave signal exposed through DEM differencing in this study suggests that the magnitude of these signals can vary between acquisitions. Consequently, some interpretations that assume uniform DEM noise may require refinement, particularly where small-magnitude elevation changes are reported.

This method lays the foundation for the application of DEM differencing in conjunction with tide modelling for other glaciers in Greenland and also for Antarctic ice shelves. The enhanced temporal resolution achieved in this study compared to that of Chapter 5 means that similar methods could be used to track grounding line variations in Antarctica, where grounding line migration is a major driver of ice shelf instability.

## 7.5 Future research directions

This section outlines several potential avenues for extending and refining the methods developed in this thesis, as well as exploring potential applications for high-resolution DEMs in glaciological research. First, I discuss possible improvements and expansions to the methods presented in each chapter. I then explore additional research opportunities to expand the use of DEMs in glaciological research. These extensions and refinements provide exciting opportunities to enhance our understanding of ice dynamics and mass balance, with potential applications across a variety of glaciated regions.

### 7.5.1 Methodological refinements and expansion

While this thesis has demonstrated the viability of using ArcticDEM for supraglacial lake depth measurement and the detection of floating ice extents and grounding lines, there remain several opportunities to refine and expand upon the methods described herein. Future research could focus on addressing the limitations identified in each study, incorporating new technologies, and extending these approaches to other glaciated regions.

Chapter 4 established ArcticDEM as a reliable dataset for lake depth measurement and discovered limitations to the RTE, such as errors introduced by varying lakebed reflectance and the need for external calibration data, which could be addressed through advanced computational approaches. Machine learning models trained with ArcticDEM and ICESat-2 to predict depths from a potential combination of optical, thermal, and/or multispectral satellite imagery could refine depth estimation by capturing the nonlinear relationships between surface reflectance, ice properties, and water depth.

Although simpler statistical approaches can be effective when relationships follow minimal models such as the RTE, depth retrieval in supraglacial lakes is complicated by spatially varying lakebed reflectance, differences in water column particulate loading, and varying illumination conditions, among other factors. These factors interact in ways that are difficult to parameterise, so integrating multiple spectral bands and ancillary datasets to produce a robust depth calculation introduces complex interactions that exceed the assumptions of conventional regression models. Machine learning approaches are well-suited to learning these complex interactions, allowing depth retrieval to benefit from the use of combined datasets where physically based inversions using equations – such as the RTE – are under-constrained.

Of particular interest is the potential use of multispectral imagery to improve depth retrieval with its ability to incorporate different bands as opposed to the use of only one wavelength band. This could offer a more robust method for estimating lake depth across different glaciated regions (e.g. elsewhere on the GrIS, or on the Antarctic ice sheet) and seasons.

Additionally, refining the calculation of $A_d$ (lake bottom reflectance) could enhance depth accuracy within the RTE, improving large-scale assessments of surface water storage and meltwater contributions to ice sheet dynamics. Currently, changes in $A_d$ affect the results of the RTE the most out of all three tuneable variables, so refining its calculation is important for the accurate calculation of lake depths. The use of other methodologies, such as DEM- and laser altimetry-based, to validate the results of this approach would help ensure accurate refinement.

For Chapter 5, future methodological refinements should focus on addressing the effects of surface velocity in DEM deviation analysis. This study highlighted the challenges posed by fast-flowing glaciers, where crevasses and ridges introduce noise that obscures the transition between the floating and grounded ice extents. One approach to address this issue is the use of velocity-corrected DEMs, where ice flow models or feature-tracking techniques are used to adjust DEMs for the displacement of surface features over time.

Another potential methodological refinement is the effective coregistration of the DEMs to another dataset such as ICESat-2 to produce an independently coregistered DEM dataset. This would reduce the issues encountered within our method, where the ice thickness change rates were different in the upstream and downstream areas, leading to discrepancies after the DEMs were artificially aligned via their upstream areas. However, the volume of DEMs required for each glacier made full linear coregistration of every DEM impractical. Instead, we applied vertical alignment based on the assumption that elevations in the upper glacier would remain constant through time. This assumption turned out to be problematic and contributed to much of the ambiguity in the results. A full linear coregistration in the x-, y-, and z- planes likely would have reduced this confusion by removing systematic offsets between DEMs. Because the vertical alignment introduced artificial elevation errors, any underlying non-linear biases, if present, were obscured. It is possible that such biases existed but were either masked by the vertical misalignment or averaged out across the large number of DEMs in each stack.

For Chapter 6, the method could be improved further by addressing the issue of satellite jitter. Jitter, in the context of satellites, is the small, unintended movement or vibration of a satellite during data collection. This can be caused by mechanical disturbances such as thrusters or thermal expansion, external forces like atmospheric drag or variations in gravitational pull, or internal system noise. Although jitter is often not visible within a single DEM, differencing two DEMs can amplify the jitter (Figure 7.1), reducing our ability to observe real patterns in the data. In terms of expansion, this method could be extended to the other Greenland floating ice tongues identified in Chapter 5 which would help us gain a more comprehensive understanding of grounding line behaviour across the ice sheet through potential backfilling of spatial and temporal gaps left by traditional SAR methods.

The focus of the study in Chapter 6 was on differencing individual DEM pairs, so coregistration accuracy was very important. We therefore applied linear coregistration. This is also the study in which non-linear biases were most evident, primarily tilt-related biases and complex jitter-related wave patterns. More sophisticated coregistration (e.g. correcting for tilt and/or skew) might have further improved the DEM alignment, but the dominant error source was the strip-level jitter, which cannot be removed through geometric coregistration. Visual checks in a GIS suggested that tilt effects were small enough to not impede grounding line identification, and that jitter was the principal limitation. Additionally, calibration against ICESat-2 or another similar dataset could improve the robustness of this method.

To predict ice sheet behaviour, we must first understand previous behaviour of the ice sheet which would be aided by knowledge of floating ice extents and grounding line locations on Greenland between 2000 and 2010, a decade for which no records currently exist. The approach detailed in Chapter 6 could be extended temporally using the Advanced Spaceborne Thermal Emission and Reflection Radiometer (ASTER) dataset, which boasts data from 2000 to present (Abrams et al., 2020), allowing for a longer historical record of floating ice extents and grounding line positions and improving our understanding of past trends.

Moreover, for the method described in Chapter 6, there is significant potential for extension to Antarctic ice shelves, using the Reference Elevation Model of Antarctica (REMA) (Howat et al., 2022) as a high-resolution (2 m) elevation dataset. By applying

this method to Antarctic ice shelves, we could confirm existing floating ice extents and grounding line records and aid the backfilling of temporal and spatial data gaps. This would aid ice sheet modellers of Antarctica by further informing their understanding of the extents of floating ice and locations of the grounding lines.

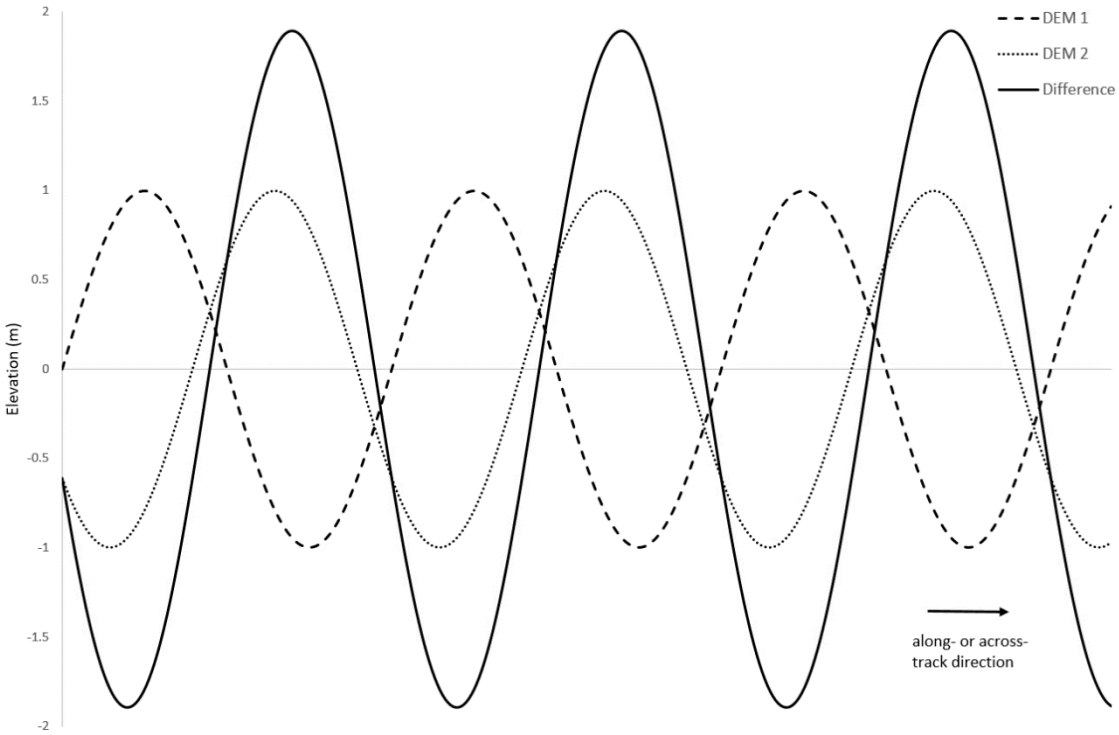


Figure 7.1: An illustration of jitter amplification along a hypothetical transect when differencing two DEMs with opposing jitter signals.

### 7.5.2 Expanding the use of DEMs in glaciological research

In this thesis, I have focused on applying ArcticDEM to measure and map specific glaciological features, However, the broader potential of DEMs expands far beyond applications to supraglacial lake depth and grounding line detection. Expanding the use of DEMs to a variety of glaciological processes and regions offers exciting prospects for enhancing our understanding of ice sheet behaviour, interactions with climate, and contributions to sea level rise.

This section outlines several opportunities for advancing ice sheet research using high-resolution DEMs. First, I discuss feature tracking for velocity mapping using time-stamped DEMs. I then examine how combining ArcticDEM with BedMachine version 5 (Morlighem et al., 2022) could track ice thickness changes over time. I then present an alternative method for grounding line detection based on ice thickness and height above

flotation and elucidate how DEMs could be used to calculate both the basal melt rates of ice tongues and their calving volumes. These approaches would offer valuable insights into ice dynamics and mass balance.

#### 7.5.2.1 Feature tracking for velocity mapping

A potential approach for measuring ice surface velocity is through the tracking of surface features such as crevasses and ridges across multiple time-stamped DEMs. This would give us valuable insights into the dynamics of glaciers and ice sheets.

Although SAR-derived velocity products provide high-quality estimates of ice flow, DEM-derived feature tracking offers several complementary advantages. DEM-based approaches can fill temporal gaps when SAR acquisitions are sparse or absent, allowing observation of seasonal or brief events. They are also less sensitive to surface coherence issues, capturing motion in areas where radar backscatter is unreliable, such as crevassed regions near the lateral margins of fjord-constrained glaciers. Because DEM tracking measures displacement via topographic changes rather than radar phase, it provides an independent velocity estimate that can be used to validate SAR products and quantify uncertainties. Additionally, DEM-derived tracking can be integrated with elevation change and thickness datasets, allowing analyses of vertical and horizontal ice motion. The use of DEMs also enables historical reconstructions from older stereo or optical imagery, extending velocity records prior to the modern SAR era. These benefits make DEM-derived feature tracking a valuable complement to existing SAR-based methods, particularly for capturing subtle, localised, and/or temporally intermittent flow features.

Using time-stamped 2 m resolution DEMs would allow for the precise identification and tracking of surface features over time with the level of detail required for accurate velocity calculations (Figure 7.2). This dataset boasts a higher spatial resolution than the optical and SAR datasets that are typically used for feature tracking, and it can provide coverage for periods or areas where other datasets may lack data due to issues arising from acquisition timing or limitations in spatial coverage. Enhanced temporal continuity would allow us to track surface feature movement across different time periods, gaining a more comprehensive view of velocity trends. Differences in spatial coverage between datasets may also mean that there are DEM data over areas that are less sampled by other data sources, improving the spatiotemporal resolution of the resulting feature dataset.

Additionally, combining DEMs with altimetry datasets could significantly enhance the feature tracking process. Altimetry datasets, such as those obtained from radar altimeters (e.g. ICESat-2), provide accurate surface elevation measurements, which could be paired with the high-resolution DEMs to track surface features with even greater precision. These altimeter measurements could complement the DEMs, particularly in areas where DEM data are sparse or inconsistent. By combining the spatial resolution of DEMs with the elevation data from altimetry, it would be possible to obtain a more comprehensive picture of ice surface movement. Moreover, DEM data could be used to map the 3-D deformation of features as they move with the ice. Traditional approaches of feature-tracking for velocity estimates do not have this capability but using DEM data to determine how velocity affects feature geometry could provide new insights into the stresses and strains within the ice sheet.

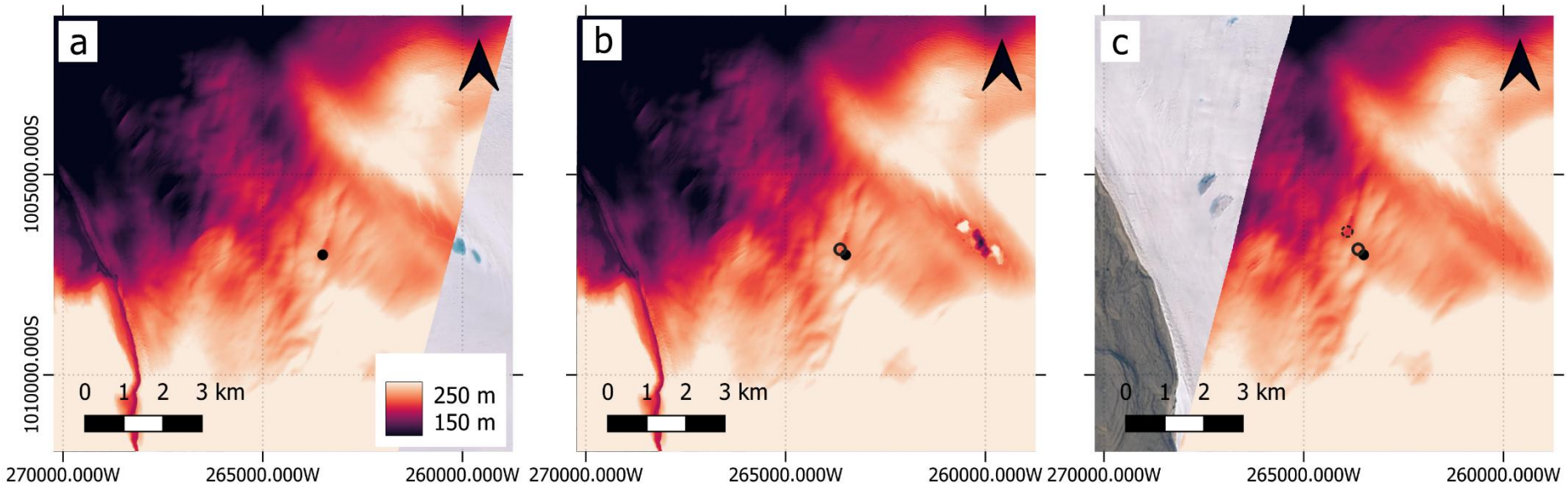


Figure 7.2: An example of how feature tracking may be used to determine the velocity of a glacier from ArcticDEM strip DEMs on Petermann Gletsjer. Panel a shows a strip DEM dated 1st May 2020, with a solid black circle marking the southern point of a crevasse visible within the strip DEM. Panel b shows a strip DEM dated approximately three months later (8th August 2020) with a solid black circle indicating the same location as the solid black circle in panel a, and a hollow black circle marking the new location of the crevasse's southern point. Panel c shows a strip DEM dated 13th May 2021 (approximately one year after the strip DEM in panel a) with a solid black circle indicating the original crevasse location, a hollow black circle indicating the location on 8th August 2020, and a dotted hollow black circle indicating its location on 13th May 2021. The distance between the solid black circle and the dotted hollow black circle in panel c is approximately 850 m, implying a velocity of approximately 825 m/yr. The base map data in panels a and c are courtesy of Earthstar Geographics via ESRI.

### 7.5.2.2 Determining changes in ice thickness over time

ArcticDEM strip DEMs have the potential for tracking ice elevation and thickness changes over time at a higher resolution than altimeters. This approach could provide valuable insights into both the fine scale detail of the ice sheet, including narrow outlet glaciers, and dynamic processes affecting mass balance.

Ice thickness at any given DEM timestamp could be estimated by subtracting a bed elevation model such as BedMachine version 5 (Morlighem et al., 2022) from the surface elevation of the strip DEM (Figure 7.3). Although BedMachine provides a time-invariant bed, this does not restrict the method. The bed acts as a fixed baseline, whilst the DEMs act as the time-varying surface. When applied to multiple DEMs, differencing these thickness estimates would reveal temporal changes in ice thickness. The main requirement of this approach would be that the uncertainty of the bed model is smaller than, or comparable to, the magnitude of the thickness changes being resolved.

For this approach to be effective, the ArcticDEM DEMs would have to be accurately coregistered to the bed elevation model. A key limitation is that this coregistration would rely on the presence of exposed bedrock, providing stable reference points. Therefore, it is likely that this method could only be applied to the ice sheet margins, where bedrock outcrops are available, rather than in the ice sheet interior.

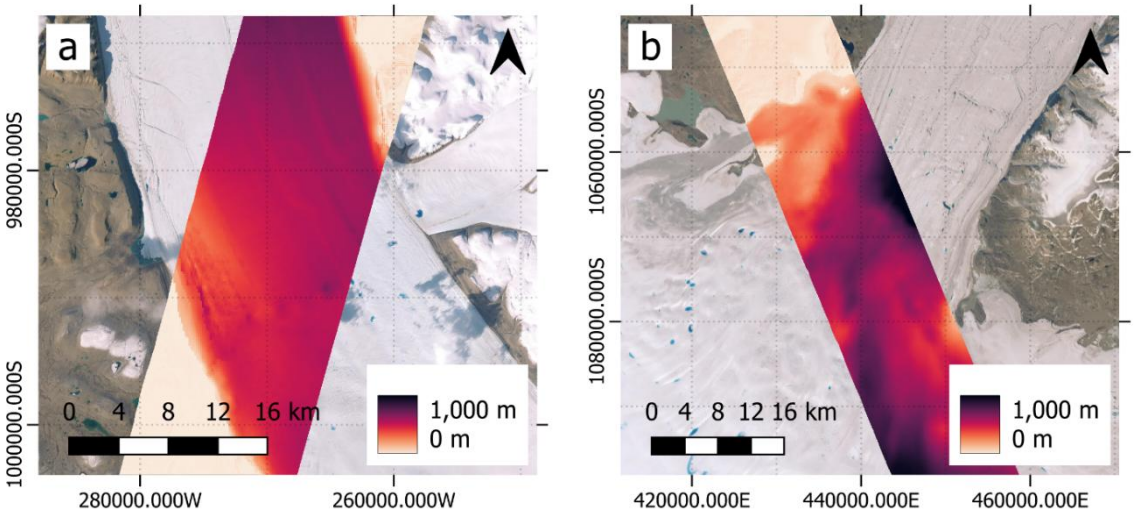


Figure 7.3: Two examples of glacier ice thickness calculated by differencing the bed elevation from BedMachine version 5 (Morlighem et al., 2022) and an ArcticDEM strip DEM coregistered to the BedMachine bed elevation layer. Panel a shows the ice thickness calculated for a strip DEM over Petermann Gletsjer, and panel b shows the ice thickness calculated for a strip DEM over

79N Gletsjer (Nioghalvfjerdsbræ). The base map data for both panels are courtesy of Earthstar Geographics via ESRI.

#### 7.5.2.3 Ice thickness for grounding line location

Another potential method for determining the grounding line location, separate from that detailed in Chapter 6, relies on the use of ice thickness calculations in conjunction with BedMachine version 5 (Morlighem et al., 2022). This method would involve inputting the BedMachine bed elevation model and the ArcticDEM time stamped DEM into the following equation to calculate the height above flotation:

$$h_f = h - H\left(1 - \frac{\rho_i}{\rho_w}\right) \tag{7.1}$$

where $h_f$ *is* the height above flotation, $h$ is the ice surface elevation (coregistered to the bed elevation per Sect. 7.5.2.2), $H$ is the ice thickness (calculated from the bed elevation and the coregistered ice surface elevation, following Sect. 7.5.2.2), $\rho_i$ is the density of the ice, and $\rho_w$ is the density of seawater.

The resulting height above flotation maps could be used to delineate the transition between floating and grounded ice, corresponding to the grounding line (Figure 7.4). By mapping this transition, it is possible to provide an alternative, physically based method for grounding line location that can complement and refine the method discussed in Chapter 6. Although we used a similar method to define height above flotation maps in Chapter 5 (see Appendix B.2) and Chapter 6, we did not use ArcticDEM strip DEMs to do so. Instead, we used bed elevation and surface elevation layers from the BedMachine version 5 product to produce an estimate of height above flotation for 2007 (the year attributed to the BedMachine product).

This ArcticDEM-based approach could offer several advantages, particularly in regions where traditional grounding line detection methods are challenging to apply. For instance, in regions with complex topography or areas where tidal variations are minimal, the use of ice thickness and height above flotation could provide a more consistent and reliable means of determining the grounding line. Moreover, this method has the potential to be widely applicable to different glaciers and ice shelves, including those in Antarctica, where similar techniques could be used to monitor grounding line changes over time.

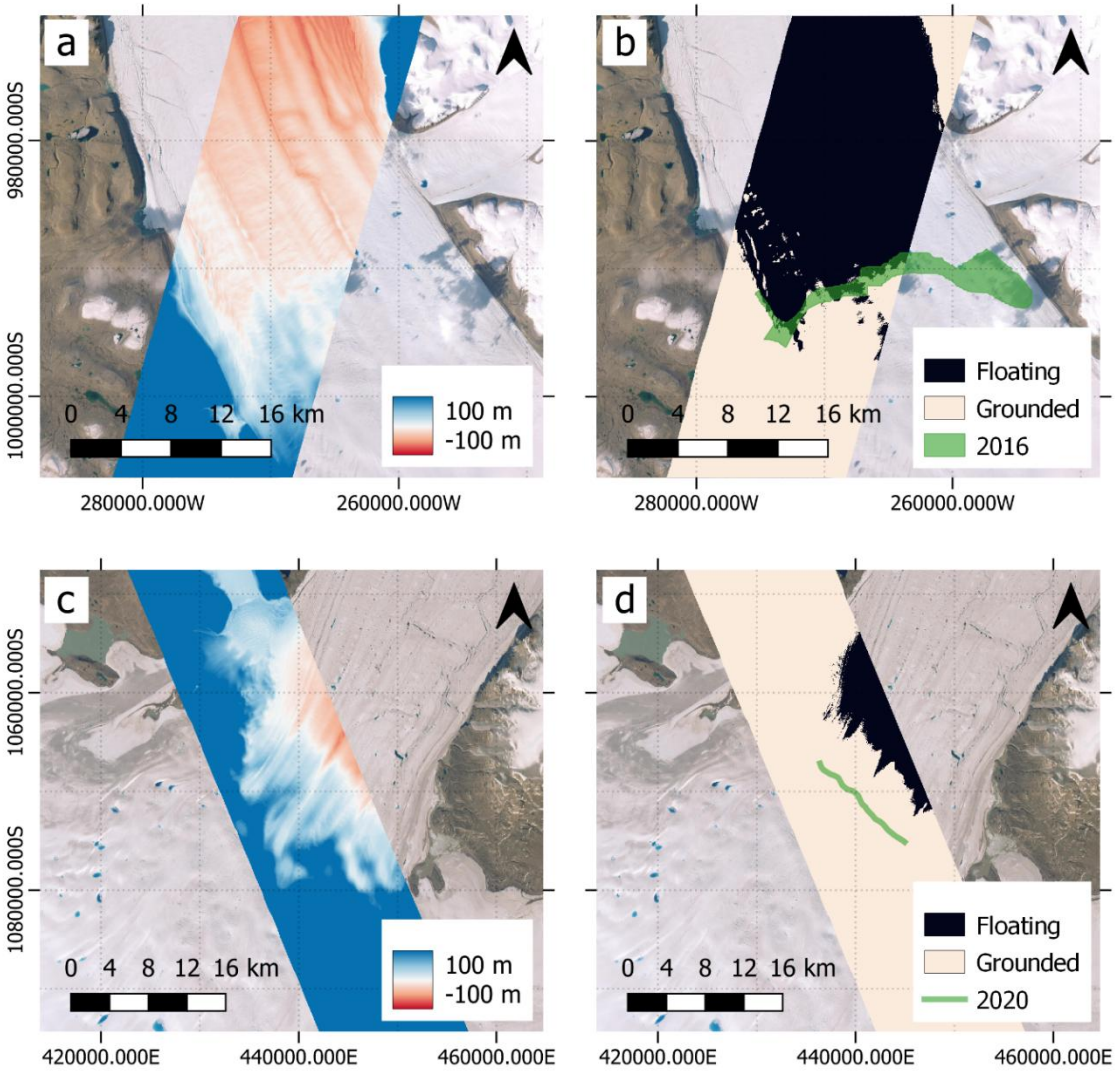


Figure 7.4: Examples of height above flotation calculations using the BedMachine version 5 bed elevation layer (Morlighem et al., 2022) and ArcticDEM strip DEMs coregistered to the BedMachine bed elevation layer. Panels a and c show the height above flotation of a strip DEM on Petermann Gletsjer (a) (dated 17th July 2016) and 79N Gletsjer (Nioghalvfjerdsbræ) (c) (dated 13th July 2021), calculated per Eq. . Where the height above flotation is negative, the ice is floating in hydrostatic equilibrium. Panels b and d show binary masks indicating the floating and grounded areas of Petermann Gletsjer (b) and 79N Gletsjer (Nioghalvfjerdsbræ) (d) as calculated from the height above flotation in panels a and c, respectively. In panel b, the green polygon indicates the spread of grounding lines from 2016 as defined by the novel method in Chapter 6. In panel d, the green line indicates the Millan et al. (2023) 2020 grounding line for reference. The base map data in all panels are courtesy of Earthstar Geographics via ESRI.

#### 7.5.2.4 Basal melt rates of ice tongues

Basal melt rates of floating ice tongues could potentially be calculated by combining DEM-derived ice thicknesses with ice velocity and surface mass balance estimates. This

approach would involve determining the ice flux through a cross-section (flux gate) near the grounding line using ice velocity data and comparing it to the surface mass balance. By tracking ice thickness changes over time and accounting for surface mass balance contributions, the residual difference could be attributed to basal melt. High-resolution DEMs could enable detailed spatial analysis of these melt rates, particularly when paired with velocity fields. Additionally, temporal sequences of DEMs could help capture variations in basal melt rates, offering insights into seasonal and long-term ice-ocean interactions. Understanding these melt patterns is essential for assessing ice shelf stability and improving predictions of future ice loss from marine-terminating glaciers and its contribution to sea level rise.

#### 7.5.2.5 Calving volumes

The volume of ice calved from a floating ice tongue could be estimated by combining measurements of calving front retreat with DEM-derived ice thickness data. This method relies on tracking changes in the calving front position over time and applying hydrostatic equilibrium assumptions to estimate ice thickness. Estimates of the calving front location over time from satellite imagery would allow for the measurement of retreat distance across the width of the ice tongue, providing the ice loss area. Ice thickness at the calving front could be determined using DEM-derived surface elevations and the principle of hydrostatic equilibrium and then multiplied by the ice loss area to find the volume of ice calved. By applying this method over time, we could assess the relative contribution of calving to ice mass loss.

## 7.6 Concluding remarks

This thesis makes a number of contributions to the field of glaciology by advancing the use of a high-resolution DEM dataset (ArcticDEM) in studying a range of Greenland ice sheet processes. It uses ArcticDEM to validate a commonly used satellite-based method for determining supraglacial lake depth and introduces novel methodologies using ArcticDEM to detect floating ice extents and grounding line locations, demonstrating the critical role of high-resolution DEMs in enhancing our understanding of ice sheet processes. The findings show that ArcticDEM offers reliable methods for monitoring key parameters of ice sheet change, at scale, while also highlighting areas for further improvement in existing methods. This work provides a solid foundation for future research by presenting robust, scalable techniques that can be refined and applied to a broader range of glaciated regions.

The results of this thesis produce several promising avenues for future studies. The methods developed here for supraglacial lake depth validation and grounding line detection represent important advancements in ice sheet monitoring, with potential for further refinement and integration with other data sources. These techniques offer a framework for expanding temporal and spatial records of ice sheet evolution, providing invaluable insights into the behaviour of ice sheets over longer timescales. Additionally, the findings support ArcticDEM's potential as a tool for diverse glaciological research, with applications extending well beyond the study of supraglacial lakes and floating ice tongues.

As a freely available, high-resolution dataset, ArcticDEM is a key resource for improving the precision and scope of glaciological studies. The methodologies developed in this thesis highlight how such high-resolution data can be leveraged to overcome existing limitations in ice sheet monitoring. The continued integration of DEM datasets into many elements of future glaciological research will be vital in understanding the challenges posed by climate change, ensuring that we are better prepared to understand and respond to the evolution of our planet's ice sheets.

# Appendix A: Chapter 4 - Evaluation of satellite methods for estimating supraglacial lake depth in southwest Greenland

# A.1 Criteria to reduce the 2019 lake inventory

A 2019 inventory (Emily Glen, personal communication, 22 July 2022) of the maximum areal extents of all water bodies in the study region was used as the basis for selecting our five lakes, with the following characteristics used as the selection criteria:

- The water body is intersected by an ICESat-2 reference ground track (removed 7519 water bodies).
- The seasonal maximum water body area is greater than 1 $km^2$ but less than 10 $km^2$. This removes small water bodies which are absent in low melt years and large water bodies which are formed by the merging of smaller water bodies, thus leaving supraglacial lakes with dimensions that were representative of the regional average (removed a further 338 water bodies).
- The water body circumference is less than 30 km; i.e. it is not a highly elongated feature such as a stream (removed a further 28 water bodies).

These characteristics reduced the 2019 inventory from 7913 to 28. The lakes were then considered for their ICESat-2 data quality, where the highest quality translates to the basins which can be most easily delineated from ICESat-2 photon refraction (Sect. 4.3.4). Additionally, the 28 lakes were visually appraised for their level of activity to ensure that they drained and refilled. These comparisons identified five lakes for which depth could be derived for all three measurement techniques. The other lake basins from the initial subset of 28 could not easily be identified by ICESat-2 or could not be resolved using the ArcticDEM digital elevation models.

# A.2 Input data

Lake-specific data were used during the course of this study, and the particulars of these data are detailed in Table A.2.1.

Table A.2.1: ArcticDEM, ICESat-2, and Sentinel-2 data used for depth retrieval in each of the five lakes. Acquisition dates are in bold text and are in the format YYYYMMDD.

| Lake number | Dataset | Filename | Date downloaded |
|---|---|---|---|
| 1 | ArcticDEM tile | SETSM_s2s041_WV01_**20200304**_1020010093157200_1020010093C80200_2m_lsf_seg1_dem | 29th November 2022 |
| | ICESat-2 track | ATL03_**20200706**005932_01630805_003_01_gt2l | 12th April 2021 |
| | Sentinel-2 tile | T22WEV_**20200702**T150759 | 19th February 2021 |
| 2 | ArcticDEM tile | SETSM_s2s041_WV02_**20210312**_10300100BB24B100_10300100BBC0A100_2m_lsf_seg1_dem | 29th November 2022 |
| | ICESat-2 track | ATL03_**20200717**114945_03380803_003_01_gt1l | 12th April 2021 |
| | Sentinel-2 tile | T22WEV_**20200717**T150921 | 19th February 2021 |
| 3 | ArcticDEM tile | SETSM_s2s041_WV01_**20200304**_1020010093157200_1020010093C80200_2m_lsf_seg1_dem | 29th November 2022 |
| | ICESat-2 track | ATL03_**20200706**005932_01630805_003_01_gt2l | 12th April 2021 |
| | Sentinel-2 tile | T22WEV_**20200704**T145921 | 19th February 2021 |
| 4 | ArcticDEM tile | SETSM_s2s041_WV01_**20200511**_1020010094C9D900_1020010098791800_2m_lsf_seg3_dem | 29th November 2022 |
| | ICESat-2 track | ATL03_**20200706**005932_01630805_003_01_gt2l | 12th April 2021 |
| | Sentinel-2 tile | T22WEA_**20200704**T145921 | 19th February 2021 |

| | | | |
|---|---|---|---|
| | ArcticDEM tile | SETSM_s2s041_WV01_**20200620**_10200100982C5E00_102001009793BD00_2m_lsf_seg1_dem | 29th November 2022 |
| 5 | ICESat-2 track | ATL03_**20190716**051841_02770403_003_01_gt1l | 12th April 2021 |
| | Sentinel-2 tile | T22WFV_**20190725**T150015 | 26th August 2022 |

# A.3 Selection of the RTE tuneable parameter values

Commonly, within the radiative transfer equation (RTE), the derivation of $A_d$ is specific to a lake, or a regional average is used (Sneed and Hamilton, 2007). We have used an individual $A_d$ for each lake because the reflectance of pixels surrounding supraglacial lakes can vary considerably. In our study, we calculated the $A_d$ values specific to each lake. The red $A_d$ values were 0.42, 0.46, 0.35, 0.58, and 0.57 for lakes 1, 2, 3, 4, and 5 respectively, and the green $A_d$ values were 0.45, 0.49, 0.40, 0.60, and 0.58 for lakes 1, 2, 3, 4, and 5 respectively.

Our derivation of $g$ is given by $2.75K_d$. In addition to this being an average of the potential range of $g$ ($2K_d$–$3.5K_d$), this coefficient of $K_d$ incorporates the concept that the value of $K_d$ is dependent on depth (Kirk, 1989). This means an average value can be expected to retrieve a more representative depth than either the lowest or highest values in the $K_d$ range.

Typically, $R_\infty$ is calculated as the reflectance of the darkest pixel in a scene containing optically deep water (Sneed and Hamilton, 2007). Optically deep water, in the case of the Greenland ice sheet, consists of open ocean pixels. To reduce the impact of atmospheric effects, $R_\infty$ is ideally calculated from either the same scene as the one containing the pixels of interest where there are open-ocean pixels or a concurrent neighbouring scene. However, it is not always possible to sample $R_\infty$ from a concurrent neighbouring scene due to the location of the pixels of interest and/or cloud cover. In this case, a non-concurrent and/or non-neighbouring scene is chosen instead (Table A.3.1). Sneed and Hamilton (2011) argued that all optically deep water has similar spectral characteristics, and, therefore, the precise method for determining this value negligibly affects the depths derived using the RTE. The findings of our RTE tuneable parameter sensitivity analysis agree with Sneed and Hamilton (2011) (Figure 4.6).

Table A.3.1: Sentinel-2 tiles used to retrieve $R_\infty$ values for each lake. Acquisition dates are in bold text and are in the format YYYYMMDD.

| Lake number | Sentinel-2 tile | Date downloaded |
|---|---|---|
| 1 | T21WXP_**20200702**T150759 | 13th January 2023 |
| 2 | T21WXP_**20200717**T150921 | 13th January 2023 |
| 3 | T20WPT_**20200704**T154819 | 13th January 2023 |
| 4 | T20WPT_**20200704**T154819 | 13th January 2023 |
| 5 | T22VDQ_**20190712**T144759 | 13th January 2023 |
| July 8th 2019 lake inventory | T21WXN_**20190708**T150809 | 13th December 2022 |

# A.4 Plausible ranges of the RTE tuneable parameters

To calculate the uncertainty of the red- and green-band RTEs for the study lakes, we had to first understand the plausible ranges of the three tuneable parameters. The range of $A_d$ was calculated as the range of $R_w$ values of every pixel in the 30 m ring of pixels around each lake, as detailed in Sect. 4.3.2. The range of $g$ was 1.5 to $3K_d$ at 0.1 intervals for every lake, where $K_d$ was calculated as the band-specific solution of Eq. 4.3 for the average $a_w$ and $b_m^{fw}$ values from Smith and Baker (1981) for both the red and green optical bands of Sentinel-2. We calculated the ranges of $R_\infty$ from the Sentinel-2 tiles detailed in Table A.2.1. We manually appraised these scenes for spurious values caused by aeroplane overpasses and sediment contamination with the aid of a band combination to highlight snow and clouds (Band 1, Band 11, and Band 12 (coastal and aerosol, shortwave infrared (1610 nm), and shortwave infrared (2190 nm)). The $R_\infty$ ranges consist of the $R_w$ values of the 10 darkest pixels from each scene, which were true dark sea pixels.

Our study includes data from the sensitivity analysis that we carried out on the tuneable parameters using the plausible ranges of $R_w$ from the 8 July 2019 lake inventory (Emily Glen, personal communication, 22 July 2022) (Figure 4.6) (Table A.4.1). The method of calculating $A_d$ was slightly different due to the scale of the data. We calculated the range of $A_d$ as the range of the average $R_w$ values of the 30 m rings of pixels around all of the lakes in the 2019 lake inventory. We used the same method to calculate $g$ and $R_\infty$ as that which we used to calculate the uncertainty for the five study lakes. The scene from which we calculated the $R_\infty$ range was spatiotemporally contiguous with the lake inventory data (Table A.3.1).

Table A.4.1: The ranges of the tuneable parameters used to find the uncertainty of the 2019 lake inventory RTE depths.

| Parameter | Band | Value range |
|---|---|---|
| $A_d$ | Red | 0.1347–0.7724 |
| | Green | 0.2055–0.7973 |
| $g$ | Red | X$K_d$ where X = 2, 2.1, 2.2, 2.3, 2.4, 2.5, 2.6, 2.7, 2.8, 2.9, 3, 3.1, 3.2, 3.3, 3.4, and 3.5, and $K_d$ = 0.4075875 |
| | Green | X$K_d$ where X = 2, 2.1, 2.2, 2.3, 2.4, 2.5, 2.6, 2.7, 2.8, 2.9, 3, 3.1, 3.2, 3.3, 3.4, and 3.5, and $K_d$ = 0.07636 |
| $R_\infty$ | Red | 0.0254–0.0260 (0.0254, 0.0257, 0.0258, 0.0258, 0.0258, 0.0259, 0.0259, 0.0260, 0.0260, 0.0260) |
| | Green | 0.0474–0.0479 (0.0474, 0.0475, 0.0477, 0.0478, 0.0478, 0.0478, 0.0479, 0.0479, 0.0479, 0.0479) |

# Appendix B: Chapter 5 - An inventory of northern Greenland's floating ice tongues using high-resolution digital elevation models

# B.1 Limiting the count of Hagen Bræ

During the analysis of our glaciers, we restricted the number of digital elevation models (DEMs) used for Hagen Bræ to ensure a balanced spatial distribution for our deviation analysis. In Figure B.1.1, we present a comparison between the counts and median absolute deviation maps of Hagen Bræ with a reduced count (Figure B.1.1a and b) and without a reduced count (Figure B.1.1c and d) to elucidate why we included this additional step.

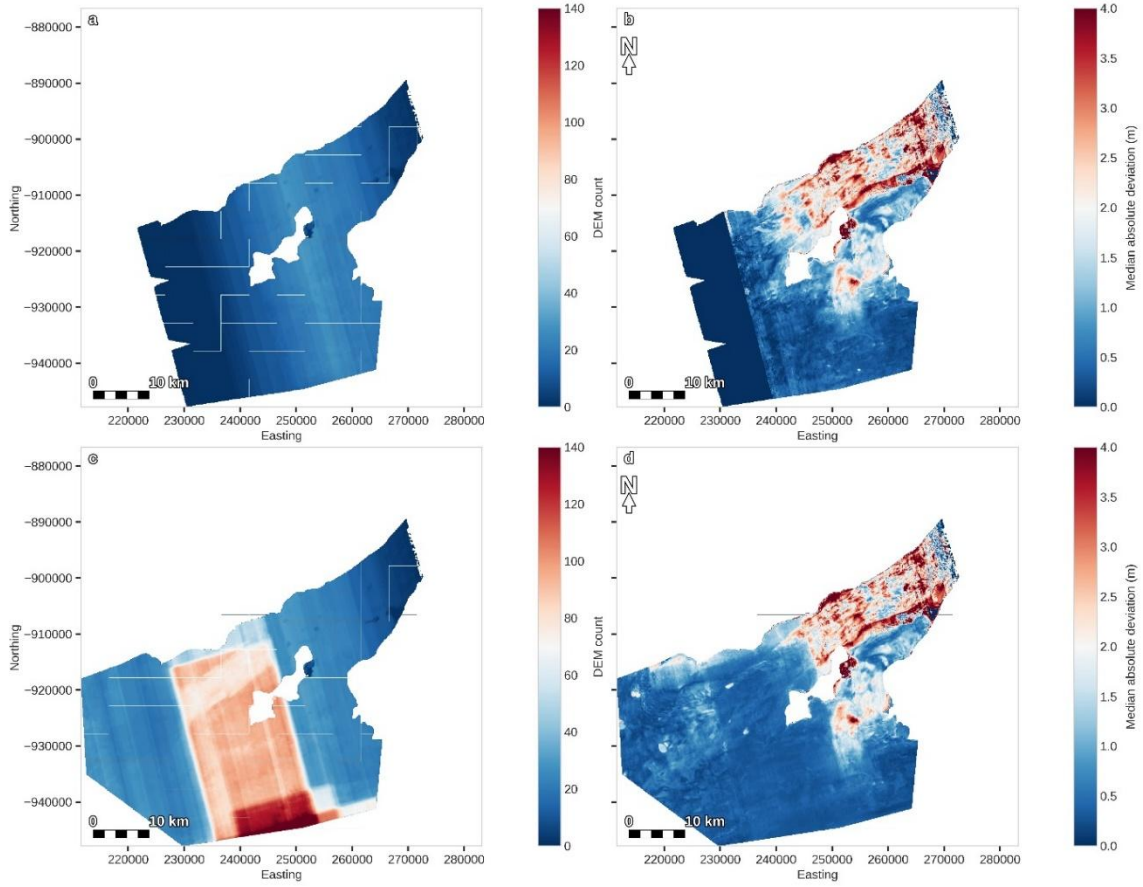


Figure B.1.1: A comparison between the reduced and non-reduced DEM counts and median absolute deviation maps for Hagen Bræ. Panel a shows the reduced DEM count, panel b shows the median absolute deviation of Hagen Bræ as derived from the reduced DEM count, panel c shows the non-reduced DEM count, and panel d shows the median absolute deviation of Hagen Bræ as derived from the non-reduced DEM count.

# B.2 Further supplementary figures

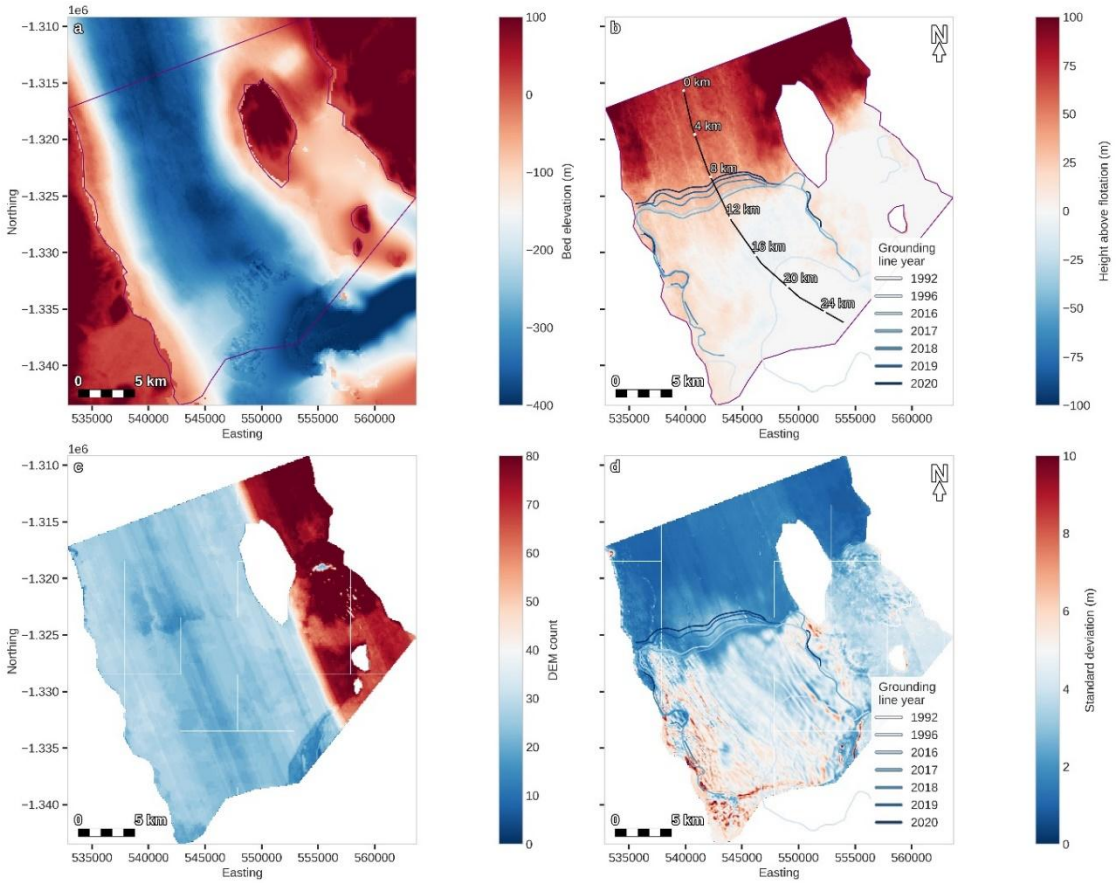


Figure B.2.1: Supplementary information relating to the geometry and DEM statistics of Storstrømmen. For each panel, the purple outline indicates the study area. Panel a is the bed elevation from BedMachine version 5 (Morlighem et al., 2022) and panel b is the height above flotation as calculated from BedMachine version 5 (Morlighem et al., 2022) using Eq. 5.1. Panel c shows the number of DEMs processed over the study area, and panel d shows the standard deviation of the DEMs where we process the data in the same way as for the median absolute deviation as shown in Figure 5.5. Additionally, in panel b and panel d we show all historical grounding lines mapped by other studies (Table 5.3).

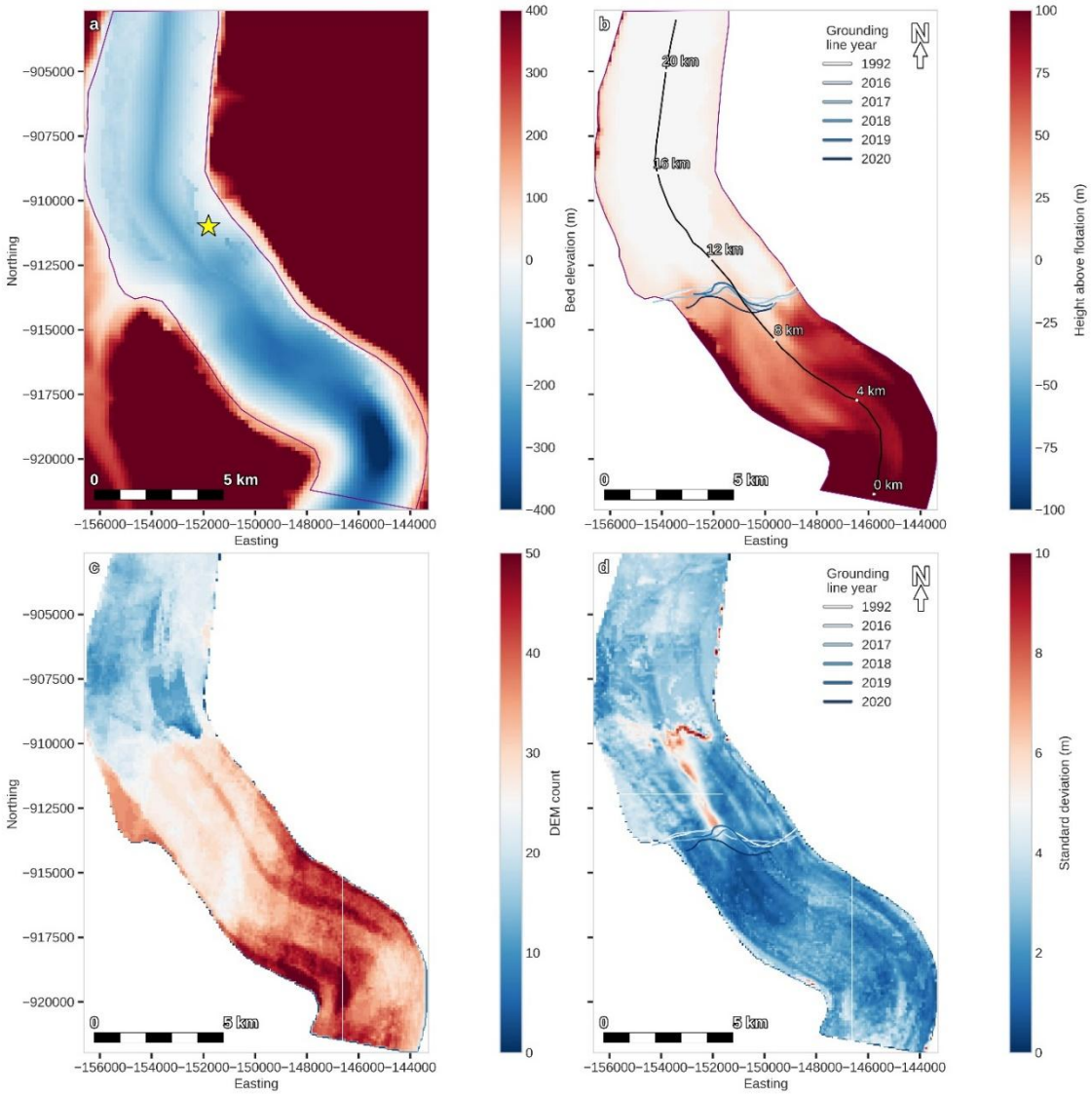


Figure B.2.2: Supplementary information relating to the geometry and DEM statistics of Steensby Gletsjer. For each panel, the purple outline indicates the study area. Panel a is the bed elevation from BedMachine version 5 (Morlighem et al., 2022) – where the yellow star indicates the area of ephemeral grounding – and panel b is the height above flotation as calculated from BedMachine version 5 (Morlighem et al., 2022) using Eq. 5.1. Panel c shows the number of DEMs processed over the study area, and panel d shows the standard deviation of the DEMs where we process the data in the same way as for the median absolute deviation as shown in Figure 5.6. Additionally, in panel b and panel d we show all historical grounding lines mapped by other studies (Table 5.3).

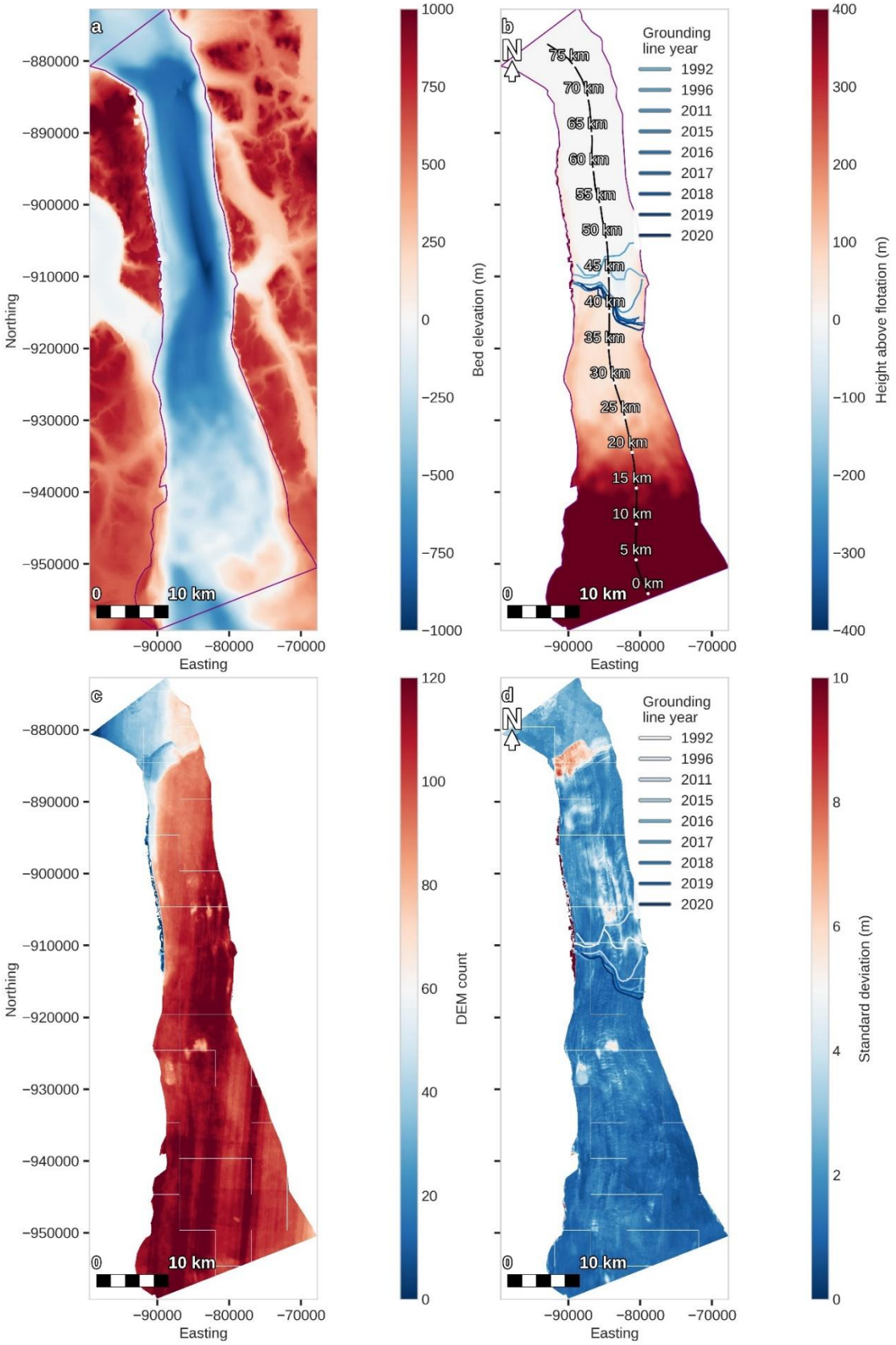


Figure B.2.3: Supplementary information relating to the geometry and DEM statistics of Ryder Gletsjer. For each panel, the purple outline indicates the study area. Panel a is the bed elevation from BedMachine version 5 (Morlighem et al., 2022) and panel b is the height above flotation as

calculated from BedMachine version 5 (Morlighem et al., 2022) using Eq. 5.1. Panel c shows the number of DEMs processed over the study area, and panel d shows the standard deviation of the DEMs where we process the data in the same way as for the median absolute deviation as shown in Figure 5.7. Additionally, in panel b and panel d we show all historical grounding lines mapped by other studies (Table 5.3).

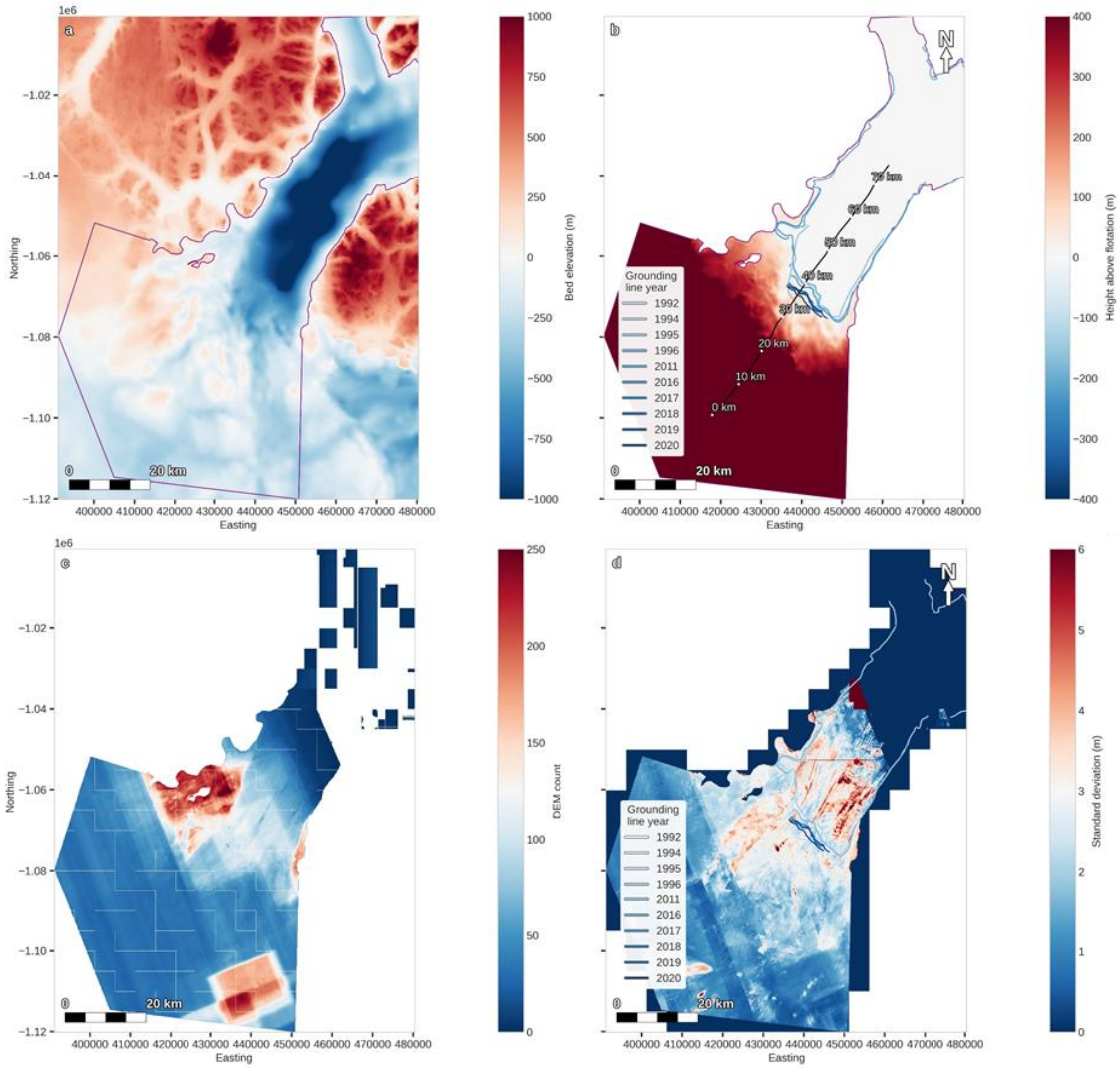


Figure B.2.4: Supplementary information relating to the geometry and DEM statistics of 79N. For each panel, the purple outline indicates the study area. Panel a is the bed elevation from BedMachine version 5 (Morlighem et al., 2022) and panel b is the height above flotation as calculated from BedMachine version 5 (Morlighem et al., 2022) using Eq. 5.1. Panel c shows the number of DEMs processed over the study area, and panel d shows the standard deviation of the DEMs where we process the data in the same way as for the median absolute deviation as shown in Figure 5.8. Additionally, in panel b and panel d we show all historical grounding lines mapped by other studies (Table 5.3).

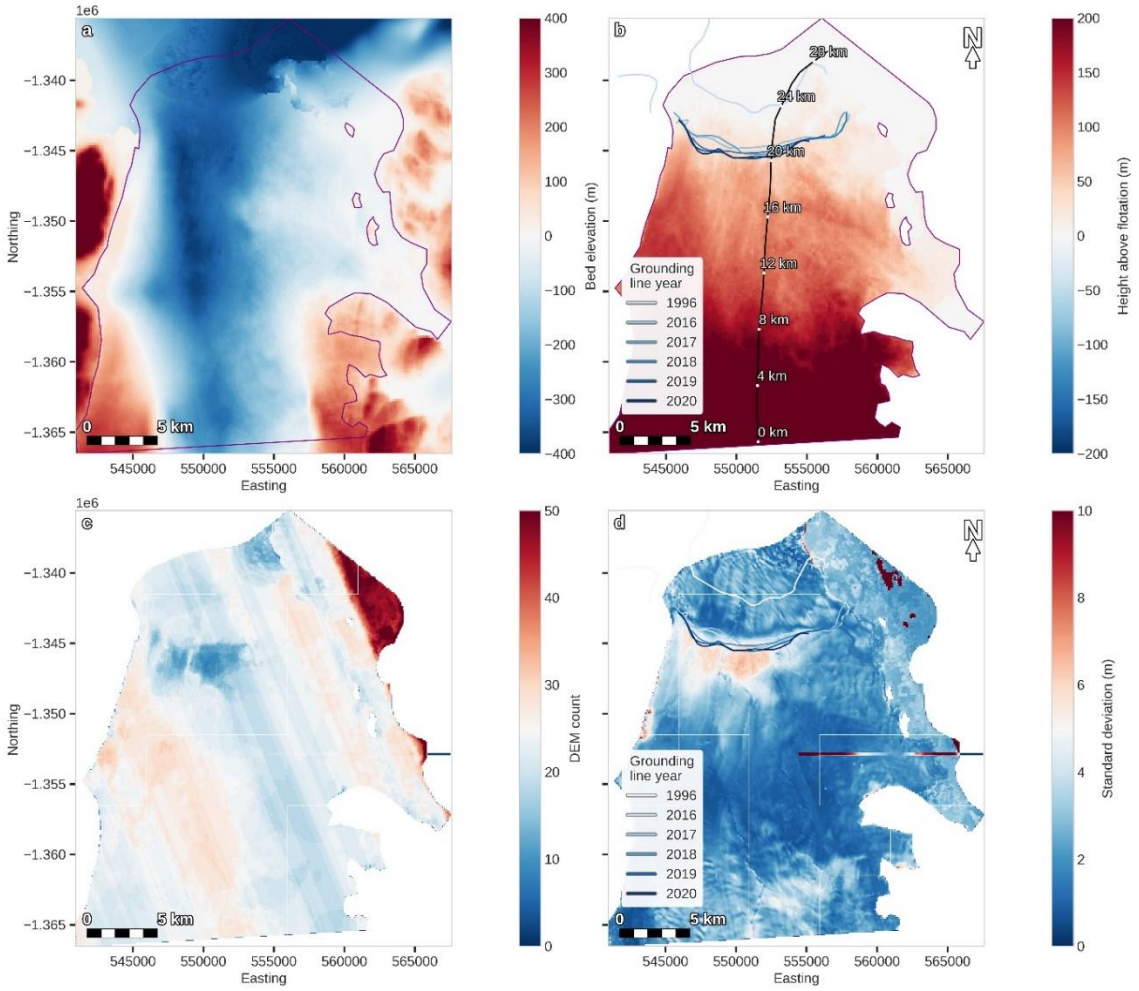


Figure B.2.5: Supplementary information relating to the geometry and DEM statistics of L. Bistrup Bræ. For each panel, the purple outline indicates the study area. Panel a is the bed elevation from BedMachine version 5 (Morlighem et al., 2022) and panel b is the height above flotation as calculated from BedMachine version 5 (Morlighem et al., 2022) using Eq. 5.1. Panel c shows the number of DEMs processed over the study area, and panel d shows the standard deviation of the DEMs where we process the data in the same way as for the median absolute deviation as shown in Figure 5.9. Additionally, in panel b and panel d we show all historical grounding lines mapped by other studies (Table 5.3).

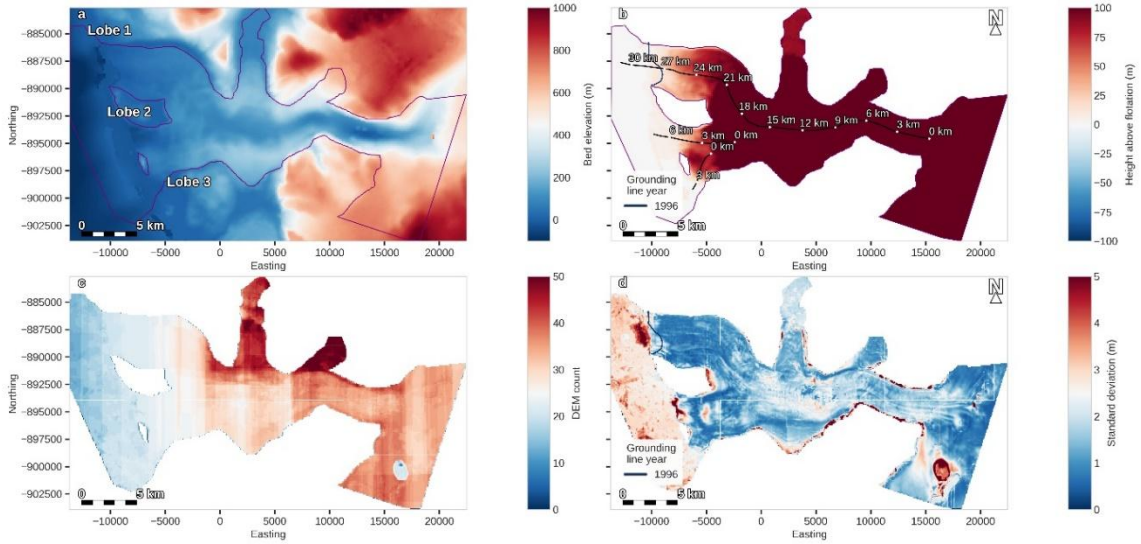


Figure B.2.6: Supplementary information relating to the geometry and DEM statistics of Brikkerne Gletsjer. For each panel, the purple outline indicates the study area. Panel a is the bed elevation from BedMachine version 5 (Morlighem et al., 2022) and panel b is the height above flotation as calculated from BedMachine version 5 (Morlighem et al., 2022) using Eq. 5.1. Panel c shows the number of DEMs processed over the study area, and panel d shows the standard deviation of the DEMs where we process the data in the same way as for the median absolute deviation as shown in Figure 5.10. Additionally, in panel b and panel d we show all historical grounding lines mapped by other studies (Table 5.3).

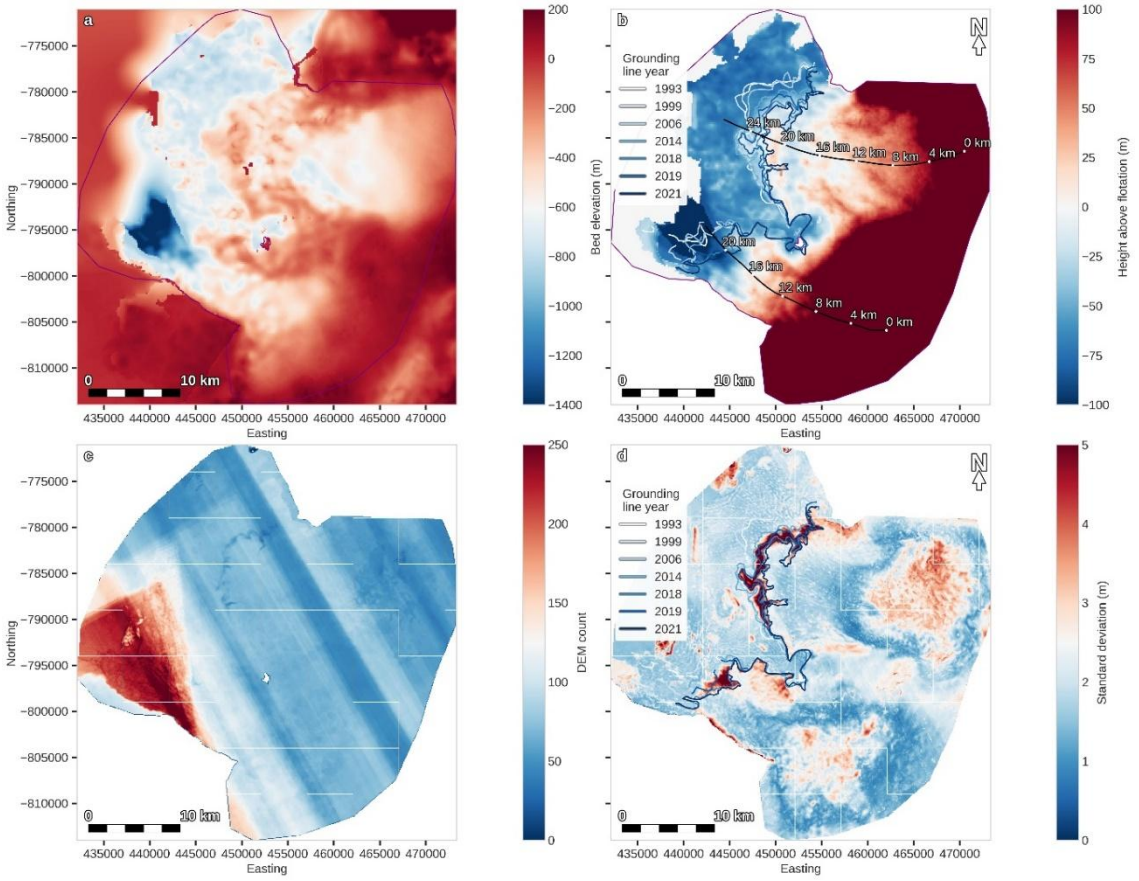


Figure B.2.7: Supplementary information relating to the geometry and DEM statistics of Flade Isblink. For each panel, the purple outline indicates the study area. Panel a is the bed elevation from BedMachine version 5 (Morlighem et al., 2022) and panel b is the height above flotation as calculated from BedMachine version 5 (Morlighem et al., 2022) using Eq. 5.1. Panel c shows the number of DEMs processed over the study area, and panel d shows the standard deviation of the DEMs where we process the data in the same way as for the median absolute deviation as shown in Figure 5.11. Additionally, in panel b and panel d we show all historical grounding lines mapped by other studies (Table 5.3).

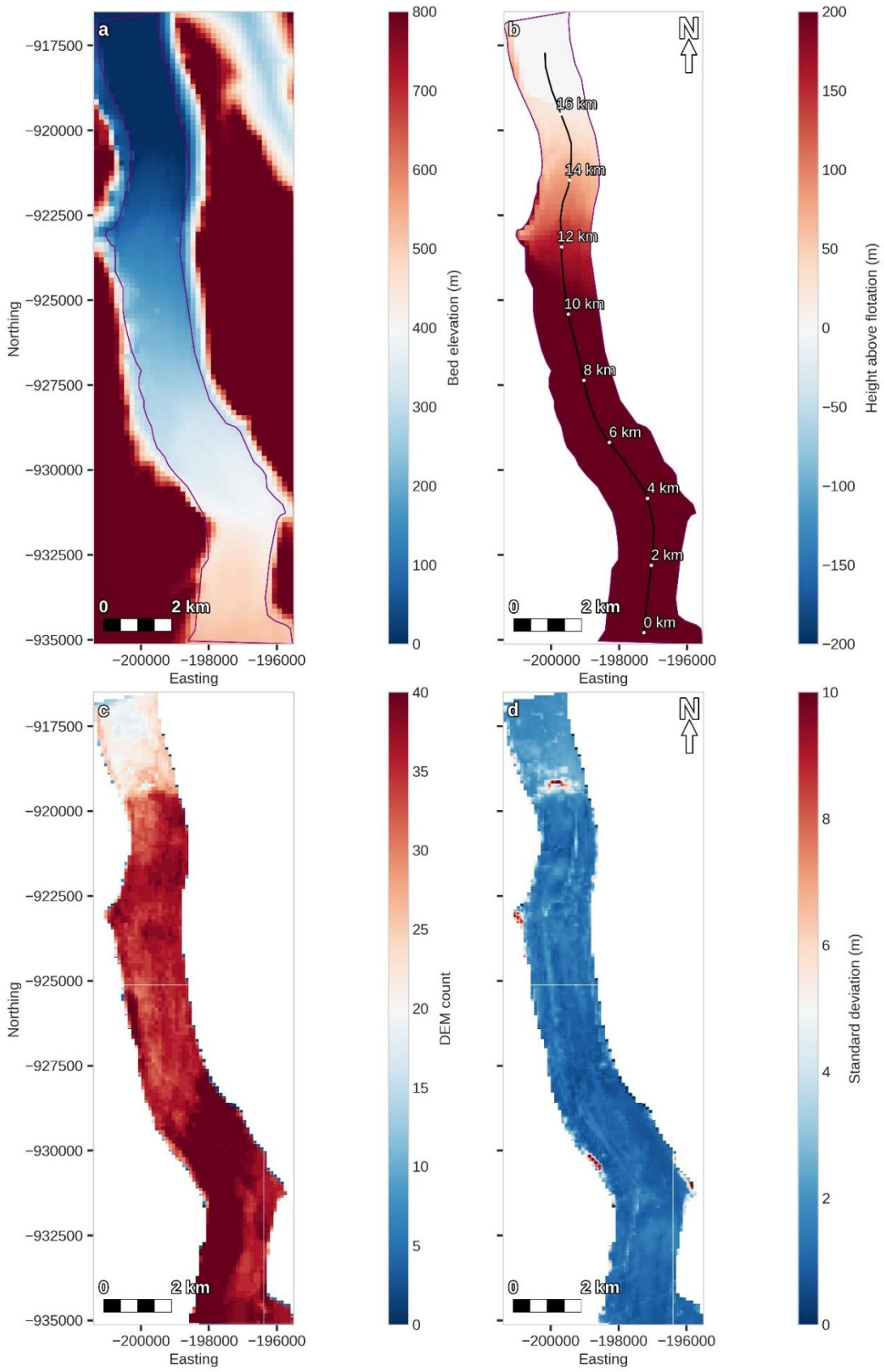


Figure B.2.8: Supplementary information relating to the geometry and DEM statistics of Newman Bugt. For each panel, the purple outline indicates the study area. Panel a is the bed elevation from

BedMachine version 5 (Morlighem et al., 2022) and panel b is the height above flotation as calculated from BedMachine version 5 (Morlighem et al., 2022) using Eq. 5.1. Panel c shows the number of DEMs processed over the study area, and panel d shows the standard deviation of the DEMs where we process the data in the same way as for the median absolute deviation as shown in Figure 5.12.

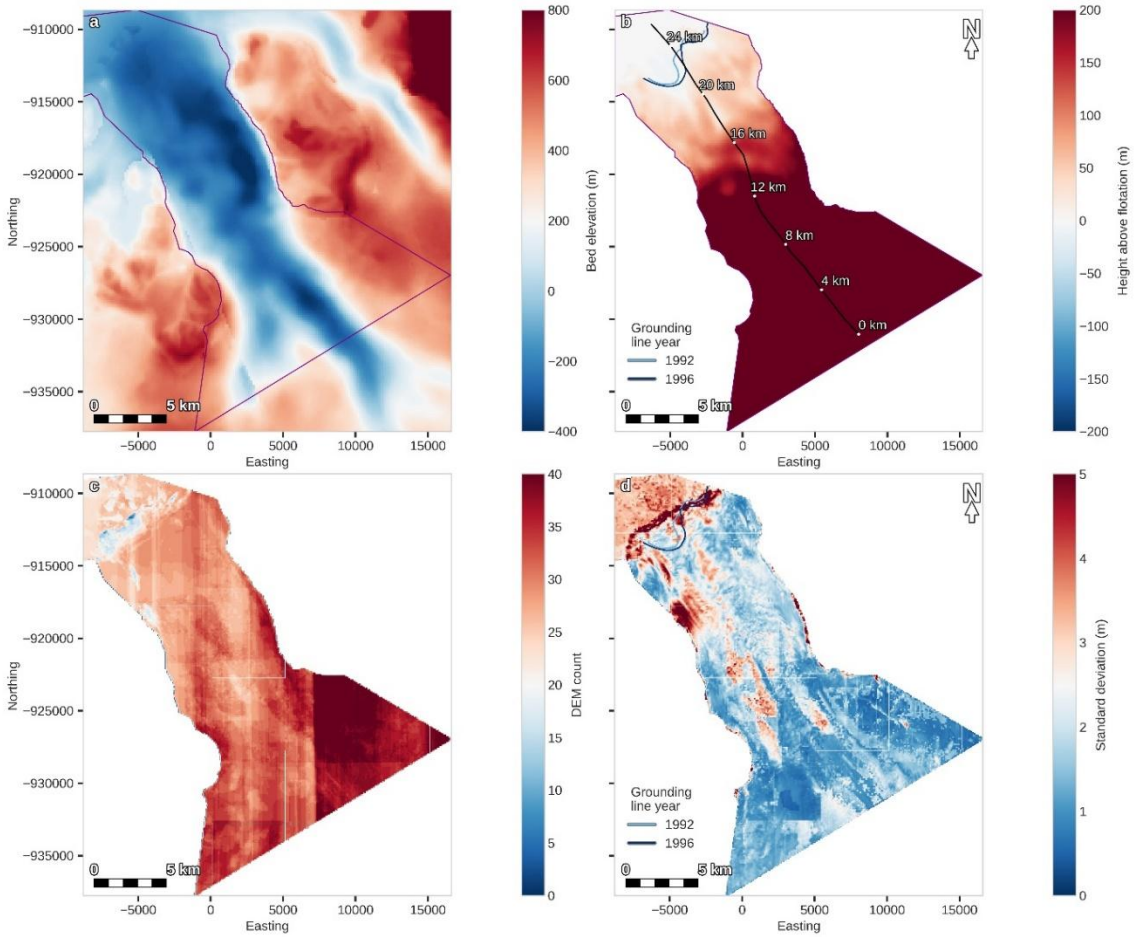


Figure B.2.9: Supplementary information relating to the geometry and DEM statistics of C. H. Ostenfeld Gletsjer. For each panel, the purple outline indicates the study area. Panel a is the bed elevation from BedMachine version 5 (Morlighem et al., 2022) and panel b is the height above flotation as calculated from BedMachine version 5 (Morlighem et al., 2022) using Eq. 5.1. Panel c shows the number of DEMs processed over the study area, and panel d shows the standard deviation of the DEMs where we process the data in the same way as for the median absolute deviation as shown in Figure 5.13. Additionally, in panel b and panel d we show all historical grounding lines mapped by other studies (Table 5.3).

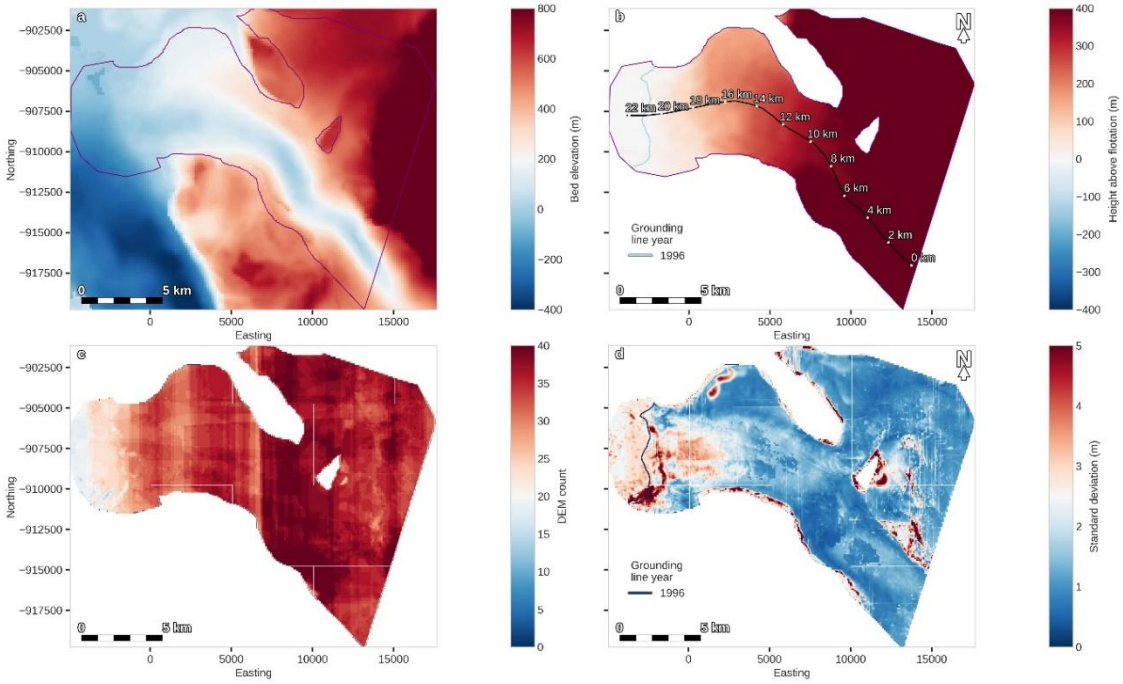


Figure B.2.10: Supplementary information relating to the geometry and DEM statistics of Harder Gletsjer. For each panel, the purple outline indicates the study area. Panel a is the bed elevation from BedMachine version 5 (Morlighem et al., 2022) and panel b is the height above flotation as calculated from BedMachine version 5 (Morlighem et al., 2022) using Eq. 5.1. Panel c shows the number of DEMs processed over the study area, and panel d shows the standard deviation of the DEMs where we process the data in the same way as for the median absolute deviation as shown in Figure 5.14. Additionally, in panel b and panel d we show all historical grounding lines mapped by other studies (Table 5.3).

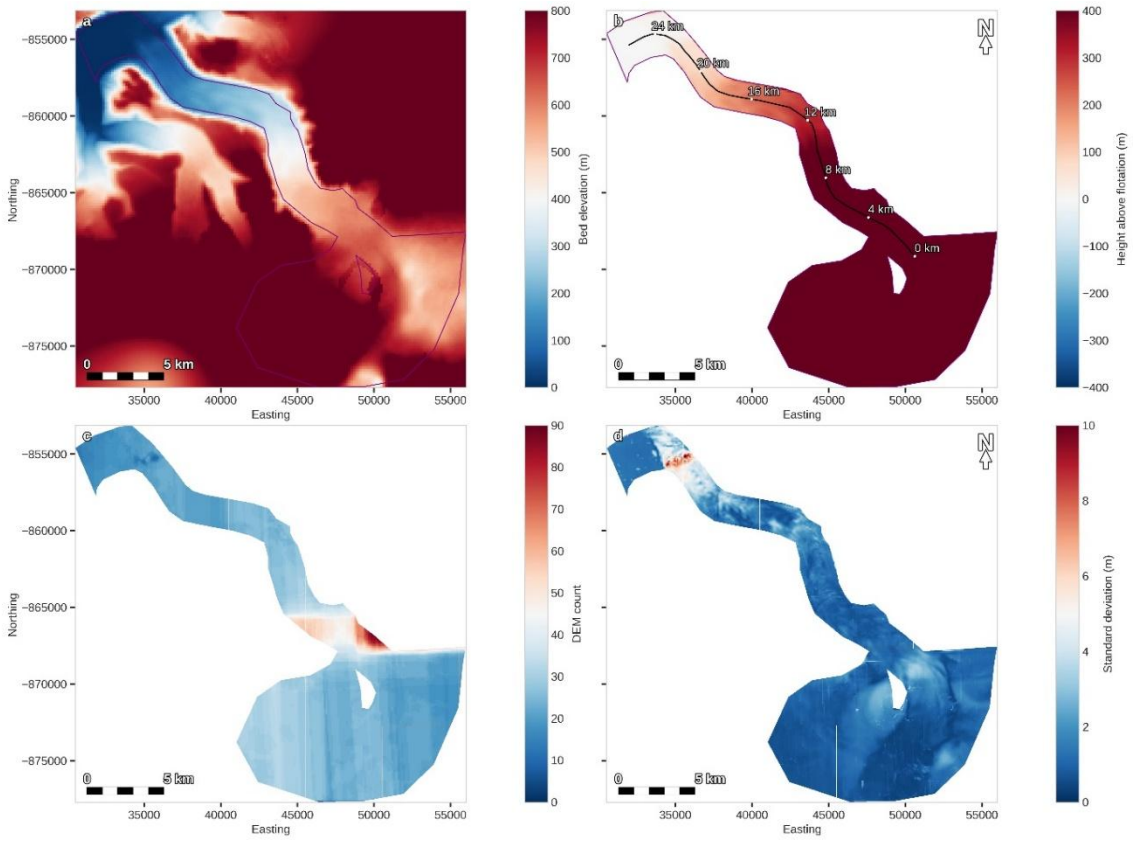


Figure B.2.11: Supplementary information relating to the geometry and DEM statistics of Jungersen Gletsjer. For each panel, the purple outline indicates the study area. Panel a is the bed elevation from BedMachine version 5 (Morlighem et al., 2022) and panel b is the height above flotation as calculated from BedMachine version 5 (Morlighem et al., 2022) using Eq. 5.1. Panel c shows the number of DEMs processed over the study area, and panel d shows the standard deviation of the DEMs where we process the data in the same way as for the median absolute deviation as shown in Figure 5.15.

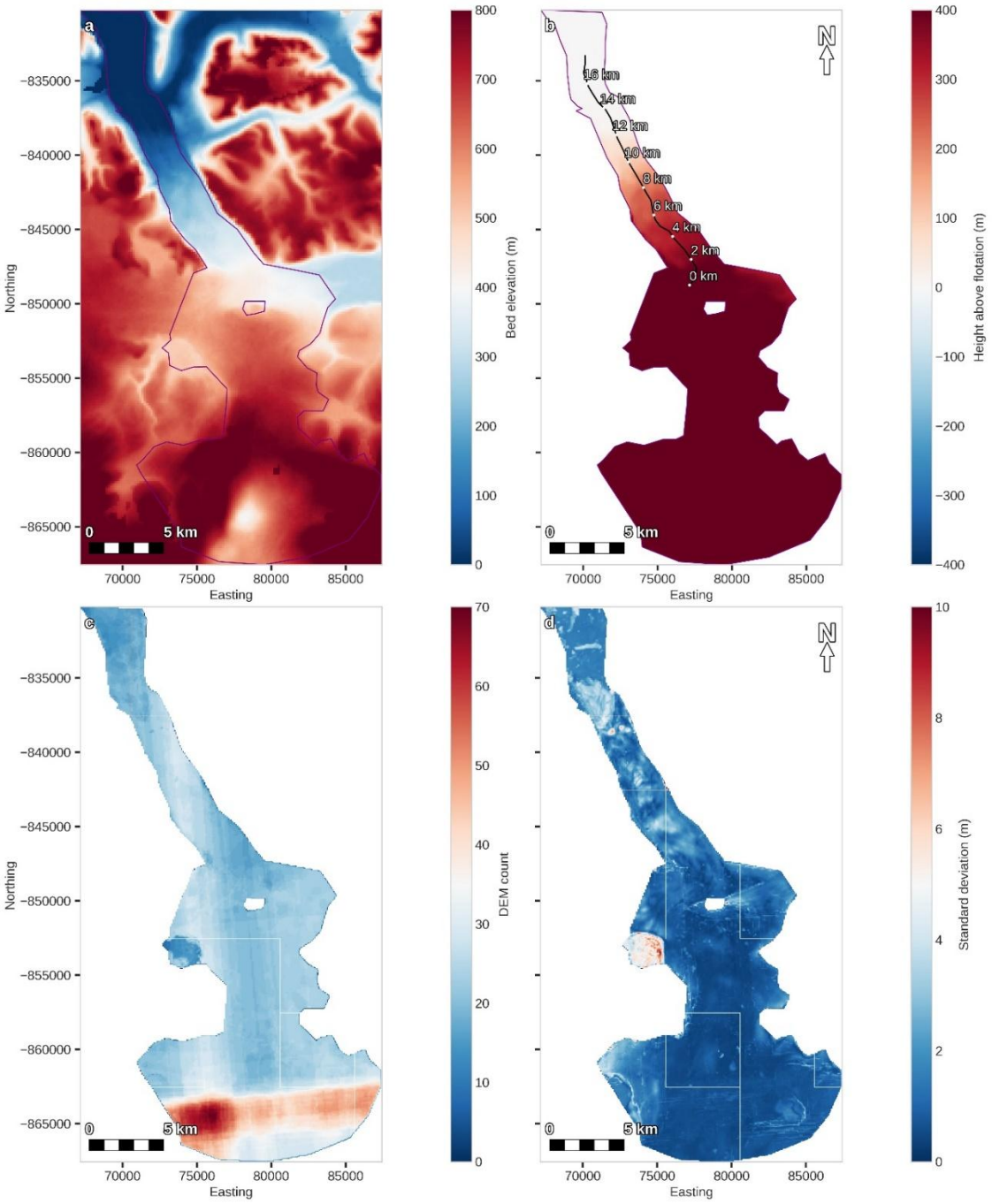


Figure B.2.12: Supplementary information relating to the geometry and DEM statistics of Henson Gletsjer. For each panel, the purple outline indicates the study area. Panel a is the bed elevation from BedMachine version 5 (Morlighem et al., 2022) and panel b is the height above flotation as calculated from BedMachine version 5 (Morlighem et al., 2022) using Eq. 5.1. Panel c shows the number of DEMs processed over the study area, and panel d shows the standard deviation of the DEMs where we process the data in the same way as for the median absolute deviation as shown in Figure 5.16.

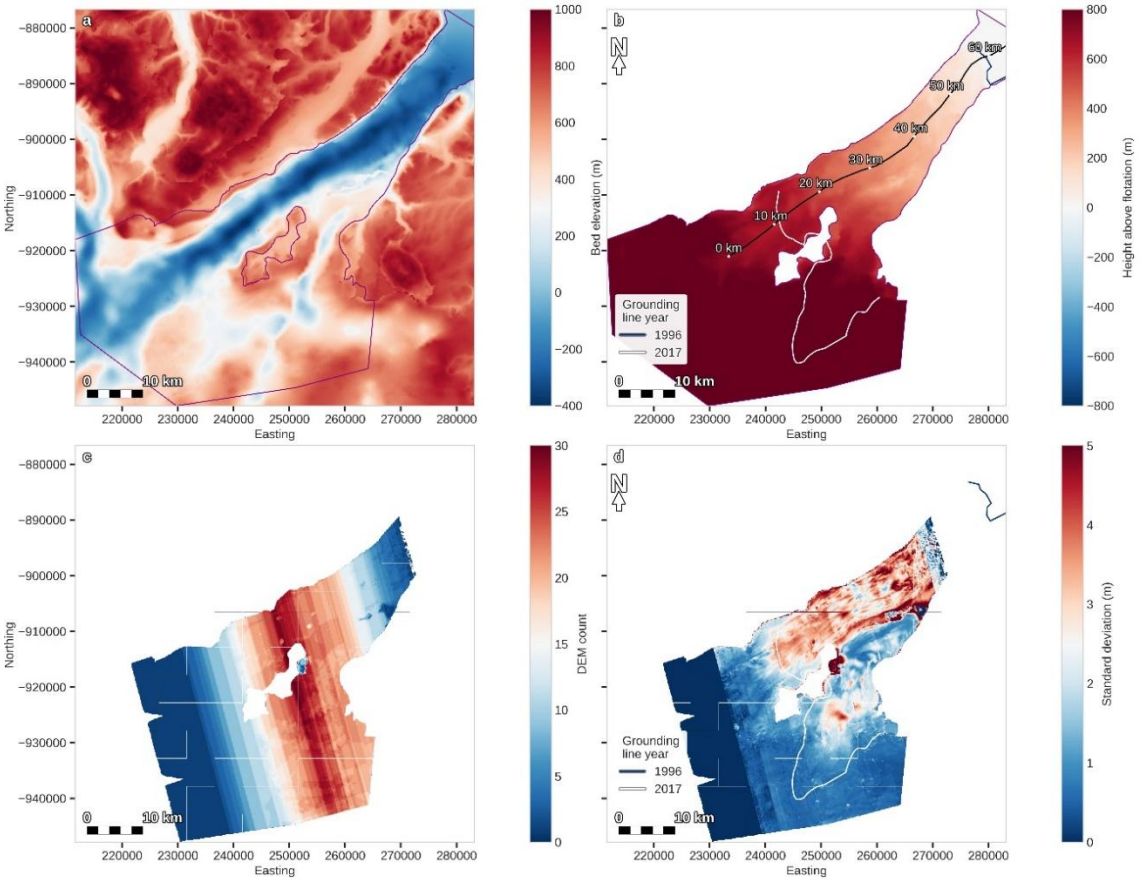


Figure B.2.13: Supplementary information relating to the geometry and DEM statistics of Hagen Bræ. For each panel, the purple outline indicates the study area. Panel a is the bed elevation from BedMachine version 5 (Morlighem et al., 2022) and panel b is the height above flotation as calculated from BedMachine version 5 (Morlighem et al., 2022) using Eq. 5.1. Panel c shows the number of DEMs processed over the study area, and panel d shows the standard deviation of the DEMs where we process the data in the same way as for the median absolute deviation as shown in Figure 5.17. Additionally, in panel b and panel d we show all historical grounding lines mapped by other studies (Table 5.3).

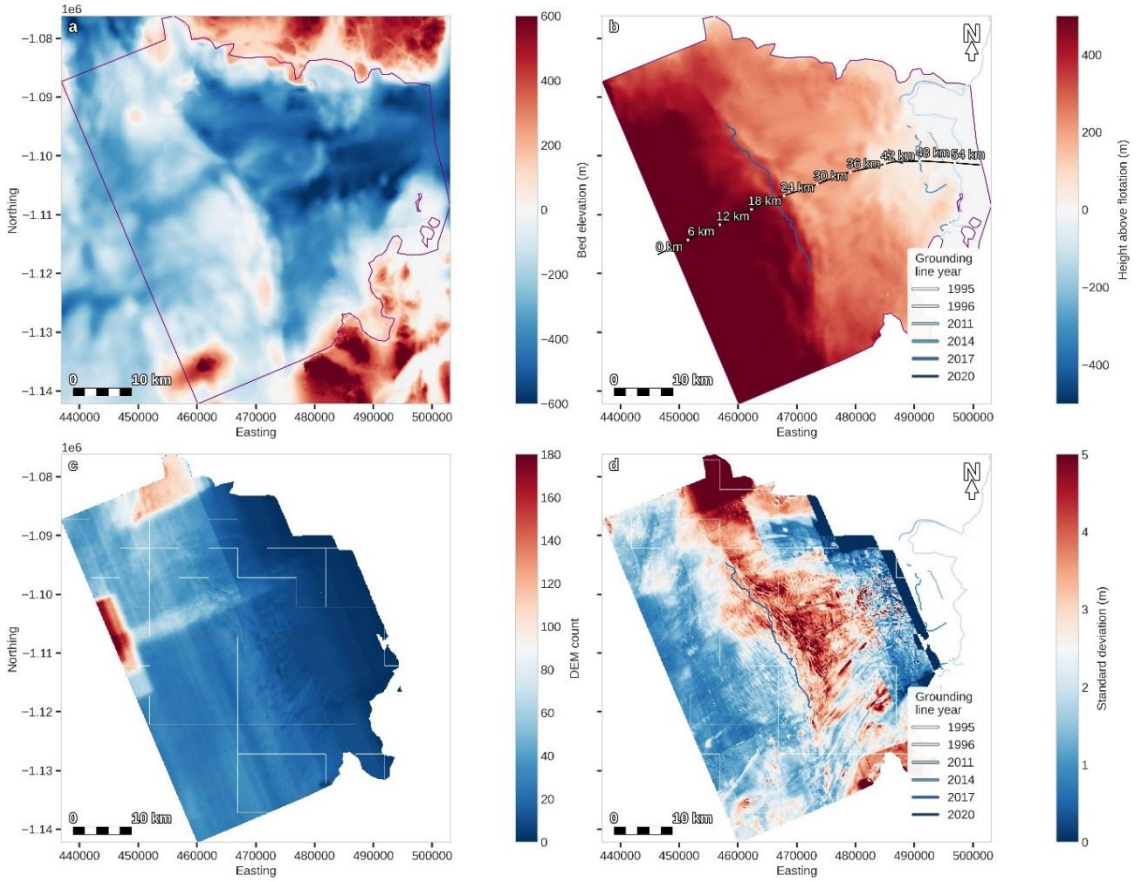


Figure B.2.14: Supplementary information relating to the geometry and DEM statistics of Zachariæ Isstrøm. For each panel, the purple outline indicates the study area. Panel a is the bed elevation from BedMachine version 5 (Morlighem et al., 2022) and panel b is the height above flotation as calculated from BedMachine version 5 (Morlighem et al., 2022) using Eq. 5.1. Panel c shows the number of DEMs processed over the study area, and panel d shows the standard deviation of the DEMs where we process the data in the same way as for the median absolute deviation as shown in Figure 5.18. Additionally, in panel b and panel d we show all historical grounding lines mapped by other studies (Table 5.3).

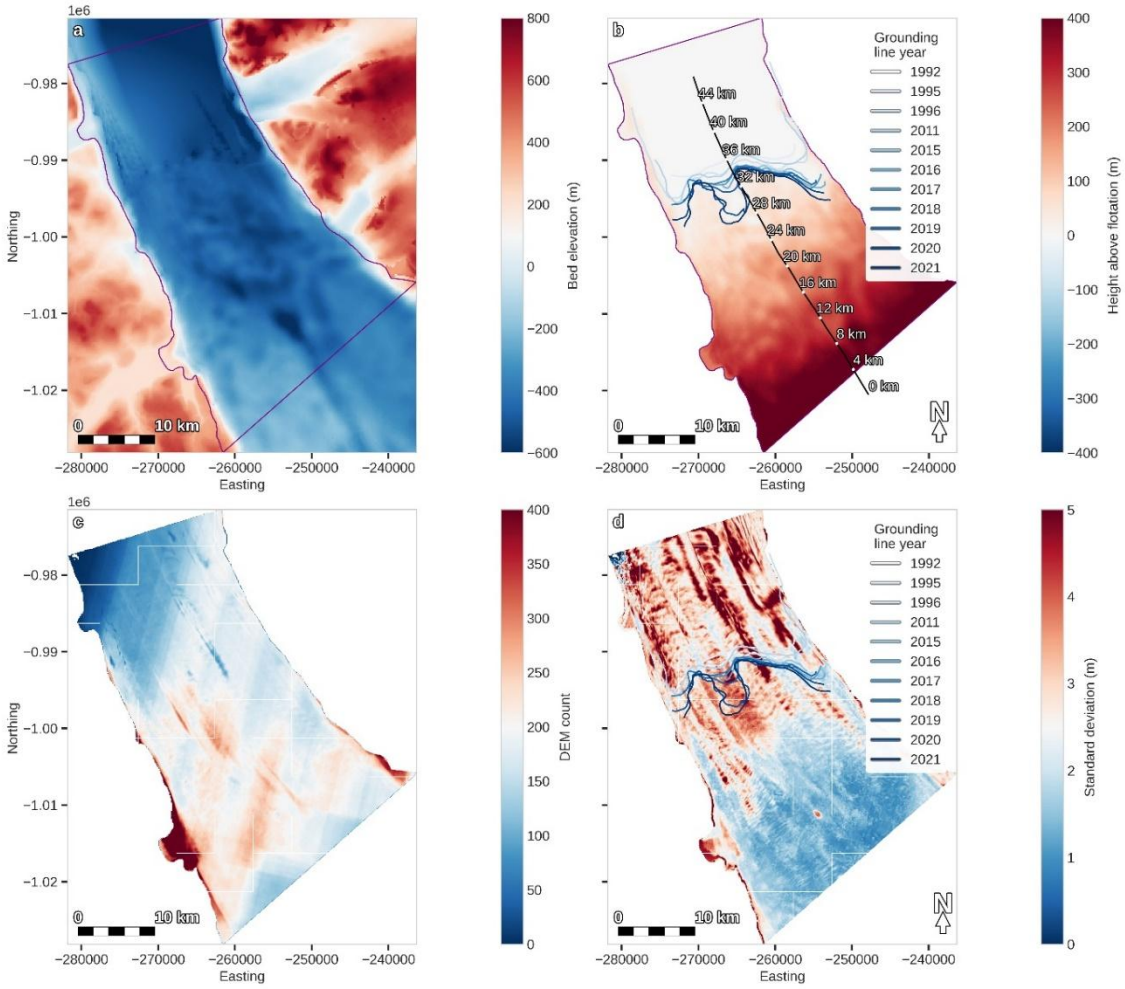


Figure B.2.15: Supplementary information relating to the geometry and DEM statistics of Petermann Gletsjer. For each panel, the purple outline indicates the study area. Panel a is the bed elevation from BedMachine version 5 (Morlighem et al., 2022) and panel b is the height above flotation as calculated from BedMachine version 5 (Morlighem et al., 2022) using Eq. 5.1. Panel c shows the number of DEMs processed over the study area, and panel d shows the standard deviation of the DEMs where we process the data in the same way as for the median absolute deviation as shown in Figure 5.19. Additionally, in panel b and panel d we show all historical grounding lines mapped by other studies (Table 5.3).

# B.3 BedMachine version 5 source data and uncertainty

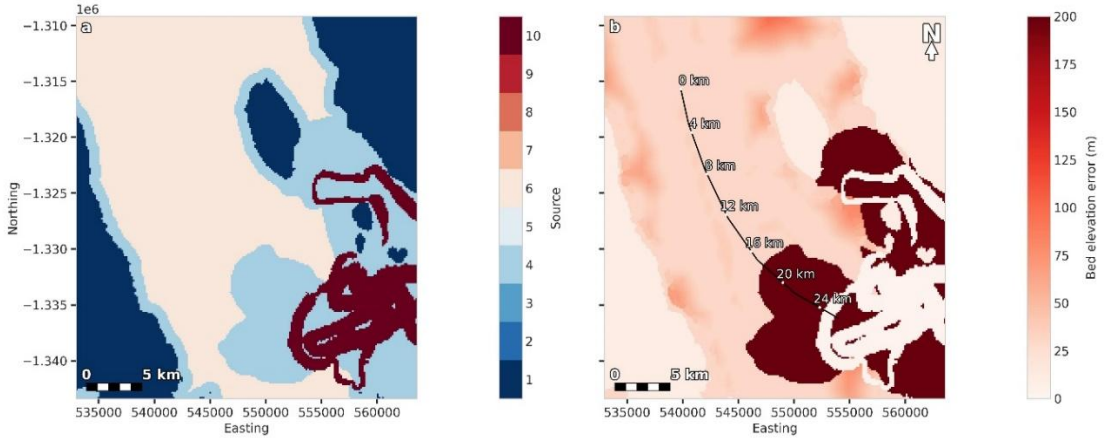


Figure B.3.1: Plots relating to the bed elevation source data type (a) and bed elevation error (b) of the BedMachine version 5 data for Storstrømmen. In panel (a), the source data types are as follows: (1) GIMPDEM (Howat et al., 2014), (2) mass conservation, (3) synthetic, (4) interpolation, (5) hydrostatic equilibrium, (6) kriging, (7) RTOPO-2 (Schaffer et al., 2016), (8) gravity inversion, (9) Millan et al. (2022b), (10) bathymetry data.

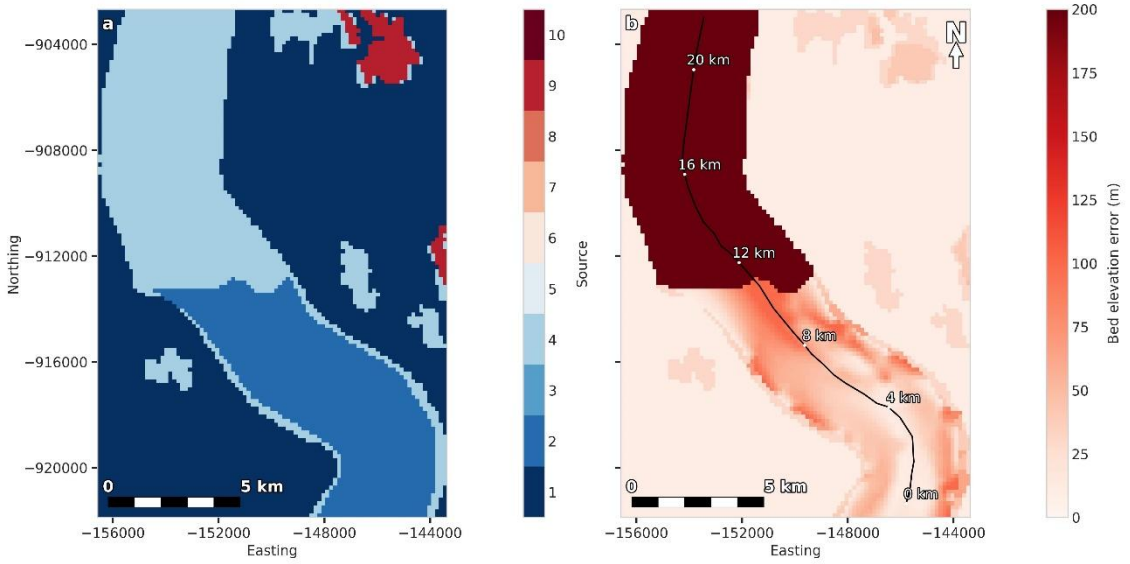


Figure B.3.2: Plots relating to the bed elevation source data type (a) and bed elevation error (b) of the BedMachine version 5 data for Steensby Gletsjer. In panel (a), the source data types are as follows: (1) GIMPDEM (Howat et al., 2014), (2) mass conservation, (3) synthetic, (4) interpolation, (5) hydrostatic equilibrium, (6) kriging, (7) RTOPO-2 (Schaffer et al., 2016), (8) gravity inversion, (9) Millan et al. (2022b), (10) bathymetry data.

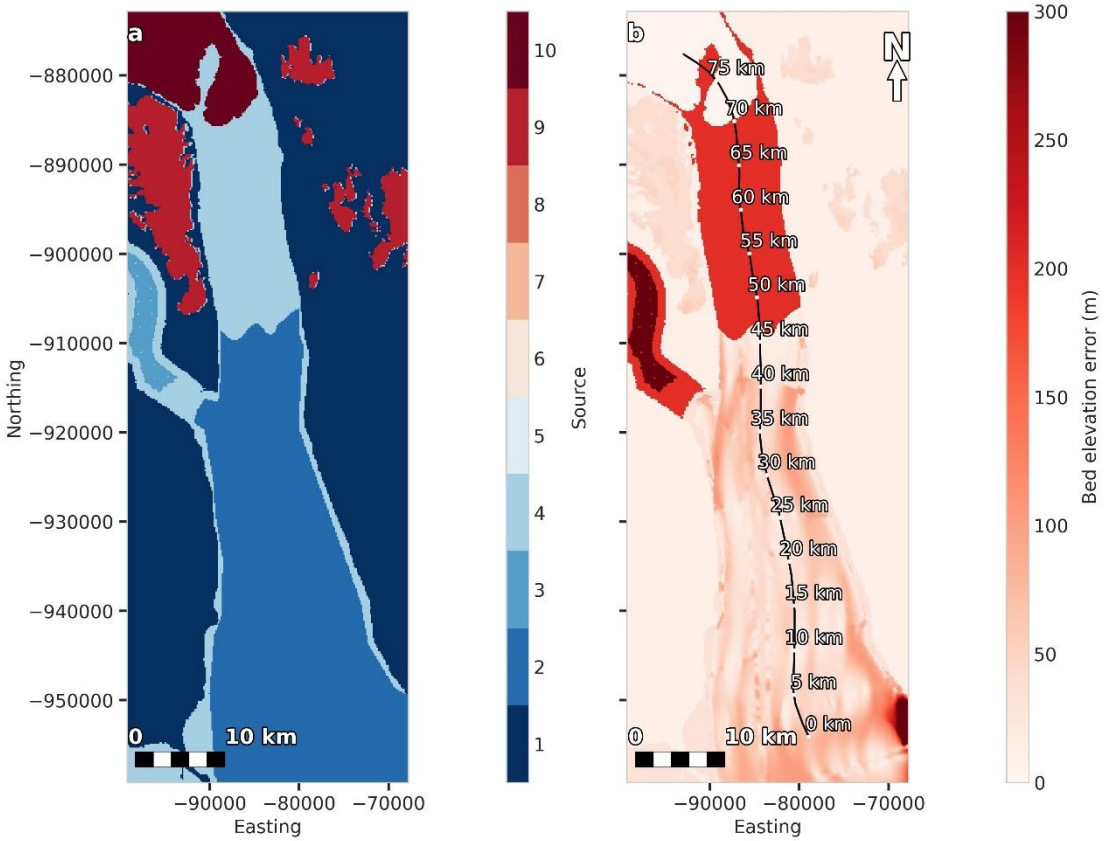


Figure B.3.3: Plots relating to the bed elevation source data type (a) and bed elevation error (b) of the BedMachine version 5 data for Ryder Gletsjer. In panel (a), the source data types are as follows: (1) GIMPDEM (Howat et al., 2014), (2) mass conservation, (3) synthetic, (4) interpolation, (5) hydrostatic equilibrium, (6) kriging, (7) RTOPO-2 (Schaffer et al., 2016), (8) gravity inversion, (9) Millan et al. (2022b), (10) bathymetry data.

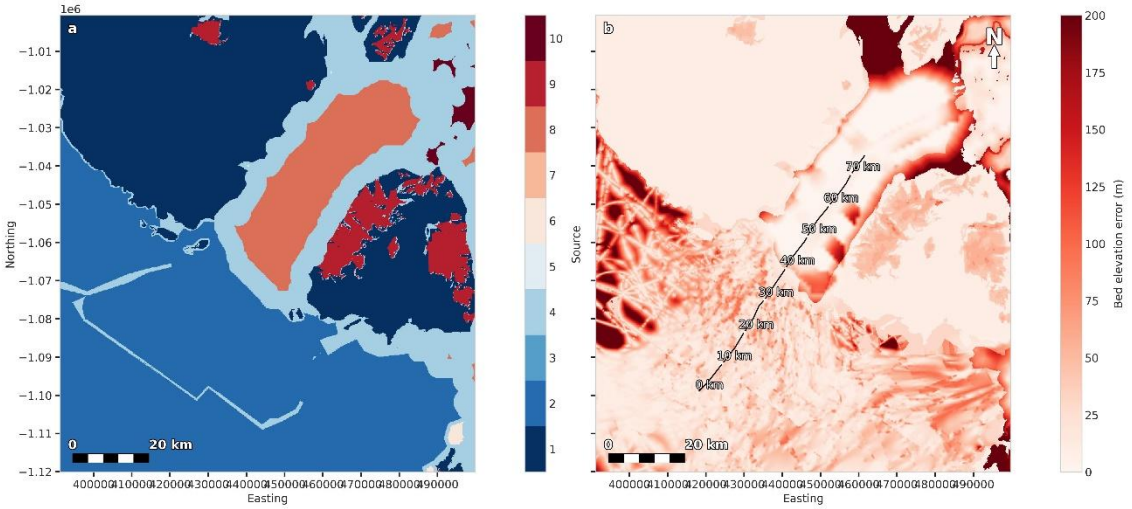


Figure B.3.4: Plots relating to the bed elevation source data type (a) and bed elevation error (b) of the BedMachine version 5 data for 79N. In panel (a), the source data types are as follows: (1) GIMPDEM (Howat et al., 2014), (2) mass conservation, (3) synthetic, (4) interpolation, (5) hydrostatic equilibrium, (6) kriging, (7) RTOPO-2 (Schaffer et al., 2016), (8) gravity inversion, (9) Millan et al. (2022b), (10) bathymetry data.

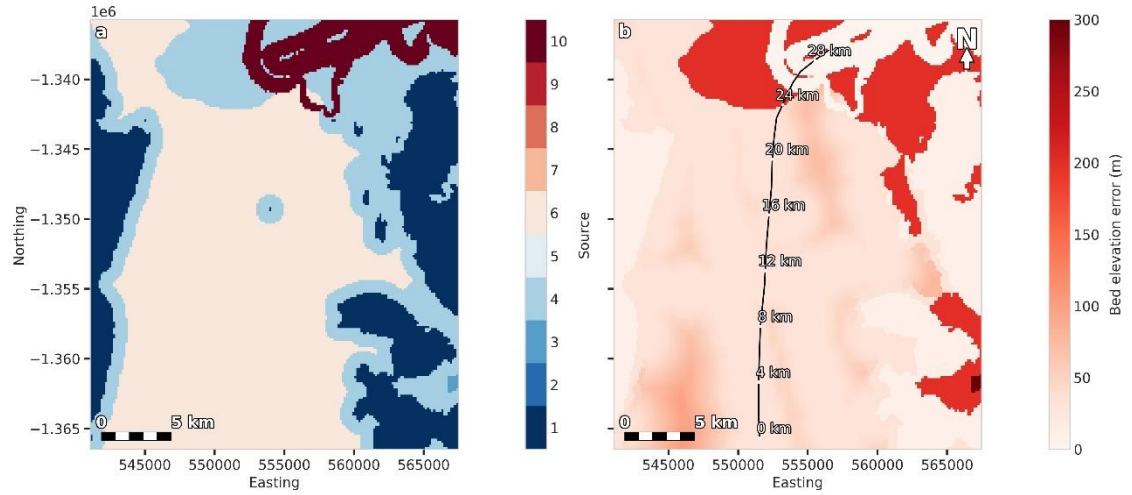


Figure B.3.5: Plots relating to the bed elevation source data type (a) and bed elevation error (b) of the BedMachine version 5 data for L. Bistrup Bræ. In panel (a), the source data types are as follows: (1) GIMPDEM (Howat et al., 2014), (2) mass conservation, (3) synthetic, (4) interpolation, (5) hydrostatic equilibrium, (6) kriging, (7) RTOPO-2 (Schaffer et al., 2016), (8) gravity inversion, (9) Millan et al. (2022b), (10) bathymetry data.

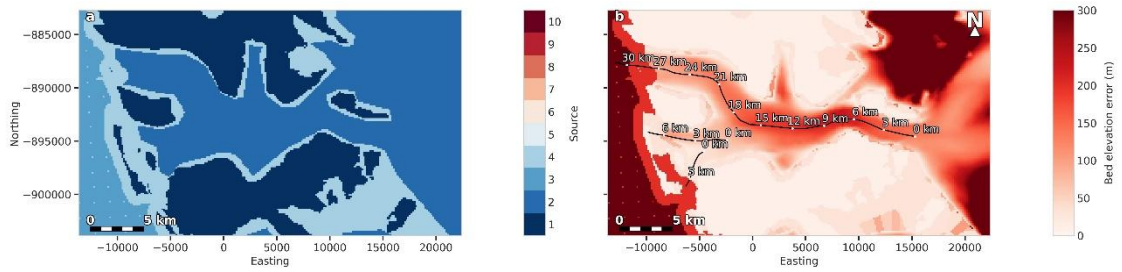


Figure B.3.6: Plots relating to the bed elevation source data type (a) and bed elevation error (b) of the BedMachine version 5 data for Brikkerne Gletsjer. In panel (a), the source data types are as follows: (1) GIMPDEM (Howat et al., 2014), (2) mass conservation, (3) synthetic, (4) interpolation, (5) hydrostatic equilibrium, (6) kriging, (7) RTOPO-2 (Schaffer et al., 2016), (8) gravity inversion, (9) Millan et al. (2022b), (10) bathymetry data.

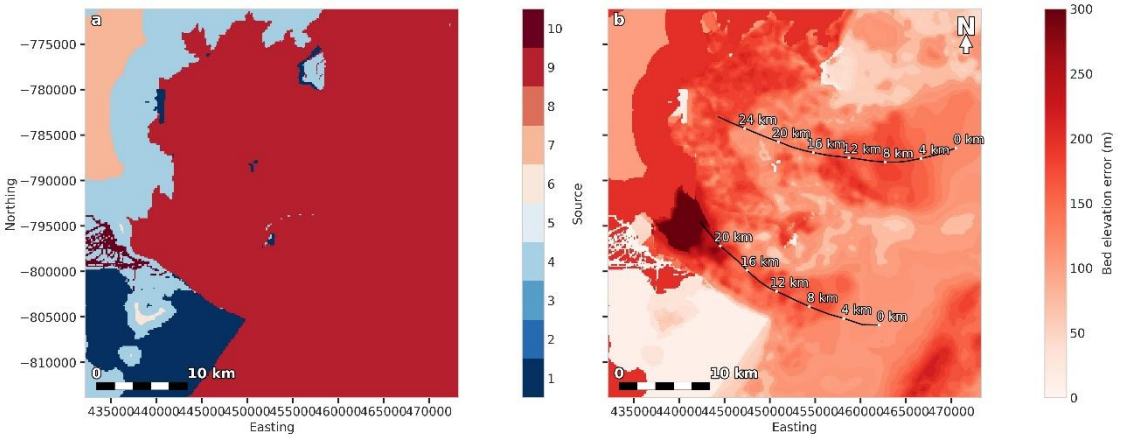


Figure B.3.7: Plots relating to the bed elevation source data type (a) and bed elevation error (b) of the BedMachine version 5 data for Flade Isblink. In panel (a), the source data types are as follows: (1) GIMPDEM (Howat et al., 2014), (2) mass conservation, (3) synthetic, (4) interpolation, (5) hydrostatic equilibrium, (6) kriging, (7) RTOPO-2 (Schaffer et al., 2016), (8) gravity inversion, (9) Millan et al. (2022b), (10) bathymetry data.

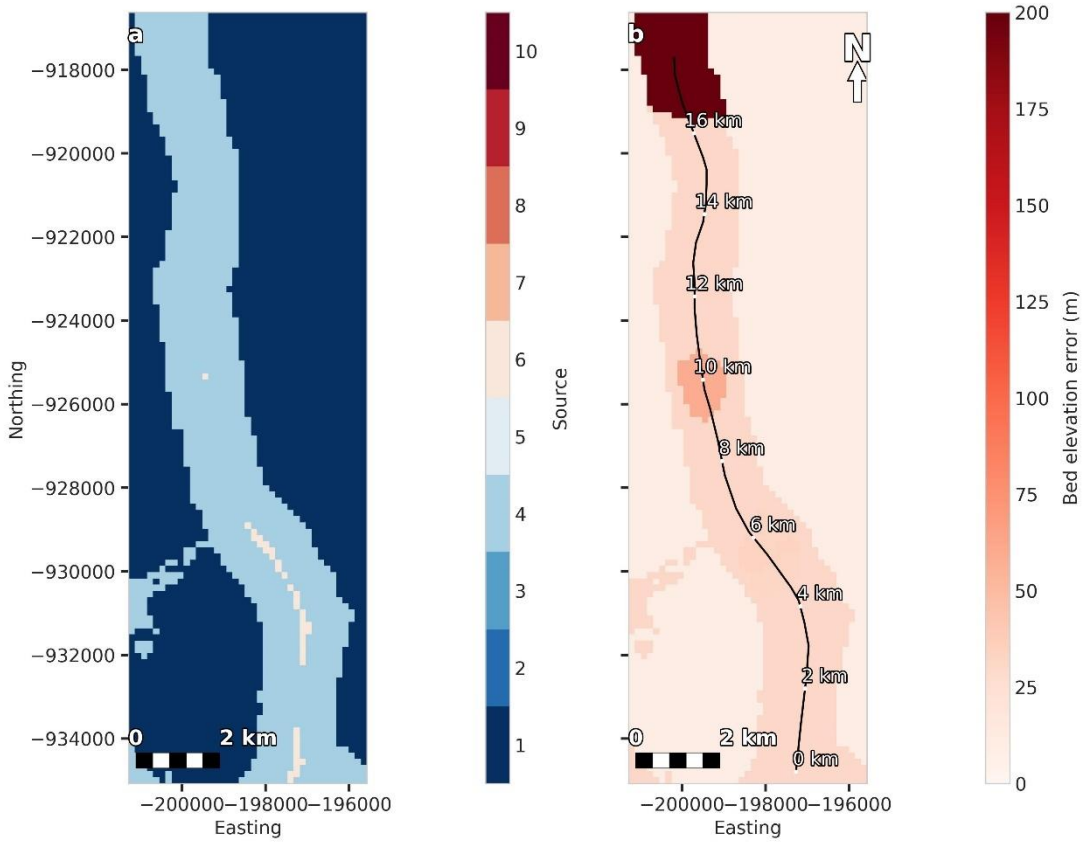


Figure B.3.8: Plots relating to the bed elevation source data type (a) and bed elevation error (b) of the BedMachine version 5 data for Newman Bugt. In panel (a), the source data types are as follows: (1) GIMPDEM (Howat et al., 2014), (2) mass conservation, (3) synthetic, (4) interpolation, (5) hydrostatic equilibrium, (6) kriging, (7) RTOPO-2 (Schaffer et al., 2016), (8) gravity inversion, (9) Millan et al. (2022b), (10) bathymetry data.

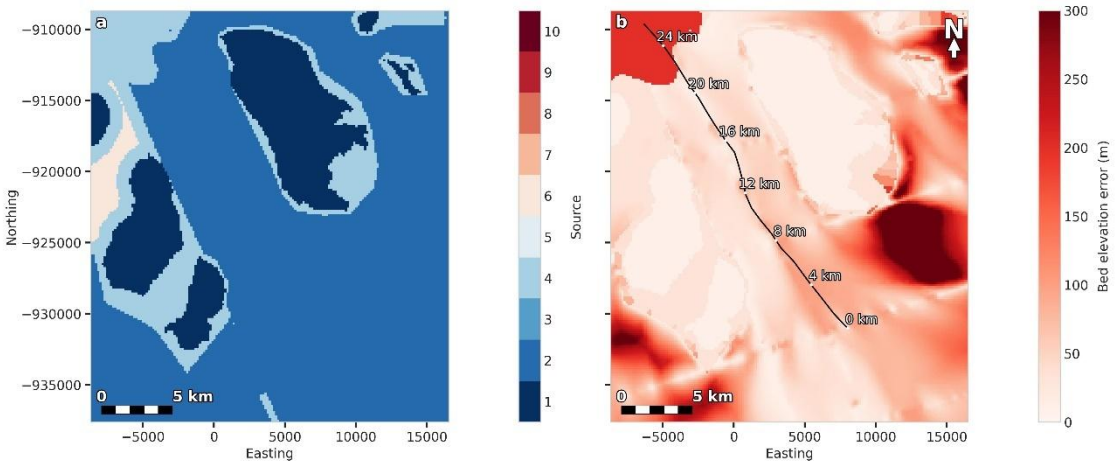


Figure B.3.9: Plots relating to the bed elevation source data type (a) and bed elevation error (b) of the BedMachine version 5 data for C. H. Ostenfeld. In panel (a), the source data types are as follows: (1) GIMPDEM (Howat et al., 2014), (2) mass conservation, (3) synthetic, (4) interpolation, (5) hydrostatic equilibrium, (6) kriging, (7) RTOPO-2 (Schaffer et al., 2016), (8) gravity inversion, (9) Millan et al. (2022b), (10) bathymetry data.

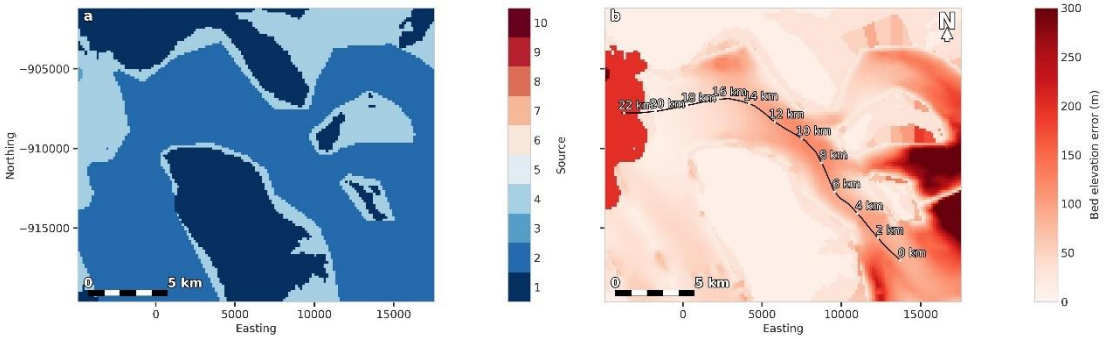


Figure B.3.10: Plots relating to the bed elevation source data type (a) and bed elevation error (b) of the BedMachine version 5 data for Harder Gletsjer. In panel (a), the source data types are as follows: (1) GIMPDEM (Howat et al., 2014), (2) mass conservation, (3) synthetic, (4) interpolation, (5) hydrostatic equilibrium, (6) kriging, (7) RTOPO-2 (Schaffer et al., 2016), (8) gravity inversion, (9) Millan et al. (2022b), (10) bathymetry data.

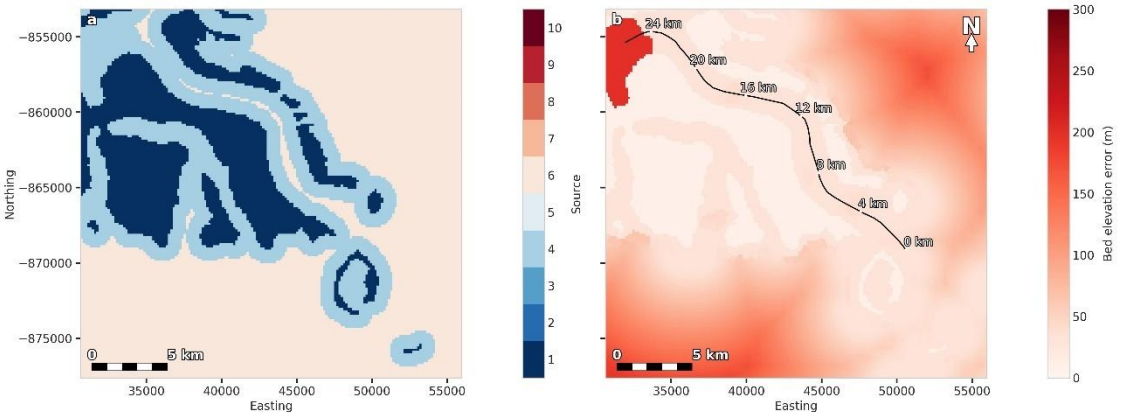


Figure B.3.11: Plots relating to the bed elevation source data type (a) and bed elevation error (b) of the BedMachine version 5 data for Jungersen Gletsjer. In panel (a), the source data types are as follows: (1) GIMPDEM (Howat et al., 2014), (2) mass conservation, (3) synthetic, (4) interpolation, (5) hydrostatic equilibrium, (6) kriging, (7) RTOPO-2 (Schaffer et al., 2016), (8) gravity inversion, (9) Millan et al. (2022b), (10) bathymetry data.

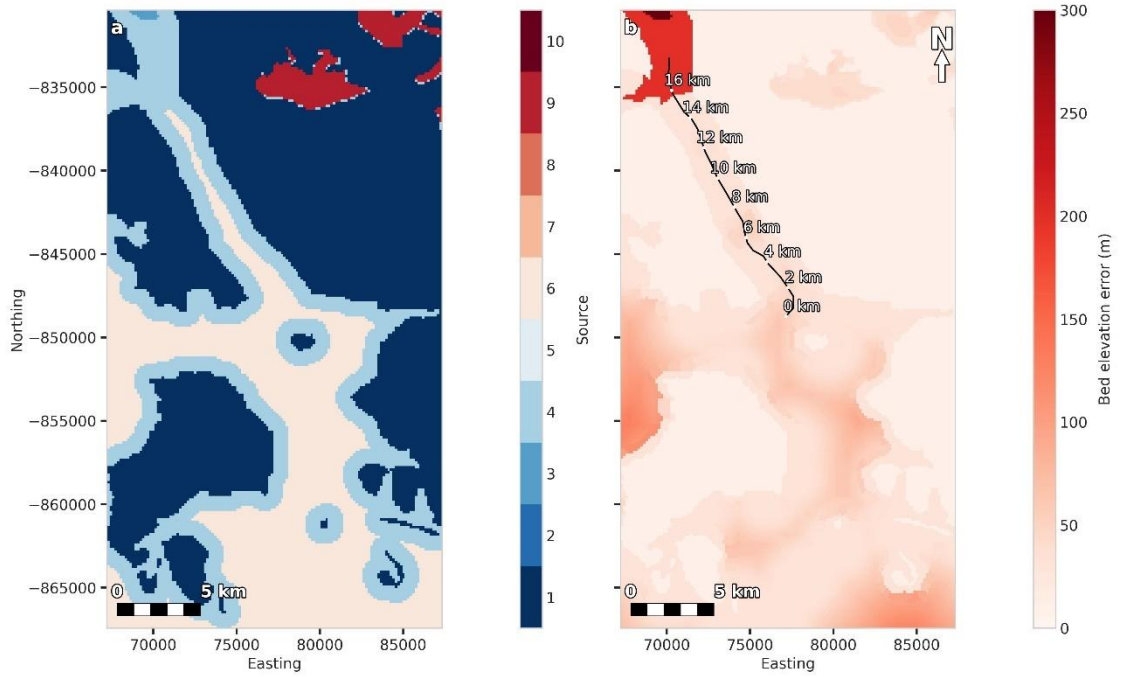


Figure B.3.12: Plots relating to the bed elevation source data type (a) and bed elevation error (b) of the BedMachine version 5 data for Henson Gletsjer. In panel (a), the source data types are as follows: (1) GIMPDEM (Howat et al., 2014), (2) mass conservation, (3) synthetic, (4) interpolation, (5) hydrostatic equilibrium, (6) kriging, (7) RTOPO-2 (Schaffer et al., 2016), (8) gravity inversion, (9) Millan et al. (2022b), (10) bathymetry data.

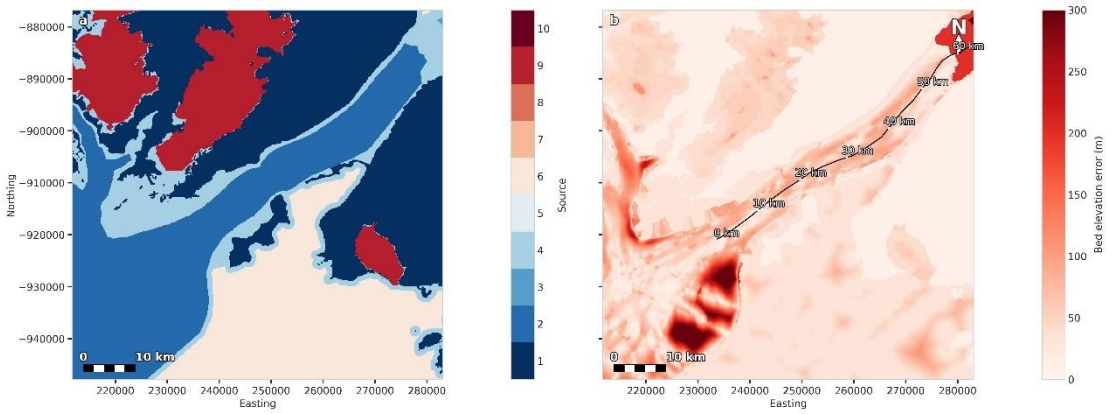


Figure B.3.13: Plots relating to the bed elevation source data type (a) and bed elevation error (b) of the BedMachine version 5 data for Hagen Bræ. In panel (a), the source data types are as follows: (1) GIMPDEM (Howat et al., 2014), (2) mass conservation, (3) synthetic, (4) interpolation, (5) hydrostatic equilibrium, (6) kriging, (7) RTOPO-2 (Schaffer et al., 2016), (8) gravity inversion, (9) Millan et al. (2022b), (10) bathymetry data.

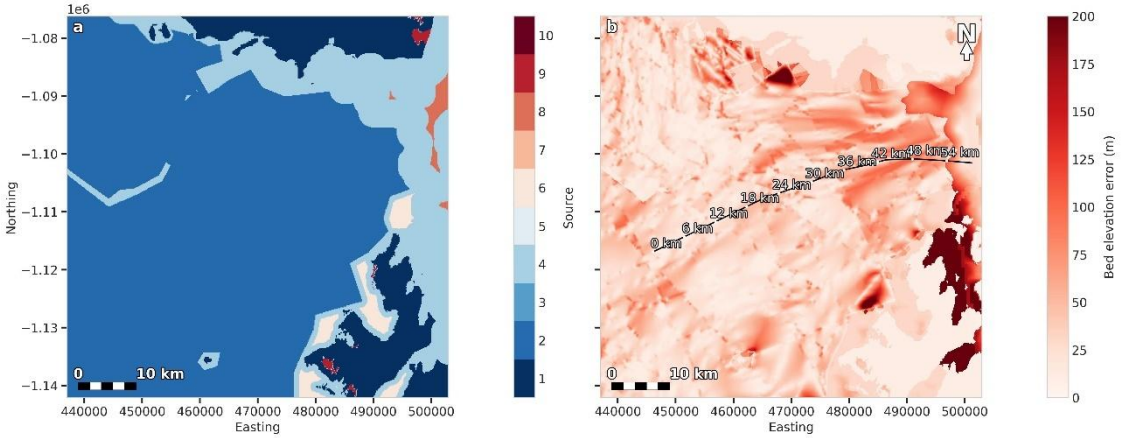


Figure B.3.14: Plots relating to the bed elevation source data type (a) and bed elevation error (b) of the BedMachine version 5 data for Zachariæ Isstrøm. In panel (a), the source data types are as follows: (1) GIMPDEM (Howat et al., 2014), (2) mass conservation, (3) synthetic, (4) interpolation, (5) hydrostatic equilibrium, (6) kriging, (7) RTOPO-2 (Schaffer et al., 2016), (8) gravity inversion, (9) Millan et al. (2022b), (10) bathymetry data.

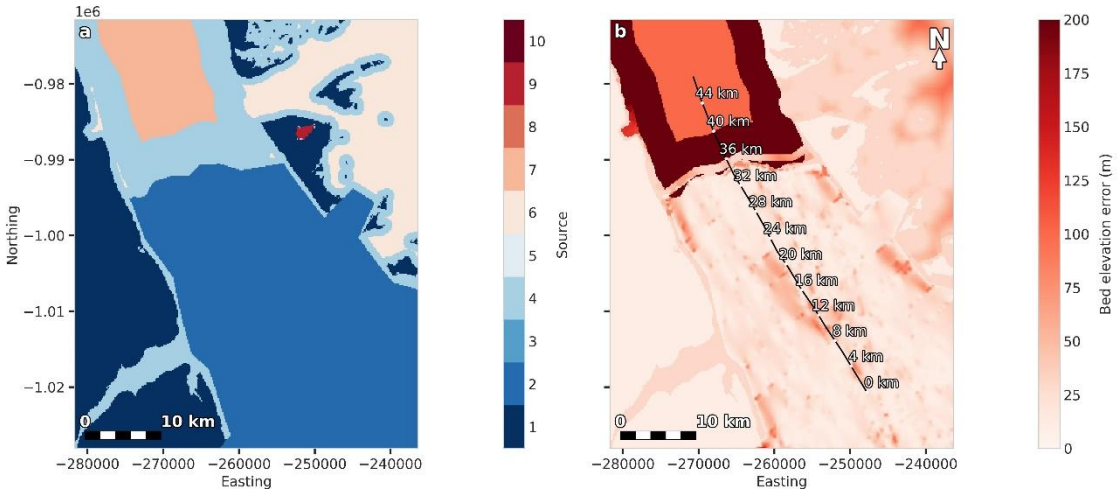


Figure B.3.15: Plots relating to the bed elevation source data type (a) and bed elevation error (b) of the BedMachine version 5 data for Petermann Gletsjer. In panel (a), the source data types are as follows: (1) GIMPDEM (Howat et al., 2014), (2) mass conservation, (3) synthetic, (4) interpolation, (5) hydrostatic equilibrium, (6) kriging, (7) RTOPO-2 (Schaffer et al., 2016), (8) gravity inversion, (9) Millan et al. (2022b), (10) bathymetry data.

# References

Abrams, M. et al. (2010) The ASTER global DEM. *Amer. Soc. Photogrammetry and Remote Sensing*, 76(4), 344–348.

Abrams, M. et al. (2020) ASTER Global Digital Elevation Model (GDEM) and ASTER Global Water Body Dataset (ASTWBD). *Remote Sensing*, 12(7), 1156.

Adegun, A.A. et al. (2023) Review of deep learning methods for remote sensing satellite images classification: experimental survey and comparative analysis. *Journal of Big Data*, 10(1), 93.

Åkesson, H. et al. (2021) Future Projections of Petermann Glacier Under Ocean Warming Depend Strongly on Friction Law. *Journal of Geophysical Research: Earth Surface*, 126(6).

Åkesson, H. et al. (2022) Petermann ice shelf may not recover after a future breakup. *Nature Communications*, 13(1), 2519.

von Albedyll, L. et al. (2018) Elevation changes of the Holm Land Ice Cap, northeast Greenland, from 1978 to 2012–2015, derived from high-resolution digital elevation models. *Arctic, Antarctic, and Alpine Research*, 50(1).

Alexander, A. et al. (2020) Pressure and inertia sensing drifters for glacial hydrology flow path measurements. *The Cryosphere*, 14(3), 1009–1023.

Alexander, P.M. et al. (2014) Assessing spatio-temporal variability and trends in modelled and measured Greenland Ice Sheet albedo (2000–2013). *The Cryosphere*, 8(6), 2293–2312.

Alley, R.B. et al. (1989) Sedimentation beneath ice shelves — the view from ice stream B. *Marine Geology*, 85(2–4), 101–120.

Arndt, P.S. & Fricker, H.A. (2024) A framework for automated supraglacial lake detection and depth retrieval in ICESat-2 photon data across the Greenland and Antarctic ice sheets. *The Cryosphere*, 18(11), 5173–5206.

Aschwanden, A. et al. (2019) Contribution of the Greenland Ice Sheet to sea level over the next millennium. *Science Advances*, 5(6).

Bannwart, J. et al. (2024) Elevation bias due to penetration of spaceborne radar signal on Grosser Aletschgletscher, Switzerland. *Journal of Glaciology*, 70(e1), 1–15.

Banwell, A.F. et al. (2014) Supraglacial lakes on the Larsen B ice shelf, Antarctica, and at Paakitsoq, West Greenland: a comparative study. *Annals of Glaciology*, 55(66), 1–8.

Bash, E.A. et al. (2018) Detecting Short-Term Surface Melt on an Arctic Glacier Using UAV Surveys. *Remote Sensing*, 10(10), 1547.

Benn, D. & Evans, D. (1997) *Glaciers and Glaciation*. 1st ed.

Benoit, L. et al. (2019) A high-resolution image time series of the Gorner Glacier – Swiss Alps – derived from repeated unmanned aerial vehicle surveys. *Earth System Science Data*, 11(2), 579–588.

Bessette-Kirton, E. et al. (2018) Using Stereo Satellite Imagery to Account for Ablation, Entrainment, and Compaction in Volume Calculations for Rock Avalanches on Glaciers: Application to the 2016 Lamplugh Rock Avalanche in Glacier Bay National Park, Alaska. *Journal of Geophysical Research: Earth Science*, 123(4), 622–641.

Bindschadler, R. et al. (2011) Getting around Antarctica: new high-resolution mappings of the grounded and freely-floating boundaries of the Antarctic ice sheet created for the International Polar Year. *The Cryosphere*, 5(3), 569–588.

Bowling, J. et al. (2021) *Surface outburst of a subglacial flood from the Greenland Ice Sheet*. Available at: doi:10.21203/rs.3.rs-569793/v1

Bowling, J.S. et al. (2019) Distribution and dynamics of Greenland subglacial lakes. *Nature Communications*, 10(1), 2810.

Box, J.E. & Ski, K. (2007) Remote sounding of Greenland supraglacial melt lakes: implications for subglacial hydraulics. *Journal of Glaciology*, 53(181), 257–265.

Brodský, L. et al. (2022) The Effect of Suspended Particulate Matter on the Supraglacial Lake Depth Retrieval from Optical Data. *Remote Sensing*, 14(23), 5988.

Brunt, K.M. et al. (2010) Mapping the grounding zone of the Ross Ice Shelf, Antarctica, using ICESat laser altimetry. *Annals of Glaciology*, 51(55), 71–79.

Brunt, K.M. et al. (2011) Analysis of ice plains of the Filchner–Ronne Ice Shelf, Antarctica, using ICESat laser altimetry. *Journal of Glaciology*, 57(205), 965–975.

Carrère, L. et al. (2022) A new barotropic tidal model for global ocean – FES2022. OSTST 2022 [PowerPoint presentation], 02 Nov. Available at https://ostst.aviso.altimetry.fr/fileadmin/user_upload/OSTST2022/Presentations/TID2022-A_new_barotropic_tide_model_for_global_ocean__FES2022.pdf (Accessed: 2025-11-17)

Chatterjee, R.S. et al. (2009) Interferometric SAR for characterization of ravines as a function of their density, depth, and surface cover. *ISPRS Journal of Photogrammetry and Remote Sensing*, 64(5), 472–481.

Chen, J. & Duan, Z. (2022) Monitoring Spatial-Temporal Variations of Lake Level in Western China Using ICESat-1 and CryoSat-2 Satellite Altimetry. *Remote Sensing*, 14(22), 5709.

Christie, F.D.W. et al. (2018) Glacier change along West Antarctica's Marie Byrd Land Sector and links to inter-decadal atmosphere–ocean variability. *The Cryosphere*, 12(7), 2461–2479.

Christoffersen, P. et al. (2011) Warming of waters in an East Greenland fjord prior to glacier retreat: mechanisms and connection to large-scale atmospheric conditions. *The Cryosphere*, 5(3), 701–714.

Christoffersen, P. et al. (2018) Cascading lake drainage on the Greenland Ice Sheet triggered by tensile shock and fracture. *Nature Communications*, 9(1), 1064.

Chudley, T.R. et al. (2019) Supraglacial lake drainage at a fast-flowing Greenlandic outlet glacier. *Proceedings of the National Academy of Sciences*, 116(51), 25468–25477.

Chudley, T.R. et al. (2025) Increased crevassing across accelerating Greenland Ice Sheet margins. *Nature Geoscience*, 18(2), 148–153.

Ciracì, E. et al. (2023) Melt rates in the kilometer-size grounding zone of Petermann Glacier, Greenland, before and during a retreat. *Proceedings of the National Academy of Sciences*, 120(20).

Clarke, G. K. C. (1976) Thermal Regulation of Glacier Surging. *Journal of Glaciology*, 16, 231–250.

Climate Change Initiative (2023) *ESA Greenland_Icesheet_CCI, Grounding Lines from SAR Interferometry*.

CNÉS (2024) *FES2022 (Finite Element Solution) Ocean Tide (Version 2022)*.

Corr, D. (2023) *Supraglacial hydrology extent and depth estimates for Greenland ice sheet from 2013 through 2022*. DOI: 10.5281/zenodo.7573884

Cowan, D. & Cooper, G. (2005) The Shuttle Radar Topography Mission—A New Source of Near-Global Digital Elevation Data. *Exploration Geophysics*, 36(4), 334–340.

Crabtree, R.D. & Doake, C.S.M. (1982) Pine Island Glacier and Its Drainage Basin: Results From Radio Echo-Sounding. *Annals of Glaciology*, 3, 65–70.

Cracknell, A. (1997) *The Advanced Very High Resolution Radiometer*.

Dai, C. et al. (2018) Estimating River Surface Elevation From ArcticDEM. *Geophysical Research Letters*, 45(7), 3107–3114.

Dai, C. et al. (2024) Applications of ArcticDEM for measuring volcanic dynamics, landslides, retrogressive thaw slumps, snowdrifts, and vegetation heights. *Science of Remote Sensing*, 9, 100130.

Das, S.B. et al. (2008) Fracture Propagation to the Base of the Greenland Ice Sheet During Supraglacial Lake Drainage. *Science*, 320(5877), 778–781.

Datta, R.T. & Wouters, B. (2021) Supraglacial lake bathymetry automatically derived from ICESat-2 constraining lake depth estimates from multi-source satellite imagery. *The Cryosphere*, 15(11), 5115–5132.

Dawid, W. & Pokonieczny, K. (2023) Generalization of digital elevation models for military passability maps development. *Advances in Cartography and GIScience of the ICA*, 4, 1–8.

Dawson, G.J. & Bamber, J.L. (2017) Antarctic Grounding Line Mapping From CryoSat-2 Radar Altimetry. *Geophysical Research Letters*, 44(23).

Dawson, G.J. & Bamber, J.L. (2020) Measuring the location and width of the Antarctic grounding zone using CryoSat-2. *The Cryosphere*, 14(6), 2071–2086.

Dell, R. et al. (2020) Lateral meltwater transfer across an Antarctic ice shelf. *The Cryosphere*, 14(7), 2313–2330.

Dell, R.L. et al. (2022) Supervised classification of slush and ponded water on Antarctic ice shelves using Landsat 8 imagery. *Journal of Glaciology*, 68(268), 401–414.

Dey, D. et al. (2024) Formation of the Atlantic Meridional Overturning Circulation lower limb is critically dependent on Atlantic-Arctic mixing. *Nature Communications*, 15(1), 7341.

Dietz, S. & Koninx, F. (2022) Economic impacts of melting of the Antarctic Ice Sheet. *Nature Communications*, 13(1), 5819.

Ditlevsen, P. & Ditlevsen, S. (2023) Warning of a forthcoming collapse of the Atlantic meridional overturning circulation. *Nature Communications*, 14(1), 4254.

Dong, Y. et al. (2022) Antarctic Ice-Sheet Meltwater Reduces Transient Warming and Climate Sensitivity Through the Sea-Surface Temperature Pattern Effect. *Geophysical Research Letters*, 49(24).

Drusch, M. et al. (2012) Sentinel-2: ESA's Optical High-Resolution Mission for GMES Operational Services. *Remote Sensing of Environment*, 120, 25–36.

Dunbar, M. (1978) Petermann Gletscher: possible source of a tabular iceberg off the coast of Newfoundland. *Journal of Glaciology*, 20(84), 595–597.

Dunmire, D. et al. (2025) Greenland Ice Sheet Wide Supraglacial Lake Evolution and Dynamics: Insights From the 2018 and 2019 Melt Seasons. *Earth and Space Science*, 12(2).

Ebi, K.L. et al. (2021) Extreme Weather and Climate Change: Population Health and Health System Implications. *Annual Review of Public Health*, 42(1), 293–315.

Echelmeyer, K. et al. (1991) Surficial glaciology of Jakobshavns Isbræ, West Greenland: Part I. Surface morphology. *Journal of Glaciology*, 37(127), 368–382.

Edwards, T. L. et al. (2014) Effect of uncertainty in surface mass balance-elevation feedback on projections of the future sea level contribution of the Greenland ice sheet. *The Cryosphere,* 8(1), 195–208.

Ehrenfeucht, S. et al. (2023) Seasonal Acceleration of Petermann Glacier, Greenland, From Changes in Subglacial Hydrology. *Geophysical Research Letters*, 50(1).

Etourneau, J. et al. (2019) Ocean temperature impact on ice shelf extent in the eastern Antarctic Peninsula. *Nature Communications*, 10(1), 304.

Fair, Z. et al. (2020) Using ICESat-2 and Operation IceBridge altimetry for supraglacial lake depth retrievals. *The Cryosphere*, 14(11), 4253–4263.

Farr, T.G. et al. (2007) The Shuttle Radar Topography Mission. *Reviews of Geophysics*, 45(2).

Fitzpatrick, A.A.W. et al. (2013) Ice flow dynamics and surface meltwater flux at a land-terminating sector of the Greenland ice sheet. *Journal of Glaciology*, 59(216), 687–696.

Fox, A.J. & Cooper, A.P.R. (1998) Climate-change indicators from archival aerial photography of the Antarctic Peninsula. *Annals of Glaciology*, 27, 636–642.

Fox-Kemper, B. et al. (2021) Climate Change 2021: The Physical Science Basis. Contribution of Working Group I to the Sixth Assessment Report of the Intergovernmental Panel on Climate Change. *Cambridge University Press*, 1211–1362.

Francis, C. R. et al. (2007) CryoSat mission and data description. *CS-RP-ESA-SY-0059*.

Freer, B.I.D. et al. (2023) Modes of Antarctic tidal grounding line migration revealed by Ice, Cloud, and land Elevation Satellite-2 (ICESat-2) laser altimetry. *The Cryosphere*, 17(9), 4079–4101.

Fricker, H.A. et al. (2009) Mapping the grounding zone of the Amery Ice Shelf, East Antarctica using InSAR, MODIS and ICESat. *Antarctic Science*, 21(5), 515–532.

Fricker, H.A. & Padman, L. (2006) Ice shelf grounding zone structure from ICESat laser altimetry. *Geophysical Research Letters*, 33(15).

Friedl, P. et al. (2018) Recent dynamic changes on Fleming Glacier after the disintegration of Wordie Ice Shelf, Antarctic Peninsula. *The Cryosphere*, 12(4), 1347–1365.

Friedl, P. et al. (2020) Remote sensing of glacier and ice sheet grounding lines: A review. *Earth-Science Reviews*, 201, 102948.

Gardner, A. S. et al. (2025). MEaSUREs ITS_LIVE Regional Glacier and Ice Sheet Surface Velocities. (NSIDC-0776, Version 2). [Data Set]. Boulder, Colorado USA. NASA National Snow and Ice Data Center Distributed Active Archive Center. https://doi.org/10.5067/JQ6337239C96. Date accessed: 20th November 2025.

Georgiou, S. et al. (2009) Seasonal evolution of supraglacial lake volume from ASTER imagery. *Annals of Glaciology*, 50(52), 95–100.

Girod, L. et al. (2015) Improvement of DEM generation from ASTER images using satellite jitter estimation and open source implementation. *The International Archives of the Photogrammetry, Remote Sensing and Spatial Information Sciences*, XL-1/W5, 249–253.

Girod, L. et al. (2017) MMASTER: Improved ASTER DEMs for Elevation Change Monitoring. *Remote Sensing*, 9(7), 704.

Glen, E. et al. (2025) A comparison of supraglacial meltwater features throughout contrasting melt seasons: southwest Greenland. *The Cryosphere*, 19(3), 1047–1066.

Goelzer, H. et al. (2017) Recent Progress in Greenland Ice Sheet Modelling. *Current Climate Change Reports*, 3(4), 291–302.

Gray, L. et al. (2002) RADARSAT interferometry for Antarctic grounding-zone mapping. *Annals of Glaciology*, 34, 269–276.

Greene, C.A. et al. (2024) Ubiquitous acceleration in Greenland Ice Sheet calving from 1985 to 2022. *Nature*, 625(7995), 523–528.

Grimes, M. et al. (2024) Spatial heterogeneity, terminus environment effects and acceleration in mass loss of glaciers and ice caps across Greenland. *Global and Planetary Change*, 239, 104505.

Hanna, E. et al. (2013) Ice-sheet mass balance and climate change. *Nature*, 498(7452), 51–59.

Harper, J. et al. (2012) Greenland ice-sheet contribution to sea-level rise buffered by meltwater storage in firn. *Nature*, 491(7423), 240–243.

Haseloff, M. & Sergienko, O. V. (2018) The effect of buttressing on grounding line dynamics. *Journal of Glaciology*, 64(245), 417–431.

Hazra, P. & Krishna, A.P. (2022) Assessment of Proglacial Lakes in Sikkim Himalaya, India for Glacial Lake Outburst Flood (GLOF) Risk Analysis using HEC-RAS and Geospatial Techniques. *Journal of the Geological Society of India*, 98(3), 344–352.

Herzfeld, U.C. et al. (2004) Derivation of deformation characteristics in fast-moving glaciers. *Computers & Geosciences*, 30(3), 291–302.

Herzfeld, U.C. et al. (2008) Elevation changes in Pine Island Glacier, Walgreen Coast, Antarctica, based on GLAS (2003) and ERS-1 (1995) altimeter data analyses and glaciological implications. *International Journal of Remote Sensing*, 29(19), 5533–5553.

Herzfeld, U.C. & Wallin, B. (2014) Spatio-temporal analysis of surface elevation changes in Pine Island Glacier, Antarctica, from ICESat GLAS data and ERS-1 radar altimeter data. *Annals of Glaciology*, 55(66), 248–258.

Higgins, A. (1991) North Greenland Glacier Velocities and Calf Ice Production. *Polarforschung*, 60(1), 1–23.

Higgins, A.K. (1988) Glacier velocities from aerial photographs in North and North-East Greenland. *Rapport Grønlands Geologiske Undersøgelse*, 140, 102–105.

Higgins, A.K. & Weidick, A. (1990) The world's northernmost surging glacier? *Zeitschrift für Gletscherkd. und Glazialgeol.*, 24(2), 111–123.

Hill, E.A. et al. (2017) A Review of Recent Changes in Major Marine-Terminating Outlet Glaciers in Northern Greenland. *Frontiers in Earth Science*, 4.

Hill, E.A. et al. (2018a) Dynamic changes in outlet glaciers in northern Greenland from 1948 to 2015. *The Cryosphere*, 12(10), 3243–3263.

Hill, E.A. et al. (2018b) Velocity response of Petermann Glacier, northwest Greenland, to past and future calving events. *The Cryosphere*, 12(12), 3907–3921.

Hill, E.A. et al. (2023) The stability of present-day Antarctic grounding lines – Part 1: No indication of marine ice sheet instability in the current geometry. *The Cryosphere*, 17(9), 3739–3759.

Hill, E.A. et al. (2024) Ocean warming as a trigger for irreversible retreat of the Antarctic ice sheet. *Nature Climate Change*, 14(11), 1165–1171.

Hogg, A.E. et al. (2016) Grounding line migration from 1992 to 2011 on Petermann Glacier, North-West Greenland. *Journal of Glaciology*, 62(236), 1104–1114.

Hogg, A.E. et al. (2018) Mapping ice sheet grounding lines with CryoSat-2. *Advances in Space Research*, 62(6), 1191–1202.

Holdsworth, G. (1969) Flexure of a Floating Ice Tongue. *Journal of Glaciology*, 8(54), 385–397.

Holland, D.M. et al. (2008) Acceleration of Jakobshavn Isbræ triggered by warm subsurface ocean waters. *Nature Geoscience*, 1(10), 659–664.

Holmes, F.A. et al. (2021) Calving at Ryder Glacier, Northern Greenland. *Journal of Geophysical Research: Earth Surface*, 126(4).

Horton, B.P. et al. (2020) Estimating global mean sea-level rise and its uncertainties by 2100 and 2300 from an expert survey. *npj Climate and Atmospheric Science*, 3(1), 18.

Hotaling, S. et al. (2021) Biological albedo reduction on ice sheets, glaciers, and snowfields. *Earth-Science Reviews*, 220, 103728.

Howat, I. et al. (2022) *The Reference Elevation Model of Antarctica - Strips, Version 4.1*.

Howat, I.M. et al. (2014) The Greenland Ice Mapping Project (GIMP) land classification and surface elevation data sets. *The Cryosphere*, 8(4), 1509–1518.

Hu, J. et al. (2021) Distribution and Evolution of Supraglacial Lakes in Greenland during the 2016–2018 Melt Seasons. *Remote Sensing*, 14(1), 55.

Hulbe, C.L. et al. (2016) Tidal bending and strand cracks at the Kamb Ice Stream grounding line, West Antarctica. *Journal of Glaciology*, 62(235), 816–824.

Humbert, A. et al. (2023) Precursor of disintegration of Greenland's largest floating ice tongue. *The Cryosphere*, 17(7), 2851–2870.

Husby, E. (2023) *Polar Geospatial Center SETSM Postprocessing Python batch_mask.py*. GitHub.

Ineson, J.R. & Peel, J.S. (1997) Cambrian shelf stratigraphy of North Greenland. *Geology of Greenland Survey Bulletin*, 173, 1–120.

Jacobel, R.W. et al. (1994) Studies of the grounding-line location on Ice Streams D and E, Antarctica. *Annals of Glaciology*, 20, 39–42.

Jóhannesson, T. et al. (2013) Ice-volume changes, bias estimation of mass-balance measurements and changes in subglacial lakes derived by lidar mapping of the surface of Icelandic glaciers. *Annals of Glaciology*, 54(63), 63–74.

Johansson, A.M. & Brown, I.A. (2012) Observations of supra-glacial lakes in west Greenland using winter wide swath Synthetic Aperture Radar. *Remote Sensing Letters*, 3(6), 531–539.

Joughin, I. et al. (1996) A Mini-Surge on the Ryder Glacier, Greenland, Observed by Satellite Radar Interferometry. *Science*, 274(5285), 228–230.

Joughin, I. et al. (2010) Greenland flow variability from ice-sheet-wide velocity mapping. *Journal of Glaciology*, 56(197), 415–430.

Joughin, I. et al. (2014) Brief Communication: Further summer speedup of Jakobshavn Isbræ. *The Cryosphere*, 8, 209–214.

Joughin, I. et al. (2016) Grounding line variability and subglacial lake drainage on Pine Island Glacier, Antarctica. *Geophysical Research Letters*, 43(17), 9093–9102.

Justice, C.O. et al. (1998) The Moderate Resolution Imaging Spectroradiometer (MODIS): land remote sensing for global change research. *IEEE Transactions on Geoscience and Remote Sensing*, 36(4), 1228–1249.

Kamb, B. (1985) Glacier Surge Mechanism: 1982-1983 Surge of Variegated Glacier, Alaska. *Science*¸ 277, 469–479.

Kappelsberger, M.T. et al. (2021) Modeled and Observed Bedrock Displacements in North-East Greenland Using Refined Estimates of Present-Day Ice-Mass Changes and Densified GNSS Measurements. *Journal of Geophysical Research: Earth Surface*, 126(4).

Kautz, L.-A. et al. (2022) Atmospheric blocking and weather extremes over the Euro-Atlantic sector – a review. *Weather and Climate Dynamics*, 3(1), 305–336.

Kelly, M.A. & Lowell, T. V. (2009) Fluctuations of local glaciers in Greenland during latest Pleistocene and Holocene time. *Quaternary Science Reviews*, 28(21–22), 2088–2106.

Kirk, J.T.O. (1989) The upwelling light stream in natural waters. *Limnology and Oceanography*, 34(8), 1410–1425.

Kochtitzky, W. & Copland, L. (2022) Retreat of Northern Hemisphere Marine-Terminating Glaciers, 2000–2020. *Geophysical Research Letters*, 49(3).

Konrad, H. et al. (2018) Net retreat of Antarctic glacier grounding lines. *Nature Geoscience*, 11(4), 258–262.

Krawczynski, M.J. et al. (2009) Constraints on the lake volume required for hydro-fracture through ice sheets. *Geophysical Research Letters*, 36(10).

Kulp, S.A. & Strauss, B.H. (2019) New elevation data triple estimates of global vulnerability to sea-level rise and coastal flooding. *Nature Communications*, 10(1), 4844.

Lampkin, D.J. & VanderBerg, J. (2011) A preliminary investigation of the influence of basal and surface topography on supraglacial lake distribution near Jakobshavn Isbrae, western Greenland. *Hydrological Processes*, 25(21), 3347–3355.

Lara, M.J. et al. (2025) A 20 m spatial resolution peatland extent map of Alaska. *Scientific Data*, 12(1), 226.

Laxon, S.W. et al. (2013) CryoSat-2 estimates of Arctic sea ice thickness and volume. *Geophysical Research Letters*, 40(4), 732–737.

Lea, J.M. (2018) The Google Earth Engine Digitisation Tool (GEEDiT) and the Margin change Quantification Tool (MaQiT) – simple tools for the rapid mapping and quantification of changing Earth surface margins. *Earth Surface Dynamics*, 6(3), 551–561.

Legleiter, C.J. et al. (2014) Mapping the bathymetry of supraglacial lakes and streams on the Greenland ice sheet using field measurements and high-resolution satellite images. *The Cryosphere*, 8(1), 215–228.

Leidman, S.Z. et al. (2021) The Presence and Widespread Distribution of Dark Sediment in Greenland Ice Sheet Supraglacial Streams Implies Substantial Impact of Microbial Communities on Sediment Deposition and Albedo. *Geophysical Research Letters*, 48(1).

Lenaerts, J.T.M. et al. (2019) Observing and Modeling Ice Sheet Surface Mass Balance. *Reviews of Geophysics*, 57(2), 376–420.

Li, G. et al. (2023a) Monitoring ice flow velocity of Petermann glacier combined with Sentinel-1 and −2 imagery. *International Journal of Applied Earth Observation and Geoinformation*, 121, 103374.

Li, J. & Zwally, H.J. (2011) Modeling of firn compaction for estimating ice-sheet mass change from observed ice-sheet elevation change. *Annals of Glaciology*, 52(59), 1–7.

Li, Q. et al. (2023b) Global Climate Impacts of Greenland and Antarctic Meltwater: A Comparative Study. *Journal of Climate*, 36(11), 3571–3590.

Li, T. et al. (2022) A high-resolution Antarctic grounding zone product from ICESat-2 laser altimetry. *Earth System Science Data*, 14(2), 535–557.

Li, T. et al. (2023c) Grounding line retreat and tide-modulated ocean channels at Moscow University and Totten Glacier ice shelves, East Antarctica. *The Cryosphere*, 17(2), 1003–1022.

Li, X. et al. (2015) Grounding line retreat of Totten Glacier, East Antarctica, 1996 to 2013. *Geophysical Research Letters*, 42(19), 8049–8056.

Li, X. et al. (2017) DEM generation from contours and a low-resolution DEM. *ISPRS Journal of Photogrammetry and Remote Sensing,* 134, 135–147.

Liu, Y. et al (2023) Bare-earth DEM generation from ArcticDEM and its use in flood simulation. *Natural Hazards and Earth System Sciences,* 23, 375–391.

Liston, G.E. et al. (2025) Modeling polar bear (Ursus maritimus) snowdrift den habitat on Alaska's Beaufort Sea coast using SnowDens-3D and ArcticDEM data. *Ecological Modelling*, 501, 110939.

Little, C.M. et al. (2019) The Relationship Between U.S. East Coast Sea Level and the Atlantic Meridional Overturning Circulation: A Review. *Journal of Geophysical Research: Oceans*, 124(9), 6435–6458.

Liu, S. et al. (2016) Attitude Jitter Detection Based on Remotely Sensed Images and Dense Ground Controls: A Case Study for Chinese ZY-3 Satellite. *IEEE Journal of Selected Topics in Applied Earth Observations and Remote Sensing*, 9(12), 5760–5766.

Livingstone, S.J. et al. (2022) Subglacial lakes and their changing role in a warming climate. *Nature Reviews Earth & Environment*, 3(2), 106–124.

Lutz, K. et al. (2024) Assessing supraglacial lake depth using ICESat-2, Sentinel-2, TanDEM-X, and in situ sonar measurements over Northeast and Southwest Greenland. *The Cryosphere*, 18(11), 5431–5449.

Lyard, F. et al. (2021) FES2014 global ocean tide atlas: design and performance. *Ocean Science*, 17, 615–649.

Lyard, F. et al. (n.d.) *FES2022 a step towards a SWOT-compliant tidal correction*.

Macdonald, G.J. et al. (2018) Seasonal evolution of supraglacial lakes on a floating ice tongue, Petermann Glacier, Greenland. *Annals of Glaciology*, 59(76pt1), 56–65.

Maier, N. et al. (2023) Wintertime Supraglacial Lake Drainage Cascade Triggers Large-Scale Ice Flow Response in Greenland. *Geophysical Research Letters*, 50(4).

Malczyk, G. et al. (2020) Repeat Subglacial Lake Drainage and Filling Beneath Thwaites Glacier. *Geophysical Research Letters*, 47(23).

Maritorena, S. et al. (1994) Diffuse reflectance of oceanic shallow waters: Influence of water depth and bottom albedo. *Limnology and Oceanography*, 39(7), 1689–1703.

Markus, T. et al. (2017) The Ice, Cloud, and land Elevation Satellite-2 (ICESat-2): Science requirements, concept, and implementation. *Remote Sensing of Environment*, 190, 260–273.

Marsh, O.J. et al. (2013) Tidally induced velocity variations of the Beardmore Glacier, Antarctica, and their representation in satellite measurements of ice velocity. *The Cryosphere*, 7(5), 1375–1384.

Mayer, C. et al. (2018) Large ice loss variability at Nioghalvfjerdsfjorden Glacier, Northeast-Greenland. *Nature Communications*, 9(1), 2768.

McCarthy, G.D. et al. (2023) Climate change impacts on ocean circulation relevant to the UK and Ireland. *Marine Climate Change Impacts Partnership*, 1–29.

Meccia, V.L. et al. (2024) Extreme cold events in Europe under a reduced AMOC. *Environmental Research Letters*, 19(1), 014054.

Meier, W.N. et al. (2021) *Sea Ice*.

Melling, L. et al. (2024) Evaluation of satellite methods for estimating supraglacial lake depth in southwest Greenland. *The Cryosphere*, 18(2), 543–558.

Melton, S.M. et al. (2022) Meltwater drainage and iceberg calving observed in high-spatiotemporal resolution at Helheim Glacier, Greenland. *Journal of Glaciology*, 68(270), 812–828.

Le Meur, E. et al. (2014) Two independent methods for mapping the grounding line of an outlet glacier – an example from the Astrolabe Glacier, Terre Adélie, Antarctica. *The Cryosphere*, 8(4), 1331–1346.

Michaels, A.F. & Silver, M.W. (1988) Primary production, sinking fluxes and the microbial food web. *Deep Sea Research Part A. Oceanographic Research Papers*, 35(4), 473–490.

Miles, K.E. et al. (2017) Toward Monitoring Surface and Subsurface Lakes on the Greenland Ice Sheet Using Sentinel-1 SAR and Landsat-8 OLI Imagery. *Frontiers in Earth Science*, 5.

Milillo, P. et al. (2019) Heterogeneous retreat and ice melt of Thwaites Glacier, West Antarctica. *Science Advances*, 5(1).

Milillo, P. et al. (2022) Rapid glacier retreat rates observed in West Antarctica. *Nature Geoscience*, 15(1), 48–53.

Millan, R. et al. (2022a) Ongoing grounding line retreat and fracturation initiated at the Petermann Glacier ice shelf, Greenland after 2016. *The Cryosphere*, 16, 3021–3031.

Millan, R. et al. (2022b) Ice velocity and thickness of the world's glaciers. *Nature Geoscience*, 15, 124–129.

Millan, R. et al. (2023) Rapid disintegration and weakening of ice shelves in North Greenland. *Nature Communications*, 14(1), 6914.

Mitcham, T. et al. (2022) The instantaneous impact of calving and thinning on the Larsen C Ice Shelf. *The Cryosphere*, 16(3), 883–901.

Mohajerani, Y. et al. (2021) Automatic delineation of glacier grounding lines in differential interferometric synthetic-aperture radar data using deep learning. *Scientific Reports*, 11(1), 4992.

Möller, M. et al. (2022) Grounding Line Retreat and Ice Discharge Variability at Two Surging, Ice Shelf-Forming Basins of Flade Isblink Ice Cap, Northern Greenland. *Journal of Geophysical Research: Earth Surface*, 127(2).

Morlighem, M. et al. (2013) High-resolution bed topography mapping of Russell Glacier, Greenland, inferred from Operation IceBridge data. *Journal of Glaciology*, 59(218), 1015–1023.

Morlighem, M. et al. (2017) BedMachine v3: Complete Bed Topography and Ocean Bathymetry Mapping of Greenland From Multibeam Echo Sounding Combined With Mass Conservation. *Geophysical Research Letters*, 44(21).

Morlighem, M. et al. (2022) *IceBridge BedMachine Greenland, Version 5*. Available at: doi:10.1002/2017GL074954

Morlighem, M. (2022) *MEaSUREs BedMachine Antarctica. (NSIDC-0756, Version 3)*. NASA National Snow and Ice Data Center Distributed Active Archive Center.

Mouginot, J. et al. (2015) Fast retreat of Zachariæ Isstrøm, northeast Greenland. *Science*, 350(6266), 1357–1361.

Mouginot, J. et al. (2018) Insights on the Surge Behavior of Storstrømmen and L. Bistrup Bræ, Northeast Greenland, Over the Last Century. *Geophysical Research Letters*, 45(20).

Moussavi, M. et al. (2020) Antarctic Supraglacial Lake Detection Using Landsat 8 and Sentinel-2 Imagery: Towards Continental Generation of Lake Volumes. *Remote Sensing*, 12(1), 134.

Moussavi, M.S. et al. (2016) Derivation and validation of supraglacial lake volumes on the Greenland Ice Sheet from high-resolution satellite imagery. *Remote Sensing of Environment*, 183, 294–303.

Münchow, A. et al. (2014) Interannual changes of the floating ice shelf of Petermann Gletscher, North Greenland, from 2000 to 2012. *Journal of Glaciology*, 60(221), 489–499.

Nelson, C.H. (2021) Climate Change Patterns. In: Springer International Publishing *Witness To A Changing Earth*. [Online]. Cham: Springer International Publishing. Available at: doi:10.1007/978-3-030-71811-4_5

Neumann, T.A. et al. (2019) The Ice, Cloud, and Land Elevation Satellite – 2 mission: A global geolocated photon product derived from the Advanced Topographic Laser Altimeter System. *Remote Sensing of Environment*, 233, 111325.

Nick, F.M. et al. (2013) Future sea-level rise from Greenland's main outlet glaciers in a warming climate. *Nature*, 497(7448), 235–238.

Noh, M.-J. & Howat, I.M. (2015) Automated stereo-photogrammetric DEM generation at high latitudes: Surface Extraction with TIN-based Search-space Minimization (SETSM) validation and demonstration over glaciated regions. *GIScience & Remote Sensing*, 52(2), 198–217.

Noh, M.-J. & Howat, I.M. (2017) The Surface Extraction from TIN based Search-space Minimization (SETSM) algorithm. *ISPRS Journal of Photogrammetry and Remote Sensing*, 129, 55–76.

North, R. & Barrows, T.T. (2024) High-resolution elevation models of Larsen B glaciers extracted from 1960s imagery. *Scientific Reports*, 14(1), 14536.

Nuth, C. & Kääb, A. (2011) Co-registration and bias corrections of satellite elevation data sets for quantifying glacier thickness change. *The Cryosphere*, 5(1), 271–290.

Onuma, Y. et al. (2023) Modelling the development and decay of cryoconite holes in northwestern Greenland. *The Cryosphere*, 17(8), 3309–3328.

Otosaka, I.N. et al. (2023) Mass balance of the Greenland and Antarctic ice sheets from 1992 to 2020. *Earth System Science Data*, 15(4), 1597–1616.

Otto, J. et al. (2022) Supraglacial lake expansion, intensified lake drainage frequency, and first observation of coupled lake drainage, during 1985–2020 at Ryder Glacier, Northern Greenland. *Frontiers in Earth Science*, 10, 978137.

Padman, L. et al. (2018) Ocean Tide Influences on the Antarctic and Greenland Ice Sheets. *Reviews of Geophysics*, 56(1), 142–184.

Palmer, S. et al. (2025) A quantile regression forest estimate of Greenland's subglacial topography. *Journal of Glaciology,* 71, e115.

Palmer, S. et al. (2015) Subglacial lake drainage detected beneath the Greenland ice sheet. *Nature Communications*, 6(1), 8408.

Palmer, S.J. et al. (2010) InSAR observations of ice elevation and velocity fluctuations at the Flade Isblink ice cap, eastern North Greenland. *Journal of Geophysical Research: Earth Surface*, 115(F4).

Parizek, B.R. & Alley, R.B. (2004) Implications of increased Greenland surface melt under global-warming scenarios: ice-sheet simulations. *Quaternary Science Reviews*, 23(9–10), 1013–1027.

Park, J.W. et al. (2013) Sustained retreat of the Pine Island Glacier. *Geophysical Research Letters*, 40(10), 2137–2142.

Parrish, C. et al. (2019) Validation of ICESat-2 ATLAS Bathymetry and Analysis of ATLAS's Bathymetric Mapping Performance. *Remote Sensing*, 11(14), 1634.

Pawlowicz, E. (1972) Airborne Radar Sounding of the Greenland Ice Sheet. *The Ohio Journal of Science*, 72(5), 266–275.

Peary, R.E. (1887) A Reconnoissance of the Greenland Inland Ice. *Journal of the American Geographical Society of New York*, 19, 261.

Philpot, W. (1987) Radiative transfer in stratified waters: a single-scattering approximation for irradiance. *Applied Optics*, 26(19), 4123–4132.

Philpot, W.D. (1989) Bathymetric mapping with passive multispectral imagery. *Applied Optics*, 28(8), 1569.

Pope, A. et al. (2016) Estimating supraglacial lake depth in West Greenland using Landsat 8 and comparison with other multispectral methods. *The Cryosphere*, 10(1), 15–27.

Porter, C. et al. (2022) *ArcticDEM – Strips, Version 4.1*.

Porter, C. et al. (2023) ArcticDEM - Mosaics, Version 4.1. *Harvard Dataverse*.

Powell, R.D. et al. (1996) Observations of the grounding-line area at a floating glacier terminus. *Annals of Glaciology*, 22, 217–223.

Ravinder, N. et al. (2024) Greenland Ice Sheet Elevation Change From CryoSat-2 and ICESat-2. *Geophysical Research Letters*, 51(24).

Rea, B.R. & Evans, D.J.A. (2011) An assessment of surge-induced crevassing and the formation of crevasse squeeze ridges. *Journal of Geophysical Research*, 116(F4), F04005.

Reeh, N. et al. (1994) Surge of Storstrømmen, a large outlet glacier from the inland ice of north-east Greenland. *Rapport Grønlands Geologiske Undersøgelse*, 162, 201–209.

Reeh, N. (2017) *Greenland Ice Shelves and Ice Tongues*. [Online]. Available at: doi:10.1007/978-94-024-1101-0_4

Reese, R. et al. (2023) The stability of present-day Antarctic grounding lines – Part 2: Onset of irreversible retreat of Amundsen Sea glaciers under current climate on centennial timescales cannot be excluded. *The Cryosphere*, 17(9), 3761–3783.

Ren, S. et al. (2024) Changes in glacier surface temperature across the Third Pole from 2000 to 2021. *Remote Sensing of the Environment,* 305.

Riedel, B. et al. (1999) The response of the Ekströmisen (Antarctica) grounding zone to tidal forcing. *Annals of Glaciology*, 29, 239–242.

Rignot, E. et al. (2001) Contribution to the glaciology of northern Greenland from satellite radar interferometry. *Journal of Geophysical Research: Atmospheres*, 106(D24), 34007–34019.

Rignot, E. et al. (2003) Contribution of the Patagonia Icefields of South America to Sea Level Rise. *Science*, 302(5644), 434–437.

Rignot, E. et al. (2011) Antarctic grounding line mapping from differential satellite radar interferometry. *Geophysical Research Letters*, 38(10), n/a-n/a.

Rignot, E. et al. (2012) Spreading of warm ocean waters around Greenland as a possible cause for glacier acceleration. *Annals of Glaciology*, 53(60), 257–266.

Rignot, E. & Kanagaratnam, P. (2006) Changes in the Velocity Structure of the Greenland Ice Sheet. *Science*, 311(5763), 986–990.

Rignot, E. & Steffen, K. (2008) Channelized bottom melting and stability of floating ice shelves. *Geophysical Research Letters*, 35(2).

Rivera, A. et al. (2005) Ice-elevation changes of Glaciar Chico, southern Patagonia, using ASTER DEMs, aerial photographs and GPS data. *Journal of Glaciology*, 51(172), 105–112.

Roberts et al. (2024) The deglacial history of 79N glacier and the Northeast Greenland Ice Stream. *Quaternary Science Reviews,* 336, 108770.

Robin, G. (1975) Radio-echo sounding: glaciological interpretations and applications. *Journal of Glaciology*, 15(73), 49–64.

Roscoe, J. (1952) Contributions to the Study of Antarctic Surface Features by Photogeographical Methods.

Ross, N. et al. (2024) Automated grounding line delineation using deep learning and phase gradient-based approaches on COSMO-SkyMed DInSAR data. *Remote Sensing of Environment*, 315, 114429.

Rossini, M. et al. (2018) Rapid melting dynamics of an alpine glacier with repeated UAV photogrammetry. *Geomorphology*, 304, 159–172.

Roy, D.P. et al. (2014) Landsat-8: Science and product vision for terrestrial global change research. *Remote Sensing of Environment*, 145, 154–172.

Ruiz-Lendínez, J.J. et al. (2023) Deep learning methods applied to digital elevation models: state of the art. *Geocarto International*, 38(1).

Scambos, T. et al. (2021) How fast is the Greenland ice sheet melting? *Arctic, Antarctic, and Alpine Research*, 53(1), 221–222.

Schaffer, J. et al. (2016) A global, high-resolution data set of ice sheet topography, cavity geometry, and ocean bathymetry. *Earth System Science Data*, 8(2), 543–557.

Schmidt, B.E. et al. (2023) Heterogeneous melting near the Thwaites Glacier grounding line. *Nature*, 614(7948), 471–478.

Schmittner, A. (2005) Decline of the marine ecosystem caused by a reduction in the Atlantic overturning circulation. *Nature*, 434(7033), 628–633.

Schoof, C. (2007) Ice sheet grounding line dynamics: Steady states, stability, and hysteresis. *Journal of Geophysical Research: Earth Surface*, 112(F3).

Schoof, C. (2010) Ice-sheet acceleration driven by melt supply variability. *Nature*, 468(7325), 803–806.

Schoof, C. et al. (2017) Boundary layer models for calving marine outlet glaciers. *The Cryosphere*, 11(5), 2283–2303.

Schröder, L. et al. (2020) Perennial Supraglacial Lakes in Northeast Greenland Observed by Polarimetric SAR. *Remote Sensing*, 12(17), 2798.

Schutz, B.E. et al. (2005) Overview of the ICESat Mission. *Geophysical Research Letters*, 32(21).

Schwans, E. et al. (2023) Model insights into bed control on retreat of Thwaites Glacier, West Antarctica. *Journal of Glaciology*, 69(277), 1241–1259.

Seehaus, T. et al. (2020) Novel Techniques for Void Filling in Glacier Elevation Change Data Sets. *Remote Sensing*, 12(23), 3917.

Selmes, N. et al. (2013) *Characterizing supraglacial lake drainage and freezing on the Greenland Ice Sheet*. Available at: doi:10.5194/tcd-7-475-2013

Sergienko, O. V. & Wingham, D.J. (2022) Bed topography and marine ice-sheet stability. *Journal of Glaciology*, 68(267), 124–138.

Shean, D.E. et al. (2019) Ice shelf basal melt rates from a high-resolution digital elevation model (DEM) record for Pine Island Glacier, Antarctica. *The Cryosphere*, 13(10), 2633–2656.

Shen, X. et al. (2022) A new digital elevation model (DEM) dataset of the entire Antarctic continent derived from ICESat-2. *Earth System Science Data*, 14(7), 3075–3089.

Shiggins, C.J. et al. (2023) Automated ArcticDEM iceberg detection tool: insights into area and volume distributions, and their potential application to satellite imagery and modelling of glacier–iceberg–ocean systems. *The Cryosphere*, 17(1), 15–32.

Siddique, M.A. et al. (2024) *Glacial Lake Outburst Flood Risk Assessment Using Logistic Regression of Remote Sensing Parameters in High Mountain Asia*. In: IEEE, Jul 7, 2024. IEEE. Available at: doi:10.1109/IGARSS53475.2024.10642557

Slater, T. et al. (2018) A new digital elevation model of Antarctica derived from CryoSat-2 altimetry. *The Cryosphere*, 12(4), 1551–1562.

Slater, T. et al. (2020) Ice-sheet losses track high-end sea-level rise projections. *Nature Climate Change*, 10(10), 879–881.

Slater, T. et al. (2021) Increased variability in Greenland Ice Sheet runoff from satellite observations. *Nature Communications*, 12(1), 6069.

Smith, B. et al. (2019) Land ice height-retrieval algorithm for NASA's ICESat-2 photon-counting laser altimeter. *Remote Sensing of Environment*, 233, 111352.

Smith, B.E. et al. (2023) Evaluating Greenland surface-mass-balance and firn-densification data using ICESat-2 altimetry. *The Cryosphere*, 17(2), 789–808.

Smith, R.C. & Baker, K.S. (1981) Optical properties of the clearest natural waters (200–800 nm). *Applied Optics*, 20(2), 177.

Smith, R.S. et al. (2021) Coupling the U.K. Earth System Model to Dynamic Models of the Greenland and Antarctic Ice Sheets. *Journal of Advances in Modeling Earth Systems*, 13(10).

Sneed, W.A. & Hamilton, G.S. (2007) Evolution of melt pond volume on the surface of the Greenland Ice Sheet. *Geophysical Research Letters*, 34(3).

Sneed, W.A. & Hamilton, G.S. (2011) Validation of a method for determining the depth of glacial melt ponds using satellite imagery. *Annals of Glaciology*, 52(59), 15–22.

Solgaard, A.M. et al. (2020) Hagen Bræ: A Surging Glacier in North Greenland—35 Years of Observations. *Geophysical Research Letters*, 47(6).

Stearns, L.A. (2011) Dynamics and mass balance of four large East Antarctic outlet glaciers. *Annals of Glaciology*, 52(59), 116–126.

Straneo, F. et al. (2010) Rapid circulation of warm subtropical waters in a major glacial fjord in East Greenland. *Nature Geoscience*, 3(3), 182–186.

Stranne, C. et al. (2021) The climate sensitivity of northern Greenland fjords is amplified through sea-ice damming. *Communications Earth & Environment*, 2(1), 70.

Stroeve, J.C. et al. (2012) The Arctic's rapidly shrinking sea ice cover: a research synthesis. *Climatic Change*, 110(3–4), 1005–1027.

Studinger, M. et al. (2022) High-resolution imaging of supraglacial hydrological features on the Greenland Ice Sheet with NASA's Airborne Topographic Mapper (ATM) instrument suite. *The Cryosphere*, 16(9), 3649–3668.

Sundal, A.V. et al. (2009) Evolution of supra-glacial lakes across the Greenland Ice Sheet. *Remote Sensing of Environment*, 113(10), 2164–2171.

Sutterley, T.C. et al. (2017) *pyTMD: Python-based tidal prediction software*. Zenodo.

Sverdrup, H.U. et al. (1942) *The Oceans: Their Physics, Chemistry, and General Biology*.

Sykes, H.J. et al. (2009) The location of the grounding zone of Evans Ice Stream, Antarctica, investigated using SAR interferometry and modelling. *Annals of Glaciology*, 50(52), 35–40.

Tarr, R.S. (1897) The Glaciers of Greenland. *Scientific American*, 76(14), 216–218.

Tedesco, M. et al. (2013) Ice dynamic response to two modes of surface lake drainage on the Greenland ice sheet. *Environmental Research Letters*, 8(3), 034007.

Tedesco, M. & Steiner, N. (2011) In-situ multispectral and bathymetric measurements over a supraglacial lake in western Greenland using a remotely controlled watercraft. *The Cryosphere*, 5(2), 445–452.

Tedstone, A.J. et al. (2013) Greenland ice sheet motion insensitive to exceptional meltwater forcing. *Proceedings of the National Academy of Sciences of the United States of America*, 110(49) 19719–12724.

The IMBIE Team (2020) Mass balance of the Greenland Ice Sheet from 1992 to 2018. *Nature*, 579(7798), 233–239.

Tuckett, P.A. et al. (2019) Rapid accelerations of Antarctic Peninsula outlet glaciers driven by surface melt. *Nature Communications*, 10(1), 4311.

Turton, J. V. et al. (2021) The distribution and evolution of supraglacial lakes on 79° N Glacier (north-eastern Greenland) and interannual climatic controls. *The Cryosphere*, 15(8), 3877–3896.

Uratsuka, S. et al. (1996) Internal and basal ice changes near the grounding line derived from radio-echo sounding. *Journal of Glaciology*, 42(140), 103–109.

Vaughan, D.G. (1994) Investigating tidal flexure on an ice shelf using kinematic GPS. *Annals of Glaciology*, 20, 372–376.

Vaughan, D.G. (1995) Tidal flexure at ice shelf margins. *Journal of Geophysical Research: Solid Earth*, 100(B4), 6213–6224.

Vermassen, F. et al. (2020) A Major Collapse of Kangerlussuaq Glacier's Ice Tongue Between 1932 and 1933 in East Greenland. *Geophysical Research Letters*, 47(4).

Wallis, B.J. et al. (2024) Change in grounding line location on the Antarctic Peninsula measured using a tidal motion offset correlation method. *The Cryosphere*, 18(10), 4723–4742.

Wang, J. and He, X. (2025) Accuracy assessment of ocean tide models in the eastern China marginal seas using tide gauge and GPS data. *Journal of Marine Science and Engineering*, 13(3), 395.

Wang, G. et al. (2024) Accelerated Basal Melt Rates of Ice Shelves in North Greenland From 2013 to 2022 Estimated With the High-Resolution ArcticDEM. *Journal of Geophysical Research: Oceans*, 129(12).

Warren, S. (1982) Optical Properties of Snow. *Reviews of Geophysics and Space Physics*, 20(1), 67–89.

Warren, S. (2019) Optical properties of ice and snow. *Philosophical Transactions of the Royal Society A*, 377(2146), 20180161.

Washam, P. et al. (2018) A Decade of Ocean Changes Impacting the Ice Shelf of Petermann Gletscher, Greenland. *Journal of Physical Oceanography*, 48(10), 2477–2493.

Wehrlé, A. et al. (2021) Greenland bare-ice albedo from PROMICE automatic weather station measurements and Sentinel-3 satellite observations. *GEUS Bulletin*, 47.

Weidick, A. (1968) Observations on some Holocene glacier fluctuations in West Greenland. *Bulletin Grønlands Geologiske Undersøgelse*, 73, 1–202.

Weidick, A. et al. (1996) Neoglacial glacier changes around Storstrommen, north-east Greenland. *Polarforschung*, 64(3), 95–108.

Wekerle, C. et al. (2024) Atlantic Water warming increases melt below Northeast Greenland's last floating ice tongue. *Nature Communications*, 15(1), 1336.

van Westen, R.M. et al. (2024) Physics-based early warning signal shows that AMOC is on tipping course. *Science Advances*, 10(6).

Williamson, A.G. et al. (2017) A Fully Automated Supraglacial lake area and volume Tracking ("FAST") algorithm: Development and application using MODIS imagery of West Greenland. *Remote Sensing of Environment*, 196, 113–133.

Williamson, A.G. et al. (2018) Dual-satellite (Sentinel-2 and Landsat 8) remote sensing of supraglacial lakes in Greenland. *The Cryosphere*, 12(9), 3045–3065.

Wilson, N. et al. (2017) Satellite-derived submarine melt rates and mass balance (2011–2015) for Greenland's largest remaining ice tongues. *The Cryosphere*, 11(6), 2773–2782.

Winstrup, M. et al. (2024) PRODEM: an annual series of summer DEMs (2019 through 2022) of the marginal areas of the Greenland Ice Sheet. *Earth System Science Data*, 16(11), 5405–5428.

WMO et al. (2022) *The 2022 GCOS ECVs Requirements (GCOS 245)*. Geneva.

Wulder, M.A. et al. (2022) Fifty years of Landsat science and impacts. *Remote Sensing of Environment*, 280, 113195.

XDEM Contributors (2023) *xdem*.

Xiao, W. et al. (2023) An automated algorithm to retrieve the location and depth of supraglacial lakes from ICESat-2 ATL03 data. *Remote Sensing of Environment*, 298, 113730.

Yang, B. et al. (2022) An elevation change dataset in Greenland ice sheet from 2003 to 2020 using satellite altimetry data. *Big Earth Data*, 8(2), 231–248.

Yang, K. et al. (2019) Surface meltwater runoff on the Greenland ice sheet estimated from remotely sensed supraglacial lake infilling rate. *Remote Sensing of Environment*, 234, 111459.

Yang, W. et al. (2020) Seasonal Dynamics of a Temperate Tibetan Glacier Revealed by High-Resolution UAV Photogrammetry and In Situ Measurements. *Remote Sensing*, 12(15), 2389.

Zeising, O. et al. (2024) Extreme melting at Greenland's largest floating ice tongue. *The Cryosphere*, 18(3), 1333–1357.

Zhang, B. et al. (2022) A 30-year monthly 5 km gridded surface elevation time series for the Greenland Ice Sheet from multiple satellite radar altimeters. *Earth System Science Data*, 14(2), 973–989.

Zhao, C. et al. (2025) Unmanned Aerial Vehicle Technology for Glaciology Research in the Third Pole. *Drones*, 9(4), 254-271.

Zhou, Q. et al. (2025) Supraglacial Lake Depth Retrieval from ICESat-2 and Multispectral Imagery Datasets. *Journal of Remote Sensing*, 5.

Zink, M. et al. (2007) *The TanDEM-X mission: Overview and status*. In: IEEE, 2007. IEEE. Available at: doi:10.1109/IGARSS.2007.4423711

Zwally, H.J. et al. (2002) Surface Melt-Induced Acceleration of Greenland Ice-Sheet Flow. *Science*, 297(5579), 218–222.